https://ntrs.nasa.gov/search.jsp?R=19950002741 2020-06-16T11:54:19+00:00Z

(NASA-CR-196312) NASA PROPULSION ENGINEERING RESEARCH CENTER, VOLUME 2 Annual Report, 1994 (Pennsylvania State Univ.) 234 p

N95-70861
--THRU--
N95-70907
Unclas

Z9/12 0042850

415463 238P

PENNSTATE

1855

PROPULSION ENGINEERING RESEARCH CENTER

1994 ANNUAL REPORT

VOLUME II

NOVEMBER, 1994

A UNIVERSITY SPACE ENGINEERING RESEARCH CENTER

SIXTH ANNUAL SYMPOSIUM
SEPTEMBER 13-14, 1994

106 RESEARCH BUILDING EAST
UNIVERSITY PARK, PENNSYLVANIA 16801

NASA PROPULSION ENGINEERING RESEARCH CENTER
ANNUAL REPORT 1994
VOLUME II

SIXTH ANNUAL SYMPOSIUM

SEPTEMBER 13-14, 1994
THE NASA LEWIS RESEARCH CENTER
CLEVELAND, OH

THE PENNSYLVANIA STATE UNIVERSITY
UNIVERSITY PARK, PA

TABLE OF CONTENTS

TABLE OF CONTENTS
(Continued)

Propulsion Engineering Research Center
Sixth Annual Symposium
NASA Lewis Research Center
Cleveland, Ohio
September 13-14, 1994

esday Morning, September 13

ministration Building

0 - 8:00 Registration and Continental Breakfast

ministration Building Auditorium

0 - 8:15 Welcome and Introductory Remarks - *L. Diehl, Chief of Space Propulsion Technology, Lewis Research Center; C. Merkle, Director of Propulsion Engineering Research Center, PSU*

Combustors and Nozzles *Chaired by G. Cox, Pratt & Whitney*

5 - 8:40 Rapid Prototype Fabrication Processes for High Performance Thrust Cells - *K. Hunt, T. Chwiedor, S. Diab, and R. Williams, Rocketdyne*

0 - 9:05 Multi-Dimensional Combustor Flowfield Analyses in a Gas-Gas Rocket Engine - *H.-H. Tsuei and C. Merkle, PSU*

)5 - 9:30 Thrust Augmentation of a Shrouded Nozzles - *O. Patton, Cleveland State University, and L. Liou, Lewis Research Center*

)0 - 9:55 NASA Lewis Advanced Subsonic Combustor Program Overview - *C.-M. Lee, Lewis Research Center*

)5 - 10:20 Characteristics of a Trapped Vortex (TV) Combustor - *W.M. Roquemore, Wright Laboratory, and K.-Y. Shu, L. Goss, and D. Trump, Systems Research Laboratory*

:20 - 10:40 Break

:40- 11:05 Density and Mixture Fraction Measurements in a GO_2/GH_2 Uni-element Rocket Chamber - *M. Moser, S. Pal, and R. Santoro, PSU*

:05 - 11:30 CFD Assessment of the Carbon Monoxide and Nitric Oxide Formation from RD-170 Hot-Fire Testing at MSFC- *T.-S. Wang and P. McConnaughey, Marshall Space Flight Center, S. Warsi, Sverdrup, and Y.-S. Chen, ESI, Inc.*

:30 - 11:55 The Effect of Incomplete Fuel-Air Mixing on the Lean Blowout Limit, Lean Stability Limit, and NO_x Emissions in Lean Premixed Gas Turbine Combustors - *W.-P. Shih, J.G. Lee, and D. Santavicca, PSU*

:55 - 12:20 Performance of Ablative Chambers - *H. Trinh, Marshall Space Flight Center*

dministration Building, Room 225

Turbomachinery Aero- and Hydro-Dynamics *Chaired by M. Proctor, Lewis Research Center*

15 - 8:40 Axial and Centrifugal Pump Meanline Performance Analysis - *J. Veres, Lewis Research Center*

40 - 9:05 SIMPLEX Turbopump Design - *M. Marsh and P. Cowan, Marshall Space Flight Center*

05 - 9:30 Computational Fluid Dynamics Analysis in Support of SIMPLEX Turbopump Design - *R. Garcia, T. Benjamin, R. Williams, L. Griffin, J. Ruf, and J. Cornelison, Marshall Space Flight Center*

30 - 9:55 Computation and Modeling of Aero-thermal Fields in Turbine Cascades and Strongly Curved Ducts - *J. Luo and B. Lakshminarayana, PSU*

:55 - 10:20 CFD in the Design of a Water-Jet-Drive System - *R. Garcia, Marshall Space Flight Center*

On - Board Propulsion Systems *Chaired by D. Byers, Lewis Research Center*

0:40 - 11:05 Performance Testing of a Fixed Configuration Microwave Arcjet Thruster - *D. Sullivan and M. Micci, PSU*

1:05 - 11:30 Orbital Maneuvering and Reaction Control Engines - *E. Hurlbert, Johnson Space Center*

1:30 - 11:55 Technology Advancements for On-Board Propulsion Systems - *D. Byers, Lewis Research Center*

1:55 - 12:20 Interface Issues for On-Board Propulsion Systems - *F. Curran and S. Schneider, Lewis Research Center*

Tuesday Afternoon, September 13

Cafeteria

12:45 - 1:30 Lunch

Administration Building Auditorium

Advanced Propulsion Applications *Chaired by G. Madzsar, Lewis Research Center*

1:45 - 2:10 Coupling Gravity, Electromagnetism, and Space-Time for Space Propulsion Breakthroughs - *M. Millis, Lewis Research Center*

2:10 - 2:35 Antiproton Catalyzed Microfission/fusion Propulsion - *P.-R. Chiang, R. Lewis, G. Smith, R. Newton, J. Dailey, W. Werthman, and S. Chakrabarti, PSU*

2:35 - 3:00 Advanced Propulsion at JPL - *R. Frisbee, Jet Propulsion Laboratory*

3:00 - 3:20 Break

3:20 - 3:45 Magnetobraking: Use of Tether Electrodynamic Drag for Earth Return from Mars - *G. Landis, NYMA*

3:45 - 4:10 Low-Cost Booster and High-Performance Orbit Insertion Propulsion - *R. Sackheim, TRW*

4:10 - 4:35 Strutjet-Powered Reusable Launch Vehicles - *A. Siebenhaar and M. Bulman, Aerojet, and S. Sasso and J. Schnackel, Martin Marietta*

4:35 - 5:00 Technology Needs for Single Stage to Orbit Propulsion - *S. Stoyanof and J. Monk, Marshall Space Flight Center*

Administration Building, Room 225

Vaporization and Combustion *Chaired by R. Woodward, Phillips Laboratory*

1:45 - 2:10 LOX Droplet Vaporization in a Supercritical Forced Convective Environment - *C.C. Hsiao and V. Yang, PSU*

2:10 - 2:35 Shadowgraphy of Transcritical Cryogenic Fluids - *R. Woodward and D. Talley, Phillips Laboratory, and T. Anderson and M. Winter, UTRC*

2:35 - 3:00 High Energy Laser as a Combustion Stability Rating Device - *K. Breisacher and L. Liou, Lewis Research Center*

3:00 - 3:20 Break

3:20 - 3:45 A Laser-Based Sizing/Velocimetry Technique to Investigate the Secondary Atomization of Aluminum Gel Propellants - *D. Mueller and S. Turns, PSU*

3:45 - 4:10 Metallized Gel Propellants: Oxygen/RP-1/Aluminum Combustion Experiments - *B. Palaszewski, Lewis Research Center*

4:10 - 4:35 Fundamental Phenomena on Fuel Decomposition and Boundary Layer Combustion Processes with Applications to Hybrid Rocket Motors - *K. Kuo, Y.-C. Lu, M. Chiaverini, and G. Harting, PSU*

Tuesday Evening, September 13

Administration Building Auditorium

5:30 - 6:30 Reception

7:30 Policy Advisory Board Dinner (off-site)

Wednesday Morning, September 14

Administration Building

7:30 - 8:00 Continental Breakfast

Administration Building Auditorium

Heat Transfer and Fluid Mechanics *Chaired by C. Merkle, PSU*

8:00 - 8:25 A Hydrogen-Oxygen Rocket Engine Coolant Passage Design Program (RECOP) for Fluid-Cooled Thrust Chambers and Nozzles - *T. Tomsik, Lewis Research Center*

8:25 - 8:50 The Least-Squares Finite Element Method for Low-Mach-Number Viscous Flows - *S.-T. Yu, NYMA*

8:50 - 9:15 Convergence Rate Enhancement of Navier-Stokes Codes on Clustered Grids - *K.-Y. Choi and G. Dulikravich, PSU*

9:15 - 9:40 The Effect of Thermodynamic Nonidealities and Transport Anomalies on Shear Layer Dynamics - *J. Oefelein and V. Yang, PSU*

9:40 - 10:00 Break

10:00 - 10:25 Computational Fluid Dynamic Modeling of Rocket Based Combined Cycle Engine Flowfields - *R. Daines and C. Merkle, PSU*

10:25 - 10:50 Multidisciplinary Propulsion Simulation Using the Numerical Propulsion System Simulator (NPSS) - *R. Claus, Lewis Research Center*

10:50 - 11:15 Effects of Transverse Oscillatory Waves on Turbulent Boundary Layers - *H.R. Jacobs, PSU*

11:15 - 11:40 Validation of Two-Equation Turbulence Models for Propulsion Flowfields - *M. Deshpande, S. Venkateswaran, and C. Merkle, PSU*

11:40 Closing Remarks - *C. Merkle, PSU*

Administration Building, Room 225

Atomization and Sprays *Chaired by W. Anderson, PSU*

8:00 - 8:25 A Model to Predict the Conditions for Liquid Drop Breakup and the Resultant Mean Fragment Size- *K. Wert and H.R. Jacobs, PSU*

8:25 - 8:50 Analytical and Experimental Studies of Impinging Liquid Jets - *H. Ryan, W. Anderson, S. Pal, and R. Santoro, PSU*

8:50 - 9:15 Fluid Property and Operational Effects on Swirl Injector Droplet Sizes - *G. Cox, Pratt & Whitney*

9:15 - 9:40 The Effects of Turbulence on Droplet Drag and Secondary Droplet Breakup- *Y.-H. Song, E. Coy, S. Greenfield, M. Ondas, T. Prevish, T. Spegar, and D. Santavicca, PSU*

9:40 - 10:00 Break

10:00 - 10:25 Shear Coaxial Injector Instability Mechanisms - *T. Kaltz, M. Glogowski, and M. Micci, PSU*

10:25 - 10:50 Acoustic Effects on Sprays - *M. Pindera and A. Przekwas, CFD Research*

10:50 - 11:15 Velocity-Modulation Atomization of Liquid Jets - *J. Dressler, Fluid Jet Associates*

11:15- 11:40 Picosecond Imaging of Sprays - *L. Wang, X. Liang, P. Galland, K. Breisacher, and L. Liou , Lewis Research Center, and P. Ho and R. Alfano, City College of New York/Institute for Ultrafast Spectroscopy and Lasers*

Wednesday Afternoon, September 14

1:00 - 3:00 Tour of NASA Lewis Research Center

Administration Building, Room 225

12:30 - 3:00 Policy Advisory Board Meeting

427083
19951027742

RAPID PROTOTYPE FABRICATION PROCESSES FOR HIGH-PERFORMANCE THRUST CELLS

N95- 70862

K. Hunt, T. Chwiedor, J. Diab, and R. Williams
Rockwell International/Rocketdyne Division Canoga Park, California 91303

ABSTRACT

The Thrust Cell Technologies Program (Air Force Phillips Laboratory Contract No. F04611-92-C-0050) is currently being performed by Rocketdyne to demonstrate advanced materials and fabrication technologies which can be utilized to produce low-cost, high-performance thrust cells for launch and space transportation rocket engines. Under Phase 2 of the Thrust Cell Technologies Program (TCTP), rapid prototyping and investment casting techniques are being employed to fabricate a 12,000-lbf thrust class combustion chamber for delivery and hot-fire testing at Phillips Lab. The integrated process of investment casting directly from rapid prototype patterns dramatically reduces design-to-delivery cycle time, and greatly enhances design flexibility over conventionally processed cast or machined parts.

I. INTRODUCTION

The present focus on advanced modular rocket engines dictates the need for development of high-performance thrust cells, which embody operational versatility, low cost, high producibility, shortened cycle times from design to hardware, and enhanced reliability and durability.

The objectives of the Air Force Phillips Lab (AFPL) Thrust Cell Technologies Program (TCTP) are to develop the fundamental materials and fabrication process technologies needed to produce reliable, high-performance thrust cells for launch and space transportation rocket engines. A thrust cell design requirements study was performed under Phase 1 of the program, in which candidate mission applications were reviewed to establish the baseline thrust cell requirements upon which subsequent hardware design and fabrication efforts would be focused. As a result of this study, a baseline thrust cell configuration supporting an integrated modular engine (IME) application was established, - specifying O_2/H_2 propellants, 1860 psia chamber pressure, 6.0 mixture ratio, and 11,500 lb*f* vacuum thrust.

II. THRUST CELL DESIGN

The objective of the TCTP Phase 2 effort is to integrate rapid prototyping techniques with conventional investment casting processes to produce near-net shape components for fabricating a

baseline thrust cell combustion chamber . Phase 2 will culminate with the delivery of a combustion chamber to Phillips Lab for hot-fire validation tests.

The Phase 2 thrust cell chamber design layout is presented in Figure 1. The chamber design features cast stainless steel coolant manifolds which are liquid interface diffusion bonded (LIDB'd) to a cast NARloy-Z coolant liner. The coolant liner structural closeout is formed by a layer of electro-deposited nickel-cobalt (EDNiCo).

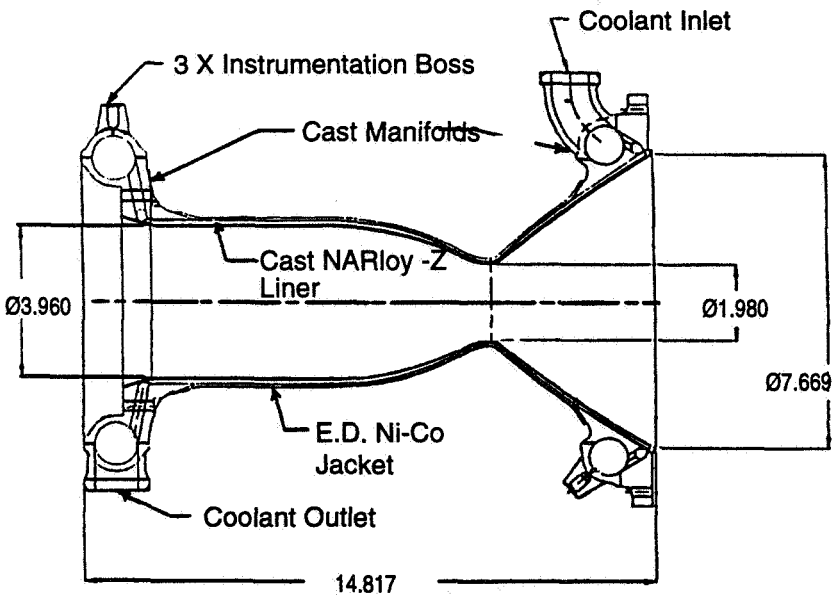

Figure 1. TCTP Phase 2 Thrust Cell Combustion Chamber Design Layout

The integrated process employed to produce the cast manifold and liner components consists of defining the geometric details of the components via 3-D computer-aided design (CAD) modeling, formatting the CAD database files such that a solid freeform replica of the component can be generated using a selective laser sintering (SLS) process, and providing the resulting SLS patterns to casting suppliers for direct mold preparation and investment. The use of directly fabricated ("rapid prototyped") casting patterns greatly reduces casting development lead times, small production quantity fabrication schedules, and development cost by eliminating the need for high-cost, labor-intensive wax injection tooling.

III. SLS PATTERN DEVELOPMENT

Rapid prototyping capability was obtained by Rocketdyne in January 1993 with the purchase of a Sinterstation 2000 SLS machine manufactured by the DTM Corporation. The SLS process is one of many emerging solid freeform fabrication technologies that electronically format a CAD database into thin cross-sections from which a desired shape can be constructed. In the SLS process, the parts are constructed by laser-sintering successive layers of heat-fusible powder. The operating principles of the process are illustrated in Figure 2. The DTM Sinterstation is equipped with a 50-watt CO_2 laser capable of sintering investment casting wax, polycarbonate, and nylon powder materials. It also has the capability of directly sintering metals and ceramics. For producing thrust cell casting patterns, the use of polycarbonate material has been adopted because (1) wax patterns are weaker (less durable) and

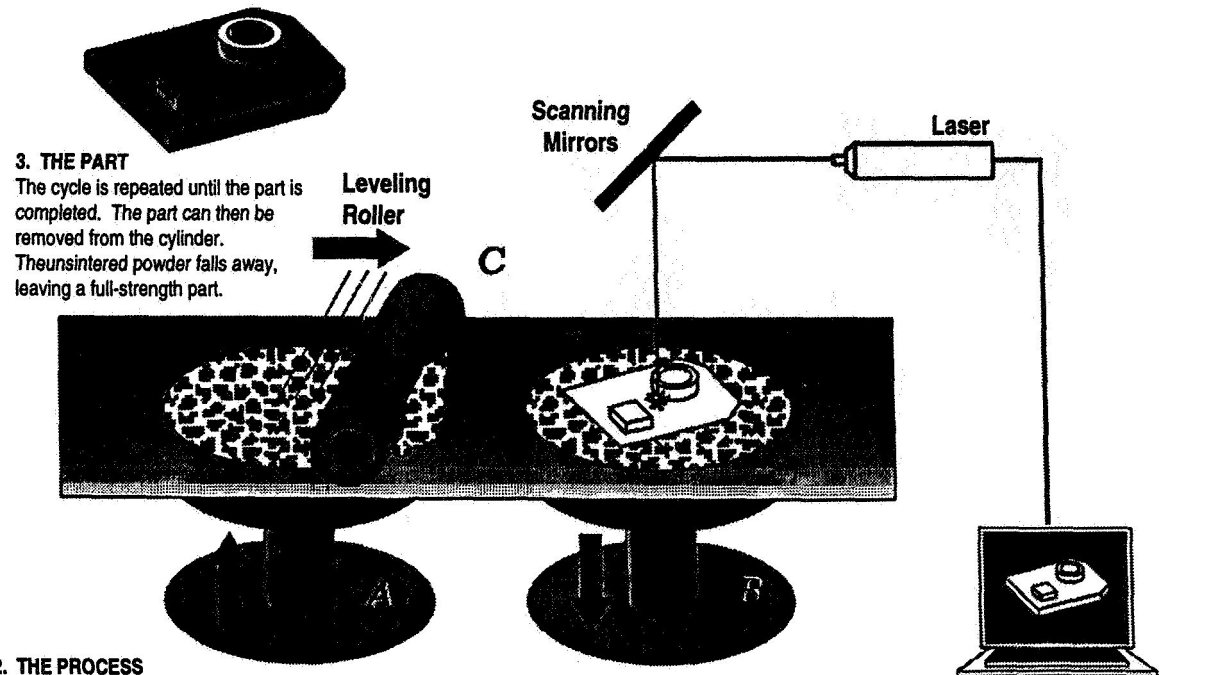

3. THE PART
The cycle is repeated until the part is completed. The part can then be removed from the cylinder. Theunsintered powder falls away, leaving a full-strength part.

2. THE PROCESS
The SLS process integrates several conventional technologies: lasers, optics, scanning systems, computers and controls.
The part process chamber consists of two cylinders and a powder leveling system. Both cylinder contain vertical stages. The powder cylinder (A) delivers powder by moving the vertical satage upwards. The part cylinder (B) receives the powder in thin layers by lowering its vertical stage a distance equal to the thickness of the cross-section being built. The roller (C) spreads and levels the heat-fusible powder.
Each layer is sintered with a laser beam, causing the powder to soften and quickly resolidify in the shape desired cross-section. Sufficient energy is supplied to bond each cross-section to the previous layer.
Areas of the powder where the laser is turned off remain unaffected and serve to support the object as each subsequent layer is applied and sintered.

1. THE DESIGN
A surfaced or solid model design is completed on a CAD/CAM/CAE system.

Figure 2. Selective Laser Sintering (SLS) Process Schematic

exhibit rougher surface finishes, and (2) the thermal expansion characteristics of nylon parts result in mold cracking during pattern burnout cycles.

To produce SLS polycarbonate patterns with the desired surface finish quality and dimensional accuracy for casting the thrust cell components, initial studies were performed to optimize Sinterstation operating parameters. With Sinterstation laser parameters (such as laser power, beam diameter, and raster scan spacing) optimized, dimensional accuracy of SLS pattern features has been consistently demonstrated to be within +/- .003 inches of design dimensions. A typical set of SLS forward manifold polycarbonate patterns produced in support of the thrust cell casting effort is shown in Figure 3.

IV. CASTING DEVELOPMENT

Casting suppliers selected to develop and provide cast parts in support of the Rocketdyne thrust cell concurrent engineering program team are Howmet, Incorporated (chamber liner castings) and Precision Castparts Corporation (PCC) (manifold castings). Liner castings were developed and produced at Howmet's Technology Center in Whitehall, Michigan; manifold castings were developed and produced at the PCC Airfoil Division's prototype foundry in Minerva, Ohio.

Figure 3. Selectively Laser Sintered (SLS) Polycarbonate Thrust Cell Forward Manifold Details

Liner Casting Development

Under the TCTP liner casting development effort, Howmet is contracted to produce a total of 13 castings—11 development castings and two "final quality" castings to support fabrication of a hot-fire deliverable combustion chamber. To date, a total of eight liner casting pours have been completed. The first high quality, full liner pour was achieved on only the sixth attempt, and is shown in Figure 4. All mold gating, shell preparation, and pouring process/parameter development is now considered to be complete by Howmet and Rocketdyne. Evaluation of cast NARloy-Z material samples and parts produced by Howmet indicates that the latest liner castings meet design requirements and inspection criteria. Mechanical properties data obtained to date indicate that cast NARloy-Z strength and ductility are very comparable to wrought material properties, and exceed the assumed design minimum values in the areas of yield strength and elongation. Cast NARloy-Z conductivity data obtained to date indicate that thermal conductivity for the fully processed cast material ranges from approximately 90 to 95% of that for wrought material. The full liner casting shown in Figure 4 is currently being processed through LIDB and EDNiCo processes at Rocketdyne as a manufacturing technology demonstration (MTD) unit, and processing of patterns and castings to support the deliverable chamber fabrication is in work.

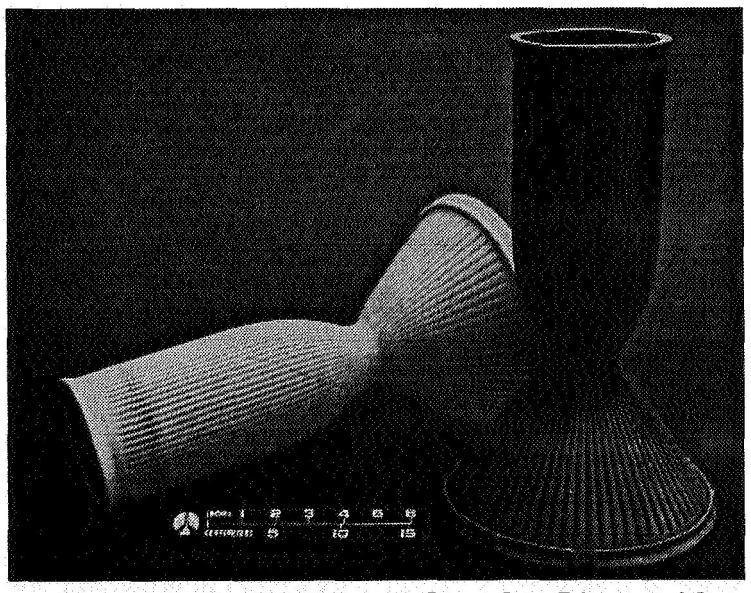

Figure 4. Cast NARloy-Z Chamber Liner (with SLS Polycarbonate Liner Pattern)

Manifold Casting Development

Under the TCTP manifold casting development effort, PCC is contracted to produce a total of 5 sets of manifold castings—three development casting sets and two "final quality" casting sets to support fabrication of a hot-fire deliverable combustion chamber. Each manifold sets consists of four castings: the forward body and shell, plus the aft body and shell. All manifolds are poured using air-melt CF-8C alloy (347CRES equivalent). Gating

development has been completed without major issues. To date, three complete sets of manifold components have been poured, and "final quality" castings have been achieved. Cast forward manifold components are shown in Figure 5. Mechanical properties testing of manifold casting material samples has indicated strength properties which exceed assumed design minimums for cast stainless steel material. The second set of forward and aft manifold parts produced by PCC have been welded and final machined in preparation for LIDB'ing to the full liner (shown in Figure 4) as a thrust cell chamber MTD unit. Processing of SLS patterns and castings in support of the deliverable thrust cell chamber is currently in work.

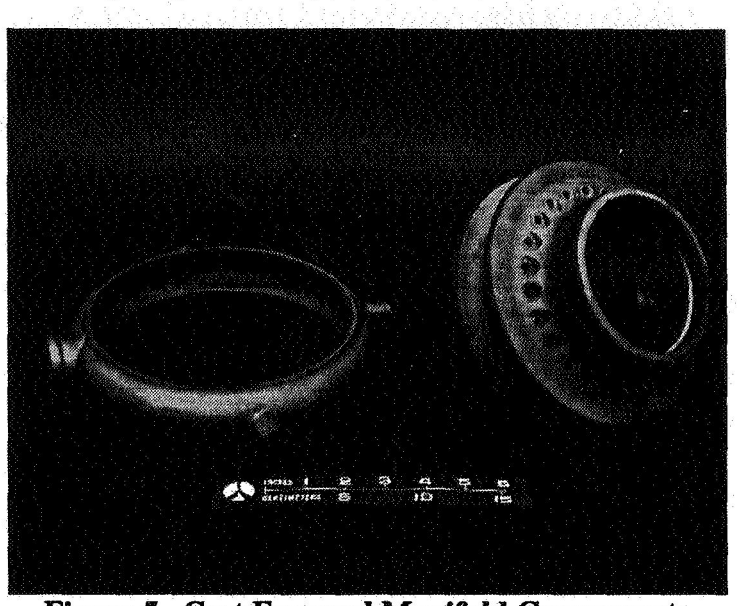

Figure 5. Cast Forward Manifold Components (Body and Closeout Shell)

V. THRUST CELL CHAMBER FABRICATION

Under the current TCTP Phase 2 plan, one LIDB/EDNiCo MTD unit, one deliverable thrust cell chamber, and one chamber spare will be fabricated. Development castings have been machined and prepared for the manifold-to-liner LIDB process. Following LIDB processing and bond joint inspection, the MTD unit will undergo the EDNiCo plating process which forms the structural closeout to the liner coolant channels. Fabrication and delivery of a hot-fire quality thrust cell combustion chamber to AFPL is currently scheduled to be completed in February 1995.

VI. CONCLUSIONS

The effort to integrate the rapid prototype SLS process with traditional investment casting processes has been a highly successful approach for producing high-quality combustion chamber components for thrust cell applications. Cast NARloy-Z and stainless steel materials and components produced to date have demonstrated acceptable characteristics with regard to dimensional conformance, inspection criteria, microstructural quality, and materials properties. Above all, through the development of paperless CAD model-to-cast part processing for thrust cell components, the Rocketdyne concurrent engineering team, including casting suppliers, has demonstrated the capability to shorten design-to-cast part lead times to approximately one month, with the flexibility to implement subsequent design changes without incurring schedule delays to accommodate tooling modification. The integrated rapid prototype casting process holds great promise for supporting the fabrication and testing of limited production components in aerospace and commercial industries.

1995

427691
P5 5
N95-70863

MULTI-DIMENSIONAL COMBUSTOR FLOWFIELD ANALYSES IN GAS-GAS ROCKET ENGINE

Hsin-Hua Tsuei*and Charles L. Merkle†
Propulsion Engineering Research Center
Department of Mechanical Engineering
The Pennsylvania State University

SUMMARY

The objectives of the present research are to improve design capabilities for low thrust rocket engines through understanding of the detailed mixing and combustion processes. Of particular interest is a small gaseous hydrogen-oxygen thruster which is considered as a coordinated part of a on-going experimental program at NASA LeRC. Detailed computational modeling requires the application of the full three-dimensional Navier Stokes equations, coupled with species diffusion equations. The numerical procedure is performed on both time-marching and time-accurate algorithms and using an LU approximate factorization in time, flux split upwinding differencing in space. The emphasis in this paper is focused on using numerical analysis to understand detailed combustor flowfields, including the shear layer dynamics created between fuel film cooling and the core gas in the vicinity on the nearby combustor wall; the integrity and effectiveness of the coolant film; three-dimensional fuel jets injection/mixing/combustion characteristics; and their impacts on global engine performance.

TECHNICAL DISCUSSION

The first part of the current research stems from interest in the mixing layers that arise from film cooling in the combustor of a small chemical rocket engine [1-5]. This engine is a small gaseous hydrogen-oxygen engine originally designed to provide auxiliary propulsion and attitude control for Space Station Freedom. It provides about 110 N (25 lbf) of thrust and uses the entire hydrogen gas flow for regenerative cooling after which about two-thirds of it is split off for wall film cooling while the remaining one-third is mixed with the oxidizer and used for primary combustion. An unknown fraction of the hydrogen cooling film mixes with the oxidizer-rich core gas and burns between the injection plane and the throat. This combustion reduces the thickness of the coolant layer and weakens its effect, but also improves the overall efficiency of the thruster. The resulting shear region that is created between this coolant layer and the hot combustion gases in the core region takes on much of the character of a classical shear layer. This shear layer, however, incorporates not only a velocity difference, but also includes large molecular weight differences, chemical reactions and strong heat release. Classical shear layer instability, unsteady vortex roll-up and related shear layer dynamics can therefore be expected in the mixing layer. The vortex roll-up, however, will be confined by the presence of the adjacent wall and the subsequent roll-up will be diminished although the

*Graduate Research Assistant
†Professor

unsteadiness remains. The issues of interest in the analysis are to document the role that these various mechanisms have on unsteady mixing in the shear layer and the integrity of the film of coolant adjacent to the wall.

Axisymmetric computational results have previously been compared with their experimental counterpart [3,4]. Comparisons have shown qualitative agreement, however, additional physics must be included to provide more accurate combustor flowfield predictions. Discrepancies arise mostly in the detailed local flowfield comparisons, including number density of major chemical species, the local temperature field and the exit velocity profile. In order to better understand where the disagreement stems from, an optical-access chamber was built in LeRC [3] to provide physical insight of the combustion chamber. Major chemical species and local temperature in the combustion chamber can therefore be detected by means of Raman scattering technique. Because the hydrogen fuel is injected through 12 ports around the chamber perimeter, detailed numerical modeling requires full three dimensional consideration to simulate the fuel jets and the mixing/ignition/combustion processes. The second part of this paper is thus centered on these issues. Preliminary three dimensional computational results for cold hydrogen fuel injection as well as the reacting flow calculations are presented. Efforts towards further comparisons with Raman measurement data are currently underway.

The numerical algorithm is based on extending earlier supersonic reacting flow calculations [6,7] to subsonic combustion problem [1,2,8]. The analysis uses an unsteady, three-dimensional, finite volume Navier-Stokes procedure that include chemical non-equilibrium effects. The governing equations can be written in a generalized coordinate system as :

$$\frac{\partial Q}{\partial t} + \frac{\partial}{\partial \xi}(E - E_v) + \frac{\partial}{\partial \eta}(F - F_v) + \frac{\partial}{\partial \zeta}(G - G_v) = H$$

where $Q = (\rho, \rho u, \rho v, \rho w, e, \rho Y_i)^T$ is the vector of primary dependent variables, and E, F, and G are the inviscid flux vectors, and E_v, F_v, and G_v the viscous flux vectors in the ξ, η and ζ directions, respectively. The vector H represents the source terms associated with chemical reactions or axisymmetry.

Numerical computation for steady flow is achieved by an implicit time-marching algorithm using an LU approximate factorization in time and flux split upwinding differencing in space. The time-accurate calculation for unsteady flow is conducted by a dual time stepping procedure [7]. The finite rate chemical reaction model used in the present work for gaseous hydrogen-oxygen combustion [6], involves nine chemical species and eighteen elementary reactions.

RESULTS

To demonstrate the dynamics of unforced hydrogen-oxygen reacting shear layers in the gas-gas combustor, we begin by investigating the effects of the wall location. The upper wall is moved radially outward while the core gas passage and the width of the splitter plate remain unchanged. Figure 1 shows results of calculations for four different outer wall locations. The location of the splitter plate (radius of 10.3 mm) and the width of its base (1.3 mm) remain unchanged. The flow velocities are chosen to match the engine baseline operating condition: the hydrogen fuel (top portion) is injected at a speed of 125 m/s while the oxygen core flow (lower portion) enters at 185 m/s, giving a nominal velocity ratio of 0.67 and a density ratio of 16. The plots show contours of the OH concentration, a reasonable indicator of the instantaneous

diffusion flame location. In Fig. 1a, the outer wall is sufficiently far away from the shear layer (radius = 30 mm) that it has little effect on the vortex dynamics. The hydrogen-oxygen interface undergoes strong distortion and roll-up in the classical sense. The small bulge near the splitter plate represents the nucleus of the next succeeding roll-up. At an intermediate wall location (radius = 22 mm) some wall interaction is observed (Fig. 1b), but strong distortion is still present. The presence of the wall appears to cause the vortex to sweep forward more strongly than in Fig. 2a when the wall is further away. It is clear that the presence of the nearby wall affects the shape of the distorted shear layer. Figure 1c shows results for when the outer wall is brought still closer to the shear layer (radius = 17 mm). At this location the wall begins to prevent roll-up and diminish the unsteadiness. The distortion hits the outer wall before the entire roll-up process is completed, and the subsequent roll-up is forced to decay. Figure 1d shows results for the case when the outer wall is very close to the splitter plate (radius = 12.7 mm); the geometry of interest for the gas-gas combustor. A quick visual inspection shows the dominant influence of the adjacent wall. For this case, the wall is too close to the shear layer to allow the strong distortions seen in the previous two plots, and consequently the ensuing vortex roll-up does not occur. The shear layer does, however, maintain a substantial amount of unsteady oscillation. Performance computations [1-3] show that this unsteadiness causes a small decrease in the combustion rate of the fuel film with a corresponding decrease in performance.

In the engine combustor, hydrogen fuel used for primary combustion is injected radially through 12 annual ports, mixes with core oxygen then ignited by a spark plug. To accurately model the fuel jets mixing and combustion characteristics, three-dimensional consideration is required in the analyses. A cylindrical combustor without the spark plug is first used to demonstrate three-dimensional capability of the present theoretical model. Preheated core oxygen enters the combustor at 2000 K, 100 m/s while the hydrogen fuel is injected at 600 K, 600 m/s. For clarity, only one-quarter of the combustor, which contains three hydrogen injection ports, is plotted. The OH radical concentration contours and temperature contours are shown in Fig. 2a and 2b, respectively. In Fig. 2a, the dark contours represent higher OH radical concentration. It is observed that the shape of the diffusion flame is totally three-dimensional. The flame surface starts to wrinkle downstream of the hydrogen injectors because a recirculation region is formed behind each injection port that induces a vortex between the jet and the combustor wall. The hydrogen jets no longer maintain their near-cylindrical cross-sectional shape and deform in response to the vortical flow above them. The core oxygen gas therefore rolls up and wraps around each hydrogen jet causing further mixing and reaction near the combustor wall, resulting in a very high OH concentration region.

Figure 2b shows the temperature contours. Darkened contours indicate higher temperature, with a maximum temperature in the flame zone about 3600 K. It is also noted that the hydrogen jet is heated up due to heat transferred from the three-dimensional diffusion flame as it travels along the chamber.

To simulate the operating ignition condition, preliminary computation of cold hydrogen fuel injection into a cold oxygen core environment is investigated to provide perspective for the mixing processes under the designed operating condition. The spark plug is included in this calculation represented by the shaded region, located just upstream of the 12 hydrogen injection ports. A quarter of the combustor which involves three injection holes is again used to show the three-dimensional effects. The operating condition is chosen to match the experiment setup, with cold hydrogen injected at 325 m/s while the room temperature oxygen core enters at 13 m/s. Figure 3 shows the hydrogen mass fraction contours at two different time levels during the hydrogen injection process. Figure 3a shows an early stage shortly after the hydrogen injection is initiated. The mushroom-like mixing front is clearly observed. In Fig. 3b, after a certain amount of

hydrogen is pumped into the chamber, the mixture front keeps growing larger in size and turns toward the streamwise direction because of interactions with the core oxygen stream. A recirculation bubble is expected downstream of the spark plug, where the mixture is ignited. The computation is still currently underway while the ignition process will be initiated when a high enough mixture ratio is maintained in the recirculation region to sustain the flame after ignition. Further comparisons with experiment data will be made to validate the accuracy of the current analyses.

ACKNOWLEDGEMENTS

This work has been supported by NASA Grant NAG 3-1020 and NAGW-1356. Partial computational support has been provided by the Center of Academic Computing at The Pennsylvania State University and the NAS Program at NASA Ames.

REFERENCES

1. Tsuei, H.-H. and Merkle, C., AIAA Paper 94-0553, Reno, NV, 1994.
2. Tsuei, H.-H. and Merkle, C., Proc. 14th Intl. Conf. on Numerical Methods in Fluid Dynamics., Bangalore, India, 1994.
3. de Groot, W. and Tsuei, H.-H., AIAA Paper 94-0220, Reno, NV, 1994.
4. de Groot, W. and Weiss, J., AIAA Paper 92-3353, Nashville, TN, 1992.
5. Weiss, J. and Merkle, C., AIAA Paper 93-0237, Reno, NV, 1993.
6. Yu, S.-T., Tsai, Y.-L. P. and Shuen, J.-S., AIAA Paper 89-0391, Reno, NV, 1989.
7. Molvik, G. and Merkle, C., AIAA Paper 89-0199, Reno, NV, 1989.
8. Venkateswaran, S., Weiss, J., Merkle, C. and Choi, Y.-H., AIAA Paper 92-3437, Nashville, TN, 1992.

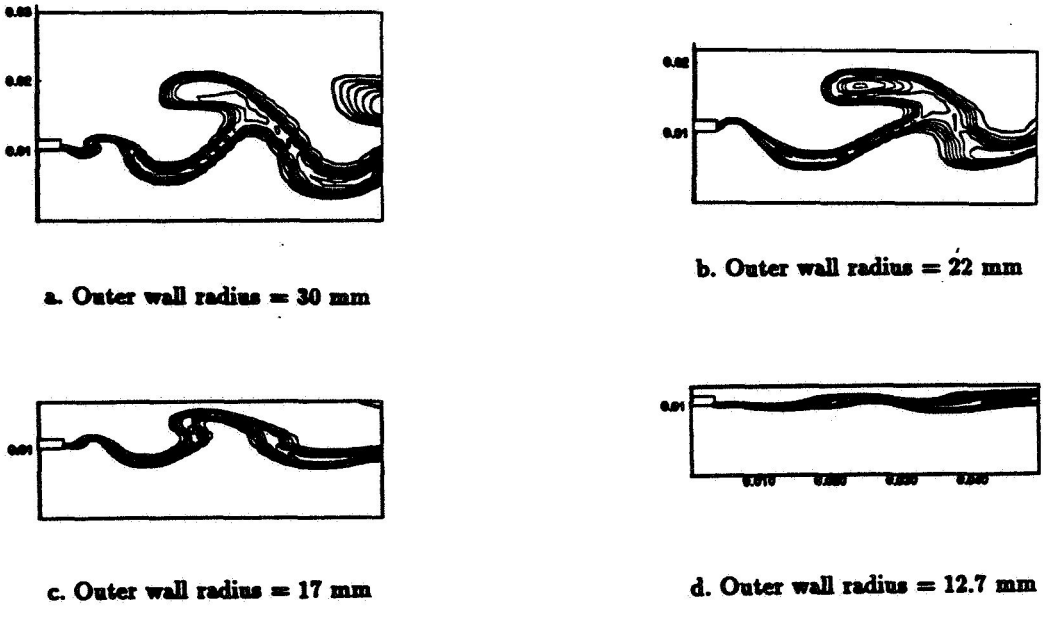

a. Outer wall radius = 30 mm

b. Outer wall radius = 22 mm

c. Outer wall radius = 17 mm

d. Outer wall radius = 12.7 mm

Figure 1. The OH radical concentration contours for four different outer wall locations.

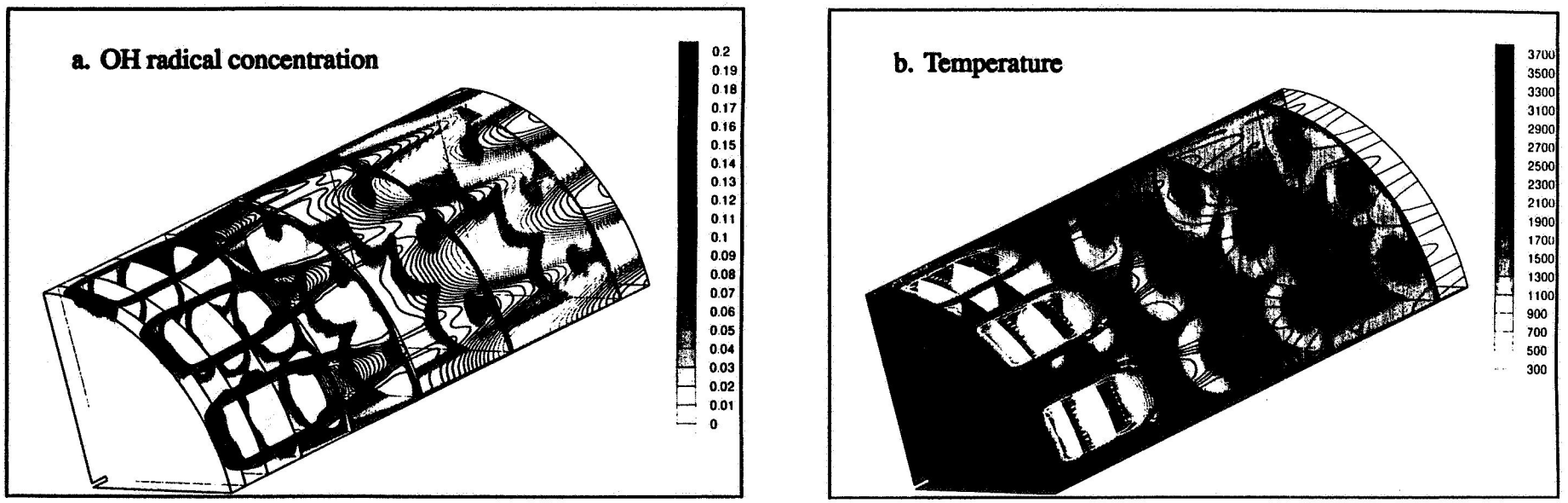

Figure 2. The OH radical concentration and temperature contours in one-quarter of the combustor.

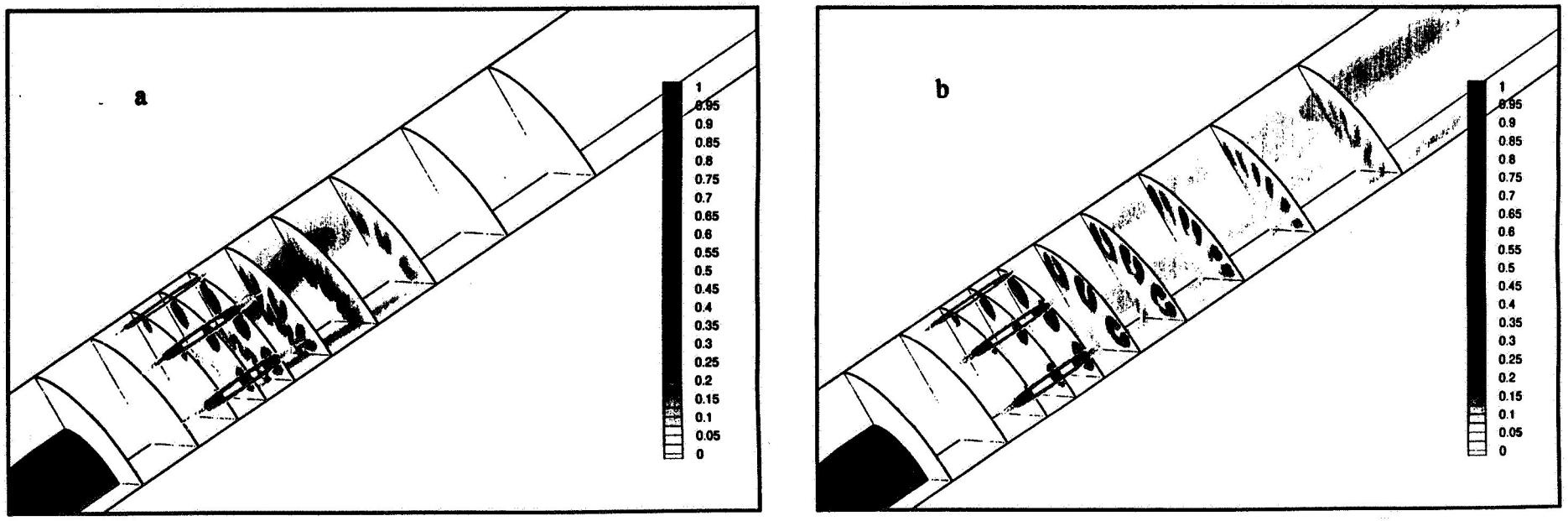

Figure 3. Hydrogen mass fraction contours at two different time levels during the injection process.

427093
P5 6

THRUST AUGMENTATION OF A SHROUDED NOZZLE

N95-70864

Owen Patton
Cleveland State U.
East 24 & Euclid Ave.
Cleveland, Ohio 44135

Larry Liou
Nasa Lewis Research Center
21000 Brookpark Road
Cleveland, Ohio 44135

SUMMARY:

The test seeks to find the effectiveness of thrust augmentation due to air entrainment at the rocket nozzle exit. Shrouds are attached to the primary nozzle to entrain the ambient air for further expansion. Compressed air is used to simulate a propellant in the primary flow; therefore, combustion and afterburning are excluded. Perfect expansion is used in the primary (unshrouded) nozzle to further rule out the suspicion that the shrouds simply act as a nozzle extension in the event that thrust augmentation is observed. The goal is to find the effectiveness of thrust augmentation as the result of air entrainment alone. Thrust and flow data are recorded for different shrouds at over, fully, and under-expanded conditions. Recorded mass flow rate data will be used to calculate the entrainment rate. Results of this experiment will be verified with a computer code.

DISCUSSION:

The test setup consists of a simple nozzle/shroud apparatus which, supported by four tabs, hangs above a thrust measuring load cell(see Figure 2). Shrouds can be adjusted or removed from the four bolts welded to the nozzle. The load cell is calibrated by placing weights upon a plate resting on the four bolts. Data collected(see Figure 3) includes upstream, chamber, and venturi pressure, upstream and downstream temperature, and thrust. The mass flow rate is found by recording the temperature and venturi pressure in the supply line. Data is stored on paper by a chart recorder.

A CFD code is currently being revised that will account for the air entrainment. Grids for this code have already been generated by a program called 3DGRAPE. Figure 4 is an example of the grid corresponding to the nozzle and shroud at zero distance from each other.

So far, data has been recorded for the fully expanded case. Figure 5 shows the thrust changes for the test shrouds, along with their corresponding geometries. Not enough data has been recorded to draw any meaningful conclusions.

REFERENCES:

TITLE: Experimental and Theoretical Investigation of the Rocket Engine-Nozzle Ejector (RENE) Propulsion System
SOURCE: Air Force Rocket Propulsion Laboratory
Research Technology Division

Air Force Systems Command
United States Air Force
Edwards Air Force Base, California 93523

REPORT
NUMBER: AFRPL-TR-65-66, April 1965

gure 1: Air Entrainment by a Shrouded Nozzle

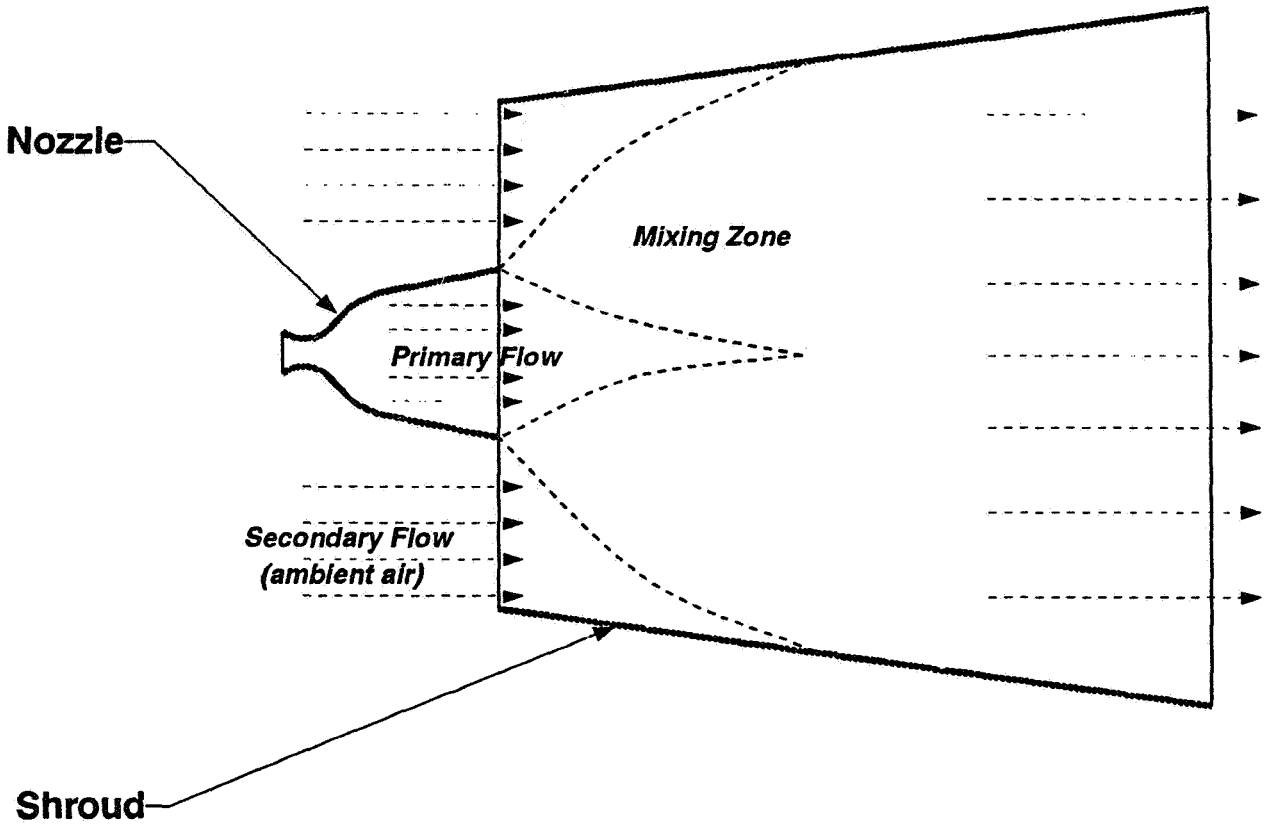

gure 2: Ejector Rig Setup (partial half section)

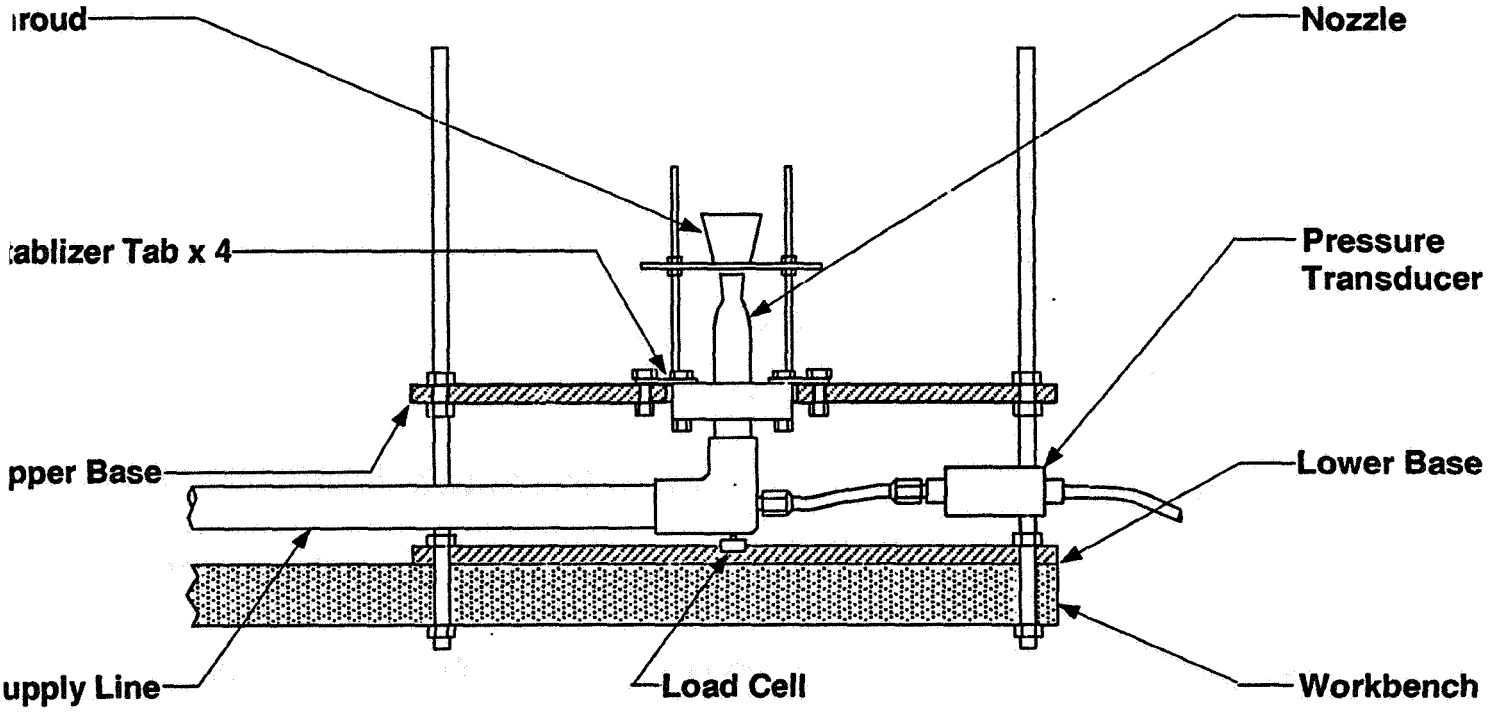

Figure 3: Vertical Control Panel

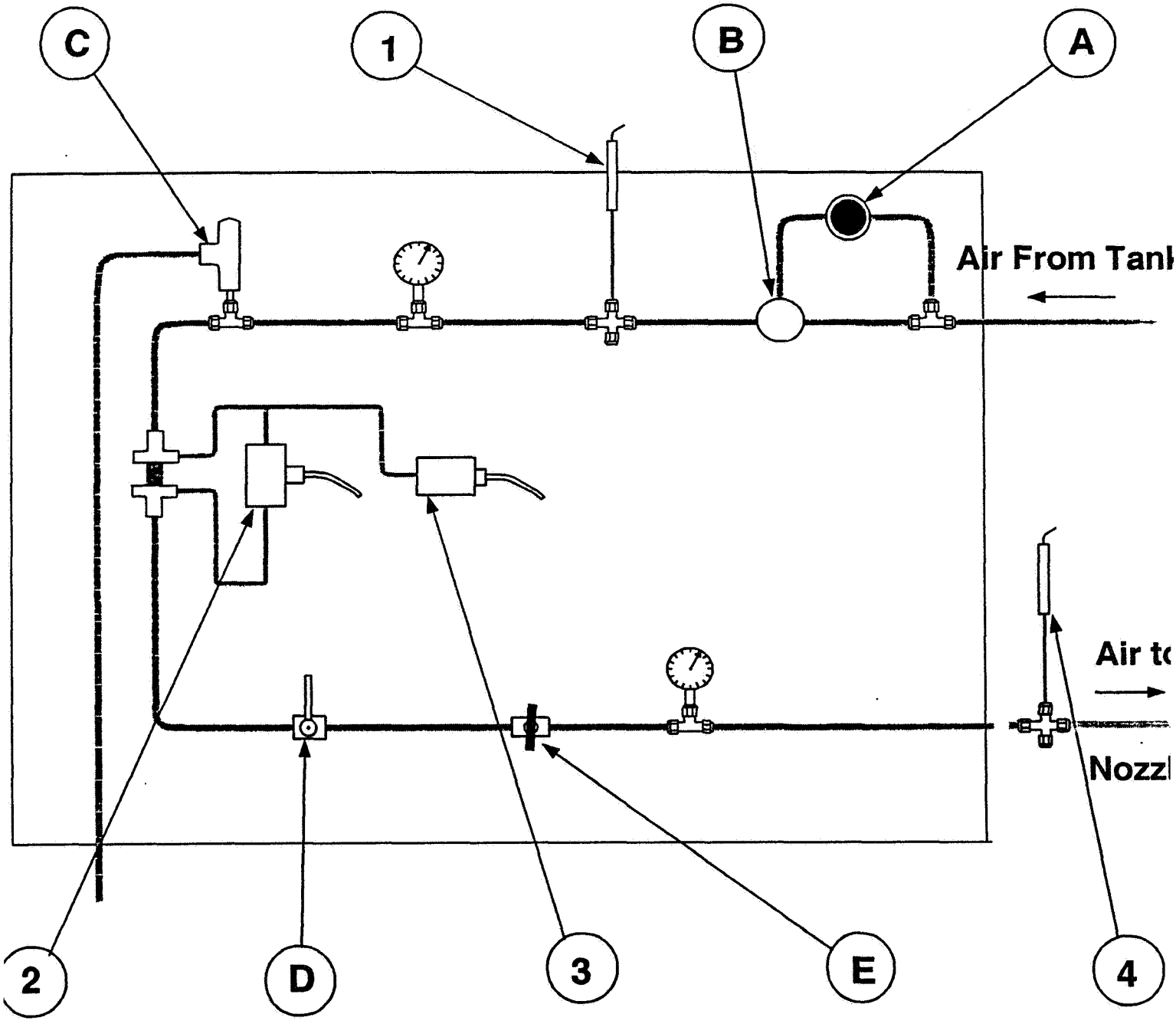

Valves:

A. Regulator

B. Reduction

C. Safety

D. Butterfly

E. Needle

Sensors:

1. Upstream Thermocouple
2. Venturi Pressure Transducer
3. Upstream Pressure Transducer
4. Downstream Thermocouple

Figure 4: Nozzle/Shoud Grid

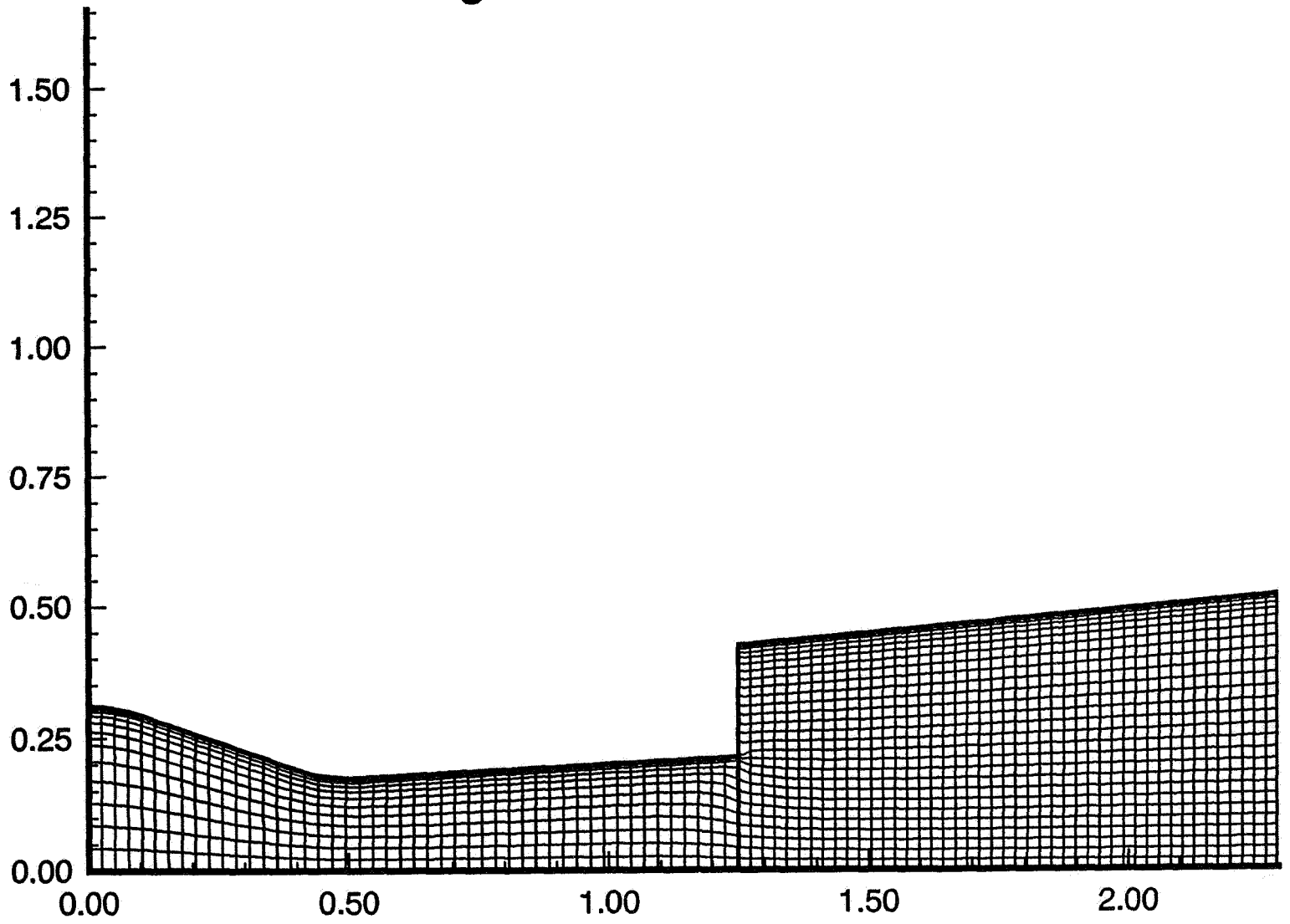

Figure 5: Initial Data

Shroud	Thrust (lb. force)	Thrust Change (lb. force)	A (in.)	B (in.)	L (in.)
none	11.1	-------	------	------	-------
first	11.3	.2	.85	1.04	1.04
second	11.1	.1	.85	.93	.93
third	11.1	0	.74	.90	.90
fourth	11.0	-.1	.74	.81	.81
fifth	11.2	.1	.67	.82	.82
sixth	11.0	-.1	.67	.74	.74
seventh	11.2	.1	.67	.74	1.48

Theoretical thrust for 90 psi. chamber pressure is 9.953 lb. force.

The chamber pressure for all the above is 91 psia.

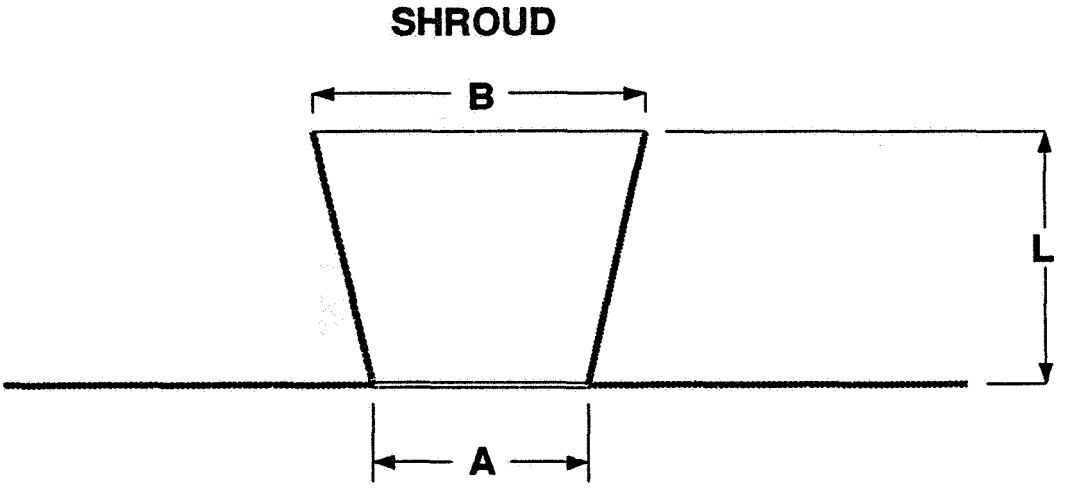

427095

NASA Lewis Advanced Subsonic Transport Program Overview

N95-70865

Chi-Ming Lee
NASA Lewis Research Center

An Advanced Subsonic Transport (AST) research program has been initiated by NASA to develop a new generation of superior U.S. aircraft and engines, and to help U.S. aeronautics industry increase their market share and competitiveness. NASA Lewis has the lead responsibility for the AST propulsion element. The top priority is to achieve a 70 percent reduction of NO_x at all operating conditions including subsonic cruise. Since the technology for the NO_x reductions does not exist, an aggressive research program has been established for its evolution.

To date the program has been initiated with study contracts with industry as well as the initiation of analytical and experimental research. To conduct the high pressure tests, a new national facility with a high temperature capability for continuous operation at 60:1 pressure ratios is being constructed at Lewis and will be operational in 1996. The general flow of the program is to first conduct fundamental experiments and analytical studies to define combustor concepts, demonstrate the 70 percent NO_x reduction in combustors in 1999, conduct a test-bed core engine demonstration in 2001, and demonstrate in 2002 the required operability and altitude relight for an Entry Into Service of the technology by industry in 2005.

427119

N95- 70866

Characteristics of a Trapped-Vortex (TV) Combustor

K.-Y. Hsu, L. P. Goss and D. D. Trump
Systems Research Laboratories, Inc.
Dayton OH 45440-3696

W. M. Roquemore
Wright Laboratory
Wright-Patterson Air Force Base OH 45433-7103

ABSTRACT

The characteristics of a Trapped-Vortex (TV) combustor are presented. A vortex is trapped in the cavity established between two disks mounted in tandem. Fuel and air are injected directly into the cavity in such a way as to increase the vortex strength. Some air from the annular flow is also entrained into the recirculation zone of the vortex. Lean blow-out limits of the combustor are determined for a wide range of annular air flow rates. These data indicate that the lean blow-out limits are considerably lower for the TV combustor than for flames stabilized using swirl or bluff-bodies. The pressure loss through the annular duct is also low, being less than 2% for the flow conditions in this study. The instantaneous shape of the recirculation zone of the trapped vortex is measured using a two-color PIV technique. Temperature profiles obtained with CARS indicate a well mixed recirculation zone and demonstrate the impact of primary air injection on the local equivalence ratio.

INTRODUCTION

All practical combustors and commercial burners use recirculating flows to stabilize the flame. Recirculation zones provide regions of low velocity fluid where burning can take place. The recirculation zones also provide mixing of fuel, air, and hot products and a continuous ignition source that sustains the flame by transporting the hot mixture back toward the incoming reactants. Swirl, bluff-bodies, and rearward facing steps or a combination of these are commonly used to create recirculation zones. Swirl is used in most practical combustors and burners; however, the operating range of swirling flames is often not so large as desired. This is due to aerodynamic instabilities of the recirculation zone. Bluff-bodies and rearward facing steps are also used to create recirculation zones that promote flame holding in much the same way as swirl-stabilized flames. However, recirculation zones behind bluff-bodies and rearward facing steps are even less stable and have longer flame lengths than those established using swirl. Also, recirculation zones established by bluff-bodies or rearward facing steps do not entrain a large quantity of free stream fluid. This limits their application to high speed, premixed combustion systems such as those encountered in ramjets and gas turbine engine afterburners.

One technique for creating a stable recalculation zone is to trap a vortex between two disks mounted in tandem. This technique has been investigated as a means of reducing drag of bluff-bodies; however, it has never been considered as a means of stabilizing a flame[1,2,3]. The objective of this paper is to evaluate the TV concept for flame stabilization. A vortex is trapped in a cavity and fuel and air are injected directly into the cavity in such a way that the vortex strength is increased. This provides a stable environment that can sustain the flame over a wide range of operating conditions.

EXPERIMENTAL

The combustor used in this study consists of a forebody and an afterbody disk as shown in Fig. 1 (a). The forebody, with diameter (d_f) of 70 mm, is located at the exit plane of the annular air duct which has a diameter of 80 mm. The blockage ratio defined as the area ratio between the forebody and the annular air duct is 76%. An annular air velocity of 50 m/s can be achieved in the facility. The annular and primary air flows originate from two air supplies and are controlled and metered separately. Fuel and primary air are delivered through concentric tubes into separate chambers in the afterbody which is 50.8 mm in diameter.

A schematic of the primary fuel and air injection plane is shown in Fig. 1 (b). Gaseous propane fuel is injected through 8 orifices (1.75 mm in diameter) and the primary air is supplied through 24 orifices (2.29 mm diameter) surrounding the fuel jets. The fuel and primary air jets are located so as to reinforce the vortex created in the cavity. Direct injection of primary air serves the following purposes : (1) provides direct control of local equivalence ratio inside the recirculation zone; (2) enhances mixing by increasing the mixing region through distributed fuel and air jets; and (3) provides cooling for the injector assembly. The separation between the forebody and the face of injector plane, H, can also be varied to optimize the condition for trapping a vortex and providing stable combustion. The pressure drop due to the annular air flow is measured by using a water manometer. The lean-blow-out limits of the combustor are established for a range of flow conditions. The effects of separation between forebody and afterbody and primary air on the combustor performance are also examined.

The velocity fields are obtained for both cold and reacting flow conditions. The instantaneous velocity field is obtained by employing the two-color Particle-Imaging Velocimetry (PIV)[4,5] technique. A pulsed Nd:YAG laser and a YAG-pumped dye laser are used to generate two different wavelengths to eliminate the ambiguity in flow direction. Cylindrical lenses are used to form a laser sheet vertically across the centerline of the burner. The spherical particles (5 μm in diameter) are seeded through primary air jets. A 35 mm camera mounted at a right angle to the laser sheet is used to take images of particles using laser illumination. A synchronization circuit is used to control the time separation between the two laser pulses. The typical time separation between two lasers is about 30 μs for the flow conditions studied. A color scanner is used to digitize the images which are stored in the computer for further analysis. The theory and experimental setup of the PIV technique are presented in Ref. 4 and 5.

The radial temperature profiles at locations inside the recirculation zone are measured by using Coherent Anti-Stokes Raman Spectroscopy (CARS). The CARS system used in this study consists of a Nd:YAG-pumped broad-band dye laser for N_2 excitation. A CCD camera interfaced with the computer is used for single-shot broad-band detection. At each location, 1000 samples were collected at a rate of 10 Hz, and the spectra are stored for data analysis. Computer software was developed to obtain temperature information by curve-fitting the band-shape of the measured N_2 spectrum.

RESULTS AND DISCUSSION

An image of a flame stabilized in the TV combustor is shown in Fig. 2 (a). The flame is stabilized within the cavity between the afterbody and the forebody. Its bright blue color indicates low soot production. The overall equivalence ratio is about 0.06 which is considerably below the lean blow-out limit of typical swirl stabilized flames. The annular air velocity is 33 m/s. The primary equivalence ratio calculated using the fuel and primary air is about 1.2. The flame is attached in the shear layer near the forebody. This is typical for all TV stabilized flames when a small amount of primary air (5% of annular air) is injected into the recirculation zone. The

instantaneous velocity field is shown in Fig. 2 (b) for the flow domain drawn in Fig. 2 (a). The center of the recirculation zone is evident in Fig. 2 (b) and corresponds to the dark region in the flame image. The plane of the velocity field also includes part of a fuel and primary air jet as is evident from the large velocities near the afterbody face. In general, increasing the fuel flow rate with the air flow rates fixed results in longer flame with a yellow sooting region near the vortex center. Increasing the primary air flow reduces the flame length and eliminates the soot formation. However, the general structure of the flame inside the cavity is essentially the same as that shown in Figs. 2 (a) and 2 (b) for a wide range of conditions.

The pressure drop across the TV combustor is measured for both cold and reacting flows. A 150 mm long 80 mm diameter Pyrex tube was used to confine the flow. The measured pressure drop does not include that across the fuel and primary air jets. The percentage of pressure drop (dp/P) as a function of H/d_f (ratio of separation H and the diameter of the forebody d_f) for cold flow conditions is shown in Fig. 3. The differential pressure between annular air and ambient is denoted by dp, and P is the ambient pressure. The pressure drop (dp/P) across the TV combustor increases as the velocity of the annular air is increased. A minimum pressure drop occurs at H/d_f = 0.6 for three different annular air flow rates. This is in good agreement with the forebody and afterbody separation found for maximum drag reduction using the TV concept[1,2,3].

The criteria for trapping a vortex are given in Ref. 1 where the afterbody diameter was found to be 0.75d_f and the separation of the forebody and afterbody was 0.55d_f. Combusting flow experiments were conducted to determine the optimum diameter of the afterbody and the separation. It was found that the condition for trapping a vortex in cold flows is near optimum for providing a visibly stable flame. This is not evident in Fig. 4 where the pressure drop as a function of H/d_f, for different conditions of primary air, in both cold and reacting cases is shown. The pressure drop is higher in combusting flows than that in the cold experiments due to heat release. Also, the pressure drop increases with the primary air flow rate for both cold and reacting flows although it is more notable for the combusting cases. The heat release appears to modify the flow pattern in such a way as to increase the effective blockage ratio and this resulted in a higher pressure drop. This is evident in the combusting case since the flame increases in diameter as the primary air flow is increased.

The effect of primary equivalence ratio on pressure drop for different H/d_f is shown in Fig. 5. The primary air flow rate determines the local equivalence ratio and thus the heat release rate in the recirculation zone. The pressure drop is expected to be a maximum at the condition of maximum heat release rate. This occurs for a primary equivalence ratio of unity for various H/d_f and is consistent with the data in Fig. 5. The local equivalence ratio in the recirculation zone may be slightly leaner than the primary equivalence ratio due to entrained air from the annular flow. The entrainment rate may also vary with flow conditions. However, the data in Fig. 5 suggest that very little air is entrained into the recirculation zone when there is primary air flow.

The lean blow-out limits for the TV combustor are illustrated in Figs 6 and 7. With zero primary air flow rate, the overall equivalence ratio at lean blow-out increases with the annular air velocity and with increasing H/d_f, as shown in Fig. 6. The slope of the lean blow-out versus H/d_f curve changes at H/d_f around 0.65. This could indicate that air entrainment might increase with large separation distance (H/d_f). The overall equivalence ratio at lean blow-out is less than 0.035 which illustrates the excellent stability of this combustor. The effect of primary air equivalence ratio on the overall lean blow-out limit is shown in Fig. 7 for an H/d_f = 0.55. These data suggest that for a fixed annular air flow rate there is a near linear relationship between the overall and primary equivalence ratio. Furthermore, for a fixed primary equivalence ratio the overall equivalence ratio at blow-out will be lower for higher annular air flow rates. It is also noted that the slopes of the curves for high and low annular air flow rates are nearly the same. It is evident

that by controlling the primary equivalence ratio, one can optimize conditions for minimum lean blow-out for different annular air flow rates.

Direct-injection of primary air and fuel into the recirculation zone of the trapped vortex has a major impact on flame stability and local equivalence ratio. This is illustrated by the temperature profiles in Figs. 8, 9, and 10 for H/df = 0.59 at three different axial locations (z = 5, 25 and 39 mm) as measured from the forebody face. The overall equivalence ratio is about 0.2 with an annular air velocity of 50 m/s and 25 slpm of fuel. Data are presented for primary air flow conditions of 56 and 280 slpm, which correspond to primary equivalence ratios of 11.1 and 2.2, respectively. In the figures, the mean temperature profiles are marked with open symbols. Closed symbols denote the fluctuations in temperature. Near the forebody as shown in Fig. 8, the temperature is relatively flat across the forebody with temperature fluctuations of about 200 K. The radial temperature profiles at an axial location near the center of vortex are relatively flat in the range of r > 20 mm, as shown in Fig. 9. The jet-dominant region can be clearly seen at r = 18 mm where fluctuation in temperature is higher than that at other locations. It is also noted that the flame increases in diameter as the primary air is increased. The primary air has a significant impact on the temperature profiles near the afterbody plane as noted in Fig. 10. The temperature in the flat region (r > 20 mm) increases by about 700 K as the primary air is increased. The maximum temperature of 2200 K equivalent to stoichiometric flame temperature has been measured for high primary flow conditions, however, the fluctuation in temperature is only about 200 K. The fluctuations in temperature are lower under the leaner condition ($\Phi_{primary}$ = 2.2) than under the rich condition ($\Phi_{primary}$ = 11.1). In general, the temperature is higher as the primary equivalence ratio approaches the stoichiometric condition, however; lower temperature are observed in the range of r < 20 mm where the primary air jets were dominant. The temperature is higher in the downstream location near the injector plane, where additional entrainment of air is expected. The flat temperature profiles indicate that the recirculation zone of the trapped vortex behaves like a well stirred reactor for most conditions. However, the temperature fluctuations are relatively large especially for the low primary air flow rate (high primary equivalence ratio). This suggest that the mixing may not be complete in the recirculation zone.

SUMMARY

The TV combustor demonstrates extremely low lean blowout and pressure drop for a wide range of flow conditions. The primary air has significant impact on the combustion characteristics, namely, stability, local stoichiometry and lean blow-out. The direct control of the primary air can maintain stable combustion over a very wide range of operating conditions that has not been achieved by other combustors. Additional data on combustion efficiency and emissions will be presented at the meeting.

REFERENCES

1. Mair, W. A., "The Effect of a Rear-Mounted Disc on the Drag of a Blunt-Based Body of Revolution", The Aeronautical Quarterly, pp. 350-360, Nov 1965.
2. Little, Jr., B. H., Whipkey, R. R., "Locked Vortex Afterbodies, J. of Aircraft, Vol, 16, No. 5, pp. 296-302, May 1979.
3. Gharib, M. and Roshko, A., "The Effect of Flow Oscillations on Cavity Drag", J. Fluid Mech., Vol. 177, pp. 501-530, 1987.
4. Goss, L. P., Post M. E., Trump, D. D. and Sarka, B., "Two Color Particle Imaging Velocimetry", J. Laser Appl., p.p. 36-42, 1991.
5. Post, M. E. and Goss, L. P., "Two-Color Particle-Imaging Velocimetry in Vortex Structures", 31st Aerospace Sciences Meeting & Exhibit, AIAA-93-0412, 1993.

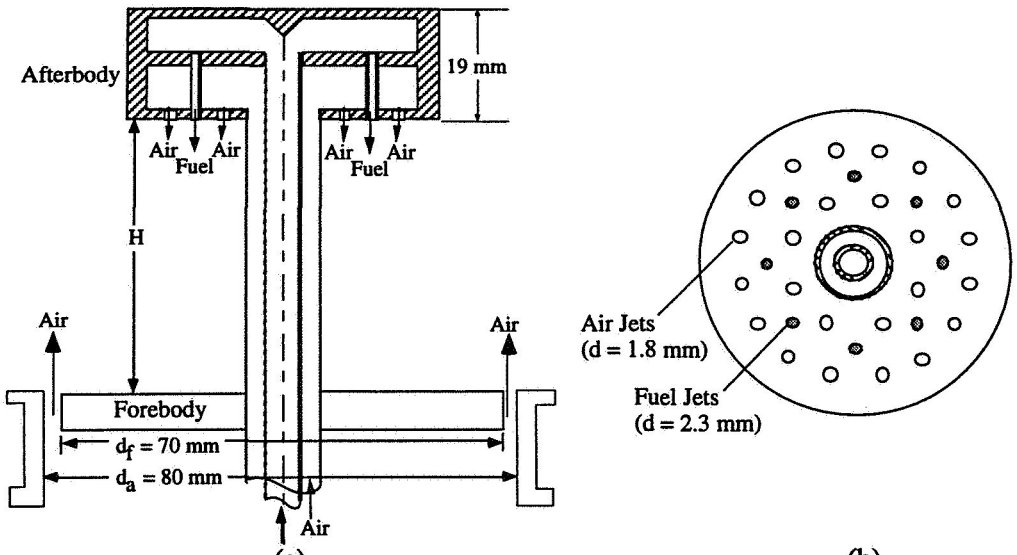

Figure 1. Schematic Diagrams of (a) Trapped-Vortex Combustor and (b) Injection Plane of Afterbody

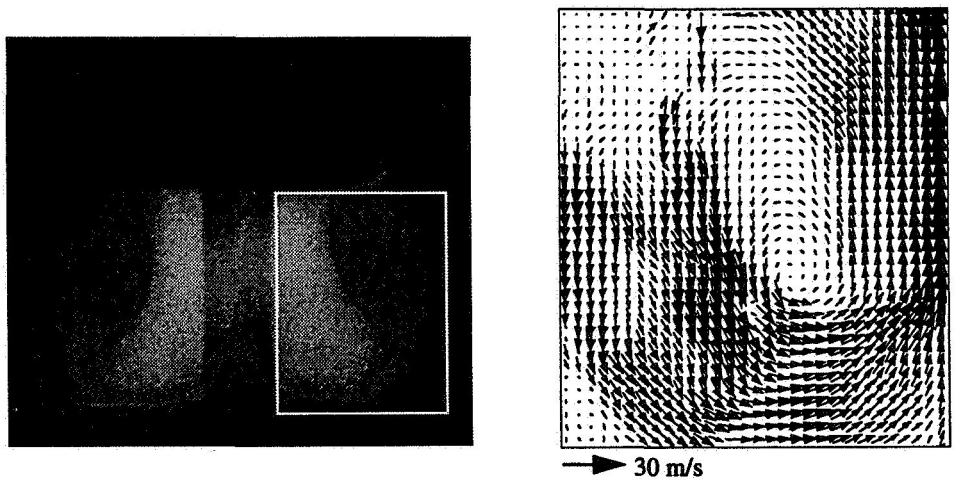

Figure 2. (a) Flame Image and (b) Instantaneous Velocity Field

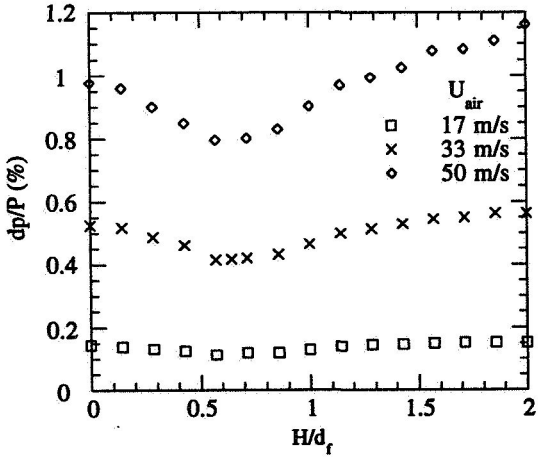

Figure 3. Pressure Drop versus H/d_f (Cold Flow without Primary Air)

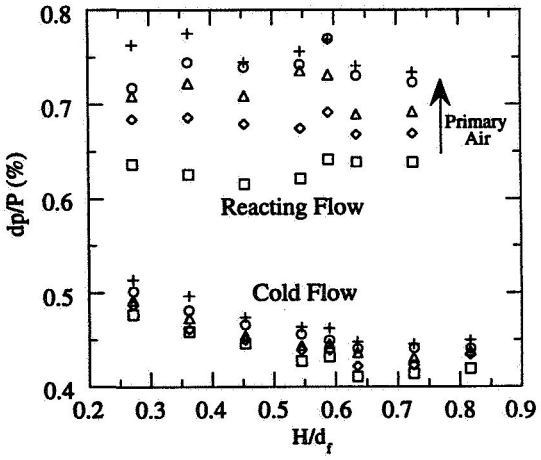

Figure 4. Comparison of Pressure Drop between Cold and Reacting Flows ($\Phi_{Overall}$ = 0.12) at U_{air} = 33 m/s

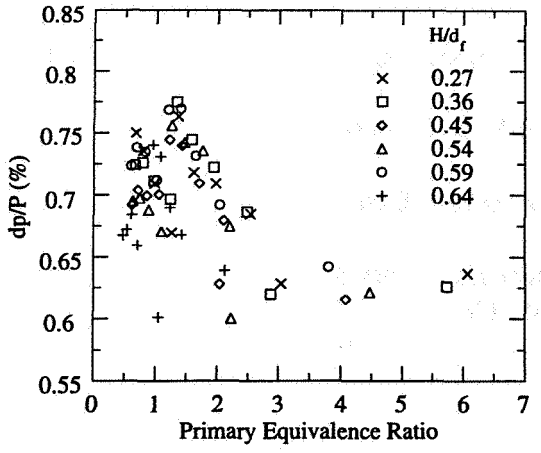

Figure 5. Pressure Drop versus Primary Equivalence Ratio at U_{air} = 33 m/s

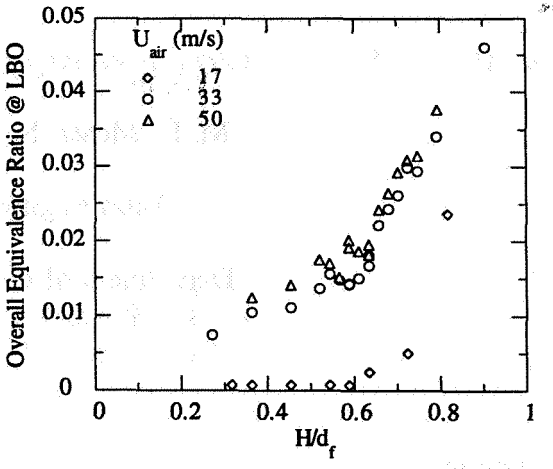

Figure 6. Effect of H/d_f on Lean Blow-out under Various Annular Air Flow Conditions

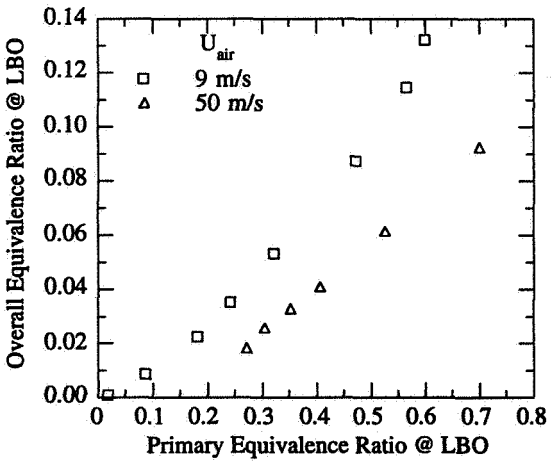

Figure 7. Relationship between Overall and Primary Equivalence Ratios at LBO (H/d_f = 0.55)

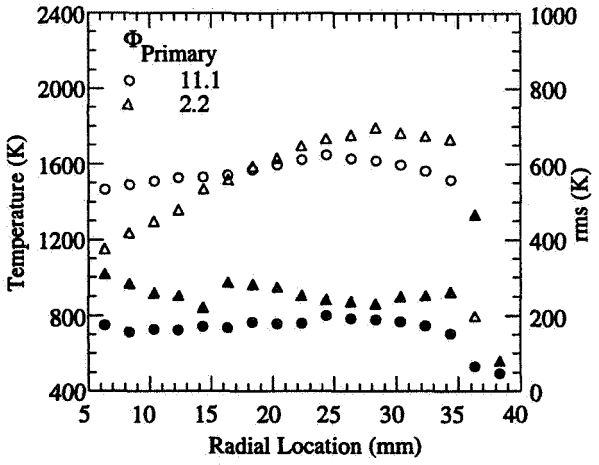

Figure 8. Temperature Profiles at z = 5 mm (H/d_f = 0.59)

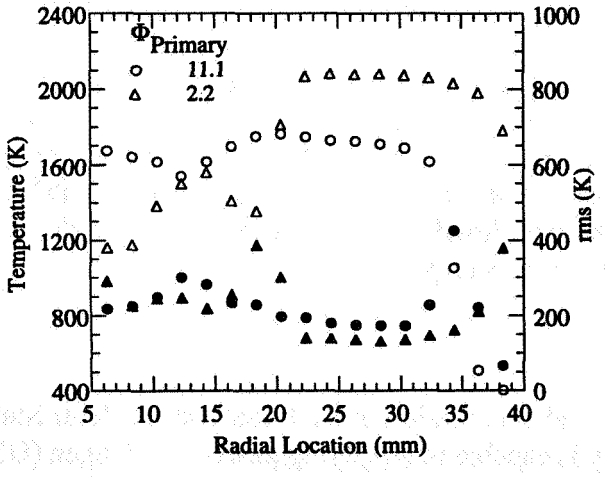

Figure 9. Temperature Profiles at z = 25 mm (H/d_f = 0.59)

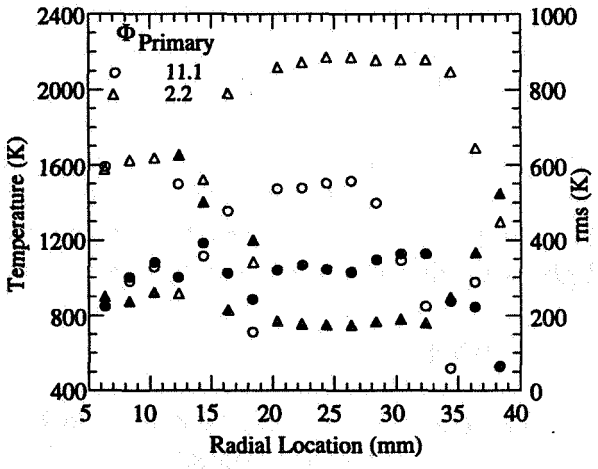

Figure 10. Temperature Profiles at z = 39 mm (H/d_f = 0.59)

Pgs 5 427124

N95-70867

Density and Mixture Fraction Measurements in a GO_2/GH_2 Uni-Element Rocket Chamber

M. D. Moser, S. Pal and R. J. Santoro

Propulsion Engineering Research Center
and
Department of Mechanical Engineering
The Pennsylvania State University
University Park, Pennsylvania 16802

Introduction

In recent years, there has been a renewed interest in gas/gas injectors for rocket combustion. Specifically, the proposed new concept of full-flow oxygen rich preburner systems calls for the injection of both oxygen and hydrogen into the main chamber as gaseous propellants. The technology base for gas/gas injection must mature before actual booster class systems can be designed and fabricated. Since the data base for gas/gas injection is limited to studies focusing on the global parameters of small reaction engines,[1,2] there is a critical need for experimental programs that emphasize studying the mixing and combustion characteristics of GO_2 and GH_2 propellants from a uni-element injector point of view. The experimental study of the combusting GO_2/GH_2 propellant combination in a uni-element rocket chamber also provides a simplified environment, in terms of both geometry and chemistry, that can be used to verify and validate computational fluid dynamic (CFD) models.

Over the past few years at Penn State, an experimental research program has focused on characterizing uni-element rocket chamber flowfields. This research has been undertaken as part of the Propulsion Engineering Research Center (PERC) at Penn State under the sponsorship of NASA. The research for this program has been conducted at the Cryogenic Combustion Laboratory at PERC, which has the capability to handle gaseous and liquid oxygen (GO_2 and LOX) as well as gaseous hydrogen (GH_2), methane and hydrocarbon fuels at flowrates comparable to single element conditions typical of rocket injectors. The work described here focuses on flowfield measurements in a uni-element (shear coaxial injector) optically accessible rocket chamber that utilizes the GH_2/GO_2 propellant combination. To date, several laser-based diagnostic techniques, including planar laser induced fluorescence (PLIF) for OH-radical fluorescence measurements,[3] laser Doppler velocimetry (LDV) for velocity field measurements,[3] and planar laser light scattering for average density and mixture fraction measurements[4] have been employed towards characterizing the combusting flowfield. The experimental results of the light scattering technique are summarized in this manuscript.

Experimental

The experiments were conducted in an optically accessible rocket chamber at Penn State's Cryogenic Combustion Laboratory. This facility is capable of supplying gaseous hydrogen (GH_2), gaseous oxygen (GO_2) and liquid oxygen (LOX) at flowrates up to 0.11 kg/s (0.25 lb/s), 0.045 kg/s (0.1 lb/s) and 0.45 kg/s (1.0 lb/s), respectively. The rocket chamber is modular in design

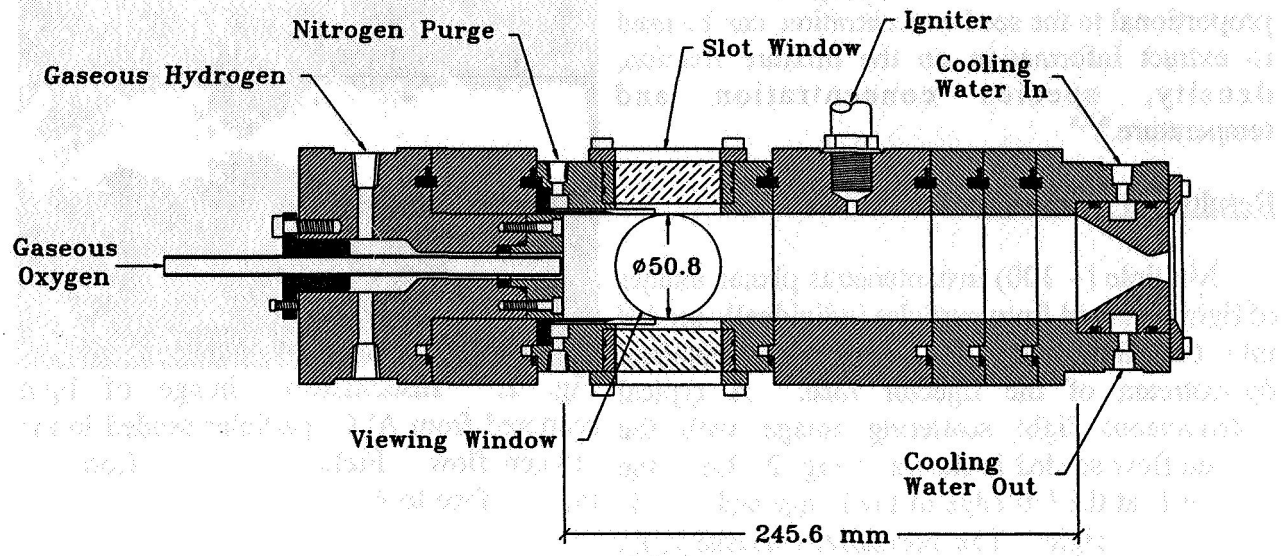

Fig. 1. Cross-sectional view of the optically accessible rocket chamber. The interior of the chamber is 50.8 x 50.8 mm.

and can be easily configured to provide optical access along the chamber length. A cross-sectional view of the rocket assembly is shown in Fig. 1. The design of the rocket chamber is detailed in Refs. 3 and 5. The chamber is comprised of several sections which include an injector assembly, igniter, window and blank sections, and a nozzle assembly. The window-section allows optical access into the combustion chamber for laser-based diagnostic techniques. Two diametrically opposed windows, 50.8 mm (2 in.) in diameter and 25.4 mm (1 in.) thick, provide optical access into the 50.8 mm (2 in.) square rocket chamber. Two slot windows measuring 6.25 x 50.8 mm (0.25 x 2 in.) on the remaining two sides provide additional optical access into the rocket chamber for laser sheet diagnostics. All windows are protected from the hot combustion gases by a gaseous nitrogen (GN_2) purge which flows across the interior window surfaces.

A shear coaxial injector introduced the propellants into the rocket chamber. The GO_2 post of the injector had an inner diameter of 7.75 mm (0.305 in.) and was flush with the injector face. The inner and outer diameters of the fuel annulus were 9.53 mm (0.375 in.) and 12.7 mm (0.5 in.), respectively. The nominal mass flowrate of GO_2 through the central tube of the shear coaxial injector was 0.042 kg/s (0.093 lb/s) while the GH_2 mass flowrate through the annulus of the injector was 0.010 kg/s (0.023 lb/s) resulting in an O/F mass flowrate ratio of four. The nozzle had a throat diameter of 11.35 mm (0.447 in.). The flowrates together with the nozzle configuration produced a chamber pressure of 1.31 MPa (190 psia). The c^* efficiency of the rocket firings is close to 98%.[3]

Laser light scattering from seed particles was used for studying the mixing characteristics of the GH_2/GO_2 combusting flowfield. The technique involves seeding each of the propellant streams individually with sub-micron Al_2O_3 particles, illuminating the flowfield with a laser sheet, and recording the scattered light. Since the seed particle mark the seeded propellant stream,

measurements of scattered light, which is proportional to the seed concentration, can be used to extract information on the mixture fraction, density, species concentration and temperature.[6,7,8]

Fig. 2. Instantaneous image of light scattered from Al_2O_3 particles seeded in the oxygen flow. Field of view is from the injector face to 45.7 mm downstream.

Results and Discussion

Multiple (~ 100) instantaneous planar images of light scattered from particles individually seeded into the GO_2 and GH_2 flows were obtained downstream of the injector face. A typical instantaneous light scattering image with the oxygen flow seeded is shown in Fig. 2. Here, the injector is at the left edge of the image and flow is from left to right. The normalized intensity, f_O, relates scattered light intensity, I, to density, ρ, and mixture fraction, ξ, by the following relation:

$$f_O = \frac{I}{I_O^\circ} = \frac{\rho(1-\xi)}{\rho_O^\circ(1-\xi^\circ)} \tag{1}$$

where I_O°, ρ_O°, and ξ° are intensity, density, and mixture fraction at a reference point, typically at the injector exit. Similarly, for the GH_2 seeded flow the following relation is obtained:

$$f_F = \frac{I}{I_F^\circ} = \frac{\rho\xi}{\rho_F^\circ\xi^\circ} \tag{2}$$

The average density in the flowfield was obtained from combining the averaged light scattering images of both the GH_2 and GO_2 seeded flows. The radial profile of average density at an axial distance of 25.4 mm (1 in.) from the injector face is compared to predictions made using the FLUENT code[9] in Fig. 3. The average density is maximum at the centerline, corresponding to the region of high oxygen concentration, and decreases with radial distance. The experimental results and code predictions agree reasonably well in terms of both maximum density and radial profile symmetry in the central region of the flowfield. However, away from the centerline, the average density does not drop off to the low values predicted by the code.

Density, mixture fraction and other parameters are derived from the individually seeded GO_2 and GH_2 scattered light images with a function relating these parameters to the product of the density and mixture fraction, $\rho\xi$. An example of such a relationship, calculated with the Chemical Equilibrium Calculation (CEC) program[10] assuming equilibrium, is shown in Fig. 4. The results of applying this function to the GH_2 seeded data and a similar function to the GO_2 data is shown in Fig. 5. The width of the high density region is greater for the results obtained from the GO_2 seeded data than for the GH_2 seeded data. In comparing Fig. 3 with Fig. 5, it is evident that the radial profile of average density obtained using averaged images is closer to that

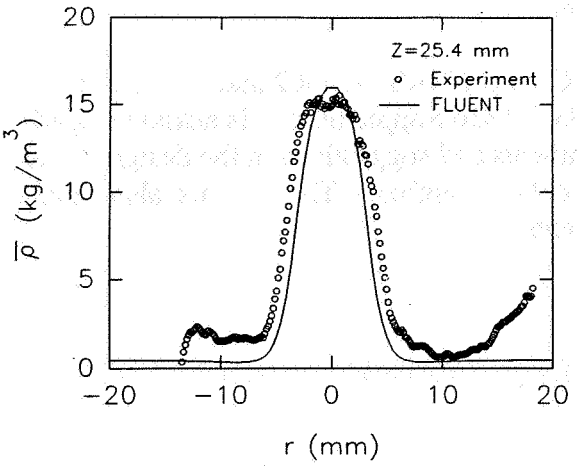

Fig. 3. Average density vs. radius at an axial distance of 25.4 mm from the injector face. Density derived from averaged light scattering images is compared with predictions made using the FLUENT code.

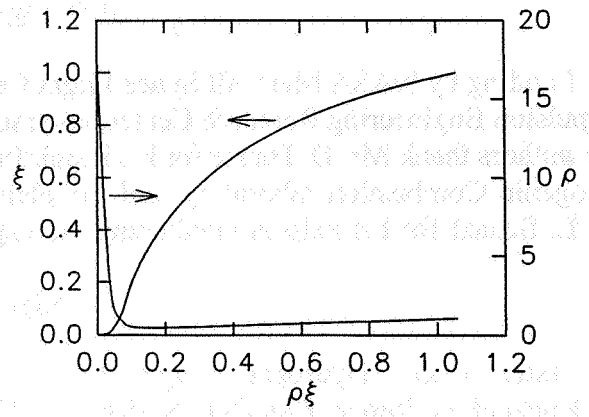

Fig. 4. Functional dependency of density, ρ, and mixture fraction, ξ, on the product, $\rho\xi$, calculated using the Chemical Equilibrium Calculation (CEC) program (Gordon and McBride [10]).

obtained using the GO_2 seeded scattered light images than the GH_2 seeded scattered light images. However, away from the centerline, the average density obtained from the GH_2 seeded scattered light images matches the code predictions.

Conclusions

Planar laser light scattering images from individual seeding of both the GO_2 and GH_2 flows depict the unsteady nature of the reacting flowfield. The direct analysis of these images provided estimates of the average density and Favre averaged mixture fraction fields in the flowfield. Estimates of average density derived by applying the equilibrium relationships to either the GH_2 or GO_2 seeded flows should yield similar results, except in regions of low signal to noise due to low seed number densities. The causes of the discrepancies observed in Fig. 5 could be due to either effects of flow conditions (i.e. the ability of the seed to follow the flow, or temperature effects) or to the data reduction methodology. These effects are being assessed through cold flow and hot fire tests with methane and oxygen.

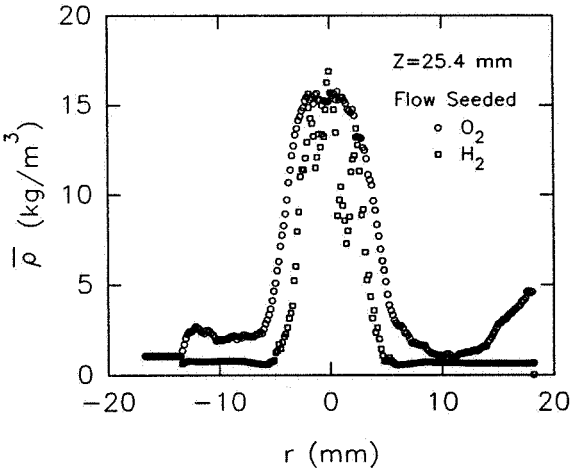

Fig. 5. Average density at an axial distance of 25.4 mm from the injector face. The radial density profiles are derived from scattered light images of both GO_2 and GH_2 seeded flows with the assumption of local equilibrium.

Acknowledgment

Funding by NASA Marshall Space Flight Center, Contract NAS 8-38862 and the Penn State Propulsion Engineering Research Center, contract NAGW 1356 Supplement 5, is acknowledged. The authors thank Mr. D. Harrje for his insightful comments and suggestions in the design of the Cryogenic Combustion laboratory and uni-element rocket chamber. The authors also thank Mr. L. Schaaf for his help in conducting the experiments.

References

1. Paster, R. D., "Hydrogen Oxygen APS Engines (High Pressure)," Contract NAS3-14352, Rocketdyne Report R8837-1, NASA CR- 12085.

2. Johnson R. J., "Hydrogen-Oxygen Catalytic Ignition and Thruster Investigation, Vol. I: Catalytic Ignition and Low Pressure Thruster Evaluations," Contract NAS3-14347, TRW Report 14549-60010-RO-00, NASA CR-120869.

3. Moser, M. D., Merenich, J. J., Pal, S., and Santoro, R. J., "OH-Radical Imaging and Velocity Field Measurements in a Gaseous Hydrogen/Oxygen Rocket," AIAA 93-2036, AIAA/SAE/ASME/ASEE 29th Joint Propulsion Conference and Exhibit, Monterey, CA, June 28-30, 1993.

4. Moser, M. D., Pal, S., and Santoro, R. J., "Uni-Element Rocket Studies," 1994 Conference on Advanced Earth-to-Orbit Propulsion Technology, NASA Marshall Space Flight Center, AL, May 17-19, 1994.

5. Pal, S., Moser, M. D., Ryan, H. M., Foust, M. J. and Santoro, R. J., "Flowfield Characteristics in a Liquid Propellant Rocket," AIAA 93-1882, AIAA/SAE/ASME/ASEE 29th Joint Propulsion Conference and Exhibit, Monterey, CA, June 28-30, 1993.

6. Stepowski, D., and Cabot G., "Laser Mie Scattering Measurement of Mean Mixture Fraction Density and Temperature by Conditional Seeding in a Turbulent Diffusion Flame," Twenty-Second Symposium (International) on Combustion, The Combustion Institute, pp. 619-625, 1988.

7. Kennedy, I. M., and Kent, J. H., "Measurements of a Conserved Scalar in Turbulent Jet Diffusion Flames," Seventeenth Symposium (International) on Combustion, The Combustion Institute, pp. 279-287, 1979.

8. Stepowski, D., "Laser Measurements of Scalars in Turbulent Diffusion Flame," Prog. Energy Combust. Sci., Vol. 18, pp. 463-491, 1992.

9. FLUENT Computer Program from Fluent, Inc.

10. Gordon, S. and McBride, B. J., "Computer Program for Calculation of Complex Chemical Equilibrium Compositions, Rocket Performance, Incident and Reflected Shocks, and Chapman-Jouguet Detonations," NASA SP-273 Interim Revision N78-17724, March, 1976.

427127
P35 5
N95-70868

CFD ASSESSMENT OF THE CARBON MONOXIDE AND NITRIC OXIDE FORMATION FROM RD-170 HOT-FIRE TESTING AT MSFC

Ten-See Wang and Paul McConnaughey
NASA Marshall Space Flight Center, Huntsville, Alabama 35812
Saif Warsi
Sverdrup Technology, Inc., Huntsville, Alabama 35806
and
Yen-Sen Chen
Engineering Sciences, Inc., Huntsville, Alabama 35805

SUMMARY:

Computational Fluid Dynamics (CFD) technology has been used to assess the exhaust plume pollutant environment of the RD-170 engine hot-firing on the F1 Test Stand at Marshall Space Flight Center. Researchers know that rocket engine hot-firing has the potential for forming thermal nitric oxides (NO_x), as well as producing carbon monoxide (CO) when hydrocarbon fuels are used. Because of the complicated physics involved, however, little attempt has been made to predict the pollutant emissions from ground-based engine testing, except for simplified methods which can grossly underpredict and/or overpredict the pollutant formations in a test environment. The objective of this work, therefore, has been to develop a technology using CFD to describe the underlying pollutant emission physics from ground-based rocket engine testing. This resultant technology is based on a three-dimensional, viscous flow, pressure-based CFD formulation, where wet CO and thermal NO_x finite-rate chemistry mechanisms are solved with a Penalty Function method. A nominal hot-firing of a RD-170 engine on the F1 stand has been computed. Pertinent test stand flow physics such as the multiple-nozzle clustered engine plume interaction, air aspiration from base and aspirator, plume mixing with entrained air that resulted in contaminant dilution and afterburning, counter-afterburning due to flame bucket water-quenching, plume impingement on the flame bucket, and restricted multiple-plume expansion and turning have been captured. The predicted total emission rates compared reasonably well with those of the existing hydrocarbon engine hot-firing test data.

DISCUSSION:

RD-170 is a regeneratively cooled, four-nozzle clustered engine which burns Kerosene fuel with liquid oxygen and was used to thrust Energia launch vehicles. Thermochemical analysis was performed for the thrust chamber at a nominal operating condition and the equilibrium products at the nozzle exit were used as the input to the propulsion system. $CH_{1.9423}$ was used as the chemical formula for Kerosene fuel. The analysis indicated that a significant amount of CO (24.569%) existed at the nozzle exit. This is the amount that could be dumped into the environment and can only be chemically reduced through afterburning. To accurately predict the contaminant concentrations of the exhaust plume, finite-rate chemical kinetics are included in the numerical modeling. The plume chemistry occurring in the flame-bucket/test-stand flow physics includes the afterburning of CO to CO_2, thermal NO_x formation and decomposition, counter-afterburning effect on CO conversion due to water quenching and its reduction effect on NO_x formation. These are described with a wet CO and a thermal NO_x finite-rate mechanisms. Production of thermal NO_x is generally negligible at low temperatures. It is therefore expected that most of the thermal NO_x will be formed in the flame front, .i.e., the plume mixing layer near the exit plane of the nozzles.

The F1 Test Stand, standing 230 feet tall with a flame bucket (deflector) attached to the aspirator, was used to test F1 engines with which Saturn launch vehicles were propelled. Not only does the flame bucket quenches the rocket exhaust plume with deluge water, but also turns the vertical flowing exhaust plume to that of a horizontal direction, after which the plume expands and dissipates into the atmosphere. Fig. 1 shows the computational domain for the F-1 Stand. The RD-170 engine is mounted vertically, firing down into the flame bucket. Due to symmetry, only half of the domain was actually computed. The four RD-170 nozzles (mounted beneath the platform that is not modeled) and the aspirator are described by Zone 1 which contains 63,360 grid points. The aspirator itself is mounted on top of the flame bucket such that the air entrainment can be promoted and the plumes are centered while impinging at a predetermined area in the flame bucket (approximately 45-degree elbow at the bottom). Ambient air is allowed

to be entrained through the top and four side boundaries of Zone 1. The flame bucket is modeled by Zone 2 which composes of 72,000 grid points. The plumes are then quenched through water deluge injecting from all four walls inside the bucket. The water injection pattern is designed as such that most of the water injects at the plume impingement area. After passing through the flame bucket, the quenched plumes expand into the vast surrounding atmosphere (Zone 3, not shown) which is described by 156,975 grid points.

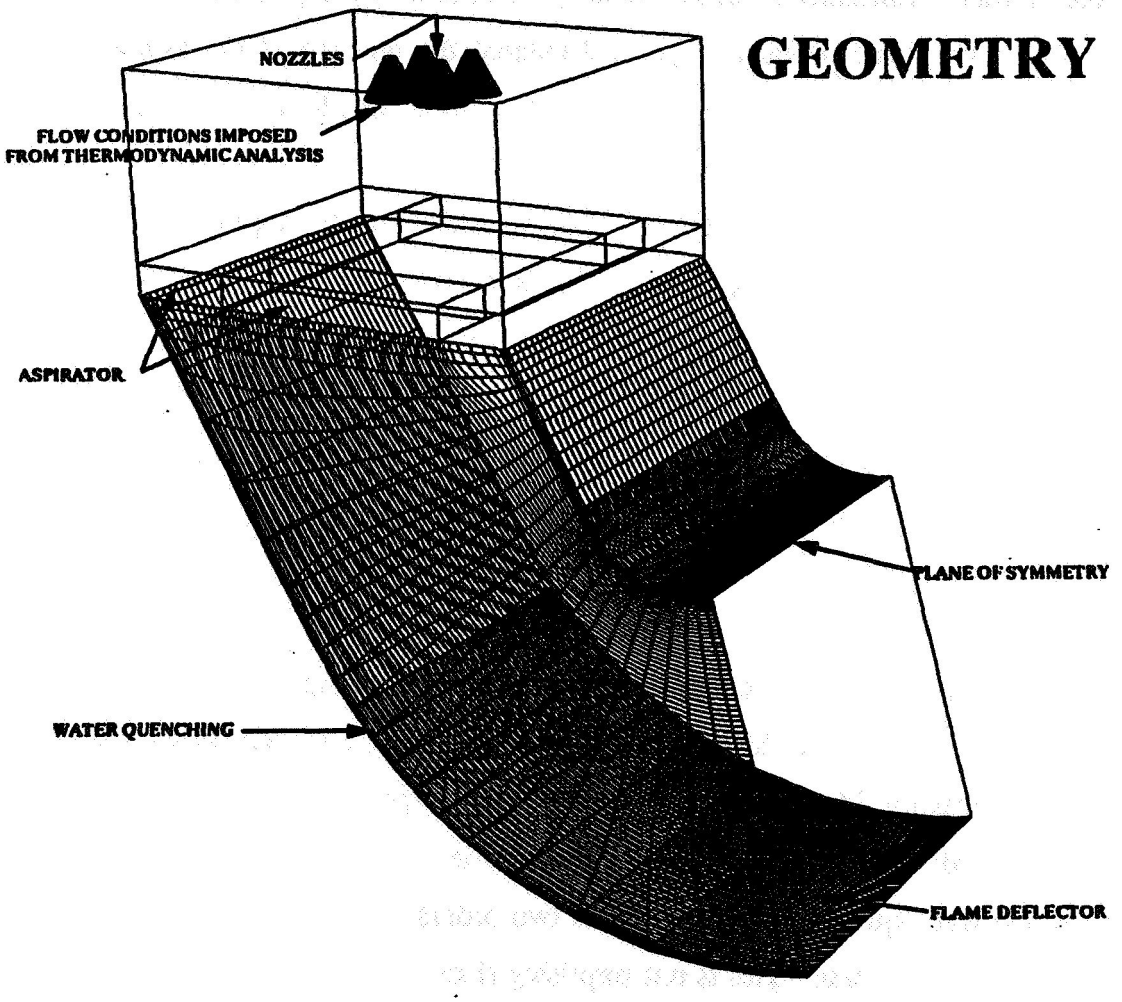

Fig. 1 Computational domain for the RD-170 nozzles and F1 Test Stand.

A frozen chemistry analysis was performed at first for a small period of elapsed time in order to establish an initial plume in the system. This not only prepared for the initial flowfields for the computation of subsequent parallel finite-rate chemistry and finite-rate chemistry with water-quenching cases, but also served as an excellent check of mass conservation using carbon balance. This procedure is allowed since the total pollutant emission rates during a nominal steady RD-170 hot-firing are desired and not those of an actual start-up sequence. The goals are therefore to compute the growth rate of NO_x and the disappearance rate of CO until they achieve asymptotic states. The result of the computation indicated a large amount of air was entrained through the aspirator. Entrained from surroundings close to the open platform, the air accelerated and mixed with the plume boundary layer and entered the opening of the aspirator, where it continuously mixed with the advancing plume boundary layer. In addition to cooling and dilution of the contaminant, the entrained air also provides the source of reactants for afterburning and thermal NO_x formation. Most of the thermal NO_x is formed near the aspirator level where it has the most mixing and the hottest temperature. This is in agreement with the characteristics of the Zeldovich mechanism. It can also be seen that the plumes impinge on the 45-degree bend section of the flame bucket where it encounters the most water-quenching, that agrees with the original design. The quenched plumes then turn and partially hit the outer wall, where it moves horizontally out, following the direction of the flame bucket.

The averaged mass fraction for CO in the add water-quenching case is more than that of the purely finite-rate chemistry case due to the counter after-burning effect of deluge water, and vice versa for that of CO_2. The higher level of OH in the finite-rate case shows a higher degree of after-burning reaction, due to higher overall plume temperature without water-quenching. Total NO_x production drops significantly in the add water-quenching case. The concentration of NO_x in the add water-quenching case is almost two orders of magnitude lower than that in the finite-rate chemistry only case. This is not surprising since the extent of thermal NO_x formation depends heavily on the local temperature. The effect of water deluge on the formation of NO_x is the reduction in peak temperature caused by the heat capacity of water. The computations were stopped when the growth rates of the plumes reached their approximate asymptotic states. Obviously, the plume energy of the finite-rate chemistry is higher than that of the add water-

quenching case. Correspondingly, the plume volume growth rate of the finite-rate case is larger than that of the add water-quenching case. These CFD results ultimately serve as the basis (input) for the subsequent meteorological cloud dispersion calculation, where the plume volume growth rate helps determining the eventual plume size and the plume energy growth rate helps determining the magnitude the plume buoyancy force.

A comparison of the calculated criteria pollutant total emission rates for RD-170 with those measured for other Kerosene-fueled engines is shown in Table 1. Since thrust levels are quite different, the measured emission rates were extrapolated to a RD-170 level by thrust ratios. Although the operations of the engines and test stands are vastly different, and there is a question on whether the point sampling technique used in the measurement representative of the whole plume. The agreement in terms of order-of-magnitude for these engines is reasonable and encouraging. Among RD-170 CFD computations, the emission rate of CO is maximum and that of NO_x is zero for the frozen chemistry case, since afterburning reactions are not turned on, whereas the effect of water deluge has reduced the CO conversion rate from 83% of the finite-rate chemistry case to that of 67%. This is of interest since the effect of water deluge also has reduced the NO_x production by 95%.

Table 1. Total emission rates

Engine	Thrust, lbf	NO_x, lb/sec	CO, lb/sec
MA5B/hot-firing	370,000	5.4/25.9*	133/641*
MA3S/hot-firing	165,000	2.7/29.1*	210/2,266*
MA3B/hot-firing	60,000	1.5/45.6*	138/4,111*
RS27/hot-firing	205,000	1.2/10.6*	94/820*
RD-170/CFD			
Frozen	1,777,000	-	1,382
Finite-Rate	1,777,000	8.0	232
Add Water	1,777,000	0.4	463

* based on extrapolation of measured emission rate to a RD-170 by thrust ratio

427130
P95 S

N95- 70869

THE EFFECT OF INCOMPLETE FUEL-AIR MIXING ON THE LEAN BLOWOUT LIMIT, LEAN STABILITY LIMIT AND NO_x EMISSIONS IN LEAN PREMIXED GAS TURBINE COMBUSTORS

W.-P. Shih, J. G. Lee and D. A. Santavicca
Propulsion Engineering Research Center
Penn State University
University Park, PA 16802

OVERVIEW:

Gas turbine engines for both land-based and aircraft propulsion applications are facing regulations on NO_x emissions which cannot be met with current combustor technology. A number of alternative combustor strategies are being investigated which have the potential capability of achieving ultra-low NO_x emissions, including lean premixed combustors, direct injection combustors, rich burn-quick quench-lean burn combustors and catalytic combustors. The research reported in this paper addresses the effect of incomplete fuel-air mixing on the lean limit performance and the NO_x emissions characteristics of lean premixed combustors. Since in actual gas turbine combustor hardware it is impossible to achieve perfect mixing of the fuel and air, an important question is how well does the fuel and air have to be mixed to achieve acceptably low NO_x emissions? The effect of incomplete fuel-air mixing on the lean stability and lean blowout limits is also studied.

The experiments were conducted in a coaxial dump combustor at 1 atmosphere pressure. The fuel used in the tests was natural gas, where the degree of fuel-air mixing was varied by changing the fuel split between upstream and downstream fuel injection locations. Three fuel split cases were studied, i.e., 100%/0%, 50%/50% and 0%/100%, where the first percentage refers to the percentage of the fuel which was introduced at the upstream (or premixed) location.

The fuel-air distribution at the combustor inlet is quantified using two-dimensional acetone fluorescence. These measurements are made both with and without combustion. A water-cooled gas sampling probe and a chemiluminescence analyzer is used to measure the concentration of NO and NO_2 along the centerline and at the exit of the combustor.

The characteristics of the acoustic noise produced by the combustor are determined from the output of a microphone. And lastly, the flame structure is characterized using two-dimensional OH fluorescence.

RESULTS

Figure 1 is a plot of NO and NO_x concentrations measured 13" downstream of the combustor inlet versus the overall equivalence ratio for the 100%, 50% and 0% premixed cases. These results clearly show the effect of incomplete fuel-air mixing on NO_x production. At equivalence ratios below approximately 0.9, there is a significant increase in the amount of NO produced as a result of incomplete fuel-air mixing. However, for equivalence ratios near stoichiometric, incomplete mixing actually results in less NO_x production. These results are similar to those previously reported.[1-3]

There is an interesting and important relationship between flame structure and degree of fuel-air mixing illustrated by the results shown in Figure 2, which shows two-dimensional OH fluorescence images taken immediately downstream of the flameholder. Three representative images are shown for the 100%, 50% and 0% premixed cases. The field of view in each image is 35 mm by 35 mm. The flame structure for the 100% premixed case is shown to be highly reproducible. The 50% and 0% premixed cases show significant variations in flame structure; however, the images appear to repeat themselves, suggesting a periodic nature to the flame stabilization process. In addition, in the 0% premixed case, the very irregular shape of the OH images suggests that the reaction zone boundaries are confined to the local fuel-rich pockets due to the poor fuel-air mixing.

The combustion process, particularly in the incompletely mixed cases, resulted in significant combustion-generated noise, which can be related to the characteristics of the flame stability. The combustion-generated noise was recorded by a sound level meter and an A/D data acquisition system. Fourior analysis of the signals revealed their frequency content. The readings of the sound level meter were 77 dB, 105 dB, and 103 dB for 100%, 50% and 0% premixed cases, respectively. The background noise in the laboratory was around 62 dB. The frequency content of the 100% premixed case was a wide band signal with the peak located near 400 Hz. For the 50% premixed case, there was a single

dominant frequency located near 375 Hz. The narrow band width indicates the noise is a pure tone. For the 0% premixed case, a frequency peak located near 400 Hz was ibserved with a slightly wider band width. Further study of the relationship between the dominant frequency of the combustion-generated noise and the periodic behavior of the flame structure is in progress.

REFERENCES

1. Appleton, J. P. and Heywood, J. B., "The Effects of Imperfect Fuel/Air Mixing in a Burner on NO Formation from Nitrogen in the Air and the Fuel," *14th Symposium (Int'l.) on Combustion*, The Combustion Institute, pp. 777-786, 1973.
2. Lyons, V. J., "Fuel/Air Nonuniformity-Effect on Nitric Oxide Emissions," *AIAA Journal*, Vol. 20, No. 5, pp. 660-665, 1981.
3. Fric, T. F., "Effect of Fuel-Air Unmixedness on NO_x Emissions," AIAA Paper No. 92-3345, 1992.

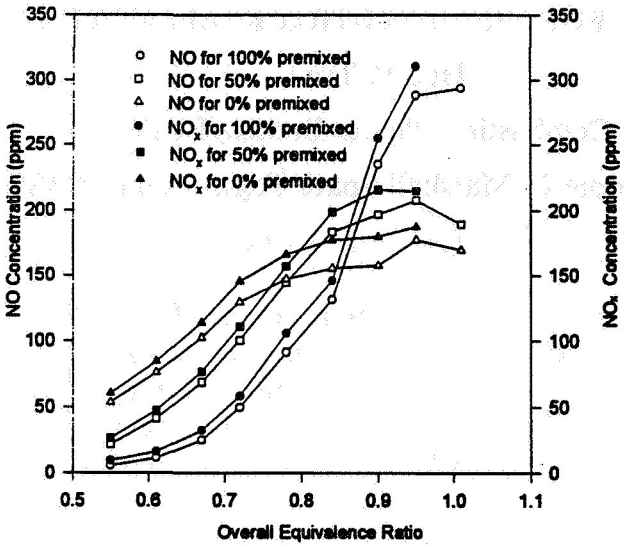

Figure 1. NO and NO_x concentrations measured 13" downstream of the combustor inlet versus overall equivalence ratio.

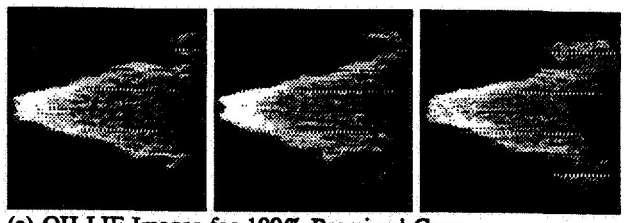

(a) OH LIF Images for 100% Premixed Case

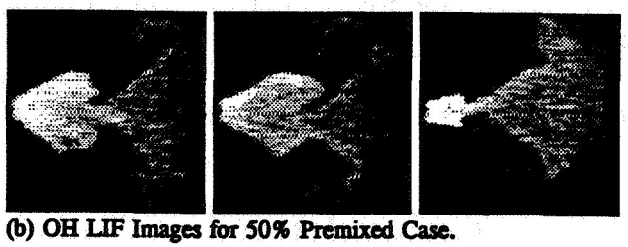

(b) OH LIF Images for 50% Premixed Case.

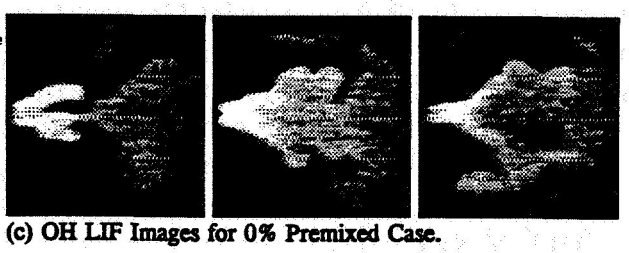

(c) OH LIF Images for 0% Premixed Case.

Figure 2. Two-dimensional OH fluorescence images of the flame structure.

427132
Pgs 7

N95- 70870

PREDICTION OF ENGINE PERFORMANCE AND WALL EROSION DUE TO FILM COOLING FOR THE "FAST-TRACK" ABLATIVE THRUST CHAMBER

Huu P. Trinh

Combustion Physics Branch/EP13

NASA/George C. Marshall Space Flight Center (MSFC)

Huntsville, Alabama

Efforts have been made at the Propulsion Laboratory, MSFC to design and develop new rocket liquid engines for small-class launch vehicles. Emphasis of the efforts is to reduce the engine development time with the use of conventional designs while meeting engine reliability criteria. Consequently, the engine cost should be reduced. A demonstrative ablative thrust chamber, called "fast-track", has been built. At the time of writing this report, the chamber will be tested in two weeks.

To support the design of the "fast-track" thrust chamber, predictions of the wall temperature and ablation erosion rate of the "fast-track" thrust chamber have been performed using the computational fluid dynamics program REFLEQS[1] (Reactive Flow Equation Solver). The analysis is intended to assess the amount of fuel to be used for film cooling so that the erosion rate of the chamber ablation does not exceed its allowable limit. In addition, the thrust chamber performance loss due to an increase of the film cooling is examined.

It is well known that physical processes occurring in the combustion chamber consist of atomization, evaporation, two-phase mixing, chemical kinetic reaction, etc... they are highly complex and strongly coupled. Due to the current simulation limitations, a number of assumptions have to be imposed to solve the problem. They are listed below:

- Only an axisymmetric flow field of the thrust chamber is simulated. The chamber inlet is divided radially into two regions. The outer region, called the film cooling ring, represents the film cooling inlet, while the inner one, called the hot core, operates at uniform mixture ratio (MR).
- The propellants being injected into the hot core region are assumed to be gaseous, completely mixed, and react in a chemical equilibrium fashion at the injector face. The film coolant is considered to be gaseous at the inlet. Its properties are estimated based on the ideal-gas relationship and the chemical equilibrium postulate.
- The estimation of the erosion rate of the ablative silica phenolic material is based on limited test data reported in 1969 by Aerojet-General Corporation[2]. The test series were conducted for a large hydrogen/oxygen thrust chamber. The only reported data (see Fig.1), which are relatively suitable for the present analysis, are the erosion rates of silica phenolic at the chamber throat. The erosion rate, then, is assumed to be a function of the chamber pressure and the ideal recovery temperature (equivalent to the adiabatic wall temperature). Moreover, the erosion rate is considered to be applicable for every point along the chamber wall.

Due to the aforementioned assumptions, the results of the present analysis should not be interpreted as representative of the actual thrust chamber characteristics. They rather provide the trend of the thrust chamber behavior and tend to portray the upper bound

on the wall temperature because of the gaseous propellant and chemical equilibrium assumptions. Consequently, the estimated erosion rate may be higher than the actual rate. On the other hand, the solutions seem to provide the lower bound on the performance loss, since the simulation excludes other combustion losses.

The calculations have been conducted for various operating conditions, film cooling flow rates, and two chamber lengths. Hence, the results provide some understandings of the sensitivity among the parameters involved. The computational domain of the thrust chamber, shown in Fig.2, is enclosed by a grid mesh size of 61x121. Typical flow field temperature and velocity within the chamber are presented in figures 3 and 4, respectively. A summary of the thrust chamber geometry and operating conditions used in the analysis is given below:

Chamber Pressure (psia)	300
Overall Mixture Ratio (MR)	2.34
Fuel (RP-1) Flow Rate (lbm/sec)	14.19
Oxidizer (LOX) Flow Rate (lbm/sec)	33.19
Fuel for Film cooling (% in mass)	0, 4, 6, 8, 12, 14
Combustion Chamber Length (in)	16.0, 21.0
Contraction Area Ratio	2.45

Because of the assumption of gaseous film coolant, the actual inlet area of the film cooling has been adjusted in order to converse its mass flow rate and inlet velocity. As a result, the inlet momentum may not be correctly simulated. To examine the solution dependence on the inlet momentum change, calculations for a fixed film cooling flow rate have been performed for several film cooling inlet momentum values by varying the inlet area, velocity, and density. As shown in figures 5 and 6, the wall temperature and erosion rate are not significantly sensitive to the change in the film cooling momentum. The wall temperatures and erosion rates for the chamber length of 16-inches at various film cooling percentages are presented in figures 7 and 8. The corresponding maximum wall temperature and erosion rate of each film cooling value are plotted in figures 9 and 10. The results indicate that the maximum values of temperature and erosion rate are located slightly upstream of the throat. Moreover, when the percentage of fuel to be used for film cooling is greater than 10%, the chamber wall conditions no longer strongly respond to an increase of film cooling. It should be noted that the additional fuel to be used for film cooling results in a higher hot core MR. The hot core flow, accordingly, has a higher temperature. Therefore, adding more film coolant no longer has a strong effect on the wall temperature reduction. On the other hand, the thrust chamber performance loss, shown in Fig. 11, linearly increases with the film coolant increase.

By extending the combustion chamber length from 16.0 to 21.0- inches, the wall temperature peak, shown in Fig. 12, increases by an amount of 10%. This result is expected, since the longer combustion chamber allows the extension of the hot gas entrainment to the boundary layer, and the chemical reaction process near the wall. The corresponding erosion rate at the peak, Fig. 13, climbs at a steep rate. As seen from Fig.1, when the recovery temperature exceeds 3500 Rankine, the erosion rate curves have steeper slopes than the rate at the low temperature. These erosion characteristics reflect the solutions for the chamber length of 21-inches, which is shown in Fig.12. Although the wall temperature, as mentioned previously, increases only 10% at the peak point, the corresponding erosion rate increases by as much as 120% due to the peak

temperature exceeding 3500 Rankine for the 21-inch long chamber.

References:

1. Przekwas,A.J., Lai,Y.G., Krishnan,A., Avva,R.K., Giridharan, M.G.,"Combustion Chamber Analysis Code, Final Report", NASA contract number: NAS8-37824.
2. Moise, J.C., Kovach R.J.,"Performance of Various Ablative Materials in a Large Hydrogen/Oxygen Thrust Chamber", AIAA paper 69-442.

Fig.1: Erosion Rate of Ablative Silica-Phenolic Material

(Data From Aerojet-General Corporation)

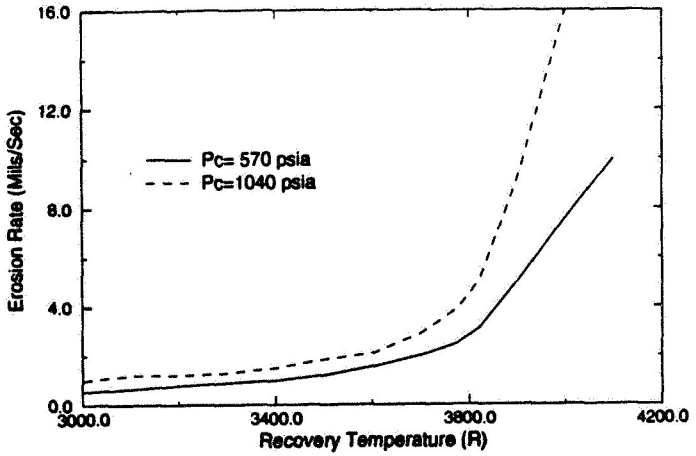

FIG.3: FAST-TRACK CHAMBER TEMPERATURE (KELVIN)
PC=300PSI, MR(overall)=2.34

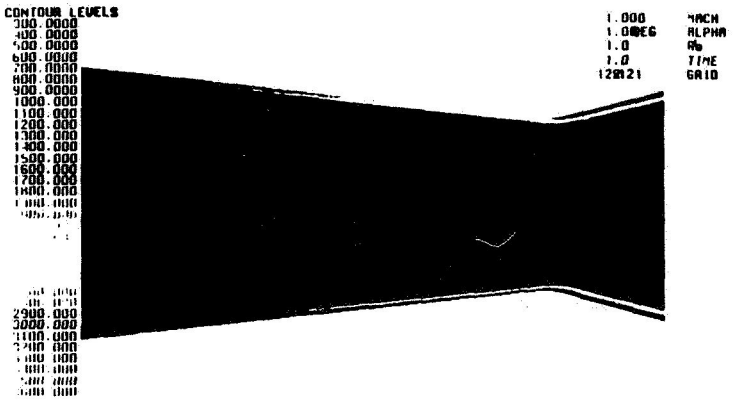

FIG.4: FAST-TRACK CHAMBER VELOCITY VECTOR
COLORED BY TEMPERATURE FIELD (KELVIN)

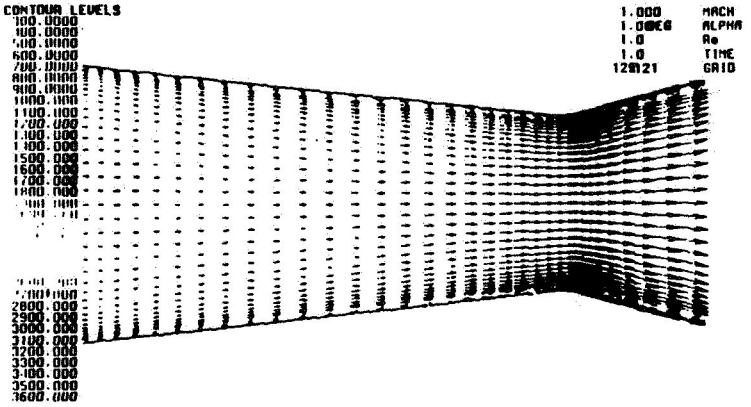

FIG.2: COMPUTATION GRID MESH (61x121)

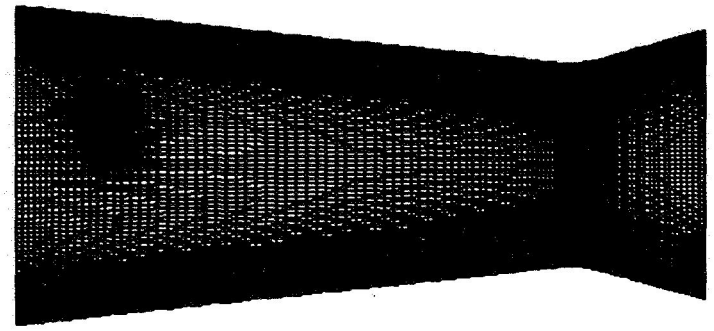

ORIGINAL PAGE IS
OF POOR QUALITY

Fig.5: Change in Wall Temperature Due To Various Film Cooling Inlet Momentum

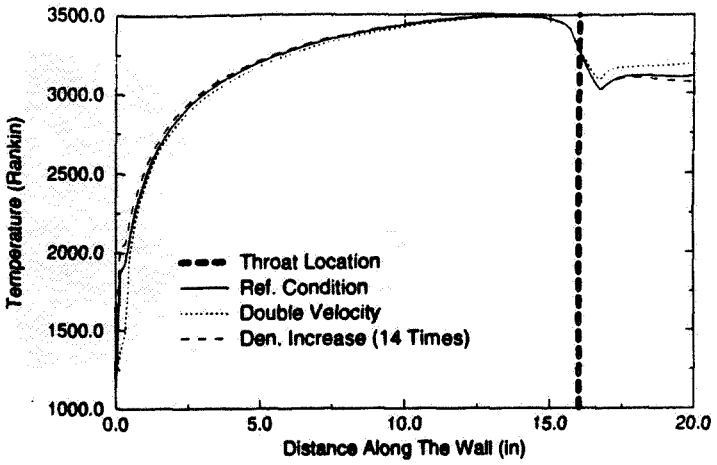

Fig.6: Change in Erosion Rate Due To Various Film Cooling Inlet Momentum

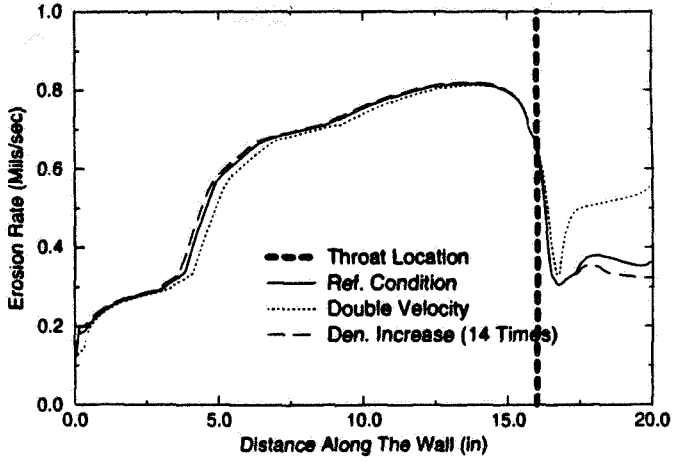

Fig.7: Wall Temperature Profiles at Various Film Cooling Rates

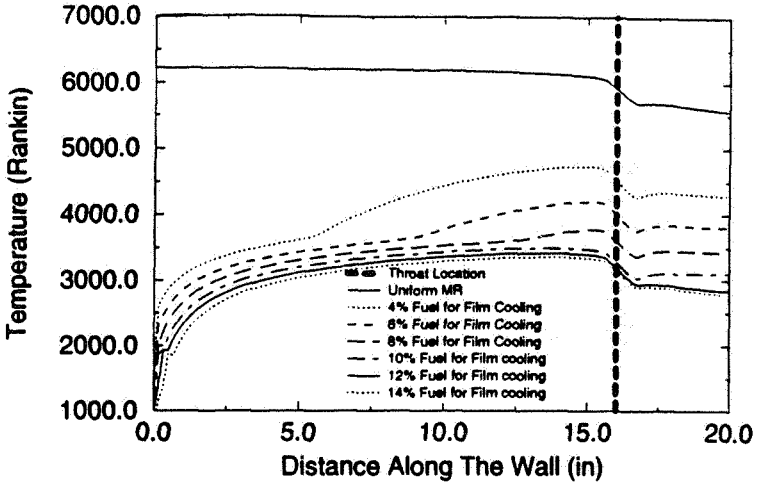

Fig.8: Wall Erosion Rate Profiles at Various Film Cooling Rates

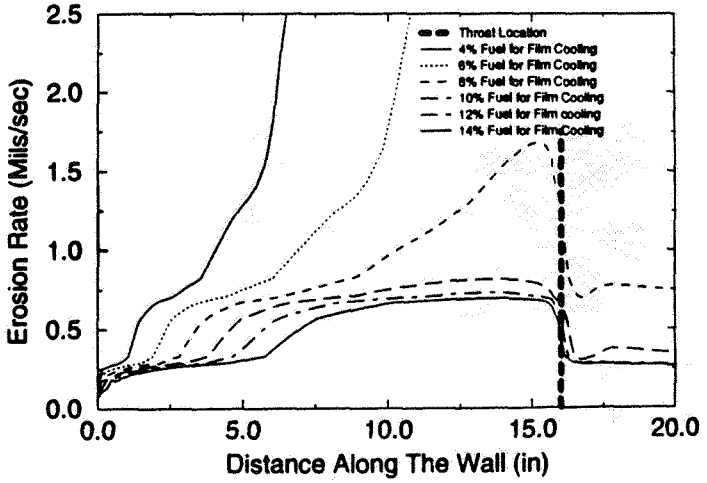

Fig.9: Change in Maximum Wall Temperature Due to Film Cooling Increase

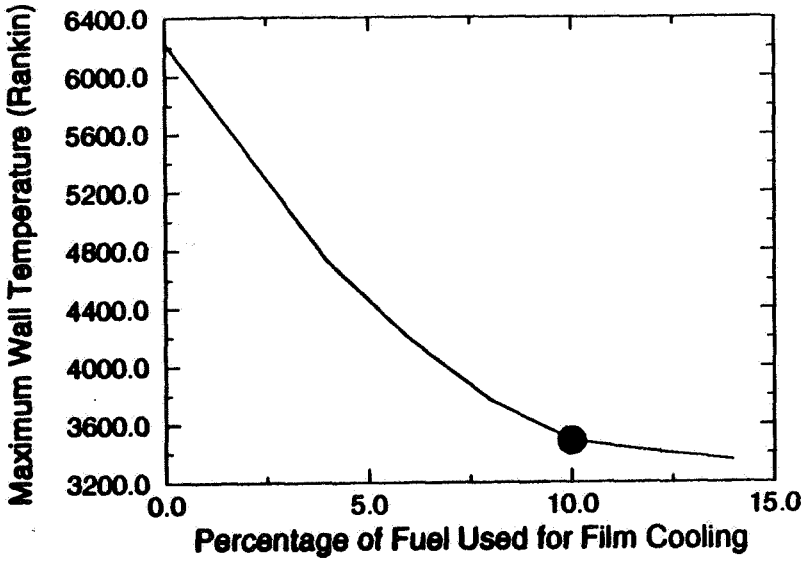

● Projected test point

Fig.10: Change in Maximum Erosion Rate Due to Film Cooling Increase

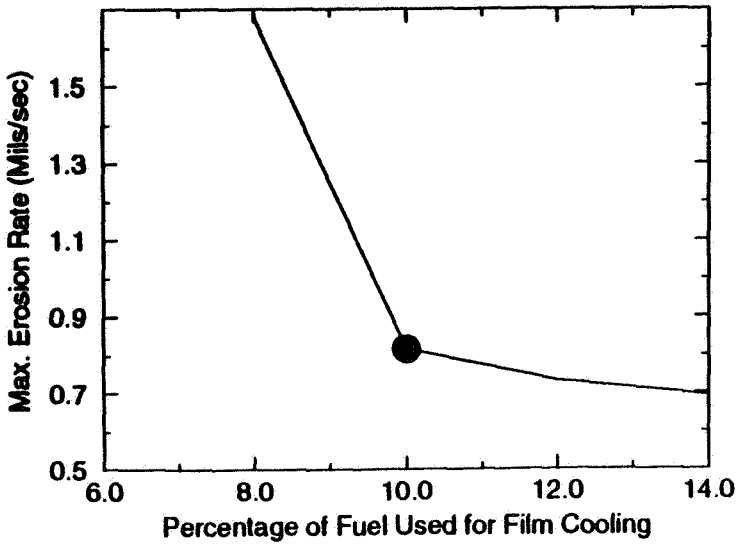

Fig.11: Performance Loss Due to Film Cooling Increase

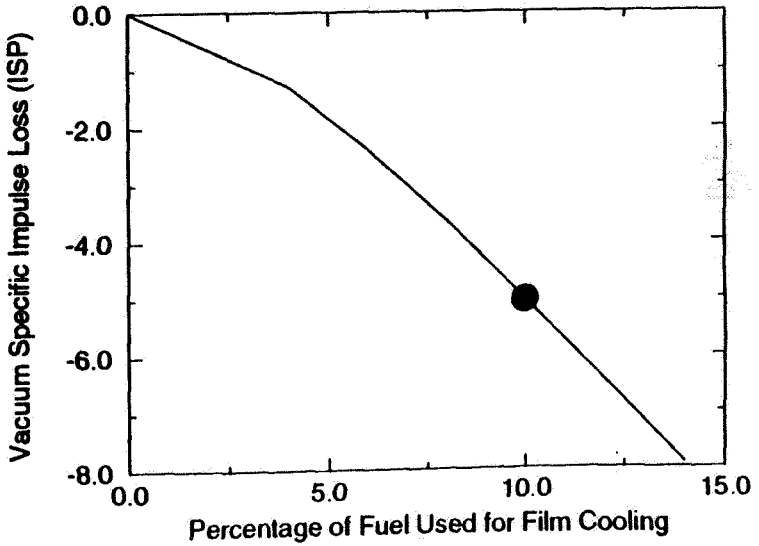

Fig.12: Wall Temperatures for Two Different Chamber Lengths (10% Fuel for Film Cooling)

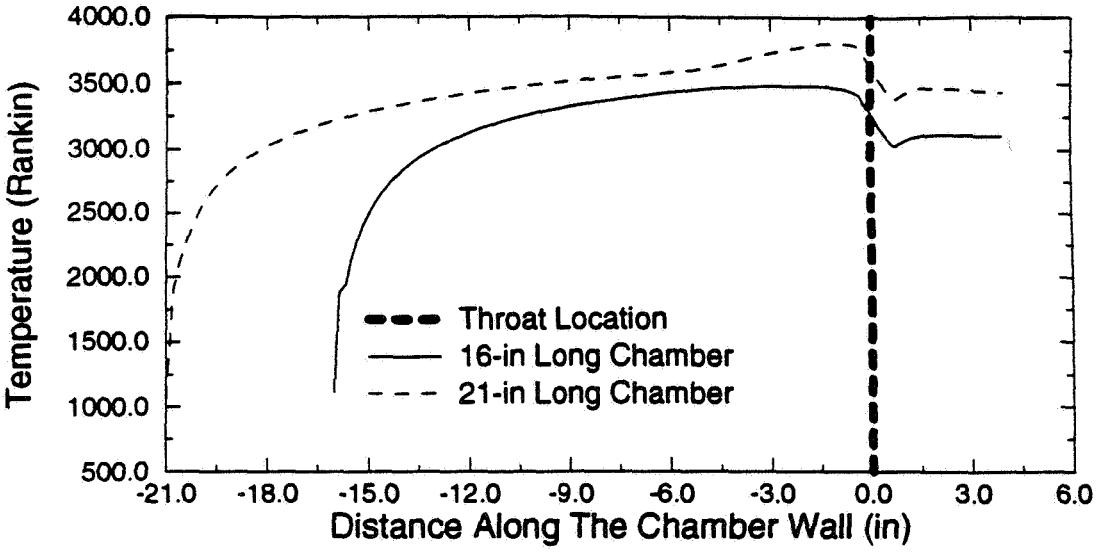

Fig.13: Wall Erosion Rate Profiles for Two Different Chamber Lengths (10% Fuel for Film Cooling)

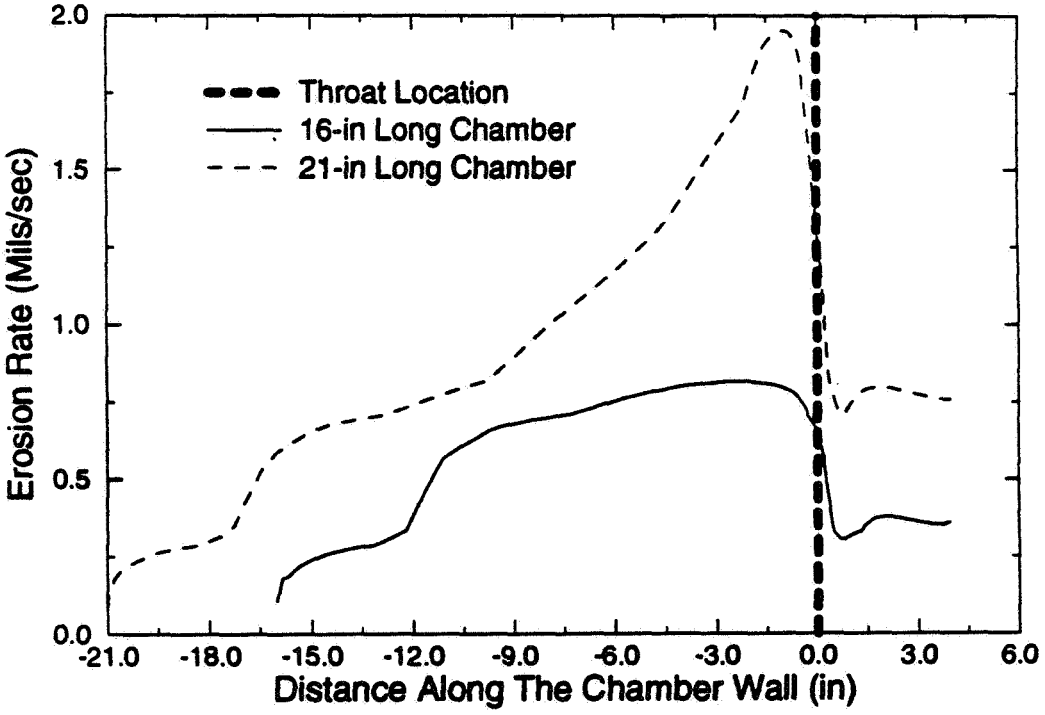

427137
P35 7

N95-70871

AXIAL AND CENTRIFUGAL PUMP MEANLINE PERFORMANCE ANALYSIS

Joseph P. Veres
NASA Lewis Research Center
21000 Brookpark Rd.
Cleveland, Ohio 44135

SUMMARY

A meanline pump flow modeling method has been developed to provide a fast capability for modeling pumps of cryogenic rocket engines. Based on this method, a meanline pump flow code (PUMPA) has been written that can predict the performance of pumps at off-design operating conditions, given the loss of the diffusion system at the design point. The design point rotor efficiency is obtained from empirically derived correlations of loss to rotor specific speed. The rapid input setup and computer run time for the meanline pump flow code makes it an effective analysis and conceptual design tool. The map generation capabilities of the PUMPA code provides the information needed for interfacing with a rocket engine system modeling code.

DISCUSSION

The pump meanline flow modeling code (PUMPA) has been written to provide a rapid evaluation of pump design concepts. Once the design operating performance is established, the code can estimates the off-design performance. The ability to predict pump off-design performance is necessary for evaluating turbopumps for rocket engine systems. During the conceptual design phase of new liquid propellant rocket engine systems, the performance of the turbopumps at off-design operating conditions can influence the design of the pump. The pump code is based on the Euler equation coupled with empirical relations for rotor efficiency. The diffusion system loss at the design point is input and varied at off-design by an empirical relation. The code provides the capability to predict pump performance at all operating conditions encountered during engine throttling. PUMPA provides an estimate of flow incidences, pump stall, losses and cavitation inception at off-design operating conditions. In the design process of pumps, a single operating point for which to optimize the geometry may not be adequate because of often conflicting system requirements. By knowledge of the flow-physics at off-design conditions, the designer can optimize the pump configuration to

provide acceptable pump and system performance during engine throttling. The match between the pump rotor and the diffusion system influences the slope of the pump map and can effect the location of the stall and cavitation inception lines. The flow along a speedline where the static pressure is equal to the vapor pressure determines the cavitation inception point. The suction performance at off-design conditions is based on empirical correlations to the suction performance at design. The pump configuration, flowpath and number of stages that will result in an acceptable system performance can be quickly determined by the use of this meanline flow modeling method.

The meanline pump flow modeling method can be used to model inducers, mixed-flow, and centrifugal pumps. The flow code has multi-stage capability with up to four stages in series. The code has empirically derived rotor loss correlations to specific speed based on tests of several rocket engine turbopump and research rigs. The predicted values of rotor efficiency and slip factor can be modified by correction factors which have a default value of 1.0. The default values of rotor efficiency correction, slip factor correction and diffusion system loss at the design point enable the pump code to estimate the stage performance at the design point, as well as at off-design operating conditions. For a given inlet pressure and temperature, the code can generate a pump map. Fluid options are liquid hydrogen, liquid oxygen, liquid nitrogen JP-4, water, and air. Fluid properties are obtained from GASPLUS (1).

A minimal number of dimensions can adequately describe the rotor and the diffusion system for each stage. Figure 1 shows the locations of some of the key parameters required to specify the dimensions of the rotor and the diffuser. The flowpath radii and the blade angles are input at the leading and trailing edges at both the hub and tip. The diffusion system dimensions are specified in terms of inlet and exit axial widths, radii, volute or diffuser throat area, volute tongue or diffuser leading edge angle and exit flange area. Pump inlet fluid conditions are specified in terms of design rotational speed, fluid flowrate, pressure, temperature and inlet swirl.

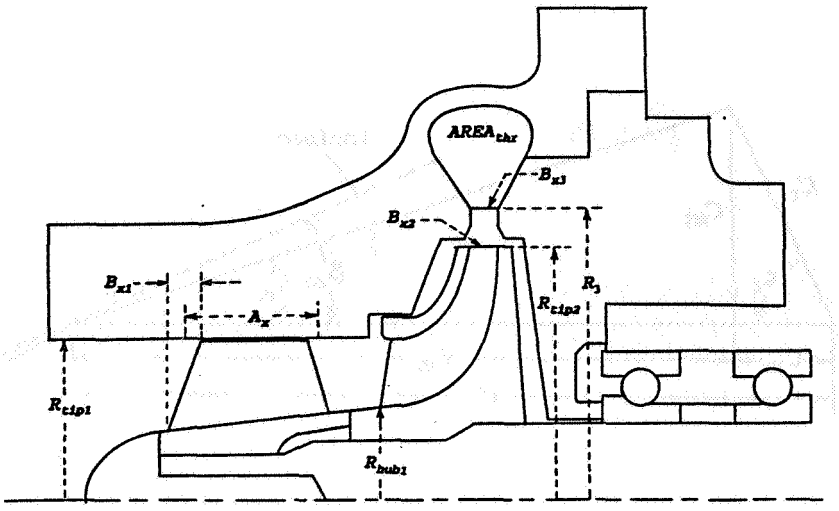

Figure 1. Pump Stage with Axial Inducer and Centrifugal Impeller.

The PUMPA code output consists of flow conditions at the rotor leading and trailing edges, as well as the diffusion system inlet and outlet. The output describes the flow conditions in terms of velocities, flow angles, pressures and temperatures. Velocities and flow angles are calculated in both the relative and the absolute frames of reference. Static and total pressures and temperatures are calculated at the discharge of the rotor and stage. The total head rise, horsepower and efficiency are summarized and plotted (2) for each stage and the overall pump.

Rotor Work

The work performed by the rotor is calculated from the Euler equation and is reflected by the inlet and exit velocity triangles and the rotor efficiency. The flow area at the rotor inlet is calculated from the input flowpath dimensions. The available flow area is compensated for the effects due to metal blockage of the rotor blade and the boundary layer blockage. The blade blockage is included in the inlet velocity triangle calculations. The meridional velocity of the fluid at the rotor leading edge root-mean-square (RMS) diameter is calculated from the mass flow and the available flow area. Figures 2, 3 show the absolute and relative components of velocity at the inlet and exit.

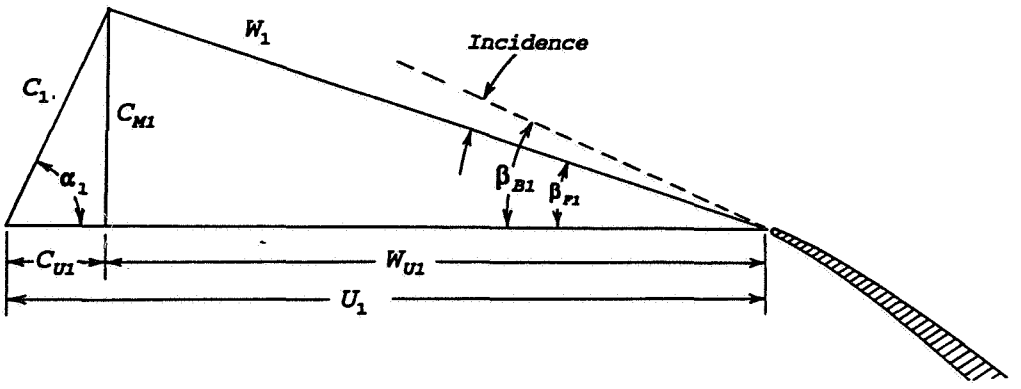

Figure 2. Rotor Inlet Velocity Triangle

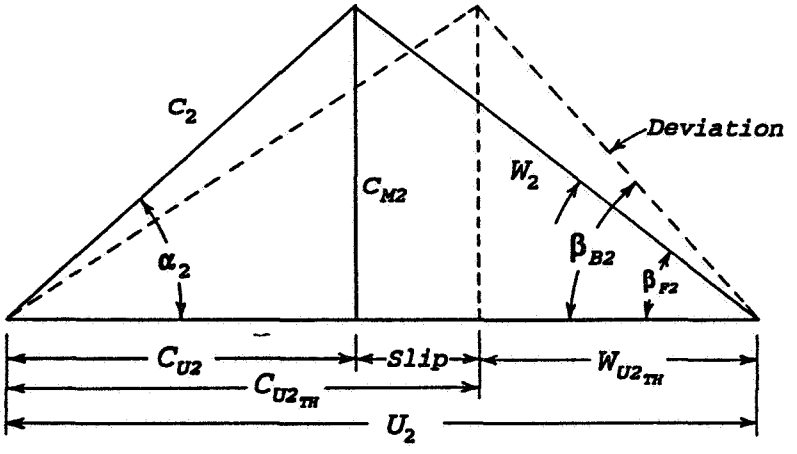

Figure 3. Rotor Exit Velocity Triangle

Rotor Efficiency

The best efficiency point (BEP) rotor efficiency in terms of total-to-total conditions is determined from empirical correlations (3). Figure 4 shows the rotor best efficiency point (BEP) polytropic efficiency database as a function of rotor dimensionless specific speed. The figure shows the relative location and expected efficiency levels for three basic types of pumps: centrifugal, mixed-flow and axial, or inducer.

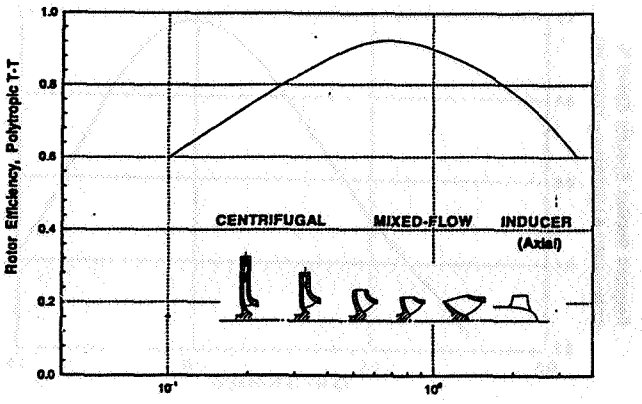

Figure 4. Rotor Efficiency at the BEP vs. Specific Speed

The off-design variation of rotor efficiency has been empirically derived from pump data. A plot showing the efficiency variation is shown in Figure 5.

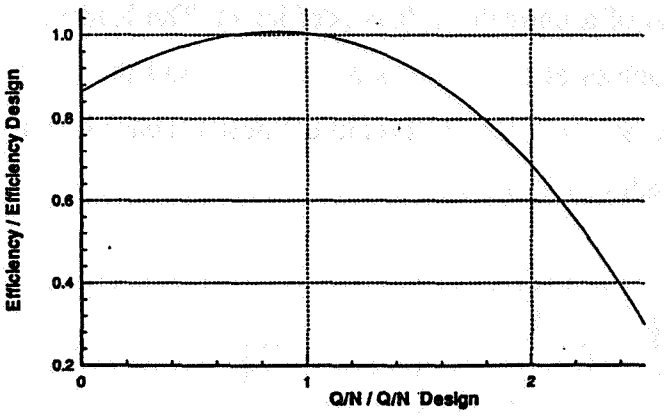

Figure 5. Rotor Efficiency at Off-Design Flow-Speed Parameter (Q/N)

Suction Performance

The net positive suction head of a pump is a function of the inlet total pressure and the vapor pressure of the fluid. Rotor suction performance is estimated by comparing the static pressure at the rotor tip (throat) region to the local vapor pressure. Typically, the highest relative fluid velocity is at the blade tip near the throat region. The high velocity causes a local reduction of static pressure and reaches a value equal to the vapor pressure at the onset of cavitation. The suction performance capability at off-design operating conditions is lower than at the design condition due in part to increased levels of incidence that result in separations and reduced flow area at the rotor leading edge (4). The suction performance at off-design flow conditions is estimated using an empirically derived map in Figure 6.

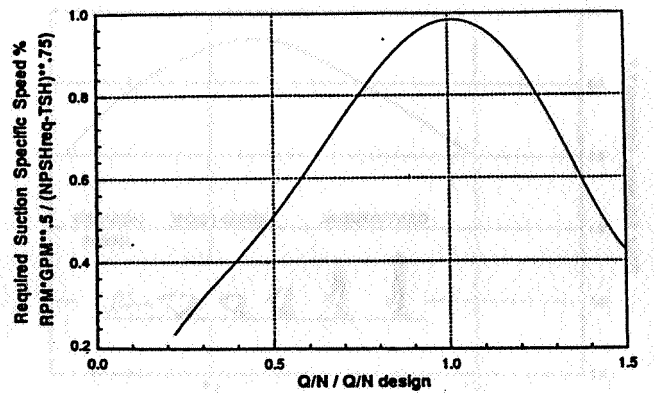

Figure 6. Suction Performance at Off-Design Flow-Speed Parameters (Q/N).

Diffusion System: Static Pressure Recovery; Total Pressure Loss

The design point total pressure loss coefficient of the diffusion system is assumed to be known and is input in terms of a normalized loss coefficient. The loading parameter is defined in terms of the velocities at the vaneless diffuser exit and the velocity at the diffusion system throat. The diffusion system pressure loss at off-design conditions is varied by empirical correlations to loading (Figure 7).

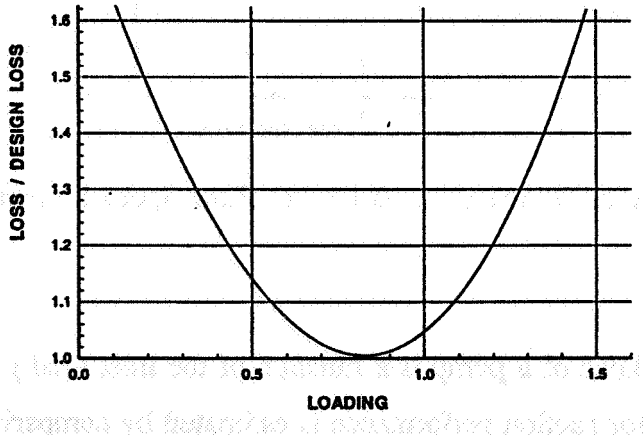

Figure 7. Diffusion System Pressure Loss Coefficient vs. Loading.

SAMPLE PUMP ANALYSIS

The PUMPA flow code can be used as an analysis tool in the conceptual design phase of new pumps since it requires minimal input and has fast setup and computer run times. The performance of candidate pump configurations can be assessed with reasonable accuracy. The code can predict the shape of the pump off-design head-flow characteristic performance map and can provide pump maps for system evaluation of the complete rocket engine. Figure 8a

shows the cross-section of a pump (Ref. 5). A PUMPA flow model of the pump resulted in the performance map shown in Figure 8b. The test data is superimposed for comparison.

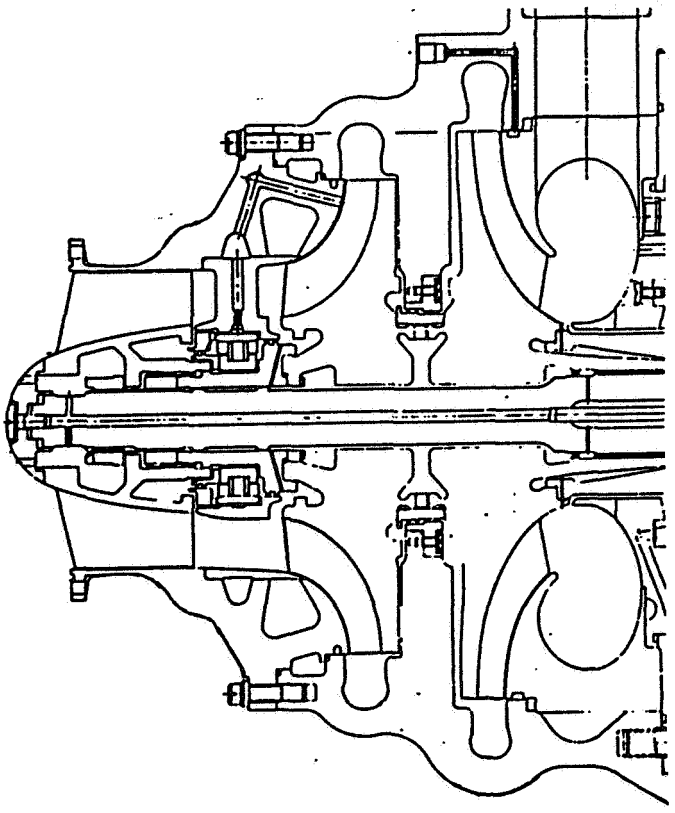

Figure 8a. XLR-129 Liquid Hydrogen Turbopump

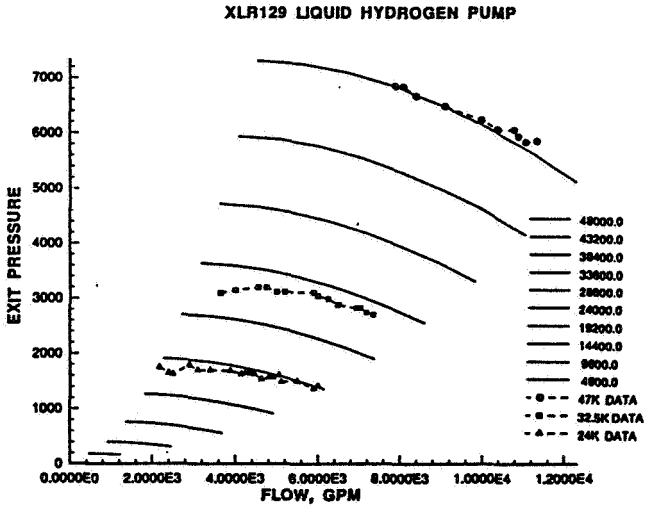

Figure 8b. Pump map with test data

REFERENCES

1. Fowler, J.R., "GASPLUS User's Manual", NASP Contractor Report 1012, Mar., 1988
2. "TECPLOT Version 6.0", Amtec Engineering, Inc., Bellevue, Washington
3. Rodgers, C., "Efficiency of Centrifugal Compressor Impellers", AGARD Conf. Proc. No. 282, Centrifugal Compressors, Flow Phenomena and Performance, Pr. 22, 55th (B) Specialists Meeting of the Propulsion and Energetics Panel of AGARD May 7, 1980.
4. Veres, J.P., "A Survey of Instabilities Within Centrifugal Pumps and Concepts for Improving the Flow Range of Pumps in Rocket Engines", JANNAF 1992, NASA TM-105439
5. Atherton, R.R."Air Force Reusable Rocket Engine Program XLR-129-P-1, Demonstrator Engine Design", Pratt & Whitney, April 1970, AFRPL-TR-70-6, Air Force Rocket Propulsion Laboratory, Air Force Systems Command, Edwards Air Force Base.

427139
Pgs 5

SIMPLEX TURBOPUMP DESIGN

N95-70872

Matt Marsh, Penny Cowan
Propulsion Laboratory
National Aeronautics and Space Administration / MSFC
Marshall Space Flight Center, AL 35812

SUMMARY

Turbomachinery used in liquid rocket engines typically are composed of complex geometries made from high strength-to-weight super alloys and have long design and fabrication cycle times (3 to 5 years). A simple, low-cost turbopump is being designed in-house to demonstrate the ability to reduce the overall cost to $ 500K and compress life cycle time to 18 months. The Simplex turbopump was designed to provide a discharge pressure of 1500 psia of liquid oxygen at 90 lbm/s. The turbine will be powered by gaseous oxygen. This eliminates the need for an inter-propellant seal typically required to separate the fuel-rich turbine gases from the liquid oxygen pump components. Materials used in the turbine flow paths will utilize existing characterized metals at 800° R that are compatible with a warm oxygen environment. This turbopump design would be suitable for integration with a 40 K pound thrust hybrid motor that provides warm oxygen from a tapped-off location to power the turbine. The preliminary and detailed analysis was completed in a year by a multiple discipline, concurrent engineering team. Manpower, schedule, and cost data were tracked during the process for a comparison to the initial goal. The Simplex hardware is in the procurement cycle with the expectation of the first test to occur approximately 1.5 months behind the original schedule goal.

DISCUSSION

I. Technology Advancements

Integrated Engineering Environment

The Simplex turbopump project demonstrated various technology advancements in parallel to the design and analysis cycle. The turbopump design process prototyped an Integrated Engineering Environment. The conceptual layouts, 2-D or 3-D geometry models, manufacturing drawings, and requirements were shared with the multiple-discipline team via an electronic bulletin board. This type of environment shortened the design release cycle from 2 years to 1 year.

Rapid Prototyping

The first parts prototyped used the Stereo-Lithography process which builds parts layer by layer out of a photo-sensitive resin cured by a laser. Design changes were implemented as a result of visually inspecting the 3-D models. The next parts prototyped utilized a Fused Deposition Modeling process which builds parts layer by layer by extruding a thin heated filament of investment casting wax. The Simplex impeller and inducer geometries were used as sample cases to produce prototype castings as a demonstration of the technology maturity level.

Oxidizer Rich Turbine Technology

Limited experience exists in U.S. technology base on the use of an oxygen rich turbine. A small scale turbopump demonstrator was built by Aerojet, Buckman et al [1] to explore oxygen rich turbine technology as well as material selections for oxygen driven turbopumps by Schoenmann [2]. This pump was designed for a Dual Expander cycle.

Extensive use of an oxygen rich turbine drive has been demonstrated in Russian engine designs, such as the RD-170, referenced by Sutton [3]. These turbines use a subsonic blade design which has lower gas velocities than a supersonic design. The Simplex turbine requires a warm, oxygen rich, supersonic impulse blade design and therefore, an oxygen rich, high gas velocity, compatible material. Extensive research of oxygen rich material testing has been conducted at White Sands, by Stoltzfus and Benz [4] and for MSFC by Beveridge [5]. From these databases K-Monel 500 was selected to meet the turbine gas path environment to minimize development cost and maximize gox compatibility.

II. Design Description

The Simplex turbopump functional performance requirements were chosen based on the maximum pressure and flow rates needed to support a 40 K pound thrust hybrid testing with the capability to power the turbine with gasses tapped off from the motor. The schematic of a hybrid tap-off cycle is shown in Figure 1. The pump discharge pressure was chosen to accommodate the system test configuration due to facility piping and the injector. The modest turbine temperature was chosen to accommodate the use of existing well characterized material in an oxygen rich environment. The functional performance requirement for the pump and turbine are shown in Table 1. A cross-section of the Simplex turbopump is shown in Figure 2. A video of the 3-D solid model geometry will be shown to explain the design and assembly of the hardware.

III. Analysis

Analysis of the Simplex design was accomplished by integrating the following disciplines: Computational Fluid Dynamics, Stress, Structural Dynamics, Thermal, Rotordynamic, Axial

Thrust Balance and Secondary Flows, Metallurgy Research, and Lubrication and Surface Physics. Preliminary analysis lead to cost effective design changes and the detailed analysis verified that all the design requirements were met with sufficient margin. A thorough description of the Simplex design analysis was presented by Marsh, Cowan, et al [6] earlier this year.

IV. Project Status

The Simplex Turbopump program includes all aspects of development from conceptual design through final turbopump testing. In the area of program management, the project focused on three specific areas - cost, schedule, and manpower. Each of these categories has been carefully tracked to generate a more current program experience database.

Total program costs include turbopump hardware, assembly / disassembly tooling, instrumentation, propellants, and facility modifications necessary to test the turbopump on MSFC's Test Stand 500. The most recent program cost projection is $ 338 K -- well below the original $ 500 K estimate. Upon program completion, comparisons between estimated and actual program costs can be made.

One of the original goals for the Simplex turbopump program was to design, fabricate, and assemble a turbopump in 18 months. This schedule allowed approximately 9 months for preliminary and detailed design and then 9 months for fabrication and assembly of the hardware. The current program schedule is shown in Figure 3. To date, the Simplex program is approximately 1.5 months behind the original 18 month goal.

The final category monitored was total manpower support. Beginning in May of 1993, the Simplex team was tasked to begin tracking the manpower expended to perform all design, analysis, and program management tasks. Thus far the average monthly labor has been equivalent to 11 full-time personnel.

Upon successful completion of the Simplex turbopump program all cost, schedule, and manpower data will be compiled as part of a growing experience database. This database can then be used to evaluate more accurately proposals for future turbomachinery applications.

V. Future Applications

Once the Simplex turbopump has been tested, future applications could be demonstrated by modifying the hardware. Possible material options are alternate metals or ceramic coatings in the turbine flow path capable of withstanding higher temperatures. An alternate turbine disk could be retrofitted to demonstrate a full ceramic disk with an innovative shaft attachment design. Other modifications could be made to the rotor support system to demonstrate the use of hydrostatic or hydrodynamic bearing technology. Low cost castings technology utilizing rapid prototyped

patterns for investment casting molds could be demonstrated as an alternative fabrication method. The initial cost of tooling for cast parts would be substantially reduced for prototype hardware.

REFERENCES

1. Buckmann, P.S., Shimp, M.R., Viteri, F. and Proctor, M., "Design and Test of an Oxygen Turbopump for a Dual Expander Cycle Rocket Engine," AIAA-89-2305, AIAA / ASME / SAE / ASEE 25th Joint Propulsion Conference, Monterey, CA, July 10-12, 1989.
2. Schoenman, L., "Selection of Burn- Resistant Materials for Oxygen - Driven Turbopumps." Journal of Propulsion and Power, Vol. 3, No. 1, Jan.- Feb. 1987.
3. Sutton, G.P., Rocket Propulsion Elements, An Introduction to the Engineering of Rockets, Sixth Edition, John Wiley & Sons, Inc., 1992, pp 213, 232-235.
4. Stoltzfus, J.M., and Benz, F.J., "Development of Methods and Procedures for Determining the Ignitability of Metals in Oxygen", TR-281-001-int-1, NASA, White Sands Test Facility, Las Cruces, New Mexico, November 1984.
5. Beveridge, J.H., Ducey, F.D., and Evleth, R.V., "Materials Compatibility with Oxidizer-Rich Gasses at Elevated Temperatures and Pressures", Final Report, NASA Contract # NAS8-36713, Acurex Corporation, Cryopro Group, March 1987.
6. Marsh, M., Cowan, P., Van Hooser, K., Forbes, J., "Simplex Turbopump Design", 1994 Conference on Advanced Earth-to-Orbit Propulsion Technology, May 17-19, 1994, MSFC.

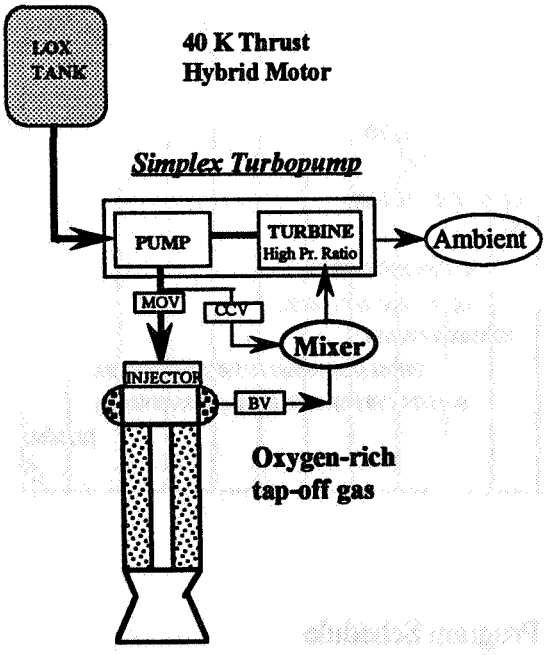

Figure 1. Hybrid Tap-off Cycle

Table 1. Turbopump Requirements

PUMP		
Pump inlet pressure	45	psia
Pump discharge pressure	1545	psia
Mass Flow rate	90	lbm/s
Rotational speed	25,000	rpm
Pump Efficiency	71.5	%
Shaft Horsepower	700	hp
TURBINE		
Turbine inlet Temperature	800	° R
Pressure Ratio	15	-
Velocity ratio	0.38	-
Nozzle Arc of Admission	45	%
Turbine inlet Pressure	800	psia
Mass flow rate	9.24	lbm/s
Efficiency	55	%

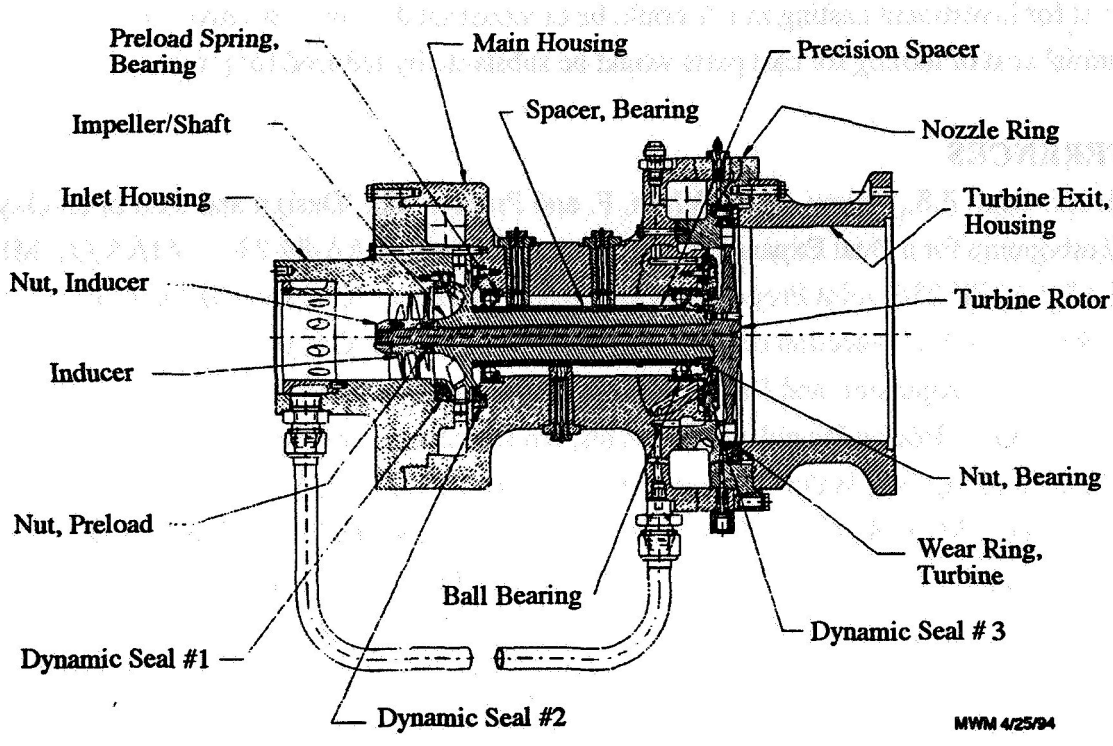

Figure 2. Drawing of Simplex Turbopump Cross Section

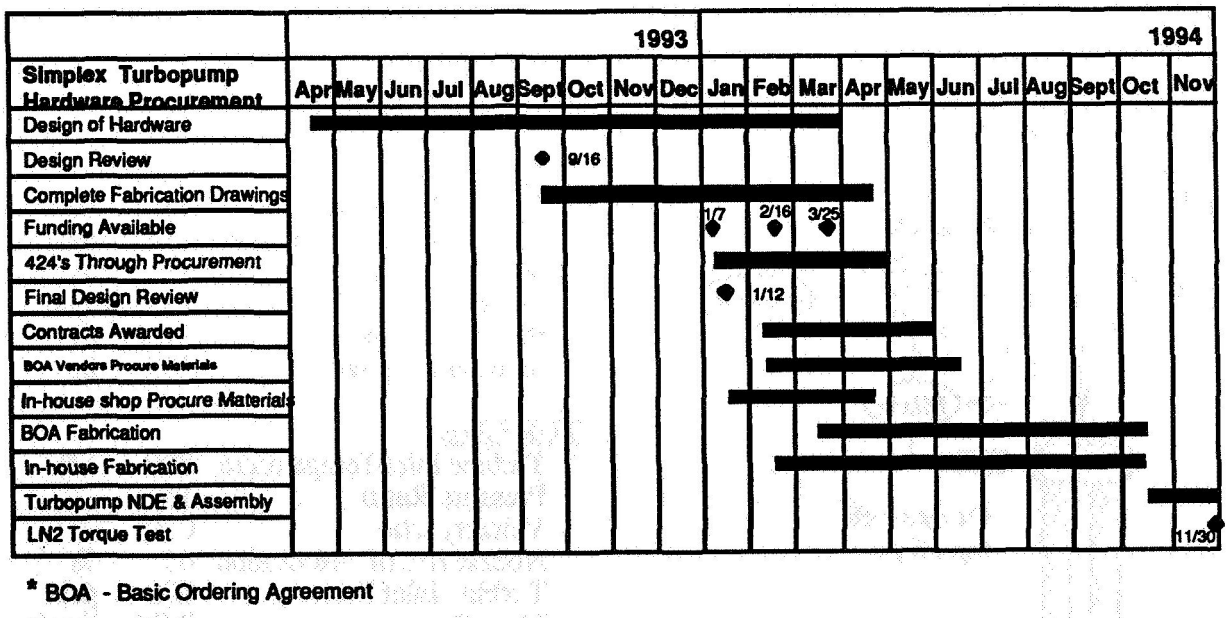

Figure 3. Simplex Turbopump Program Schedule

BS S 427143

COMPUTATIONAL FLUID DYNAMICS ANALYSIS IN SUPPORT OF THE SIMPLEX TURBOPUMP DESIGN

N95-70873

Roberto Garcia, Lisa W. Griffin, Theodore G. Benjamin
Joni W. Cornelison, Joseph H. Ruf, and Robert W. Williams
Computational Fluid Dynamics Branch
NASA/Marshall Space Flight Center
Marshall Space Flight Center, AL 35812

OVERVIEW:

Simplex is a turbopump that is being developed at NASA/Marshall Space Flight Center (MSFC) by an in-house team. The turbopump consists of a single-stage centrifugal impeller, vaned-diffuser pump powered by a single-stage, axial, supersonic, partial admission turbine. The turbine is driven by warm gaseous oxygen tapped off of the hybrid motor to which it will be coupled. Rolling element bearings are cooled by the pumping fluid. Details of the configuration and operating conditions are given by Marsh [1]. CFD has been used extensively to verify one-dimensional (1D) predictions, assess aerodynamic and hydrodynamic designs, and to provide flow environments. The complete primary flow path of the pump-end and the hot gas path of the turbine, excluding the inlet torus, have been analyzed. All CFD analyses conducted for the Simplex turbopump employed the pressure based Finite Difference Navier-Stokes (FDNS) code using a standard k-ε turbulence model with wall functions. More detailed results are presented by Garcia et. al. [2]. To support the team, loading and temperature results for the turbine rotor were provided as inputs to structural and thermal analyses, and blade loadings from the inducer were provided for structural analyses.

DISCUSSION:

The hot gas path of the Simplex turbine consists of an inlet torus, a ring of twelve converging-diverging nozzles, a wheel of 95 impulse rotors, and a 7.6 inch diameter exhaust pipe. Six of the nozzles are blocked in a pattern of one active arc of admission and one inactive arc so it operates at 45% admission. The total pressure at the inlet of the nozzle is 800 psi, and the total-to-static pressure ratio is 15. The impulse turbine pressure drop is taken across the nozzle. The inlet total temperature is 800° R. The total mass flow rate is 1.54 lbm/sec per nozzle. The wheel speed is 25,000 rpm, and the turbine is to supply 700 hp. The velocity ratio of the rotor is 0.355.

The nozzle analysis is fully three-dimensional (3D). The inlet to throat area ratio is 2.42, and the exit to throat area ratio is 2.78. A total pressure of 800 psi was held constant at the inlet and a static pressure of 53.3 psi was held constant at the exit. The walls of the nozzle were assumed to be "no-slip" and adiabatic and to have a zero normal pressure gradient. The results show the nozzle is overexpanded The pressure at the exit of the diverging section is approximately

40 psi and then increases to the back pressure across an oblique shock. Some attempts were made to resize the nozzle to ensure isentropic flow, but size constraints limited modifying the nozzle design. Pressure at the exit of the nozzle varies from 35 psi to 75 psi. The mach number reaches 3.5 at the exit of the divergent section and shocks down to 2.5 at the exit to the nozzle ring. The variation in the velocity at the exit is acceptable.

The rotor analysis included design parametrics. The Simplex rotor blades are straight in the radial direction, so even though tip leakage would produce some 3D effects, calculations could be performed two dimensionally (2D) at the midspan. The inlet boundary was at the nozzle exit. Flow conditions obtained from the 1D nozzle flow analysis were imposed. A static pressure of 53.3 psi was imposed at the exit. Results are shown in figure 1. There is a separation on the suction surface of the blade. The calculated power output per full flowing rotor is 31.7 hp. Six

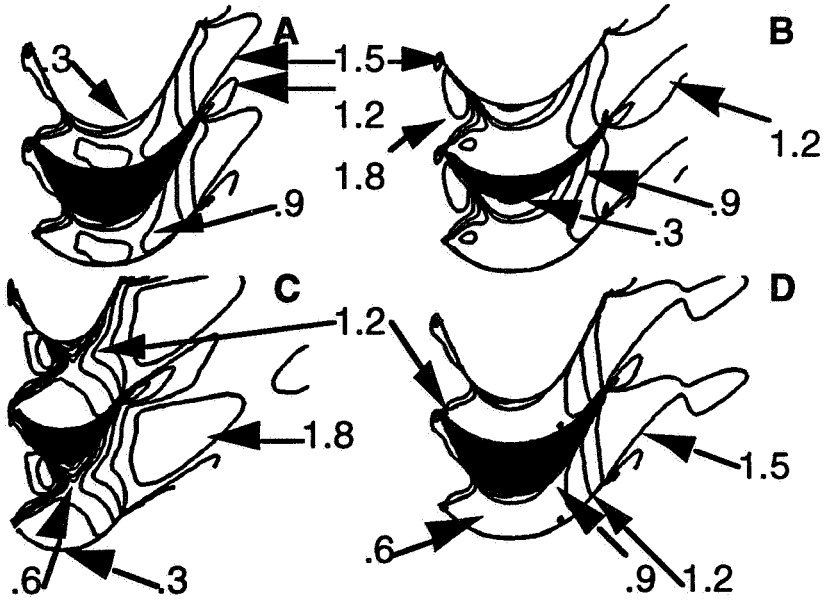

Figure 1. Two-dimensional rotor parametrics, showing mach number contours

alternate blade designs did not improve the flow field. After this, a 3D shrouded rotor was analyzed. Losses of 12% for partial admission and 5% for tip leakage were assumed based on the literature. The flow field improved relative to the 2D rotor by producing a smaller separated region and a slight increase to 950 hp, which is sufficient.

The objectives of the disk cavity analysis were to determine the effect of the bearing coolant leakage on axial thrust and on turbine performance. The initial bearing coolant circuit consisted of 4.5 lbm/sec of liquid oxygen (LOX) being diverted from the impeller discharge to cool the bearings. Of this coolant flow, 2.7 lbm/sec was returned to the impeller inlet and 1.8 lbm/sec leaked into the turbine disk cavity. The maximum transient load to which the bearings can

respond is 4,400 lbf. It was assumed that for a worst case the fluid would remain a liquid throughout the entire cavity. The cavity was modeled from the seal exit to the hot gas path. The flow field was assumed to be axisymmetric. The change in pressure from seal exit to hot gas path was calculated to be 1,100 psi, and the increase was basically linear with radius. The resultant axial force on the disk was 15,000 lbf. The performance loss due to coolant leakage into the hot gas path was estimated to be 15 points in turbine efficiency. Clearly, the axial load and performance detriment with the initial coolant circuit were unacceptable. The bearing coolant circuit was redesigned with 3.5 lbm/sec returning externally to the inducer inlet and 1.5 lbm/sec vented overboard. A small amount of gas from the turbine primary flow path is drawn into the cavity, across the straight seal, and out the overboard drain. For this case, the fluid in the cavity was assumed to be entirely a gas. Because this assumption necessitated imposing pressures at inlet and exit boundaries where pressures were known, the modeled domain included the disk cavity, rotor, and exhaust pipe. It was modeled as a 3D, periodic wedge that included one rotor passage. A pressure of 40 psi was assumed at the cavity/seal interface based on estimates from a forced vortex calculation. The rotor flow field is similar to that of the stand alone model. The pressure rise from seal to platform is approximately 30 psi. The pressure rise on the back side of the disk from centerline to platform is approximately 20 psi. The resultant force on the disk of 300 lbf is manageable. Flow of approximately 0.001 lbm/sec was calculated to be pulled from the hot gas path and into the cavity.

The pump flow path of the Simplex turbopump consists of an axial inlet, a three-bladed inducer, a six-bladed impeller, an eight-vaned diffuser, and a single-discharge volute. The minimum inlet LOX pressure is 45 psi at 164°R flowing at 89.8 lbm/sec, yielding a required suction specific speed (Nss) of approximately 25,000 at the design point speed. The discharge pressure required is 1,500 psi, 85% of which is generated by the radial impeller. Steady-state analyses were performed on each of the subcomponents that comprise the pump main flow path.

As a result of axisymmetric analyses of the pump inlet the inducer retaining nut was simplified from a parabolic curve shape to a shape made up of three flat surfaces. The inducer inlet relative flow angle is very similar for both geometries. Subsequent analyses were performed to arrive at an acceptable bearing coolant reentry scheme. The aforementioned bearing cooling circuit redesign necessitated routing the bearing coolant discharge back to the pump inlet outer diameter. Design iterations resulted in a design incorporating 10 reentry holes two inches upstream of the inducer. This configuration produced very little disturbance to the incoming flow.

The inducer analyses used the hub-to-shroud velocity distributions obtained from the inlet analysis. All cases assumed non-cavitated conditions. Grid sensitivity studies showed that while details of the flow field were affected by grid density, the overall performance and flow features were captured by coarse grids. The original inducer had a tip solidity of 2.68, but generated very

little head over the last third of the blade chord due to the small amount of diffusion through the inducer, producing losses nearly as large as the work input in the latter portion of the blade. The chord was reduced by one-third to improve the efficiency of the inducer, which coincided with rotordynamic needs to reduce the rotating mass outboard of the pump-end bearing. The resulting design produces a non-cavitated total pressure rise of 197 psi with a net hydraulic efficiency of 73%. The inducer flow field exhibited the typical secondary flow patterns present in these high-solidity rotating channels. Figure 2 shows an x-r projection of the flow through the inducer. The typical region of backflow is present at the inducer inlet near the blade tip. The inlet region of recirculation extends completely across the channel. Radially inward flow near the pressure surface tip was caused by the low momentum fluid (in the absolute reference frame) near the stationary shroud. This phenomenon was magnified by the model's zero tip clearance. The circumferentially averaged hub-to-shroud velocity profile was also obtained from these results.

The Simplex impeller incorporates six full-length blades with no partial blades and generates a total pressure rise of 1,300 psi. All but one of the cases were performed used the circumferentially averaged hub-to-shroud inducer-exit velocity profile as the inlet velocity condition. One case was run that included the actual inducer-exit velocity field (no averaging) and two impeller channels. The blade loading on adjacent blades was nearly identical, indicating that the clocking was acceptable. The baseline impeller design was determined to be acceptable. Typical of a centrifugal impeller, the hydraulic efficiency for the Simplex impeller was predicted to be high (95.6%). Analyses performed at off-design conditions showed that the impeller is insensitive to small variations in the incoming flow angle. The inlet relative flow angle was varied from 13° to 23° (18° being the design point average angle) and the head coefficient varied from +10% to -7.5%, respectively, about the design point. The discharge absolute flow angle was nearly invariant over this range of inlet angle, which simplifies the design and analysis of the diffuser. Figure 3 shows the circumferentially averaged impeller exit hub-to-shroud flow distribution.

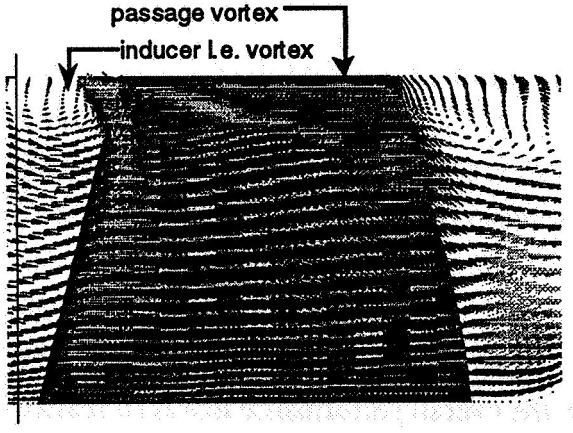

Figure 2. Inducer velocity vectors near the pressure surface, axial-radial projection

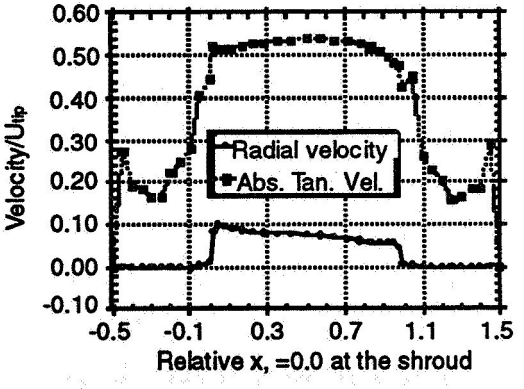

Figure 3. Impeller exit hub-to-shroud circumferentially averaged velocity profile

The initial CFD evaluation of the diffuser was performed on a 2D plane modeling a single diffuser channel. Results showed that at the impeller discharge flow angle of approximately 10°, some separation on the pressure surface of the vane would reduce performance. Since the impeller discharge angle was 11.8°, the diffuser performance was not acceptable. This necessitated a 3D model of the eight diffuser channels and volute, which allowed the inclusion of the hub-to-shroud velocity profile obtained from the impeller. The separation seen at the higher inlet flow angles cases studied in the 2D model worsened in the 3D results. The separation did not encompass the entire span of the vane but is limited to the span locations where the inlet flow angle was largest. The static pressure increase (ΔP) from the impeller exit to the diffuser exit was 118 psi. Therefore, parametrics were performed on a 3D 45° single-passage segment of the diffuser beginning at the impeller exit and proceeding through the diffuser exit. An exit region of constant circumferential cross-sectional area was appended downstream of the diffuser. A comparison between the full-geometry baseline design and the single-passage baseline validated this approach. Several design changes compatible with schedule and fabrication requirements were evaluated. The solution entailed a cutback on the leading edge of the vanes, which increased the flow angles at the entrance to the vanes and eliminated the blockage of flow by adjacent blades, yielding a ΔP of 288 psi.

REFERENCES:

1. Marsh, M., "Simplex Turbopump Design," to be printed in the Proceedings of the 1994 Conference on Advanced Earth-to-Orbit Propulsion Technology, (R. J. Richmond and S. T. Wu eds) May 17-19, 1994 Marshall Space Flight Center, AL.

2. Garcia, R., Griffin, L. W., Benjamin, T. G., Cornelison, J. W., Ruf, J. H., Williams, R. W., "Computational Fluid Dynamics Analysis in Support of the Simplex Turbopump Design," to be printed in the Proceedings of the 1994 Conference on Advanced Earth-to-Orbit Propulsion Technology, (R. J. Richmond and S. T. Wu eds) May 17-19, 1994 Marshall Space Flight Center, AL.

427145 | N95-70874

COMPUTATION AND MODELING OF AERO-THERMAL FIELDS IN TURBINE CASCADES AND STRONGLY CURVED DUCTS

J. Luo and B. Lakshminarayana
Dept. of Aerospace Engineering
The Pennsylvania State University

SUMMARY

Advanced turbulence models are crucial for accurate prediction of rocket engine flows, due to existance of very large extra strain rates, such as strong streamline curvature. Numerical simulation of the turbulent flow in a strongly curved turn-around duct (TAD) has been carried out with a Reynolds stress model (RSM), an algebraic Reynolds stress model (ARSM) and a k-ε model. The RSM model and the ARSM model are found to capture the turbulence damping due to the convex curvature, but underpredict the turbulence enhancement caused by the concave curvature. To capture the concave curvature effects, it is necessary to modify the ε-equation. The modification of ε equation suggested by Launder et al. provides the correct trend, but over-corrects the curvature effects.

A comparative study of two modes of transition in gas turbine, the by-pass transition and the separation-induced transition, has been carried out with several low-Reynolds-number (LRN) k-ε models. Effects of blade surface pressure gradient, freestream turbulence and Reynolds number on the blade boundary layer development, and particularly the inception of transition are examined in detail. The present study indicates that the turbine blade transition, in the presence of high freestream turbulence, is predicted well with LRN k-ε models employed.

DISCUSSION

Although considerable research has been carried out to model curved turbulent shear flows, most of them deal with mildly curved flows. Previous computation of strongly curved flows, e.g., the turn-around-duct (TAD) flow of Monson et al. (1990), indicated the need for improved turbulence models. Since most turbulence models have been developed using the data for simple shear layers in local equilibrium, they are not accurate for non-equilibrium flows, such as strongly curved flows. The objective of the present work is to develop turbulence models for flows with strong streamline curvature. A secondary objective is to study the effect of transition on turbine flowfield and heat transfer.

Various eddy-viscosity models have been used in previous computations of the TAD flow. In the present investigation, a low-Reynolds-number Reynolds stress model (RSM), developed by Shima (1988) on the basis of the RSM model due to Launder et al. (1975), is employed. The transport equation for Reynolds stress components is given by,

$$\frac{D\overline{u_i u_j}}{Dt} = -\overline{u_i u_k}U_{j,k} - \overline{u_j u_k}U_{i,k} + \overline{\frac{p}{\rho}\left(\frac{\partial u_i}{\partial x_j} + \frac{\partial u_j}{\partial x_i}\right)}$$

Convection Production Pressure-strain

$$-\frac{\partial}{\partial x_k}\left[\overline{u_i u_j u_k} + \frac{\overline{pu_j}}{\rho}\delta_{ik} + \frac{\overline{pu_i}}{\rho}\delta_{jk} - \nu\frac{\partial \overline{u_i u_j}}{\partial x_k}\right] - 2\nu\overline{\frac{\partial u_i}{\partial x_k}\frac{\partial u_j}{\partial x_k}}$$

Diffusion Dissipation

where $\overline{u_i u_j}$ is Reynolds stress tensor, and U_i is mean velocity component. The RSM model has one obvious advantage over the eddy-viscosity model since the production term is exact. The modeling of the pressure-strain correlation enables the RSM model to capture the anisotropy of turbulence. The formulations for the above terms are given by Launder et al. (1975) and Shima (1988) and have been incorporated into the Navier-Stokes code.

The details of the present 2-D Navier-Stokes procedure can be found in Luo & Lakshminarayana (1993).The transport equations for individual Reynolds stresses $-\overline{uu}$, $-\overline{vv}$, $-\overline{ww}$ and $-\overline{uv}$ are solved. These equations are discretized in the same way as the k and ε equations and are also integrated by the 4-stage Runge-Kutta method. The RSM equations are numerically much stiffer than the eddy-viscosity models. It is necessary to adopt stability enhancing measures, e.g., the normal components of the Reynolds stress tensor are required to be positive during iteration and the Schwarz inequality (i.e., $\overline{u_i u_j}^2 \Big/ \overline{u_i^2 u_j^2} \le 1.0$) has to be satisfied. A second-order artificial dissipation term is added to the RSM equations to prevent odd-even decoupling, since the convective fluxes are discretized with central differences.

Computation of Turn-Around Duct Flow with Reynolds Stress Model

The prediction for the TAD flow using the RSM model is compared with the data due to Monson et al. (1990). The results obtained by the ARSM and k-ε models are also included for comparison. The RSM model successfully captures the turbulence damping effects of convex curvature (inner wall of the duct), but underpredicts the turbulence enhancement caused by strong concave curvature (outer wall), as can be seen from Fig. 1b, 1c, where U_m is the bulk velocity. It has been suggested (e.g, Monson et al.) that the Taylor-Gortler vortices also contribute to the turbulence enhancement in the concave region. However, Barlow & Johnston (1988) found that the turbulence enhancement was due almost entirely to increased energy in large-scale vortices (radial inflows and outflows). They did not observe the Taylor-Gortler vortices. The under-prediction of the turbulence enhancement by all the models (see Fig. 1b & 1c) can be attributed to poor modeling of the source term in the ε-equation. Indeed, there is really no reason -- other than convenience and simplicity -- to assume that the influence of mean strain on the spectral transfer of energy from large to small scales is represented by exactly the same interactions between the Reynolds stress and mean velocity gradients as those that generate turbulent kinetic energy (i.e., P_k). The present formulation of the ε-equation may work well for cases in local equilibrium ($P_k \approx \varepsilon$). For non-equilibrium

flows, such as those in the concave region, the source term in the ε-equation should not be so rigidly linked to that of the k-equation. It is known that the viscous dissipation is dominated by small scales, on which the curvature effects are small, while the turbulence energy is generated at large scales, which are greatly influenced by streamline curvature.

Launder et al (1977) modified the destruction term in the ε equation to be $-C_{\varepsilon 2}(1- C_c Ri_t)(\varepsilon^2/k)$. The Richardson number Ri_t is defined as: $Ri_t = (k^2/\varepsilon^2)(U/r^2)(\partial(Ur)/\partial n)$, where r is the curvature radius of streamline, U is the streamwise component of mean velocity, and n is the normal direction. The proposed additional term acts to destroy large eddies (reduce the length scale) in stabilizing curvatures and augment the length scale in destabilizing curvatures. By introducing this curvature modification into the ε-equation, all the models captured strong turbulence amplification in the concave region (Figs. 2b & 2c), confirming the above analysis in retrospect. However, this modification is not tensorially invariant, and the curvature effects have been over-corrected. Efforts are underway to improve the modeling of this source term. Specifically, the time scale controlling the spectral energy transfer rate is being modified to capture the differing flow structures in concave and convex curved regions.

Prediction of Turbine Blade Transition and Heat Transfer

An improved understanding and predictive capability of turbine viscous flowfield and heat transfer is crucial in achieving higher turbine performance and efficiency. The mode of transition in gas turbine is by-pass transition (in which the 2-D Tollmien-Schlichting instability wave is by-passed) or separated-flow transition. A comparative study of these two modes of transition, on the C3X and Mark II turbine blades (Hylton et al. 1983), has been carried out with three LRN k-ε models due to Chien (1982, denoted as CH), Lam-Bremhorst (1981, denoted as LB) and Fan, et al. (1993, denoted as FL), respectively. For both cascades, the downstream Reynolds no. (Re) varied from $1.5x10^6$ to $2.5x10^6$, the total temperature (T_0) at the inlet was 700-800 (^{0}k), and the freestream turbulence intensity (Tu_∞) was 6.5% to 8.3%. All parameters are significantly higher than those of the VKI cascade computed by Luo & Lakshminarayana (1993).

The surface pressure (P) distribution and the acceleration factor ($K=(\nu/U_e^2)dU_e/dS$, U_e is mainstream velocity and S is streamwise distance) distribution are shown in Fig. 3a & 3b, where ARC is total surface distance. For values of K larger than $3.0x10^{-6}$ (re-laminarization criterion), transition is suppressed for low freestream turbulence, and the turbulent boundary layer begins to re-laminarize. A knowledge of K is thus very useful in understanding turbine boundary layer transition. The prediction of heat transfer, using a 151x99 H-grid, for the Mark II airfoil is presented in Fig. 4a. On the pressure side, all the calculations are in good agreement with the data. On the suction side, the boundary layer (TEXSTAN) calculation is terminated around S/ARC=0.26 due to separation, while all the N-S calculations have captured the transition due to separated flow. The transition location as indicated by both the skin friction coefficient (Fig. 4b) and the shape factor (Fig. 4c) is in agreement with the heat transfer distribution. In Fig. 4d, the calculated momentum thickness Reynolds number Re_θ on the pressure surface near the trailing edge

reaches only around 500, far below a value of 2000 usually considered as the lower limit for fully turbulent boundary layers, thus suggesting the boundary layer remains transitional along the entire surface.

The calculated heat transfer for the C3X is plotted in Fig. 5a, the performance of various models is similar to that shown in Fig. 4a. As shown in Fig. 5b, the LB model provides an accurate simulation of the transition process in which the velocity profile (u^+~y^+) in the outer layer evolves from a laminar boundary layer (linear-law) to that of a fully turbulent boundary layer (log-law). The pressure-gradient effect is examined in Fig. 6. On the suction surface, the increase in local heat transfer rate caused by the separation-induced transition (on Mark II) is much sharper than that caused by nominal by-pass transition (on C3X). For the C3X airfoil, the Reynolds number effect on the heat transfer is reflected in both the transition onset location and general level of heat transfer (see Fig. 7). The higher the Reynolds number, the earlier is the transition, and the higher is the heat transfer rate. The turbulence length scale has significant effect on the predicted suction surface heat transfer near the stagnation point as well as the transition location, as shown in Fig. 8.

It is concluded that the transition on turbine blades with high freestream turbulence can be predicted well with LRN k-ε models, provided that the artificial dissipation is kept minimum. In both measurement and computation, the separation-induced transition leads to much sharper increase of local heat transfer than the nominal by-pass transition. The Lam-Bremhorst's k-ε model provides the best prediction of transition.

ACKNOWLEDGEMENTS

This work was supported by the U.S. National Aeronautics and Space Administration through contract NAS 8-38867 monitored by Lisa Griffin of Marshall Space Flight Center (MSFC). The authors wish to acknowledge NASA for providing the supercomputing resoures at NASA MSFC.

REFERENCES

Barlow, R. S. & Johnston, J. P., 1988, "Structure of a Turbulent Boundary Layer on a Concave Surface," *J. Fluid Mech.*, Vol. 191, p. 137.

Chien, K. Y., 1982, "Prediction of Channel and Boundary-Layer Flows with a Low-Reynolds Number Turbulence Model," *AIAA Journal*, Vol. 20, No. 1.

Fan, S., Lakshminarayana, B. and Barnett, M., 1993, "Low-Reynolds-Number k-ε Model for Unsteady Turbulent Boundary-Layer Flows," *AIAA Journal*, Vol. 32, No. 10, pp. 1777-1784.

Hylton, L. D., Mihelc, M. S., Turner, E. R., Nealy, D. A., and York, R. E., 1983, "Analytical and Experimental Evaluation of the Heat Transfer Distribution Over the Surface of Turbine Vanes," NASA CR-168015, May.

Lam, C. & Bremhorst, K., 1981,"Modified form of the k-ε Model for Predicting Wall Turbulence," *J. Fluid Engr.*, Vol. 103, P.456.

Launder, B.E., Reece, G.J. and Rodi, W., 1975,"Progress in the Development of a Reynolds-Stress Turbulence Closure," *J. Fluid Mech.*,Vol. 68, p.537.

Launder, B., Priddin, C.H. and Sharma, B., 1977, "The Calculation of Turbulent Boundary Layers on Curved and Spinning Surfaces," *ASME J. of Fluids Engr.*, Vol. 98, p.753.

Luo, J. & Lakshminarayana, B., 1993, "Navier-Stokes Analysis of Turbine Flowfield and Heat Transfer," AIAA 93-7075, ISABE, Tokyo, Japan, to appear on *J. of Propulsion and Power*.

Monson D. J., Seegmiller, H. L., McConnaughey, P. K. & Chen, Y. S., 1990, "Comparison of Experiment with Calculations Using Curvature-Corrected Zero & Two Equation Turbulence Models for a Two-Dimensional U-Duct," AIAA Paper 90-1484, June.

Shima, N., 1988, "A Reynolds Stress Model for Near-wall and Low-Reynolds-Number Regions," *J. of Fluids Engr.*, Vol. 110, pp.38-44.

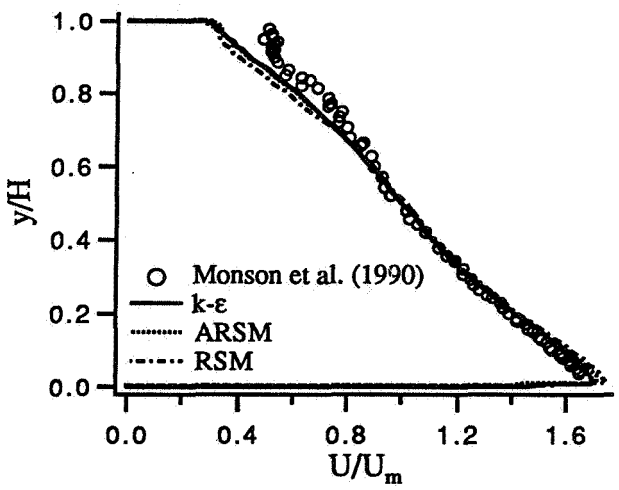

Fig. 1a Longitudinal velocity profile, θ=60 deg. (y=normal distance from inner wall, H=duct height).

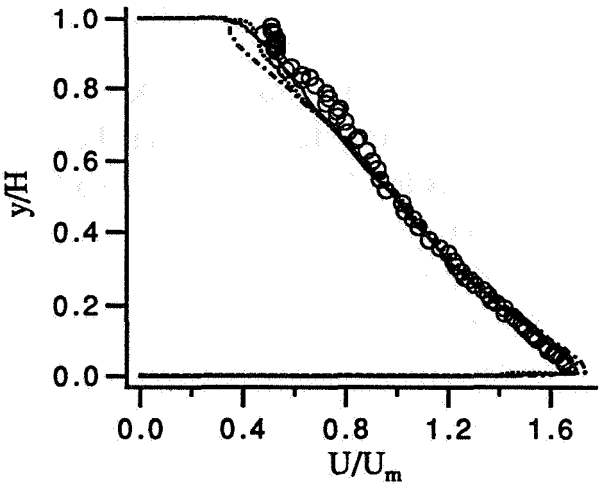

Fig. 2a Longitudinal velocity profile, θ=60 deg. (Legend as in Fig. 2b)

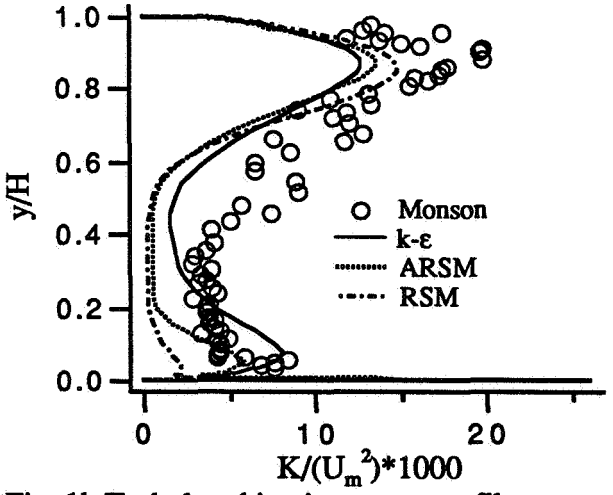

Fig. 1b Turbulent kinetic energy profile.

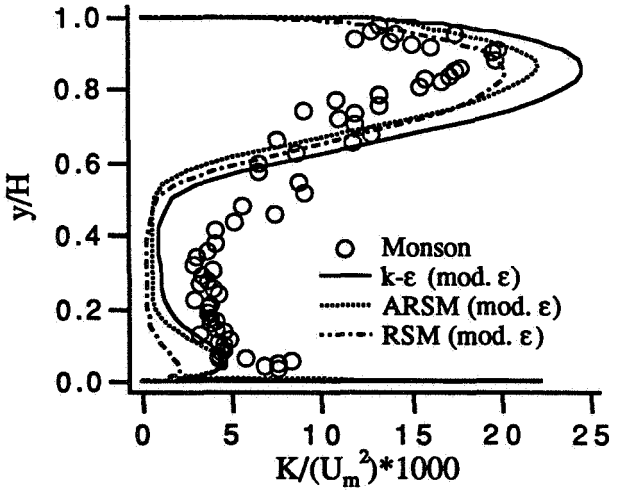

Fig. 2b Turbulent kinetic energy profile.

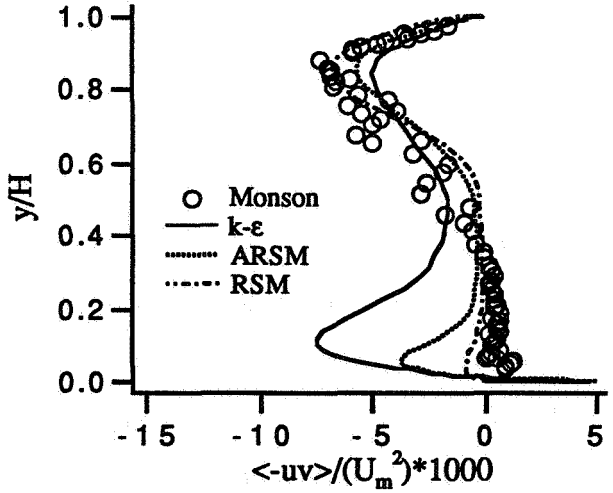

Fig. 1c Turbulent shear stress profile

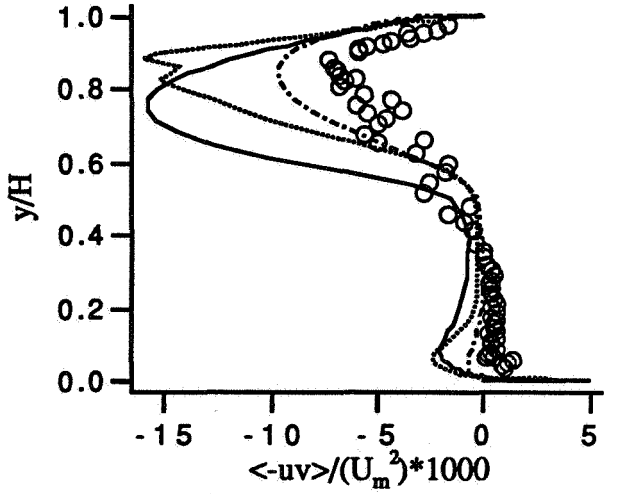

Fig.2c Turbulent shear stress profile(legend as in Fig.2b)

(all the above 6 figures are for predictions at θ=60 deg)

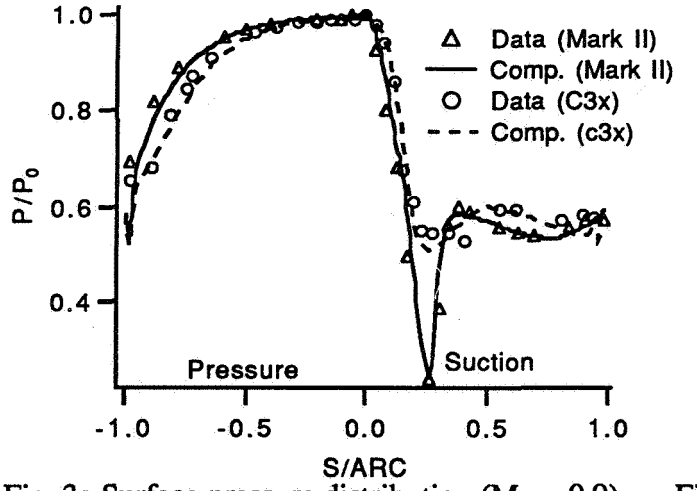

Fig. 3a Surface pressure distribution (M_{is2}=0.9)

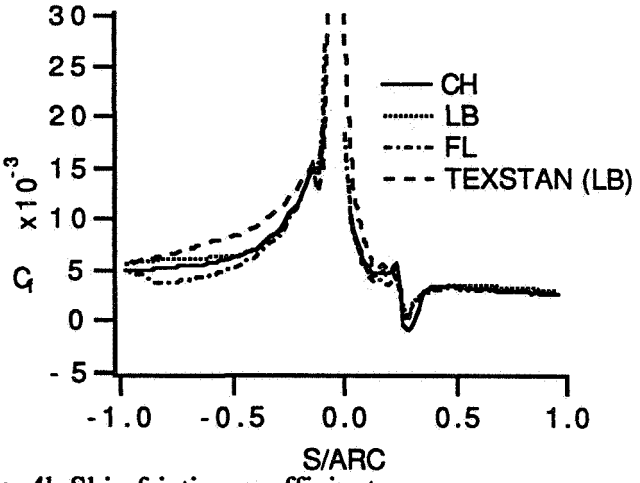

Fig. 4b Skin friction coefficient

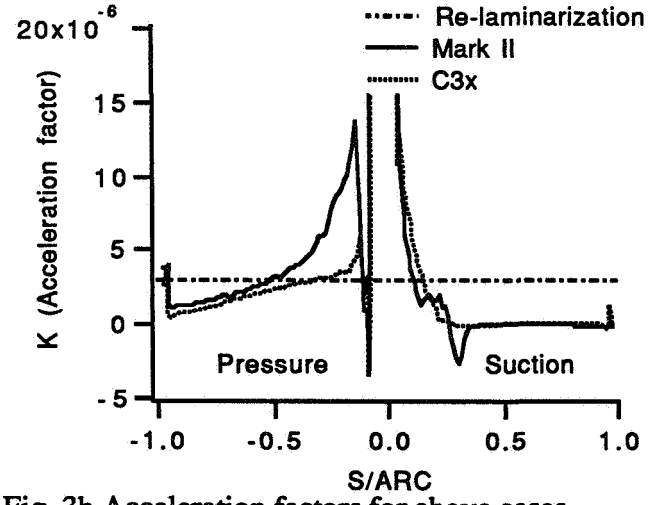

Fig. 3b Acceleration factors for above cases

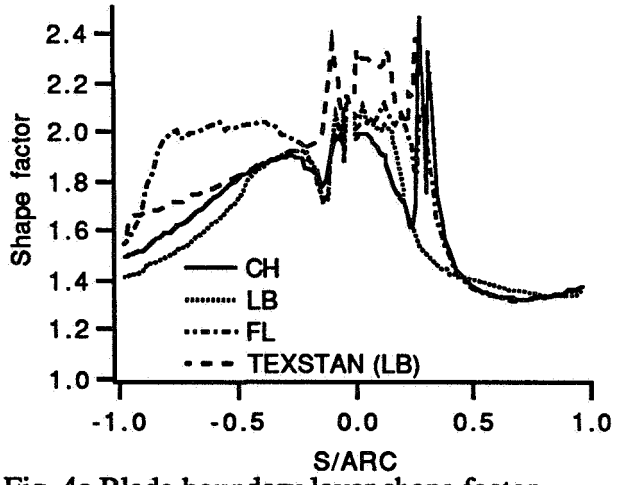

Fig. 4c Blade boundary layer shape factor

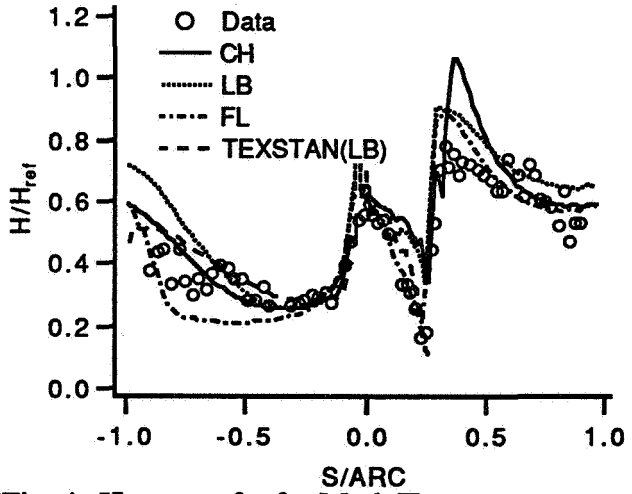

Fig. 4a Heat transfer for Mark II
(M_{is2}=0.90, Re_{is2}=1.6*10^6, Tu_∞=8.3%)

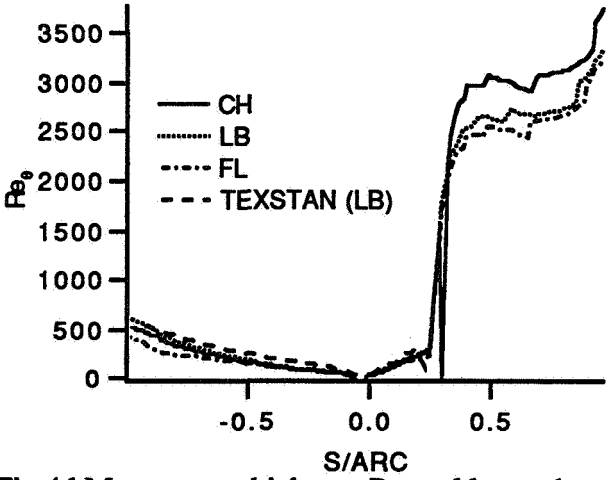

Fig 4d Momentum thickness Reynolds number

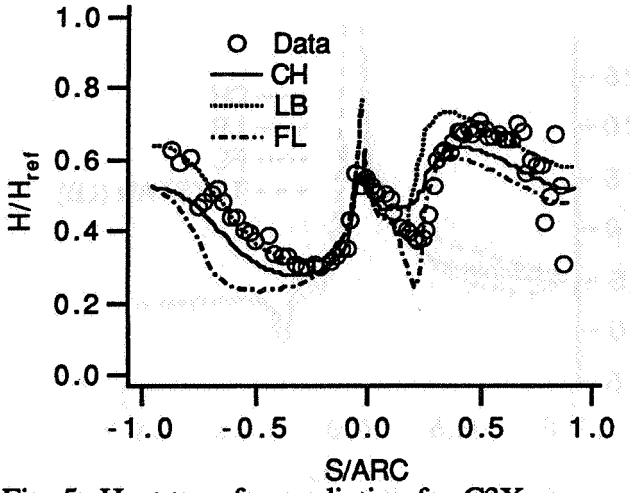

Fig. 5a Heat transfer prediction for C3X. (M_{is2}=0.90, Re_{is2}=1.5*10^6, Tu_∞=8.3%)

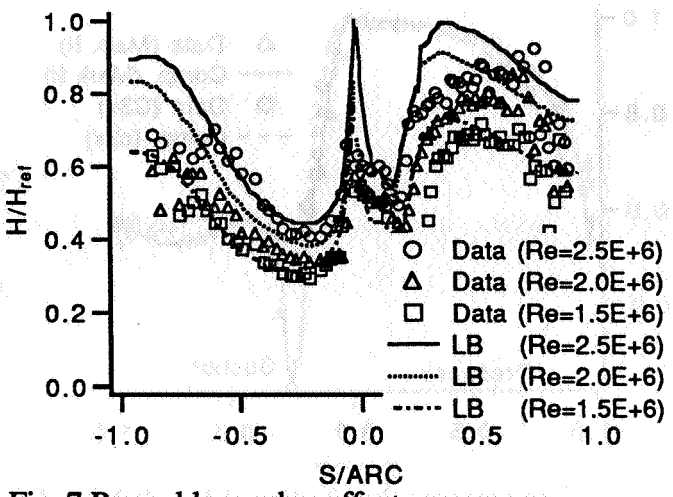

Fig. 7 Reynolds number effect

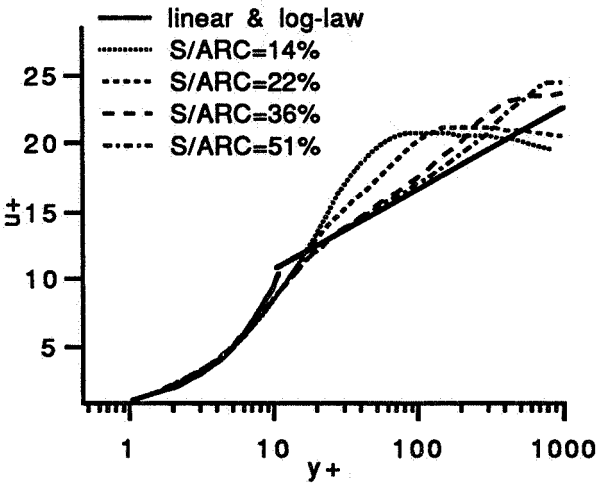

Fig. 5b Velocity profile along suction surface (LB)

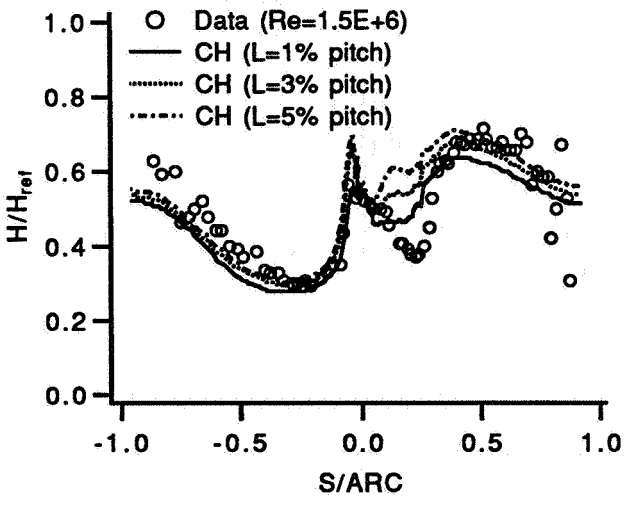

Fig. 8 Freestream turbulence length scale effect

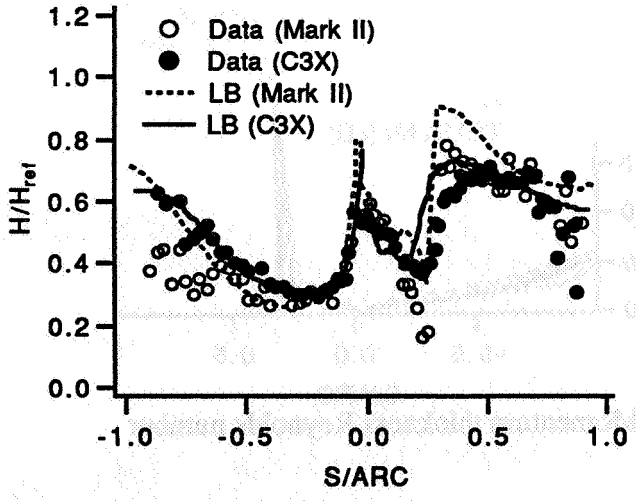

Fig. 6 Pressure gradient effect

427151 Pg 5 6

N95-70875

COMPUTATIONAL FLUID DYNAMICS (CFD) IN THE DESIGN OF A WATER-JET-DRIVE SYSTEM

Roberto Garcia
NASA/Marshall Space Flight Center
Marshall Space Flight Center, AL 35812

SUMMARY

NASA/Marshall Space Flight Center (MSFC) has an ongoing effort to transfer to industry the technologies developed at MSFC for rocket propulsion systems. The Technology Utilization (TU) Office at MSFC promotes these efforts and accepts requests for assistance from industry. One such solicitation involves a request from North American Marine Jet, Inc. (NAMJ) for assistance in the design of a water-jet-drive system to fill a gap in NAMJ's product line. NAMJ provided MSFC with a baseline axial flow impeller design as well as the relevant working parameters (rpm, flow rate, etc.). This baseline design was analyzed using CFD, and significant deficiencies identified. Four additional analyses were performed involving MSFC changes to the geometric and operational parameters of the baseline case. Subsequently, the impeller was redesigned by NAMJ and analyzed by MSFC. This new configuration performs significantly better than the baseline design. Similar cooperative activities are planned for the design of the jet-drive inlet.

DISCUSSION

NAMJ is a small company in Arkansas which manufactures water-jet-drives. NAMJ's product line has a gap in the 350 to 500 hp range. They identified a potential market demand for a drive system in that range and solicited help from NASA/MSFC's TU Office. The TU Office coordinates requests made by industry for NASA support. The goal of these activities is to make American industry more competitive by transferring NASA technology and providing industry with access to NASA expertise. NAMJ requested NASA support in the analysis of their proposed 350-500 hp system as well as information on pump testing and testing instrumentation. MSFC agreed to perform the requested analyses because it would benefit U.S. industry. The large customer identified by NAMJ was currently using a foreign manufactured jet-drive-system. Also, in general, the entire marine jet-drive industry had not made use of CFD to improve their designs. MSFC has demonstrated and promoted the value of using CFD in the design process [1, 2, and 3]. A final reason for performing this study is that it provided MSFC with the opportunity to identify and

remedy shortcomings in MSFC's analysis procedure and the opportunity to expand MSFC's pump analysis experience base.

NAMJ provided MSFC with a baseline design (figure 1) along with the operating characteristics (table 1). This design was a scaled version of a 30 year old design. A significant effort was required at MSFC to generate a gridi of the baseline design because the geometry definition had to be extracted from difficult to read drawings. Furthermore, the blade profile was specified only for the pressure surface. With the available information, MSFC was able to create a camber line definition and a thickness distribution at two radial stations. Defining the camber line and thickness distribution was necessary to facilitate the planned geometric parametrics (cases 3-5, table 1). The grid for the baseline case, as for all the

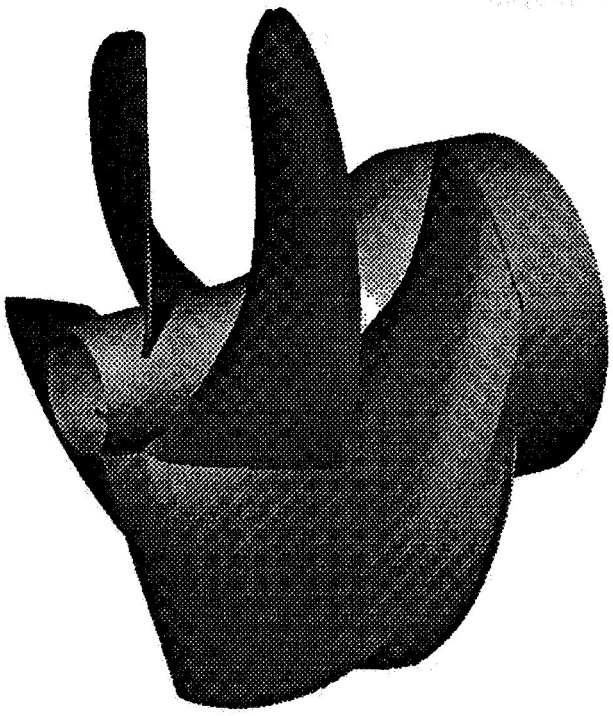

Figure 1 Baseline impeller

Table 1. Impeller Cases Analyzed

case #	1 (baseline)	2	3	4	5	6	7
rpm	2800	2800	2800	2800	2800	2600	2600
tip flow coefficient	.259	.181	.259	.259	.259	.171	.137
tip blade angle							
inlet	13.1	13.1	13.1	20.8	16.3	12.9	12.9
exit	24.1	24.1	29.5	28.6	24.1	32.2	32.2
hub-to-tip radius ratio							
inlet	.185	.185	.185	.185	.185	.400	.400
exit	.525	.525	.525	.525	.525	.700	.700
full blade tip solidity	1.38	1.38	1.27	0.75	0.92	1.66	1.66
leading edge sweep	9.1	9.1	9.1	21.5	21.5	25.6	25.6

other impeller cases, was generated using the code TIGER [4], available from Mississippi State University. TIGER is an extremely efficient and user-friendly turbomachinery grid generation code developed under the guidance of NASA/Lewis Research Center. Typical grids were generated in under one hour. The baseline impeller consisted of four full length blades and four partial blades. However, since TIGER does not have the capability to include partial blades in grids (a capability MSFC is interested in adding) and since we were interested in simplifying the model, it was decided to include only the full blades in the studies. A further simplification was to reduce tip clearance to zero in the model. This simplification was not too far from the actual case where the tip clearance is less than 0.5% of the blade height. The CFD code FDNS [5] developed under MSFC support was used to solve the flowfield on grids that had 44,500 points for cases 1-5 and 91,500 points for cases 6 and 7. Convergenced solutions were typically obtained overnight on NASA/MSFC's CRAY YMP computer, after running from five to eleven CPU hours.

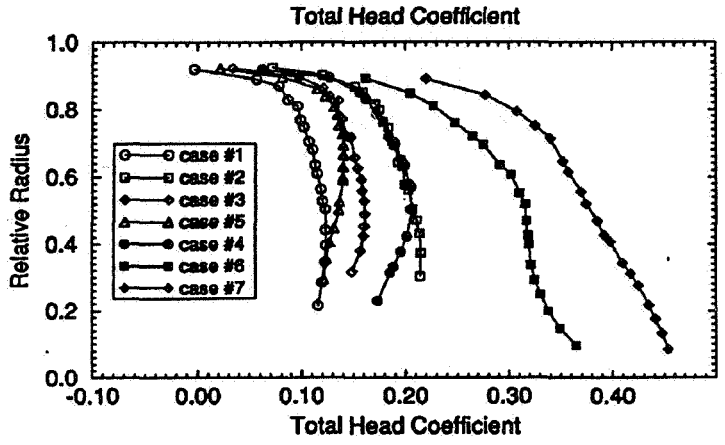

Figure 2. Predicted head coefficient for the simplified cases analyzed (zero tip clearance, no partial blades)

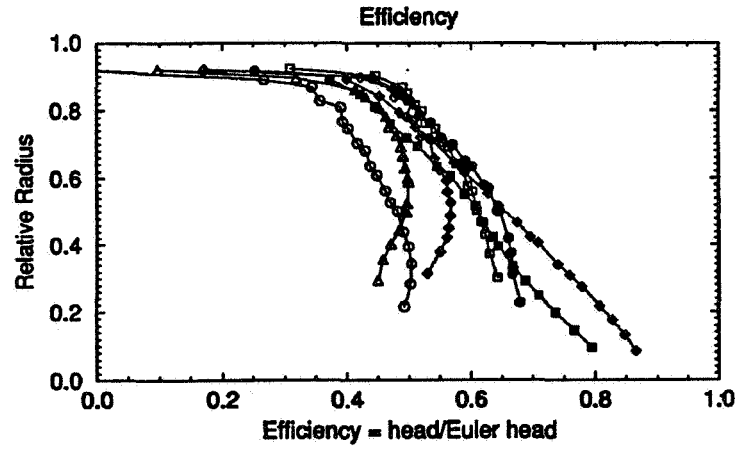

Figure 3. Predicted efficiency for the simplified cases analyzed (zero tip clearance, no partial blades)

CFD results for the baseline configuration verified initial suspicions that the flow rate provided was

too large for the given rpm. The leading edge had a negative incidence throughout the span except near the tip. Because of this, the head coefficient was low (figure 2) as well as the efficiency (figure 3). MSFC then performed four additional analyses in order to determine performance sensitivity to various parameters. Case 2 used the same geometry as the baseline but at a reduced flow (70% of the baseline) such that the blade leading edge had a positive incidence. As expected, the head coefficient increased (figure 2) as well as the efficiency (figure 3) indicating that this reduced flow coefficient was closer to the design point than the baseline. This result implied that to improve pump performance, the nozzle area in the jet-drive should be reduced to increase the backpressure on the impeller and to reduce the flow rate through the pump. Case 3 was run under the baseline conditions but with the blade camber increased by 50% (table 1). The performance predicted for this configuration lies between the performance of case 1 and of case 2. Increasing the camber beyond that of case 3 was deemed not likely to produce further increases in performance due to separation at the blade trailing edge along the hub.

Case 5 was performed prior to case 4. Case 5 assessed the effect of increasing the sweep of the leading edge in the baseline design. Since the sweep was accomplished by cutting back on the baseline blade, the mean blade leading edge angle increased. This produced a modest improvement in performance over the baseline case. Besides these performance improvements, the increased sweep leading edge was deemed desirable from the standpoint of structural robustness. Case 4 retained the increased sweep but featured a completely reprofiled blade. The hub and shroud contour remained unchanged as did the operating parameters. However, the blade was designed using a tip blade angle to incidence ratio consistent with rocket engine design. The hub-to-shroud angle distribution follows a free vortex distribution from inlet to exit (figure 4). The resulting design is predicted to perform

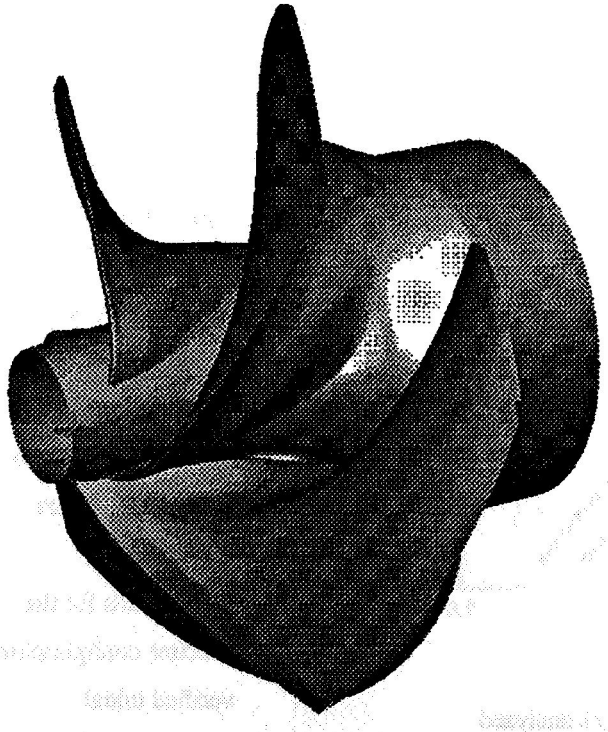

Figure 4. MSFC modified impeller for case 4

nearly as well as the reduced flow case.

Based on these results and on consultation with a third party, NAMJ presented MSFC with a new geometry to analyze (case 6) which featured reprofiled blades and a new hub contour (figure 5). The performance predicted for case 6 was higher than all the previous cases. This was due to be increased hub-to-tip radius ratios and increased solidity that allowed a 75% increase in camber and to the reduced inlet flow coefficient. However, observation of the results indicated that further reduction in flow coefficient was necessary to achieve peak performance. This was modeled in case 7 which featured a 20% reduction in flow from case 6. NAMJ has requested similar MSFC support for the design of the impeller inlet which, at high boat speed, can generate as much thrust as the pump.

CONCLUSION

MSFC is serious about transferring technology to industry. This activity benefited a U.S. company facing foreign competition by using NASA developed technology and expertise. MSFC benefited by expanding its pump analysis experience base and by improving on its CFD analysis procedure. The value of using CFD in the design process has also been demonstrated by providing engineering information on various design concepts and identifying the shortcomings and strengths of each prior to initiating manufacture of the first development article. Not only will this result in a better final product but in a shorter (less expensive) development cycle.

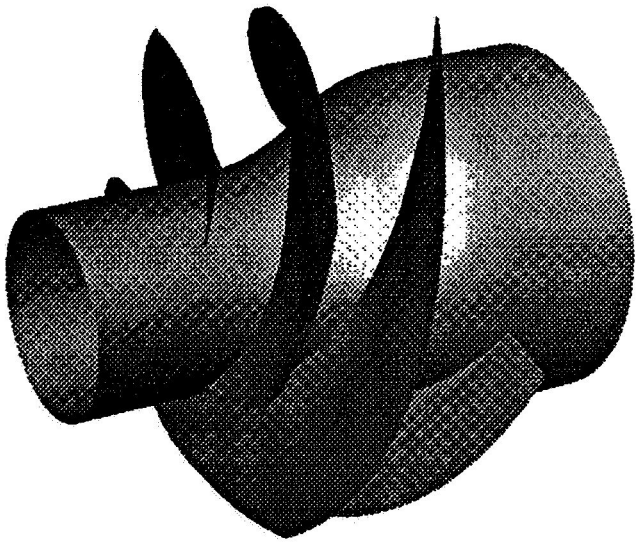

Figure 5. NAMJ redesigned impeller for case 6

REFERENCES

1. R. Garcia, E. D. Jackson, and L. A. Schutzenhofer, "A Summary of the Activities of the NASA/MSFC Pump Stage Technology Team," 4th International Symposium on Transport Phenomena and Dynamics of Rotating Machinery, ASME, April 5-9, 1992, Honolulu, HI.

2. R. Garcia, P. McConnaughey, and A. Eastland, "Activities of the Marshall Space Flight Center Pump Stage Technology Team," AIAA 92-3222, AIAA/SAE/ASME/ 28th Joint Propulsion Conference and Exhibit, July 6-8, 1992, Nashville, TN.

3. R. Garcia, P. McConnaughey, and A. Eastland, "Computational Fluid Dynamics Analysis for the Reduction of Impeller Discharge Flow Distortion," AIAA 94-0749, AIAA 32nd Aerospace Sciences Meeting and Exhibit, January 10-13, 1994, Reno, NV.

4. Shih, M. H., "Towards a Comprehensive Computational Simulation System for Turbomachinery," Dissertation, Mississippi State University, May 1994.

5. G. C. Cheng, Y. S. Chen, R. Garcia, and R. W. Williams, "Numerical Study of 3D Inducer and Impeller for Pump Model Development," AIAA 93-3003, AIAA 28th Fluid Dynamics Conference, July 6-9, 1993, Orlando, FL.

427154
pgs 5

N95- 70876

PERFORMANCE TESTING OF A FIXED CONFIGURATION MICROWAVE ARCJET THRUSTER

D. J. Sullivan and M. M. Micci

Propulsion Engineering Research Center
Department of Aerospace Engineering
The Pennsylvania State University
University Park, PA 16802

SUMMARY

The microwave arcjet thruster uses microwave energy to create a free-floating plasma discharge within a microwave resonant cavity. This discharge typically absorbs 99% of the input power and converts it to thermal energy which is then transferred to the flowing propellant gas. Recent modifications have allowed the thruster to be operated in a fixed configuration where neither the cavity geometry nor the tuning mechanisms are adjusted. The prototype has demonstrate its ability to operate in this fixed configuration using a variety of propellant gases, i.e. nitrogen, helium, ammonia, and hydrogen. The current design is capable of efficient operation over a wide range of power levels (250 W to over 6000 W). Current work is focused on obtaining LIF velocimetry data of the velocity profile at the exit plane of the nozzle.

TECHNICAL DISCUSSION

This work is a continuation of an ongoing effort at Penn State to develop a prototype microwave powered satellite propulsion system. The device, which in previous papers has been referred to as a microwave resonant cavity electrothermal thruster, will for the sake of brevity be referred to as the microwave arcjet. The development work at Penn State has spanned most of the last decade and has entailed an extensive experimental effort which has been augmented by numerical simulations. Results of early studies have indicated that a design based upon a cylindrical cavity operating in the TM_{011} resonant mode would be best suited for thruster applications. A microwave arcjet of this type uses microwaves to form and maintain a plasma within the cavity; cold gas passes through the cavity, is heated by the plasma source, and passes out of the device through a nozzle to produce thrust.

The microwave arcjet is characterized by a free-floating ac plasma discharge. The location of the discharge, which forms at regions of maximum power density, is determined by the pattern of electric power density within the cavity. Proper cavity design produces patterns which result in an axially located plasma which is positioned directly upstream of a nozzle incorporated into one end of the cavity. Operation in this configuration has the net effect of producing a flow constriction be-

C-2

tween the plasma discharge and the nozzle inlet. It is in this constricted region that the bulk of the heating process occurs. The microwave discharge typically resides very close to the nozzle inlet, which may cause erosion of the nozzle during high power operation. Therefore while some erosion may be a concern, the erosion is not of a critical electrical component as is the case with the conventional arcjet.

Work on the microwave resonant cavity design for thruster applications was initiated by Michigan State University [Ref. 1] in the early 1980's. This work was continued at Penn State by Balaam and Micci [Ref. 2], Mueller and Micci [Ref. 3], and Sullivan and Micci [Ref. 4]. These experimental studies quantified the plasma formation process, and the effectiveness of using the plasma discharge to heat a flowing propellant. The results of the experimental and numerical work [Ref. 5] at Penn State which were augmented by some preliminary high power work at NASA LeRC [Ref. 6], were used to develop a design of a first-generation microwave arcjet prototype. A full description of this device and the relevant theory have been presented in an earlier paper [Ref. 4] and will not be repeated here. The prototype was designed to remove many of the undesirable operational features of the earlier cavities. The design demonstrated that it could consistently produce stable discharges located in the desired position within the cavity at operating conditions up to 300 kPa and 2.2 kW. This design also demonstrated that it could be successfully operated using a variety of propellant gases, i.e., He, N_2, H_2, and NH_3. The initial work concentrated on qualifying the thruster performance in terms of vacuum I_{sp} as a function of specific power, where the vacuum I_{sp} was calculated using an ideal one-dimensional isentropic analysis. The results off this analysis yielded initial performance estimates for the prototype microwave arcjet. Representative values from this testing are given in Table 1.

Recent design modifications have been made which have allowed for improved performance of the microwave arcjet. A schematic of the modified device is shown in Figure 1. The main component of the prototype thruster is a resonant cavity which operates in the TM_{011} mode. The thruster is designed such that the plasma forms directly upstream of a graphite nozzle which is incorporated into the stationary short of the cavity. The formation of the plasma discharge near the inlet of the nozzle produces the most efficient transfer of thermal energy to the propellant gas.

The major modification of the thruster has been to make the resonant cavity a two section pressure vessel where the two sections are connected by a shunt line and cutoff valve. The two pressure sections are separated by a 0.635 cm thick boron-nitride plate. The incorporation of this plate was feasible because electric field pattern measurements which were conducted in previous experiments showed that a thin plate of boron-nitride placed at the mid-plane of a TM_{011} resonant cavity of these dimensions had only a minor effect on the overall resonant field pattern within the cavity. If the shunt valve is open, the pressure is equal in both chambers of the cavity and thus a pressure differential does not exist across the boron-nitride pressure plate. This configuration allows for high

pressure operation without the risk of fracturing the pressure plate. The seal on the coaxial line is facilitated by a 0.635 cm thick teflon ring. If the shunt valve is closed the nozzle side of the cavity can be sealed and pumped down to a low pressure while maintaining an elevated pressure on the power inlet side of the cavity. This condition is used to cause the plasma to preferentially form within the low pressure side of the cavity in the desired location near the nozzle.

The second modification was to incorporate a full converging diverging nozzle into the prototype. The nozzle has an area ratio of 153 and is constructed of high density graphite. The conical nozzle has a 30 degree half-angle converging and a 15 degree half-angle diverging section. The diameter of the nozzle throat is 0.10 cm. The nozzle is located in the center of the stationary short, and because it is a conductor, it enhances the field density pattern on the axis of the cavity, thus insuring that the field pattern in the region of the nozzle closely resembles the ideal pattern. The microwave breakdown occurs in the vicinity of the nozzle and the plasma forms within the inlet of the nozzle; the plasma location is shown schematically in Figure 1.

The insertion depth of the coupling probe is adjustable, however, because of the pressure seals, adjustments cannot be performed during operation of the thruster. The device has to be disassembled in order to change the coupling probe insertion depth. The length of the resonant cavity of the prototype can also be changed by adjusting the position of a movable shorting plate, however, because of the nature of the pressure seals, the cavity length can also not be adjusted during actual thruster operation. Thus, for any given test, the geometry of the prototype design is fixed.

As stated earlier, the initial tests with the microwave arcjet prototype concentrated on qualifying the device's basic operating characteristics. These preliminary tests neither operated the thruster at the maximum powers or pressures available to the test facility, nor did they attempt to qualify whether or not the thruster could successfully be operated in a fixed configuration. The most recent testing has begun to examine both these aspects.

The modifications of the thruster have allowed for reliable operation of the thruster at pressures up to 500 kPa absolute. Previous testing could not exceed 300 kPa without risking damage to the boron-nitride pressure plate. At the time of this writing, higher pressure operation has not been explored, this is due solely to limitations of the gas feed system and does not reflect an operational limit of the microwave arcjet prototype.

The thruster has also been reliably operated at the maximum power output of the microwave generator. The nominal output of the generator is 2.2 kW. A complimentary experimental program which is using a cavity identical to the one described here has shown that the thruster can operate at power levels up to 6 kW [Ref. 7].

The primary goal of the current testing has been to demonstrate the fixed configuration operation of the microwave arcjet. It was identified early in the development stages of this prototype that fixed configuration operation was essential if this device was to be considered a viable satellite

propulsion option. The requirement that the thruster geometry be varied between start-up and steady state operation would clearly be unacceptable for any feasible station keeping system.

The fixed configuration operation consists of fixing the cavity length, the position of the coupling probe and the adjustments of the three stub tuner. The plasma is then initiated in the nozzle side of the cavity at low pressure (~50 kPa) by the application of microwave power. Once initiated the plasma can be brought to operating conditions by increasing both power and mass flow rate. This type of operation has been demonstrated for both helium and nitrogen propellants. Typical performance data for these tests are given in Table 2 and Table 3. Using these propellants at input power levels of 2000 W the thruster has been continuously operated for periods up to 2.5 hrs.

Additional testing has demonstrated that both hydrogen and ammonia plasmas can be repeatable initiated at low pressures of 5-10 kPa within a fixed configuration system and that these plasmas can be brought to atmospheric pressures. While the work with these two gases has been limited in extent, work with ammonia has demonstrated that plasmas can repeatedly be operated at 300 kPa at 2200 W of input power with coupling efficiencies of 99%.

The current program is concentrating on determining the exhaust plume velocity profile at the exit plane of the nozzle using Laser Induced Fluorescence (LIF) velocimetry. The work in progress is concentrating on using this technique to determine the velocity profile of the thruster operating on nitrogen and exhausting into the ambient lab atmosphere. This work will either use the 654.48 nm band head of the 1st positive system, or a small amount of hydrogen will be used to seed the flow thus allowing the use of the 656.28 nm transition of the hydrogen atom.

Once this work has been completed the microwave arcjet will be mounted within the 1m x 1.5 m vacuum tank and extensive hydrogen and ammonia testing will commence. This work will include LIF velocimetry of the exhaust plume utilizing the 656.28 nm transition of atomic hydrogen. The data gained from these experiments will allow a qualitative comparison between the microwave arcjet and the hydrogen arcjet for which similar data has been obtained [Ref. 8].

REFERENCES

[1] Hawley, M. C., et al., "*Review of Research and Development on the Microwave Electrothermal Thruster*," Journal of Propulsion and Power, Vol. 5, No. 6, Nov-Dec 1989, pp. 703-712.

[2] Balaam, P., Micci, M.M., "*Investigation of Free-Floating Resonant Cavity Microwave Plasmas for Propulsion*," Journal of Propulsion and Power, Vol 8, No. 1, Jan-Feb 1992, pp. 103-109.

[3] Mueller, J., Micci, M.M., "*Microwave Waveguide Heated Plasmas for Electrothermal Propulsion*," Journal of Propulsion and Power, Vol. 8, No. 5, Sept.-Oct 1992, pp. 1017-1022.

[4] Sullivan, D. J., Micci, M. M., "*Development of a Microwave Resonant Cavity Electrothermal Thruster Prototype*," IEPC-93-036, AIAA/AIDAA/DGLR/JSASS 23rd International Electric Propulsion Conference, Seattle, WA, September 13-16, 1993.

[5] Venkateswaran, S., Schwer, D. A., Merkle, C. L., *"Numerical Modeling of Waveguide Heated Microwave Plasmas,"* Journal of Fluids Engineering, Vol 115, No. 4, December 1993, pp. 732-741.

[6] Power, J. L., Sullivan, D. J., *"Preliminary Investigation of High Power Microwave PLasmas for Electrothermal Thruster Use,"* AIAA-93-2106, AIAA/SAE/ASME/ASEE 29th Joint Propulsion Conference, Monterey, CA, June 1993

[7] Read, M. E., Physical Sciences Inc., Alexandria, VA, Personal Communication, June 1994.

[8] Liebeskind, Hanson, R. K., Cappelli, M. A., *"Velocity Measurements in a Hydrogen Arcjet Using LIF,"* AIAA-91-2112, AIAA/SAE/ASME/ASEE 27th Joint Propulsion Conference, Sacramento, CA, June 1991.

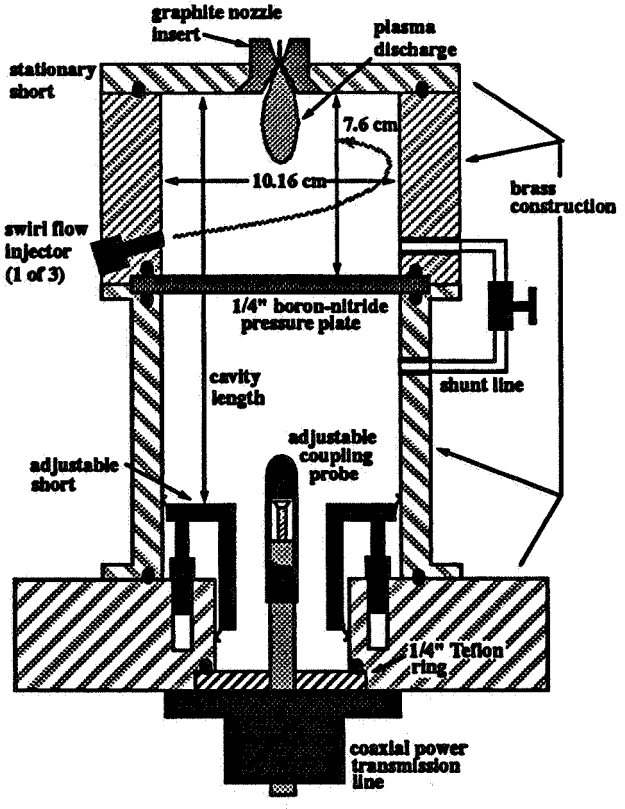

Figure 1: Schematic of the modified microwave arcjet prototype. The diameter of the cavity is 10.16 cm and the theoretical resonant length is 15.87 cm. While both the length of the cavity and the depth of the coupling probe can be adjusted, they must remain fixed during thruster operation. The entire cavity is divided into two pressure chambers which are connected by a shunt line and valve.

Table 1: Performance Estimates from Isentropic Analysis

Gas	Isp (s)	Specific Power (MJ/kg)	Thermal Efficiency
Helium	625	18	90%
Nitrogen	235	7	33%
Ammonia	425	18	55%
Hydrogen	1040	97	50%

Table 2: Nitrogen Performance Data

Incident Power (W)	Coupling Efficiency	Pressure (kPa abs)	Specific Power (MJ/kg)
1442	99%	433	4.21
1442	93%	358	5.05
1442	93%	328	5.51
1660	98%	407	6.31
1731	99%	408	6.43
1803	99%	448	6.35
1820	98%	478	4.12
2091	99%	498	4.31

Table 3: Helium Performance Data

Incident Power (W)	Coupling Efficiency	Pressure (kPa abs)	Specific Power (MJ/kg)
1442	98%	307	24.03
1658	98%	322	27.64
1803	98%	345	28.93
1803	98%	365	27.31
1947	98%	400	27.62
2236	99%	445	17.28

42715G
Pgs 5

N95-70877

Orbital Maneuvering and Reaction Control Systems

Eric Hurlbert
Propulsion and Power Division
NASA - Johnson Space Center

Orbital maneuvering systems (OMS) and reaction control systems (RCS) provide capabilities to spacecraft that include orbit circularization, rendezvous maneuvers, attitude control, and re-entry delta velocity. The mission and vehicle requirements can place severe demands on the orbital maneuvering and reaction control systems. In order to perform proper trade studies and to design these systems, the mission and vehicle configuration must be well defined. In the absence of a clearly defined mission and vehicle configuration, the research and development of basic technologies must support future design efforts by providing a range of options and data from which to select. This paper describes the key OMS and RCS requirements and technology.

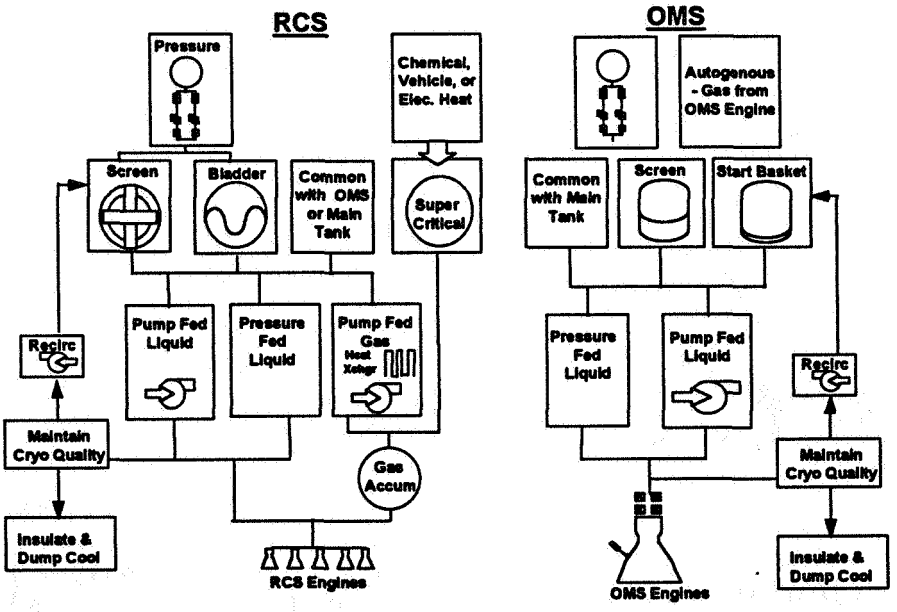

Figure 1 Design Options for OMS and RCS

In general, the mission of a spacecraft may include delivering payloads to orbit, transporting humans to orbit, providing a platform for research, landing material on the moon, or exploring the solar system. Each of these missions places unique requirements on OMS and RCS that must be fully understood.

In the case of the space shuttle, its mission is to deliver payloads and humans to orbit, to provide an orbiting platform for research and observation, and to assemble a space station. The space shuttle consists of a reusable winged orbiter, expendable tanks, and reusable boosters. Given this mission and vehicle, storable propellants were found to be optimum. Both Apollo and the space shuttle use storable propellants, which have provided 100% mission reliability. Key technology developments were engine life, combustion stability, and material compatibility.

Key Requirements

The requirements for the OMS and RCS are essentially derived from the shuttle mission and the vehicle configuration. The following is a list of key design drivers for OMS and RCS systems.

Ascent to Orbit Duty Cycle - The ascent duty cycle includes critical spacecraft maneuvers during ascent or aborts. For example, the shuttle requires the RCS to provide roll control in the event 2 SSME's are out. The shuttle also requires the RCS to quickly maneuver the shuttle away from the external tank duration separation to prevent recontact. This requires a system with 870 lbf thrusters. Key future technology developments are dual mode or thrust engines which perform high thrust maneuvers as well as low thrust docking maneuvers.

Duty Cycle On Orbit - This includes total burn duration, total number of pulses, and the duration on orbit. The Shuttle RCS has a total life of 20,000 seconds and a cycle life of 20,000 pulses. The duration on orbit can range from hours to years. The space shuttle duration is about 15 days. During this period the RCS is continuously active for attitude control, thermal control, rendezvous, and debris avoidance. For simplicity, this drives the RCS and OMS design to either have a gas or an ambient liquid in the feedlines. If the propellant is allowed to become two-phase, either a recirculation pump or a propellant dump is probably required prior to engine start. The shuttle uses storable liquids and avoids any complications. Key technologies for future vehicles, with on orbit duration greater than hours, include supercritical storage and delivery of gaseous oxygen, subcritical liquid-to-gas propellant (i.e. LH_2) feed systems, and testing of ambient hydrocarbon or alcohol fuels for RCS applications.

Entry Duty Cycle Requirements - A reusable vehicle requires RCS until aerosurfaces become effective. This can require a large amount of propellant in a short period of time. The

shuttle uses 1100 lbm or more of propellant in 30 minutes. This can be significant in designing systems that utilize gaseous propellant in terms of accumulator sizing, supercritical tank heat addition, and liquid-to-gas conversion heat exchangers and pumps.

Redundancy Requirements - This defines the number of thrusters required and can significantly complicate systems. In the case of the shuttle, the RCS is used to back up the OMS engines, which requires an 800 second burn duration for the aft facing RCS engines. In total there are 38 primary and 6 vernier RCS thrusters. Future vehicles programs may select to avoid this complication of RCS back-up, however some redundancy is required due to the value of human life and payload. Key technologies to reduce the number of thrusters may be dual mode or thrust engines, which allow combination of duties.

Total Impulse and Mass Requirements - As the total impulse requirement increases, the necessity for a higher total system performance increases. The shuttle OMS engine at a specific impulse of 315 seconds at 55:1 expansion is reneratively cooled. Future vehicles may require higher performance to meet total impulse and vehicle mass requirements. Key technologies are higher system performance propellants, high temperature chamber materials, advanced cooling techniques, and efficient combustor designs.

Packaging or Volume Constraints - The size of the system can be critical as payload space or aerodynamic drag considerations compete with the OMS and RCS design. The propellants, N2O4 and MMH, reduce system volume in the externally mounted pods on the space shuttle. Key future technologies areas include high density propellants oxidizers such as liquid oxygen and hydrogen peroxide, and the fuels such as RP1, alcohol, and other hydrocarbons.

Ground Operations - While not as significant in ground operation requirements as main propulsion, an OMS and RCS design is driven to the use of non-toxic, non-flammable, non-explosive, low leakage, ambient propellants in a long life, simple, low maintenance system. The shuttle system, while simple, uses the toxic propellants MMH and N2O4. Key future technology areas are low toxicity propellants such as liquid oxygen, hydrogen peroxide, RP1, and alcohol.

Zero-G Acquisition - The RCS tanks are required to provide acquisition of propellants and venting of gases under zero-G conditions. The shuttle RCS tank uses screens positioned 360 degrees around the tank, that remain wetted by surface tension forces. Storable propellants do

not require venting. Key future technologies are supercritical storage tanks and zero-g vent systems.

Reliability - Reliability is a function of the number of components and the complexity of those components. The shuttle uses a pressure fed system with hypergolic ignition. Key future technology areas are supercritical propellant storage for a pressure fed system, reliable non-hypergolic ignition, and testing of ambient hydrocarbon fuels for OMS/RCS.

Cost and Schedule - Cost and schedule includes both DDTE and Operations. The three most important questions are does it meet the mission, how much does it cost, and what is the schedule. These issues are directly tied to complexity and technology readiness. Key future technologies, that will end up being used, are those that can answer these three questions.

Trade Study Selection Criteria For Future OMS and RCS System

The selection criteria must include all program considerations and be as quantitative as possible. Figure 2 lists a hierarchy of attributes that can weighted against each other to allow comparison of various design options. Details on each design option such as mass, volume, number of components, number of measurement instruments, toxicity, technology readiness, etc. need to be accumulated from schematics and design analysis. One possible method for comparing the options, once all the design details have been determined, is the Analytic Hierarchy Process (AHP). Relative weights between the high level attributes should be chosen by the program managers.

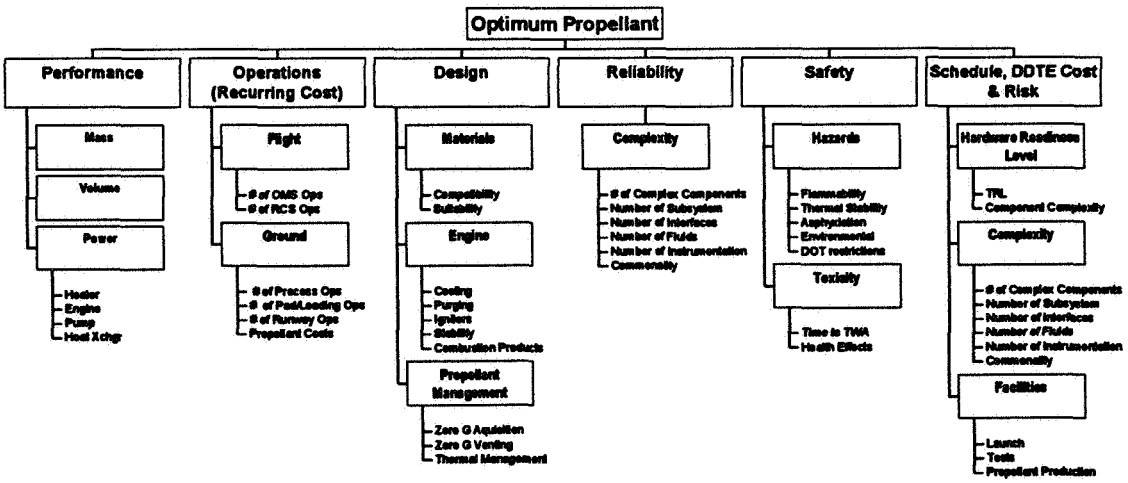

Figure 2. Hierarchy For Selection Propellant for OMS and RCS

ORIGINAL PAGE IS
OF POOR QUALITY

Summary of Key Technologies

A chart showing the key future OMS and RCS system technologies is shown in figure 3. The chart decomposes the components of an OMS and RCS System into technology development areas. The chart also indicates where the developments would be applicable.

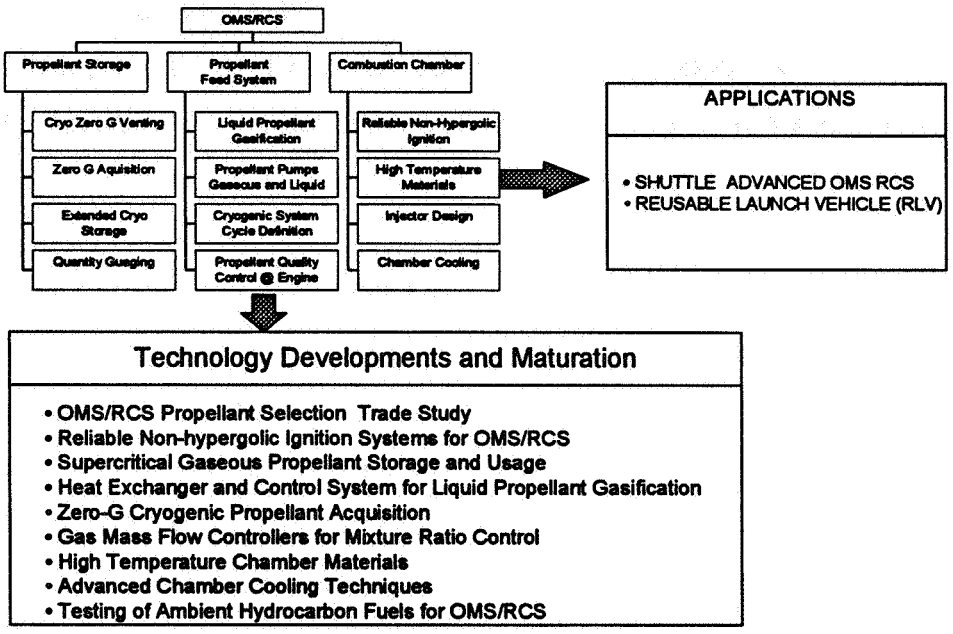

Figure 3. Technology Development Areas

Conclusion

Storable propellants have provided reliable propulsion for Apollo and Space Shuttle programs, with the major technology developments being engine chamber life, combustion stability, and material compatibility. For future OMS and RCS systems, the goal is to reduce toxicity and ground operations, but not at the expense of simplicity, reliability, and cost. To meet the future needs, new technologies are required. Detailed trade studies using well defined vehicle requirements are needed to provide a basis for sound decisions.

ORIGINAL PAGE IS
OF POOR QUALITY

427159
B53

N95-70878

Technology Advancements for On-Board Propulsion Systems

David Byers

NASA Lewis Research Center

Cleveland, Ohio

On-board propulsion systems are required for all classes of space missions and usually represent a predominant fraction of the mass delivered to space by launch systems. Significant mission cost and performance benefits may, therefore, be gained via use of advanced on-board propulsion and strong international programs are in place to develop new technologies (Figure 1). The NASA Office of Space Access and Technology (OSAT) sponsors a program to identify, develop, and transfer on-board electric and low thrust chemical propulsion systems with potential for major impacts on the performance and competitiveness of U.S. space systems. The paper will briefly describe the overall content of the on-board propulsion program and then highlight some critical technologies with potentials for long term impacts.

Discussion

On-board propulsion functions are critical to nearly all space missions and include auxiliary propulsion system (APS) for launchers, drag makeup, attitude control, stationkeeping and repositioning, planetary retro, and many other in-space "delta V" requirements. These propulsion systems are a predominant fraction of the mass delivered by Earth launchers for a broad set of missions. Figure 2 shows on-board propulsion system masses required for several mission classes. The penalties represented on Figure 2 are fundamental and several global developments, such as the increased use of smaller launchers, requirements to maximize the number of satellites per launch, and new propulsion requirements such as de-orbit, can be expected to increase the fractional mission impacts of in-space propulsion well beyond present levels.

The NASA OSAT sponsors a program with goals of developing and inserting new, on-board propulsion technologies. Due to the extreme range of on-board propulsion requirements, both electric and low thrust chemical propulsion systems are developed in the program. The program includes the full scope of technical development from Fundamentals, to Technology, thru Technology Insertions (Figure 3). The program elements of electric and low thrust chemical Technology and Technology Insertions have been covered in depth in recent publications (Refs. 1, 2, and 3). This paper will review the Fundamentals portion of the OSAT program. The review, which includes research on diagnostics and models, fluid and plasma flows, materials and propellants, is intended to both provide status and illuminate basic research areas expected to be of long term interest to the program.

References

1. Bennett, Gary L., et. al., "Enhancing U.S. Competitiveness: The NASA Electric Propulsion Program," AIAA 94-2735, June 1994.

2. Schneider, Steven J., "High Temperature Thruster Technology for Spacecraft Propulsion," Acta Astronautica, Vol. 28, pp. 115-125, 1992.

3. Curran, Francis M., Brophy, John R., and Bennett, Gary L., "The NASA Electric Propulsion Program," AIAA 93-1935, June 1993.

DEVELOPMENT ○
RESEARCH □
(1) GOVERNMENT SPONSORED

	ON-GOING INTERNATIONAL R,T, & D PROGRAMS(1)						
	JAPAN	RUSSIA	USA	WESTERN EUROPE			
				FRANCE	GERMANY	UK	ESA
ELECTRIC							
ORBIT CONTROL	○	○	○	○	○	○	○
ORBIT CHANGE/TRANSFER	□	□	○/□			□	
LOW THRUST CHEMICAL							
ORBIT CONTROL	□	?	○	○	○	○	
ORBIT CHANGE/TRANSFER	□	?	○	○	○	○	○

FIGURE 1. INTERNATIONAL PROGRAMS IN ON-BOARD PROPULSION

EARTH-ORBIT

- GEOSATS
  - > 60% GTO MASS
  - ON-ORBIT LIFE LIMITER
- LEO/MEO SATS
  - OFTEN DOMINANT SUBSYSTEM MASS (> 25%)
  - AFFECTS # OF SATS PER LAUNCH
  - DEORBIT POLICY IMPACTS TBD
- SPACE STATION
  - RESUPPLY WAS ~ 1.1 EQUIVALENT ORBITERS/YEAR
- ORBITER
  - ACS ~ 27 KLBS (DUE EAST)

PLANETARY

- DOMINANT INJECTED MASS (> 60%)

FIGURE 2. STATE-OF-ART ON-BOARD PROPULSION PENALTIES FOR SEVERAL MISSION CLASSES

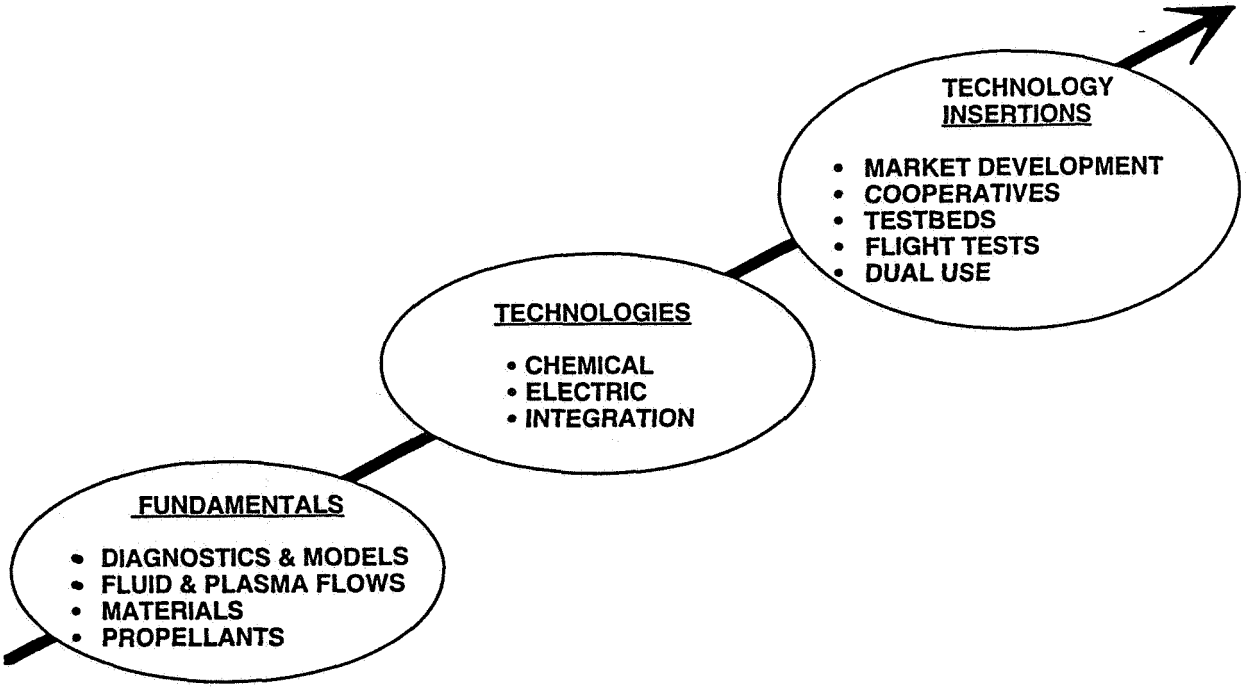

FIGURE 3. SCOPE OF THE NASA OSAT ON-BOARD PROPULSION PROGRAM

427160
Pgs 5

N95-70879

Interface Issues for On-Board Propulsion Systems

Frank M. Curran and Steven J. Schneider
NASA Lewis Research Center
21000 Brookpark Road
Cleveland, Ohio 44135

Overview

Integration issues associated with the use of new chemical and electric propulsion technologies are a primary concern to the user community. Experience indicates that integration impacts must be addressed to the satisfaction of both spacecraft builders and operators prior to the acceptance of new propulsion systems. The NASA Lewis Research Center (LeRC) conducts an aggressive program to develop and transfer new propulsion technologies and this includes a major effort to identify and address integration issues associated with their use (Refs. 1,2). This paper provides an overview of integration issues followed by a brief description of the spacecraft integration program at LeRC.

Discussion

On-board propulsion systems are a major mass driver in a broad range of space missions. Because of this, the application of high performance propulsion technologies can provide significant benefits which can be used to reduce launch vehicle requirements, increase spacecraft life, and/or improve payload capabilities. Acceptance of new propulsion technologies requires both high mission benefit and technology demonstrations sufficient to reduce the perceived risks of potential users to acceptible levels. In addition to performance, reliability, and manufacturing considerations, these demonstrations must include tests to show that the new system will not adversely impact spacecraft systems or functions. A schematic showing the interrelationships between a spacecraft and an electrothermal arcjet system are shown in Figure 1. This example was chosen for its timeliness. The arcjet was developed through a joint NASA/industry program and first flown in a commercial application in December 1993. Many of the integration issues shown in the figure can be addressed via straightforward engineering changes in electrical, propellant delivery, and other spacecraft systems. Several, however, are unique to advanced propulsion systems as shown in Figure 2. These can further be broken into thermal impacts and issues associated with the plasma plume. The former, while problematic, are well defined and will not be discussed in detail here. The latter are often not well characterized and so not amenable to standard treatments and will be the primary focus of this paper. Plumes from both chemical and electrical thrusters represent sources of contamination/degradation of sensitive spacecraft sensors and surfaces. With chemical thrusters, the major contamination source is unburned fuel which can condense on unprotected surfaces during thruster operation. Degradation due to electric thruster plumes is by and large caused by sputtering due to high energy particles. The effects of both thermal loading and momentum exchange due to direct impingement of plume flows must also be considered. In contrast to chemical thrusters, high performance electric rocket plumes are often highly ionized and associated particles and fields present issues related to communication signal transmission and electromagnetic interference unfamiliar to many spacecraft designers and users.

To directly address user concerns associated with plume flows, the LeRC On-Board propulsion program supports extensive efforts aimed at characterizing both small rocket plume flows and their impacts on spacecraft systems. The program is composed of three major elements - fundamentals, testbed development, and specific technology transfer efforts. These are designed to encompass both near- and far-term development programs and are illustrated in Figure 3.

As shown in the figure, the LeRC program in fundamentals includes both theoretical and experimental efforts to characterize plume flows. This part of the program is structured to provide the tools necessary to address integration issues both now and in the future. A major fraction of program resources are directed toward the development of sophisticated numerical plume models based on Direct Simulation Monte Carlo (DSMC) techniques. Early goals of the effort are to develop and validate models of simple non-ionized flows and the impacts of ground test facilities on experimental results. To date, numerical results have been shown to match well with experimental data obtained from small resistojet thrusters. It is hoped that anticipated advances in computational capabilities can be leveraged in the near future to develop codes for charged flows based either on DSMC or other advanced techniques.

In addition to the DSMC work, the LeRC program also funded the development of a plume/communications impacts model which has now been used in industry to evaluate the effects of arcjet plumes on satellite communications links for realistic configurations.

The diagnostics effort includes both intrusive and non-intrusive diagnostics for the evaluation of plume flows. Many of these have found application both in the direct assessment of specific integration issues, as noted below, and in plume code validations.

A major part of the integration effort at LeRC has focused on the development of high fidelity testbeds for space propulsion related research. These testbeds have been used extensively in cooperative programs associated with program technology transfer efforts. Examples of existing capabilities are shown in Figure 4. In addition to direct thrust measurements, installed diagnostic capabilities include intrusive probes for plume measurements such as electron number density and temperature, current density profiles and ion energy distribution, and contamination/degradation effects. Non-intrusive diagnostics to evaluate both axial and azimuthal ion velocity profiles are available as are capabilities to directly monitor communications impacts. The major propulsion testbed is located in the Electric Power Laboratory. The facility itself is a large vacuum chamber approximately 5 m in diameter and 20 m in length. This chamber is pumped both by a large gaseous helium cryopanel and a set of 20 oil diffusion pumps backed by a mechanical pumping system.

One example of a joint NASA/industry cooperative program is illustrated in Figure 5. The participants in this program were General Electric's Astro-Space Division (GE - now Martin Marietta), the spacecraft manufacturer, and the Rocket Research Company (now Olin Aerospace), the arcjet suppliers. Similar programs with industry and other government agencies have addressed integration issues associated with other advanced propulsion systems. The objective of this particular test was to retire risks perceived both by GE and AT&T, the end user of the spacecraft. Concerns centered on plume impacts on spacecraft surfaces, electrostatic discharge phenomena, and EMI. Samples of typical

spacecraft materials were supplied for the test by GE along with experimental equipment for electrostatic discharge tests. GE also made available a flight-type brassboard PPU which was developed under their program with RRC. RRC provided arcjet hardware and support. The testing was performed in the large space propulsion testbed at LeRC with an array of antennas for radiated EMI measurements installed. Spacecraft materials samples were arranged so that exposure to the plume would approximate on-orbit conditions. Detailed comparisons of pre- and post-test measurements of critical physical properties of the spacecraft materials samples showed that no significant degradation resulted from plume exposure during the test. Similarly, the effects of electrostatic discharge phenomena were found to be negligible. EMI levels in regions of interest to the commercial satellite user community were within acceptable limits. EMI above standard limits was still measured in low frequency ranges and this remains an open issue.

As noted above, new high performance propulsion systems often present non-standard interface issues which require unique treatments. Integration issues are a major concern to the aerospace community and these concerns are expected to grow as time passes and more invasive systems are considered. The LeRC program will continue to develop the tools and testbeds required to identify and address critical integration concerns.

1. Bennett, G. L., et al., "An Overview of NASA's Electric Propulsion Program," IEPC-93-006, September 1993.

2. Curran, F. M., et al., "The NASA Low Thrust Propulsion Program," AIAA-92-3703, July 1993.

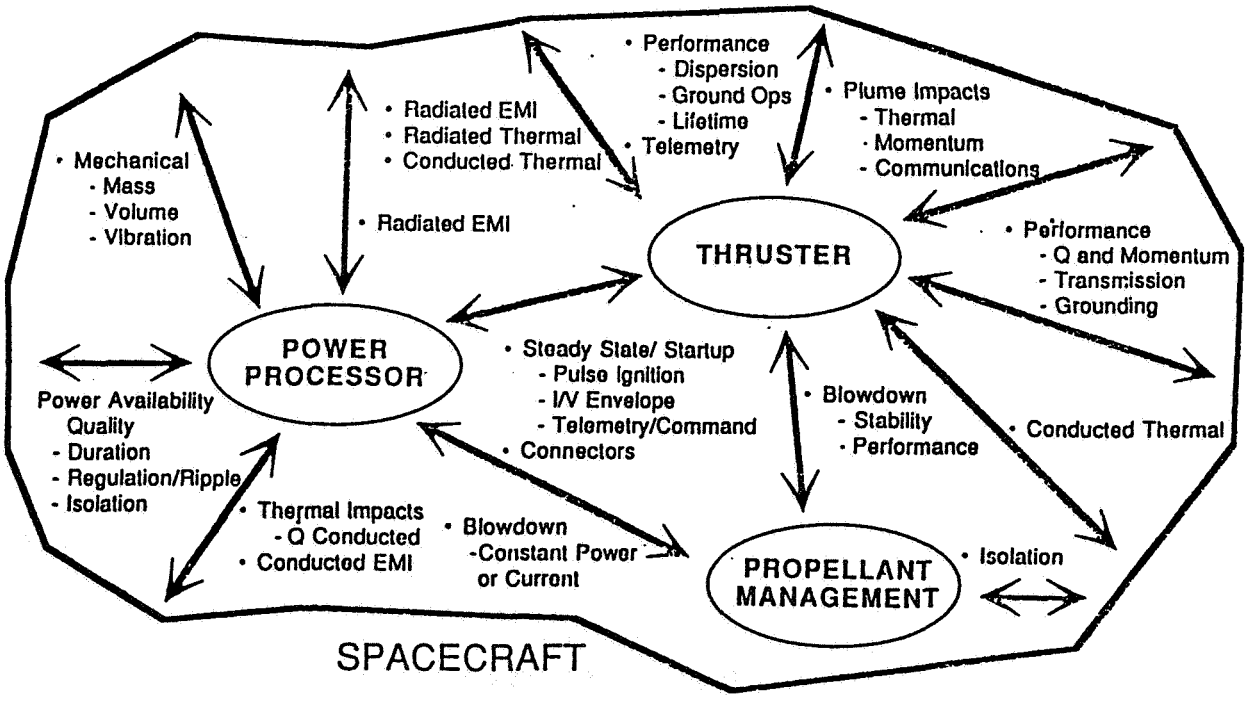

Figure 1. Arcjet System/Spacecraft Interrelationships.

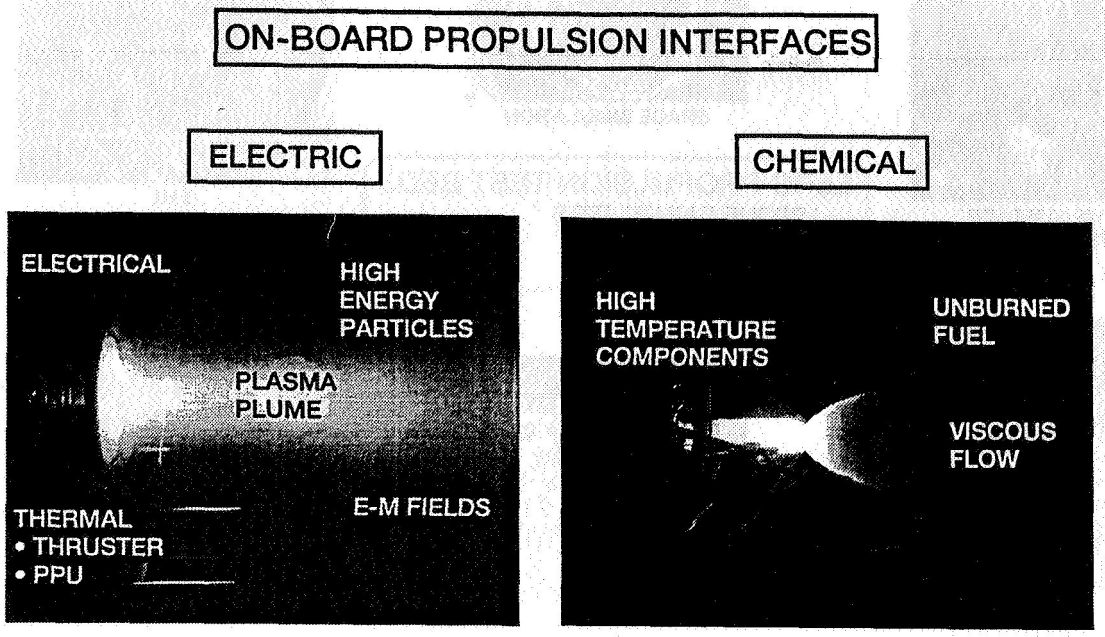

Figure 2. Interface Issues Unique to High Performance Propulsion Systems.

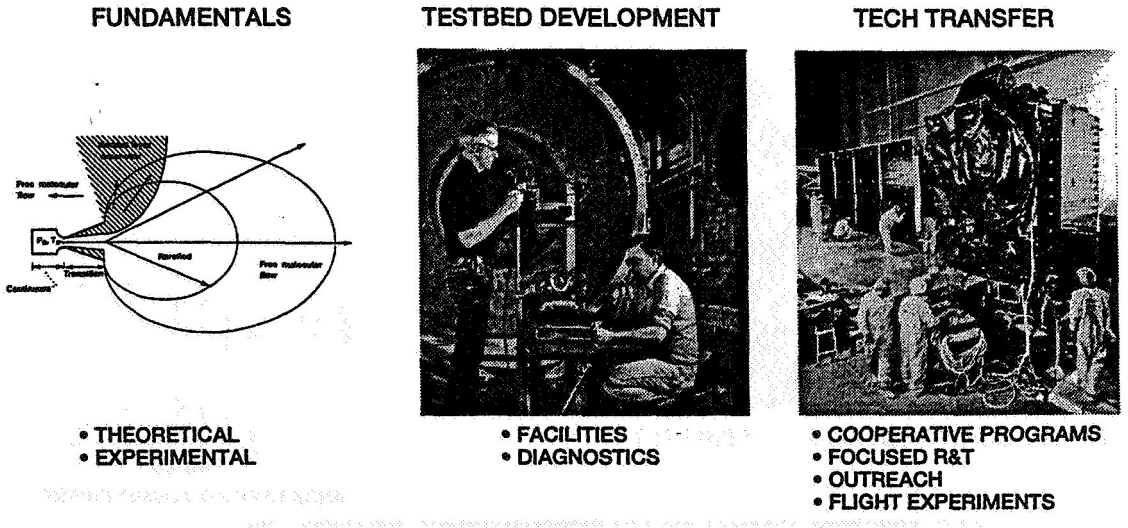

Figure 3. LeRC Spacecraft Integration Program.

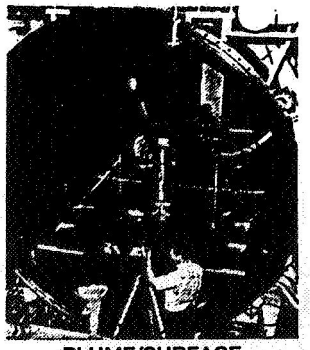

PLUME/SURFACE INTERACTIONS

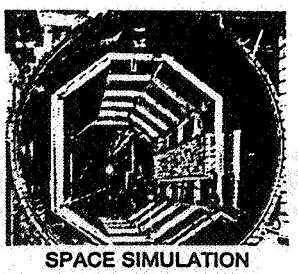

SPACE SIMULATION

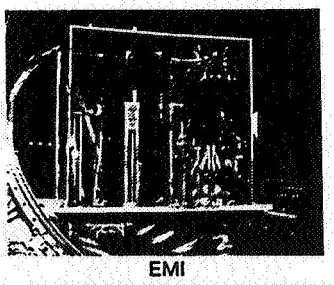

EMI

LeRC PROPULSION TEST BEDS
- UNIQUE CAPABILITIES
- ACCESSIBLE
- LOW COST

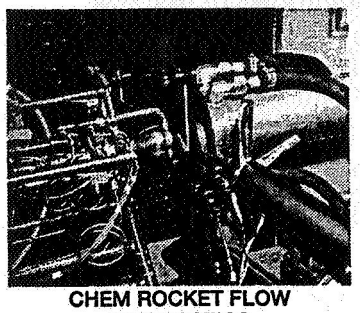

CHEM ROCKET FLOW DIAGNOSTICS

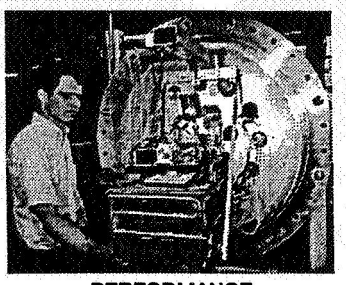

PERFORMANCE

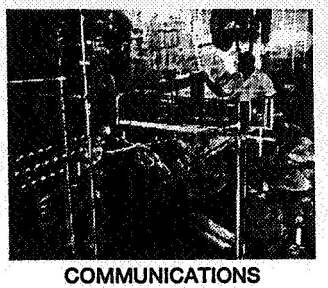

COMMUNICATIONS IMPACTS

Figure 4. Test Bed Capabilities at LeRC.

LERC–GE–RRC ARCJET COMPATIBILITY EVALUATION

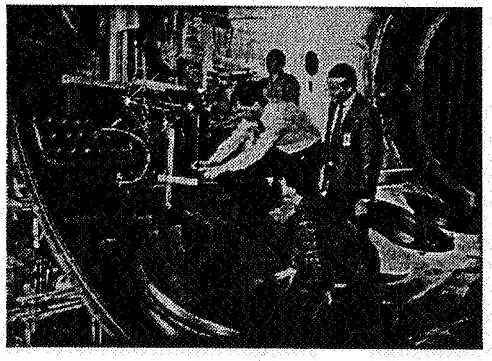

DIRECT EXPERIMENTAL ASSESSMENTS

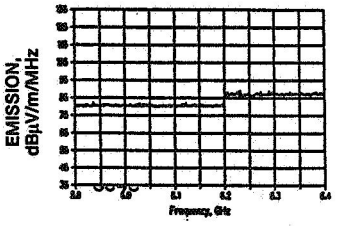

AMBIENT BROADBAND CONDITIONS

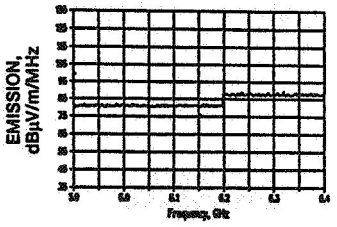

ARCJET/PPU BROADBAND EMISSIONS

- PLUME COMPATIBILITY WITH S/C DEMONSTRATED
  - RADIATED/CONDUCTED EMI
  - S/C CHARGING
  - CONTAMINATION/DEGRADATION
- REQUIRED FOR MAINTENANCE OF TELSTAR 4 DECISION

Figure 5. Joint Industry/NASA Cooperative Program Example.

427162
Pgs 5

N95-70880

COUPLING GRAVITY, ELECTROMAGNETISM AND SPACE-TIME FOR SPACE PROPULSION BREAKTHROUGHS

Marc G. Millis
NASA Lewis Research Center
Cleveland OH

SUMMARY:

Spaceflight would be revolutionized if it were possible to propel a spacecraft without rockets using the coupling between gravity, electromagnetism, and space-time (hence called "space coupling propulsion"). New theories and observations about the properties of space are emerging which offer new approaches to consider this breakthrough possibility. To guide the search, evaluation, and application of these emerging possibilities, a variety of hypothetical space coupling propulsion mechanisms are presented to highlight the issues that would have to be satisfied to enable such breakthroughs. A brief introduction of the emerging opportunities is also presented.

APPROACH:

Although studies have identified possible effects and theories related to the goal of space coupling propulsion [1-4], there is no problem definition against which to assess and augment this information. To correct this deficiency, a problem definition is derived from examining a variety of hypothetical propulsion mechanisms. These hypothetical mechanisms assume a priori that coupling propulsion is possible in order to illustrate the physics that would be required to make these mechanisms feasible. This is simply the first step of the Scientific Method: recognition and formulation of the problem.

HYPOTHETICAL PROPULSION MECHANISMS:

Fundamentally there are two different force producing mechanisms, collisions and interactions with fields. Analogies to these fundamental mechanisms are used to envision several different hypothetical propulsion mechanisms.

Propulsion using collisions: Conventional rocket propulsion is fundamentally based on the collisions between the propellant and the rocket. These collisions thrust the rocket in one direction and the propellant in the other. By definition, space coupling propulsion does not use propellant, so one must presuppose that space contains some form of reactive media. Assuming that there exists a media of momentum-carrying particles or waves throughout space, several propulsion mechanisms can be envisioned that induce propulsive forces using asymmetric collisions with these waves or particles, as depicted in figures 1 through 4.

Propulsion using fields: A second set of space coupling mechanisms is based on using fields. Electric fields accelerate charges and gravitational fields accelerate masses. For space coupling propulsion, one must presuppose that space contains properties from which fields can be

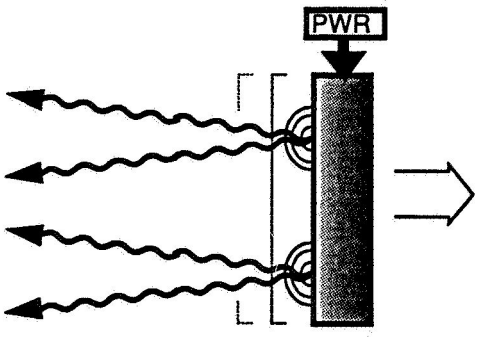

Figure 1: Radiation Emission Propulsion:
Analogous to the photon rocket, expulsion of momentum carrying waves creates propulsive forces.

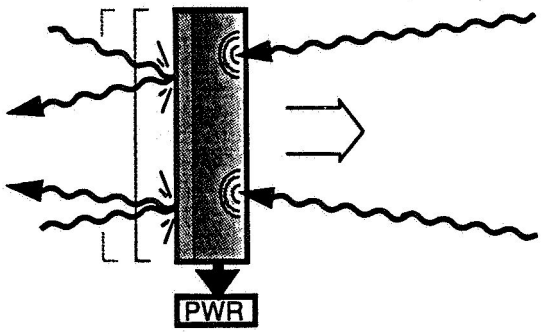

Fig. 2: Reflection/Absorption Propulsion:
Analogous to a radiometer vane, a net difference in radiation pressure exists across the reflecting and absorbing sides.

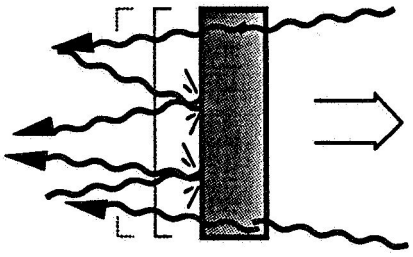

Fig. 3: Reflection/Transmission Propulsion:
Analogous to a diode, space radiation passes through one direction and reflects from the other, creating a net difference in radiation pressure.

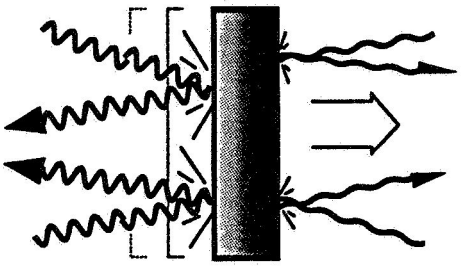

Figure 4: Differential Pressure Propulsion:
Analogous to creating a pressure gradient in a fluid, one side raises the media's intensity and the other lowers the intensity to create a net difference in radiation pressure.

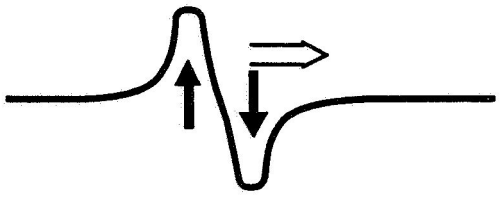

Figure 5: Differential Field Propulsion:
Analogous to a pressure gradient in a fluid, or to "negative mass propulsion" (ref. 17), a local field is induced in the otherwise flat scaler potential, resulting in gradient at the vehicle to produce thrust.

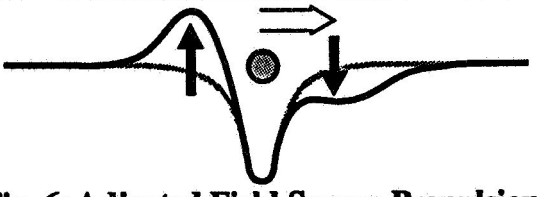

Fig. 6: Adjusted Field Source Propulsion:
Similar to differential field propulsion, this version assumes that a symmetric field is initially present and then adjusted asymmetrically to induce a gradient. This version evokes the need to describe fields as having an effective reaction mass.

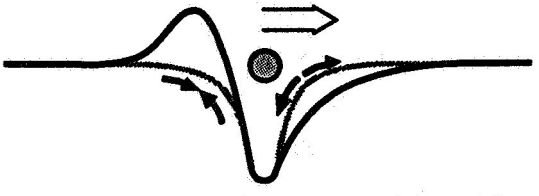

Figure 7: Asymmetric Tension Propulsion:
Almost identical to figure 6, this version assumes that the gradient is induced by altering the characteristics of space (Newton's constant G, or EM constants ε_0 or μ_0). This also evokes the issue of field reaction mass.

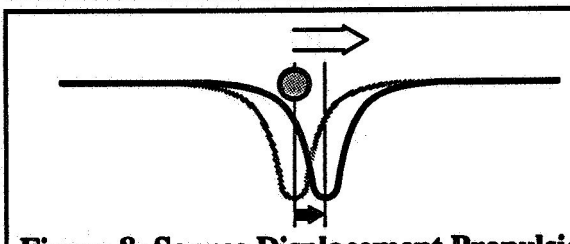

Figure 8: Source Displacement Propulsion:
This method assumes that a field's source is a separate entity from that which reacts to the field and that it has no inertia. By sustaining a displacement of the source from the reactant, the reactant accelerates.

induced, and in particular, that *controllable asymmetric fields* can be induced across the vehicle, and that these asymmetric fields can be *carried along with the vehicle* as the vehicle is propelled. Several examples are depicted in figures 5 through 8.

A critical and guiding issue with field propulsion is conservation of momentum. For field propulsion, the fields themselves must act as the reaction mass. This is difficult to conceptualize. To consider gravitationally flat space as a reaction mass, for example, a formalism of Mach's Principle or some other formalism which assigns an effective reaction mass to the scalar potential is required. Such formalisms do not yet exist.

PROBLEM STATEMENT:

From the hypothetical mechanisms, several common issues are revealed: (1) The space vacuum must contain something that can act as a reaction mass that satisfies these conditions; (a) must have an equivalent mass density sufficient to be used as a reaction mass, (b) must be available equally across all space and in all directions, and (c) must be tangible. (2) A coupling mechanism must exist with a property of space satisfying the above conditions and which satisfies these conditions; (a) must be able to induce asymmetric reaction forces, (b) must be controllable, (c) must be sustainable, (d) must be effective enough to propel the vehicle, and
(e) must satisfy conservation of energy and momentum.

The above is a checklist for evaluating or envisioning space coupling propulsion concepts.

EMERGING POSSIBILITIES:

Properties of space: Although the vacuum is generally thought to be empty, there are several known properties that are indicative of reactive media. These include the Cosmic Background Radiation[5] (figure 9), Zero Point Electromagnetic radiation[6] (figure 10), virtual pairs[7] (figure 11), dark matter[8] and the very-low-density intergalactic gas[9] (estimated to be only 10^{-28} g/cm^3). Based on the existence of gravitational and electromagnetic fields, it is reasonable to assume that space contains properties from which fields can be induced. It is also possible to consider the media in space as a property from which "pressure" fields can be induced.

Coupling mechanisms: Using the formalism of General Relativity, it has been confirmed that electromagnetism and gravity are coupled[9] (figure 12), but it is not yet known how to use these couplings for propulsion. It has been suggested that an intense magnetic field would induce accelerations[10], and it has been suggested that by warping the space-time metric, faster-than-light travel may be possible using a mechanism similar to that of figures 6 or 7[11].

Also, new theories are emerging that suggest alternative couplings between gravity and electrodynamics. These include theories that define inertia and gravity in terms of Zero Point Energy[12, 13] and alternative derivations of Maxwell equations that include mass terms[1, 14].

In addition to theories, there are some unusual experimental observations that also hint of unexplored couplings between mass and electromagnetics[15, 16].

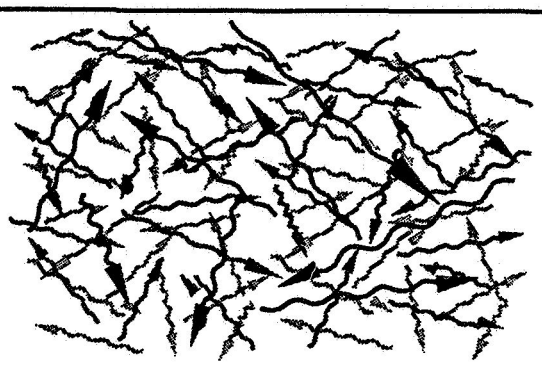

CBR Characteristics:

- Isotropic electromagnetic radiation
- Blackbody spectrum
- Velocity variant spectrum
- Peak frequency $\approx 2\times10^{2}$ GHz
- Mass energy density $\approx 10^{-34}\ g/cm^3$

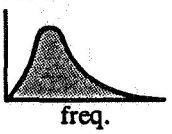

Figure 9: Cosmic Background Radiation

Presumed to be the residual thermal energy of the Big Bang, a blackbody spectrum of microwaves exists throughout all space. Coincident with the mean rest frame of the universe, this media constitutes an absolute reference frame. Velocity can be measured relative to this frame by measuring Doppler shifts fore and aft.

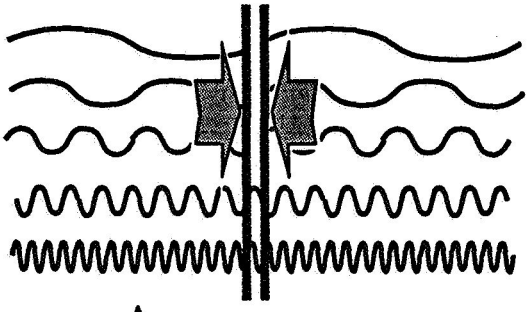

$F \propto A/d^4$

$F(A=1cm^2, d=0.5\mu m) = 0.2$ mg

ZPE Characteristics:

- Isotropic electromagnetic radiation
- Cubic frequency spectrum
- Lorentz invariant spectrum
- Cut-off frequency $\approx 10^{33}$ GHz
- Mass energy density $\approx 10^{54 \pm 38}\ g/cm^3$
- ZPE = $\frac{1}{2}\ h \times$ freq.
- Affects absolute zero, $T_{0Earth} = 4\times10^{-20}$ °K

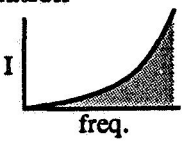

Figure 10: Casimir Effect as Evidence of Zero Point Energy

Two parallel conducting plates will attract each other when closely spaced because more electromagnetic modes exist outside than are allowed between, resulting in a net radiation pressure forcing the plates together. The electromagnetic background that gives rise to this effect is Zero Point Energy (ZPE), a consequence on the non-zero energy of the lowest energy state of a harmonic oscillator, theoretically equal to the frequency times half Planck's constant. ZPE is also evidenced by the Lamb shift and deviations from classical heat of vaporizations for cryogens near absolute zero. (ZPE of solid H = 200 cal/mole, for solid He = 50 cal/mole)

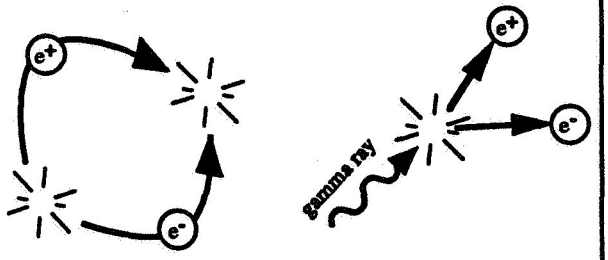

Figure 11: Virtual Pairs

Empty space is theorized to contain a sea of spontaneously created and annihilated electron-positron pairs. Gamma ray decay into pairs can be interpreted as corroborating physical evidence.

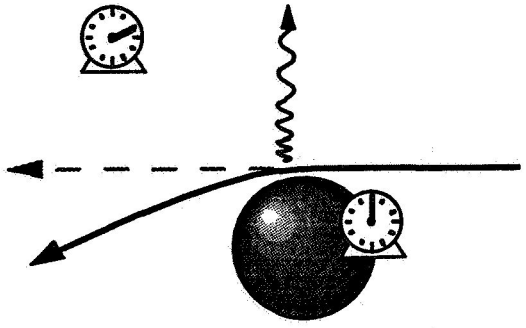

Figure 12: General Relativity

Gravity bends light, red-shifts light, and slows time.

CLOSING REMARKS:

Given the hypothetical examples, problem statement, and emerging evidence, a next step toward seeking this propulsion breakthrough is to compare the emerging physics with the problem statement and then to suggest areas warranting further investigation.

REFERENCES:

1. Cravens, D. L., *Electric Propulsion Study*, AL-TR-89-040, Air Force Astronautics Lab, (Aug 1990).

2. Forward, R., *21st Century Space Propulsion Study*, AL-TR-90-030, Air Force Astronautics Lab, (Oct 1990).

3. Evans, R. A., *BAe University Round Table on Gravitational Research*, (DCAF 070093), (Nov 1990).

4. Mead, F. ,Jr., et al, *Advanced Propulsion Concepts - Project Outgrowth*, AFRPL-TR-72-31, (JUN 1972).

5. Muller, R. A., **"The Cosmic Background Radiation and the new Aether Drift"**, In *Scientific American*, Vol. 238, N. 5, p. 64-74, (May 1978).

6. Boyer, T. H., **"The Classical Vacuum"**, In *Scientific American*, p. 70-78, (Aug 1985).

7. Von Baeyer, H. C., **"Vacuum Matters"**, In *Discover*, Vol. 13, No. 3, p. 108-112, (March 1992).

8. Krauss, L. M., **"Dark Matter in the Universe"**, In *Scientific American*, p. 58-68, (Dec 1986).

9. Misner, C. W., Thorne, K. S., and Wheeler, J. A., *Gravitation*, W.H.Freeman & Co., New York (1973).

10. Minami, Y., **"Space Strain Propulsion System"**, In *Proceedings of the Sixteenth International Symposium on Space Technology and Science, Sapporo, 1988*, p. 125-136, (MAY 1988).

11. Alcubierre, M., **"The warp drive: hyper-fast travel within general relativity"**, In *Classical and Quantum Gravity*, Vol 11, p. L73-L77, (1994).

12. Haisch, B., Rueda, A., & Puthoff, H. E.,**"Inertia as a Zero-Point Field Lorentz Force"**, In *Physical Review A*, Vol. 49, No. 2, p. 678-694, (FEB 1994)

13. Puthoff, H. E., **"Gravity as a zero-point-fluctuation force"**, In *Physical Review A*, Vol. 39, N. 5, p. 2333-2342, (Mar 1, 1989).

14. Williams, P. E., (US Navy), *The Possible Unifying Effect of the Dynamic Theory*, LA-9623-MS, Los Alamos Scientific Laboratory, New Mexico 87545, UC-34, Univ. of California, (May 1983).

15. Saxl, E. J., **"An Electrically Charged Torque Pendulum"**, In *Nature*, Vol. 203, N. 4941, p. 136-138, (JULY 11, 1964).

16. Woodward, J. F., **"A Stationary Apparent Weight Shift From a Transient Machian Mass Fluctuation"**, In *Foundations of Physics Letters*, Vol. 5, No. 5, p. 425-442, (1992).

17. Bondi, H., **Negative Mass in General Relativity**, In *Reviews of Modern Physics*, Vol. 29, No. 3, p 423-428, (July, 1957).

427164 Pgs 5 | N95-70881

ANTIPROTON CATALYZED MICROFISSION/FUSION PROPULSION

Pi-Ren Chiang, Raymond A. Lewis and Gerald A. Smith
Department of Physics
and
Richard Newton
Department of Nuclear Engineering
and
James Dailey and W. Lance Werthman
Department of Aerospace Engineering
and
Suman Chakrabarti
Department of Mechanical Engineering
PENNSYLVANIA STATE UNIVERSITY
303 Osmond Laboratory, University Park, PA 16802

ABSTRACT

Inertial confinement fusion (ICF) utilizing an antiproton catalyzed hybrid fission/fusion target is discussed as a potential energy source for interplanetary propulsion. A proof-of-principle experiment underway at Phillips Laboratory, Kirtland AFB, and antiproton trapping experiments at CERN, Geneva, Switzerland, are presented. The ICAN propulsion concept is described and results of performance analyses are reviewed. Future work to further define the ICAN concept is outlined.

I. INTRODUCTION

Inertial confinement fusion (ICF) can provide thrust and high Isp for propulsion applications from plasma created in antiproton-catalyzed microexplosions. The antiproton induced ignition of fission reactions under conditions of high compression has been described previously (Lewis 1991). Here we provide an overview of the full microfission/fusion concept, including a proof-of-principle experiment at the Phillips Laboratory to demonstrate subcritical antiproton-catalyzed microfission. Recent advances made by our group in the trapping of antiprotons are reviewed as well. The ICAN propulsion concept is discussed with regard to its features and performance, and our future work is outlined.

II. ANTIPROTON-CATALYZED MICROFISSION/FUSION

In 1992 large fission and neutron yields from antiproton annihilation at rest in a natural uranium target were observed (Chen et al. 1992). Calculations indicate that short bursts of

antiprotons could induce temperatures of several keV in a small compressed pellet. These conditions are appropriate for ignition of a hydrogen fusion burn within the microsphere. Targets with yields up to 100 GJ have been considered (Kanzleiter 1991). Compression is provided by light ion beams, such as from PBFA-2 (VanDevender and Cook 1986).

A proof of principle experiment at the SHIVA Star facility at the Phillips Laboratory, Kirtland AFB, is underway to demonstrate subcritical neutron multiplication due to antiproton fission in targets compressed to 10-40 Mbar pressure. Antiprotons are released from a Penning trap storage device, accelerated to 1.2 MeV by a radiofrequency quadrupole (RFQ), and focused onto the compressed target inside and imploding solid liner driven by the SHIVA Star capacitor bank. Figure 1 shows a close up of the target region, indicating the liner moving in rapidly and compressing a hydrogen working fluid. A short 50 ns burst of antiprotons ignites the target as it reaches peak compression.

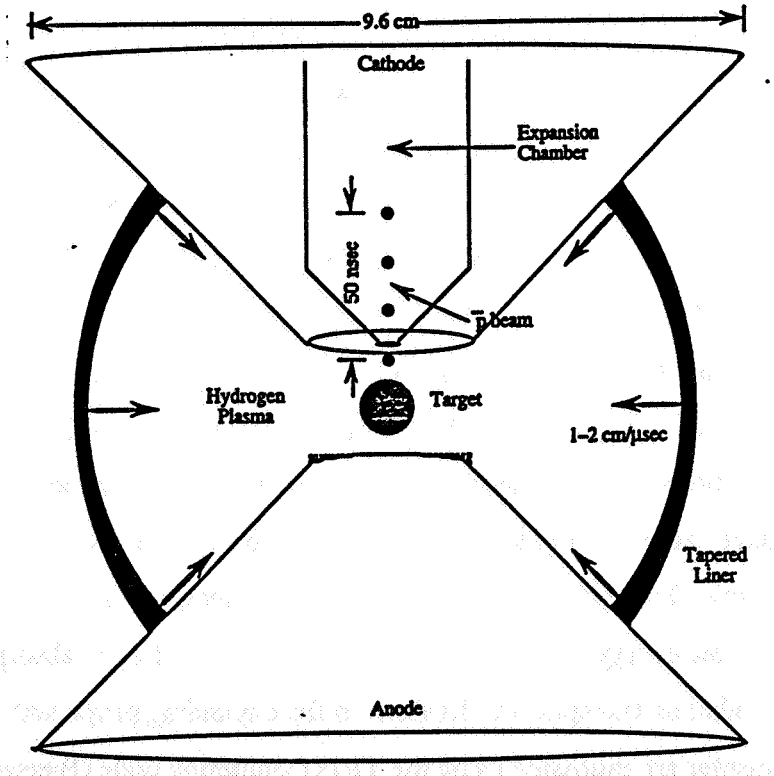

Figure 1. Solid Liner during Compression Cycle

III. ANTIPROTON TRAPPING EXPERIMENTS

In collaboration with the P-15 group at Los Alamos National Laboratory (Holzscheiter et. al., 1993), in July, 1993 we trapped up to 721,000 antiprotons from single beam shots at the Low

Energy Antiproton Ring (LEAR) at CERN. Figure 2 shows the Catcher Trap and transfer optics to the Portable Trap. With improved vacuum, using multipulse injection and electron cooling in the catcher trap we hope to trap and confine several milliion antiprotons before the end of 1994.

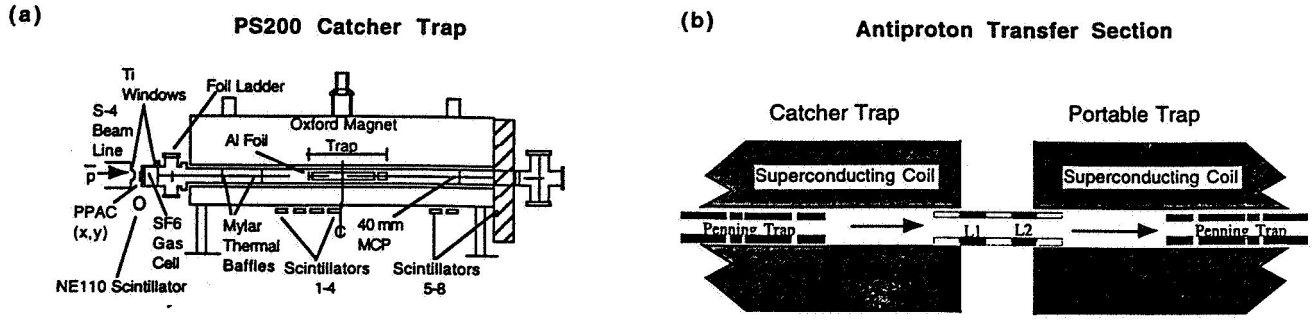

Figure 2. Schematics of (a) Catcher Trap and (b) Transfer Optics to the Portable Trap

IV. ICAN PROPULSION SYSTEM

The ICAN propulsion concept envisioned by our group is a derivative of the MEDUSA canopy concept proposed by Solem (1994), which is itself a variant of the ORION pusher plate system (Augenstein 1991). In the ICAN concept, a large, hemispherical canopy two km in radius is used to intercept debris from the explosion, transferring its momentum to the spacecraft via the expansion and contraction of the canopy, which serves as the shock absorber necessary to smooth out the acceleration. A detailed version of the canopy is shown in Figure 3, where we have used titanium for the canopy because of its high operating temperature and tensile strength.

The principle concerns associated with the ICAN system are momentum transfer to the canopy from the high energy propellant ions, along with the associated performance and sputtering damage, the radiation damage caused by neutrons and x-rays reradiated by the expanding propellant, and canopy heating. To assist us in investigating these issues, several computer codes have been developed to simulate energy release in the microfission/fusion target, absorption by the propellant, and MHD and radiation transport mechanisms in the expanding propellant. Canopy damage and momentum transfer are evaluated using the TRIM sputtering code (Biersack and Eckstein, 1984).

We have chosen as a prototypical target one which releases 98 GJ of energy. This energy is produced in a target consisting of a bout 1.0 g of nuclear fuel. The nuclear fuel is in a molar ratio of 9:1 of DT:U. Initially, the proportions of energy produced in the target are 83% radiation,

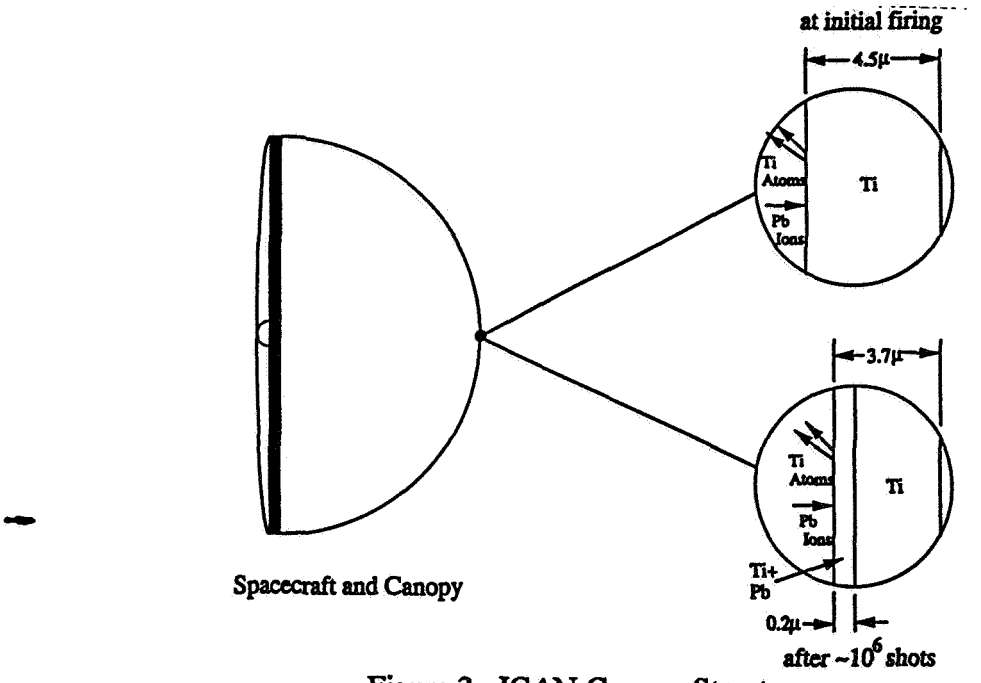

Figure 3. ICAN Canopy Structure

15% neutron kinetic energy, and 2% random ion and electron kinetic energy. A high Z propellant, lead, was chosen due to its high absorption cross-section with respect to the radiation generated by the ICAN target.

Accurate simulation of the propellant expansion process following the deposition of this energy requires a sophisticated model, including an accurate equation-of-state, a radiation transport model, and a thermal conduction model. Our Plasma Propulsion Dynamics (PPDYN) code utilizes a single-temperature radiation model in a one-dimensional MHD code to determine the amount of energy deposited in the propellant. Analysis of the propellant performance yielded the thrust and Isp curves shown in Figure 4, as a function of the propellant mass per shot. A clear tradeoff exists between thrust and Isp, which plays a significant role in mission analysis.

V. FUTURE WORK

We are presently working to expand the capabilities of our plasma propulsion dynamics code to allow analysis of alternate propellants and mixtures of propellants in an effort to enhance performance and decrease canopy damage. In addition, we have begun analyzing various mission scenarios which utilize the high-Isp, low thrust ICAN system. Alternative canopy structures and materials also need to be considered in order to minimize sputtering damage and maximize system performance.

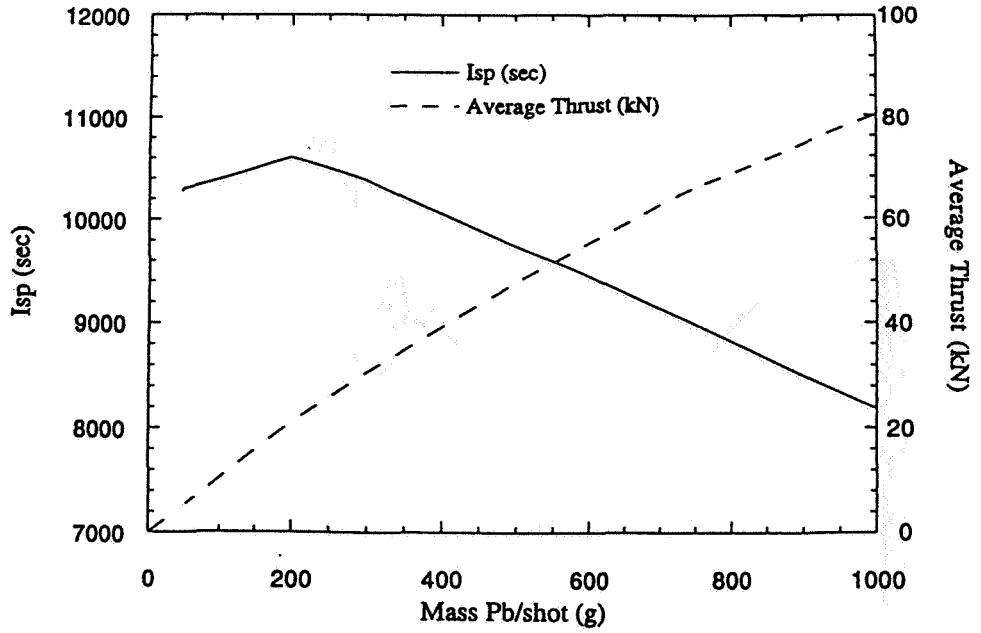

Figure 4. Thrust and Isp vs. Propellant Mass at 1 Hz Firing Rate

VI. ACKNOWLEDGMENTS

This work is supported in part by AFOSR, Jet Propulsion Laboratory, NSF, Penn State Center for Space Propulsion Engineering, grant #NAGW-1356 (suppl.8), and Rocketdyne Division, Rockwell International Corporation.

VII. REFERENCES

Augenstein, B.W. (1991) "Some Aspects of Interstellar Space Exploration-New Orion Systems, Early Precursor Missions", (IAA-91-716, 42nd Congress of the International Astronautical Federation, Oct. 5-11, 1991, Montreal, Canada.

Biersack, J.P., and W. Eckstein (1984) Appl. Phys. A34: 73.

Chen, B., T.A. Armstrong, R.A. Lewis, R. Newton, G.A. Smith, J.P.l Bocquet, F. Malek, H. Nifenecker, M.Maurel, E. Monnand, P. Perrin, C. Ristori, G. Ericsson, T. Johansson, G. Tibell, M. Rey-Campagnolle, S. Polikanov, T. Krogulski, and J. Mougey (1992) Phys. Rev. C45: 2332-2337.

Holzscheiter, M., R.E.Brown, J.B. Camp, S. Cornford, T. Darling, P. Dyer, T. Goldman, S. Hoibraten, K. Hosea, R.J. Hughes, N. Jarmie, R.A. Kenefick, N.S.P. King, D.C. Liaon, M.M. Nieto, M.M. Midzor, S.P. Parry, J. Rochet, R.A. Ristinen, M.M. Schauer, J.A. Schecker, and R.C. Witteborn (1993) Nucl. Phys. A558: 709c-718c.

Kanzleiter, R.J. "Thermodynamics of Nuclear Reactions Initiated by Antiproton Annihilations" (1991) M.S. Thesis, Penn State University.

Lewis, R.A. et al. (1991) Nucl. Sci. & Eng. 109:411-415

Solem, J. (1994) JBIS 47: 229-238.

VanDevender, P., and D.L. Cook (1986) Science 232: 831-836.

N95-70882

THE NASA-JPL ADVANCED PROPULSION PROGRAM

42716 8
pg 8

Presentation to the
Pennsylvania State University
Propulsion Engineering Center
Sixth Annual Symposium
NASA Lewis Research Center
Cleveland Ohio
September 13-14, 1994

JPL

Robert H. Frisbee

Jet Propulsion Laboratory
California Institute of Technology
Pasadena California

JPL

ABSTRACT

The NASA Advanced Propulsion Concepts (APC) program at the Jet Propulsion Laboratory (JPL) consists of two main areas. The first involves cooperative modeling and research activities between JPL and various universities and industry; the second involves research at universities and industry that is directly supported by JPL. The cooperative research program consists of mission studies, research and development of ion engine technology using C60 (Buckminsterfullerene) propellant, and research and development of lithium-propellant Lorentz-force accelerator (LFA) engine technology. The university / industry - supported research includes research (modeling and proof-of-concept experiments) in advanced, long-life electric propulsion, and in fusion propulsion.

These propulsion concepts were selected primarily to cover a range of applications from near-term to far-term missions. For example, the long-lived pulsed-xenon thruster research that JPL is supporting at Princeton University addresses the near-term need for efficient, long-life attitude control and station-keeping propulsion for Earth-orbiting spacecraft. The C60-propellant ion engine has the potential for good efficiency in a relatively low specific impulse (Isp) range (10,000 - 30,000 m/s) that is optimum for relatively fast (< 100 day) cis-lunar (LEO/GEO/Lunar) missions employing near-term, high-specific mass electric propulsion vehicles. Research and modeling on the C60-ion engine is currently being performed by JPL (engine demonstration), Caltech (C60 properties), MIT (plume modeling), and USC (diagnostics). The Li-propellant LFA engine also has good efficiency in the modest Isp range (40,000 - 50,000 m/s) that is optimum for near- to mid-term megawatt-class solar- and nuclear-electric propulsion vehicles used for Mars missions transporting cargo (in support of a piloted mission). Research and modeling on the Li-LFA engine is currently being performed by JPL (cathode development), Moscow Aviation Institute (engine testing), Thermacore (electrode development), as well as at MIT (plume modeling), and USC (diagnostics). Also, the mission performance of a nuclear-electric propulsion (NEP) Li-LFA Mars cargo vehicle is being modeled by JPL (mission analysis; thruster and power processor modeling) and the Rocketdyne Energy Technology and Engineering Center (ETEC) (power system modeling). Finally, the fusion propulsion research activities that JPL is supporting at Pennsylvania State university (PSU) and at Lawrenceville Plasma Physics (LPP) are aimed at far-term, fast (< 100 day round trip) piloted Mars missions and, in the very far term, interstellar missions.

JPL

OUTLINE

- Overview of the NASA-JPL Advanced Propulsion Concepts (APC) Program
- Cooperative Research Activities with University / Industry
  - Mission Studies
  - C60-Propellant Ion Thruster
  - Li-Propellant Lorentz Force Accelerator (LFA)
- University / Industry – Supported Research
  - Advanced Long-Life Electric Propulsion
  - Fusion
- Summary

JPL

APC PROGRAM

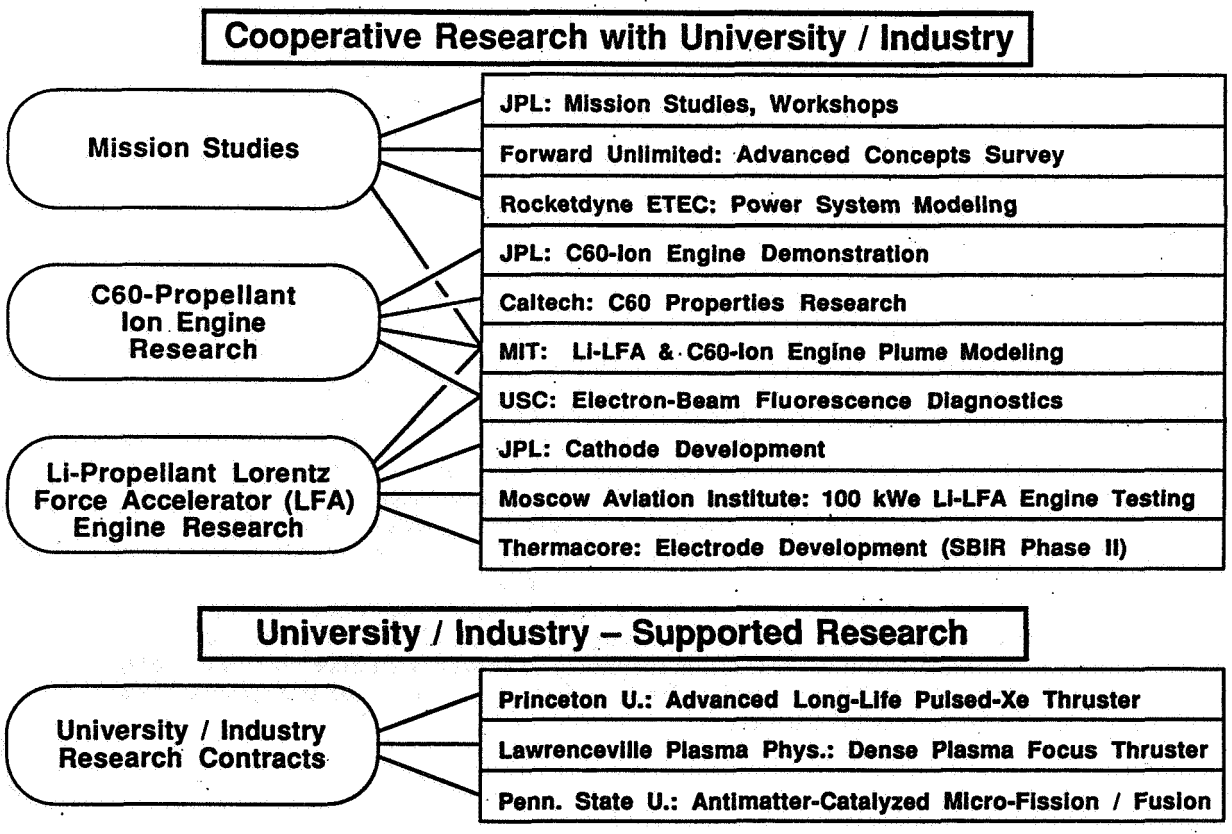

JPL SELECTION CRITERION REQUIRED TO DOWN-SELECT AMONG MANY COMPETING EP CONCEPTS

• Performance which offers unique capabilities for a well defined class of missions

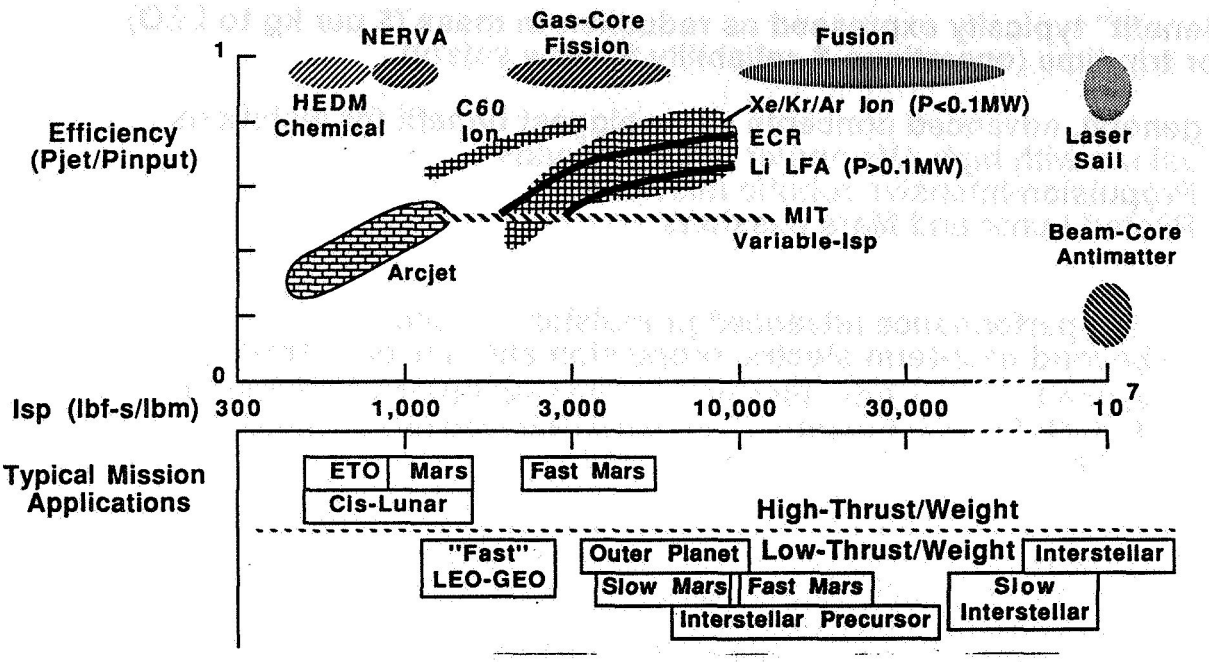

JPL SELECTION CRITERIA

Concepts / Criteria	Adv. Long-Life EP	C60-Ion	Li-LFA	Fusion
Must have projected performance which offers unique capabilities for a well defined class of missions	Very long-life attitude control, station-keeping	Good eff. in Isp range optimum for "fast" (< 100 day), high-specific mass EP near-Earth (LEO/ GEO/Lunar) missions	Good eff. in Isp range optimum for high-power (>1 MWe), high-specific mass EP Mars missions	"Fast" (< 100 day R.T.) piloted Mars missions; interstellar missions
Must use an environmentally acceptable propellant (no Hg, etc.)	Xe	C60 (Spacecraft contamination)	Li (Spacecraft contamination)	Some tritium, negligible amount of antiprotons
Must be an area where small amounts of funding can have a large impact, especially with co-funding from other agencies		Leverage funding from AFOSR, Caltech Pres. Fund	Leverage funding from DoE (SP-100) Leverage Russian expertise	Leverage funding from AFPL, AFOSR

NEAR-TERM ⟹ FAR-TERM

JPL

INTRODUCTION TO MISSION STUDIES

- "Mission Studies" is a generic term for feasibility analyses aimed at assessing the "benefit" of an advanced propulsion concept
  - "Benefit" typically expressed as reduction in mass ($ per kg to LEO) or trip time (operations & reliability $, crew safety)
  - In general, advanced concepts show biggest benefit for ambitious missions with high ΔVs and/or large payloads
    - Propulsion-intensive robotic missions
    - Piloted Lunar and Mars missions

- Assess high-performance advanced propulsion concepts (Those beyond near-term electric propulsion and fission thermal)
  - Advanced NEP & SEP
  - Adv. Chemical
  - Adv. Fission
  - Fusion
  - Antimatter
  - Beamed Energy / Momentum
  - ET Resources
  - Others

- Use results of mission studies to guide technology programs :
  - High-leverage / critical technologies
  - Long-lead time technologies
  - Critical feasibility / proof-of-concept experiments

JPL

SP-100 / Li-LFA NEP MASS vs TRIP TIME FOR MARS CARGO MISSIONS

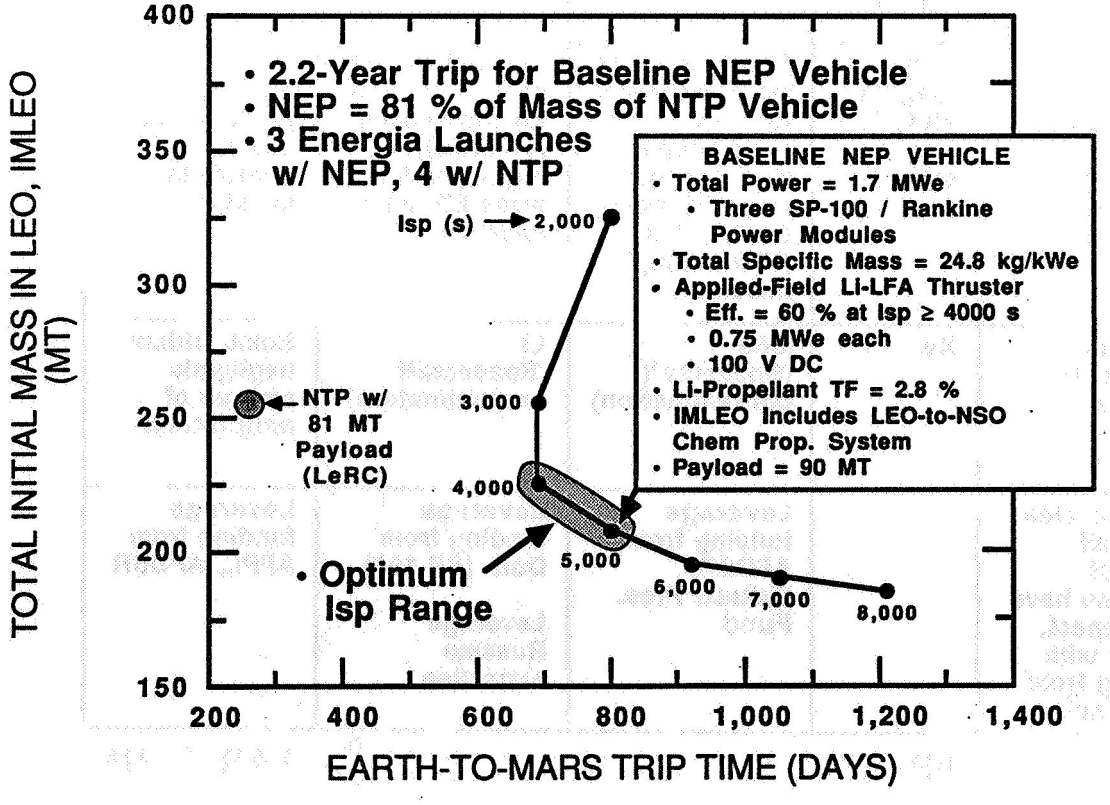

Li LORENTZ FORCE ACCELERATORS OFFER HIGH PERFORMANCE AND EXTENDED LIFETIME

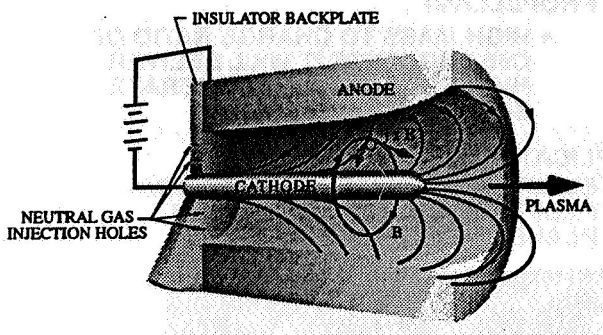

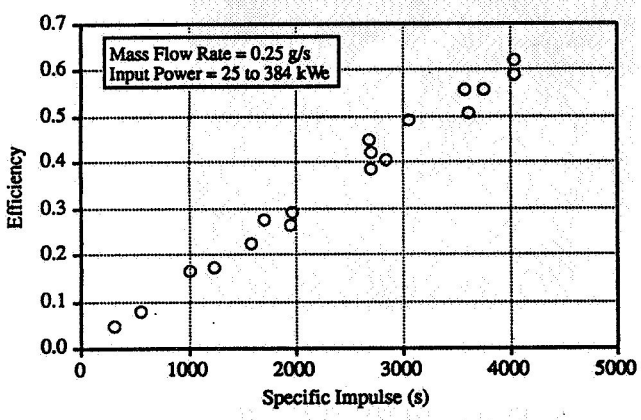

- Use of electromagnetic body forces to accelerate a quasineutral plasma permits very high power processing capability (100's of kW to MW in a single engine)
- The low ionization potential of Li propellant results in very high efficiencies at high specific impulses
- Tungsten cathodes have low operating temperatures with Li propellant because Li adsorbed on tungsten significantly reduces the work function of the surface
- Li condenses on vacuum chamber walls at room temperature, resulting in significantly reduced pumping requirements and lower ground test costs
- Primary technical issues:
  - Verification of high performance
  - Demonstration of adequate engine life
  - Potential for spacecraft contamination

ADDRESSING THE KEY TECHNICAL ISSUES IN LFA TECHNOLOGY

- Li thruster peformance characterization at the Moscow Aviation Institute
  - First NASA-funded contract for electric propulsion with a Russian institute initiated June 1994
  - The research will provide detailed characterization of a 100 kWe-class Li thruster with a performance goal of 45% at 4000 s
- Examination of the potential for spacecraft contamination
  - Li backflow calculated for a high power thruster using a plume model developed by the Space Power and Propulsion Laboratory at MIT
  - Preliminary results indicate that spacecraft surface temperatures of 500-540 K are required to prevent bulk condensation and that plume shields can significantly reduce the Li flux to the spacecraft
- Characterization of life-limiting cathode failure mechanisms
  - Models of cathode erosion phenomena, cathode thermal behavior and near cathode plasma characteristics being developed at JPL
  - Experimental verification of model assumptions and predictions being performed in a dedicated high-current cathode test facility
- Development of cathodes for Li engines
  - Porous tungsten cathode and anode with integral Li vaporizers being developed by Thermacore, Inc. in a Phase II SBIR
  - Electrode testing to be performed by Princeton University

ELECTROSTATIC PROPULSION USING C60 MOLECULES

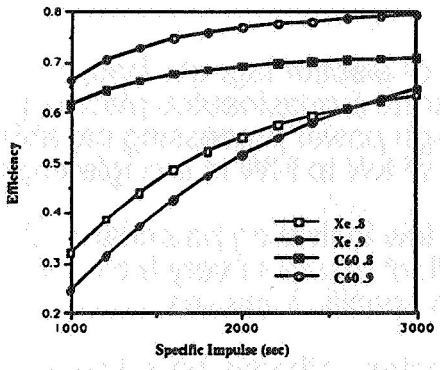

CALCULATED PERFORMANCE OF C60 AND XENON ION THRUSTERS FOR TWO PROPELLANT UTILIZATION EFFICIENCIES

OBJECTIVES:

- DEVELOP AN ELECTROSTATIC THRUSTER WHICH USES C60 AS A PROPELLANT
  - HIGH MASS TO CHARGE RATIO OF C60 SUGGESTS IT WILL DELIVER HIGH EFFICIENCY AT MODERATE SPECIFIC IMPULSE

APPLICATIONS:

- ELECTRIC THRUSTER FOR STATION KEEPING, ORBIT TRANSFER AND PLANETARY MISSIONS

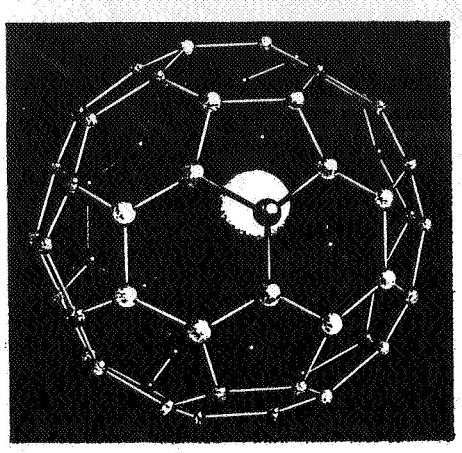

ACCOMPLISHMENTS:

- RADIO FREQUENCY AND ELECTRON BOMBARDMENT ION THRUSTERS BUILT AND OPERATED
- STUDIES OF C60 THERMAL PROPERTIES AND IONIZATION PHENOMENA CONDUCTED

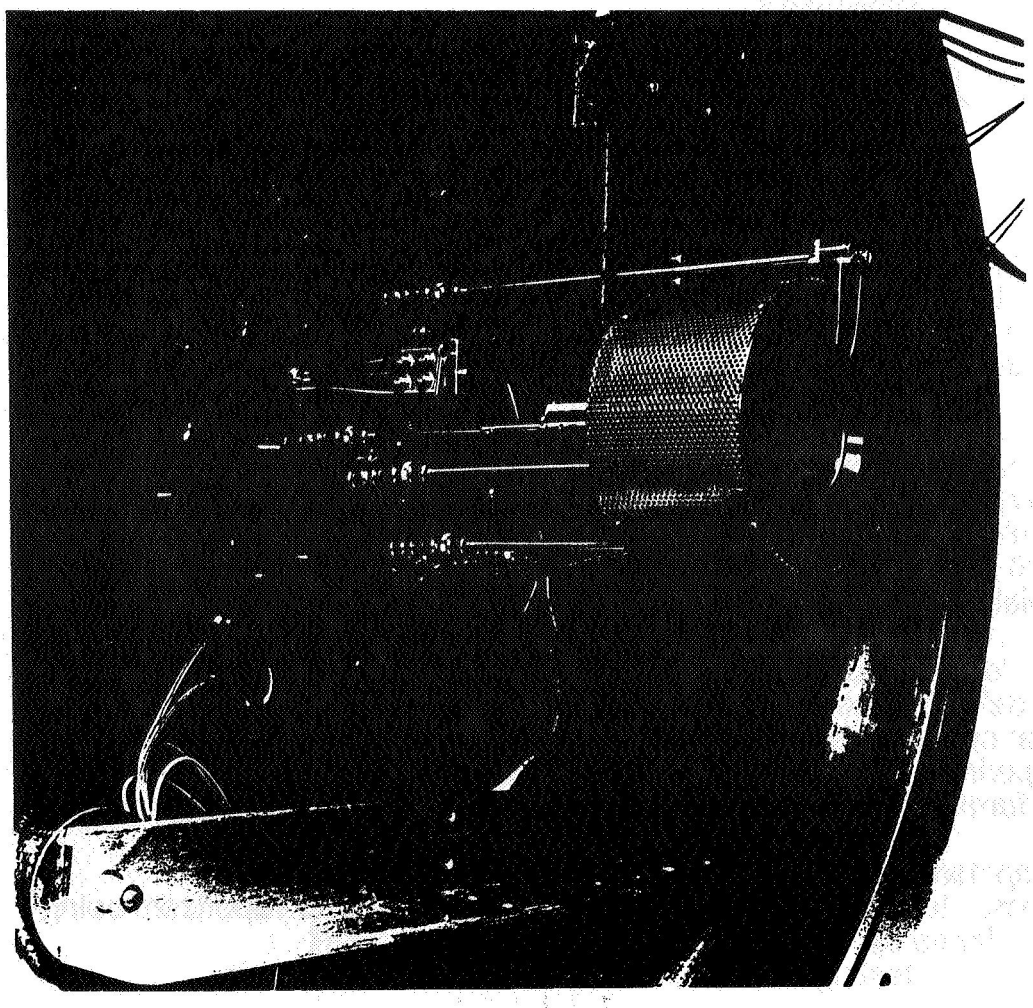

JPL INERTIAL CONFINEMENT FUSION (ICF) PROPULSION CAN ENABLE RAPID HUMAN EXPLOARATION OF THE SOLAR SYSTEM

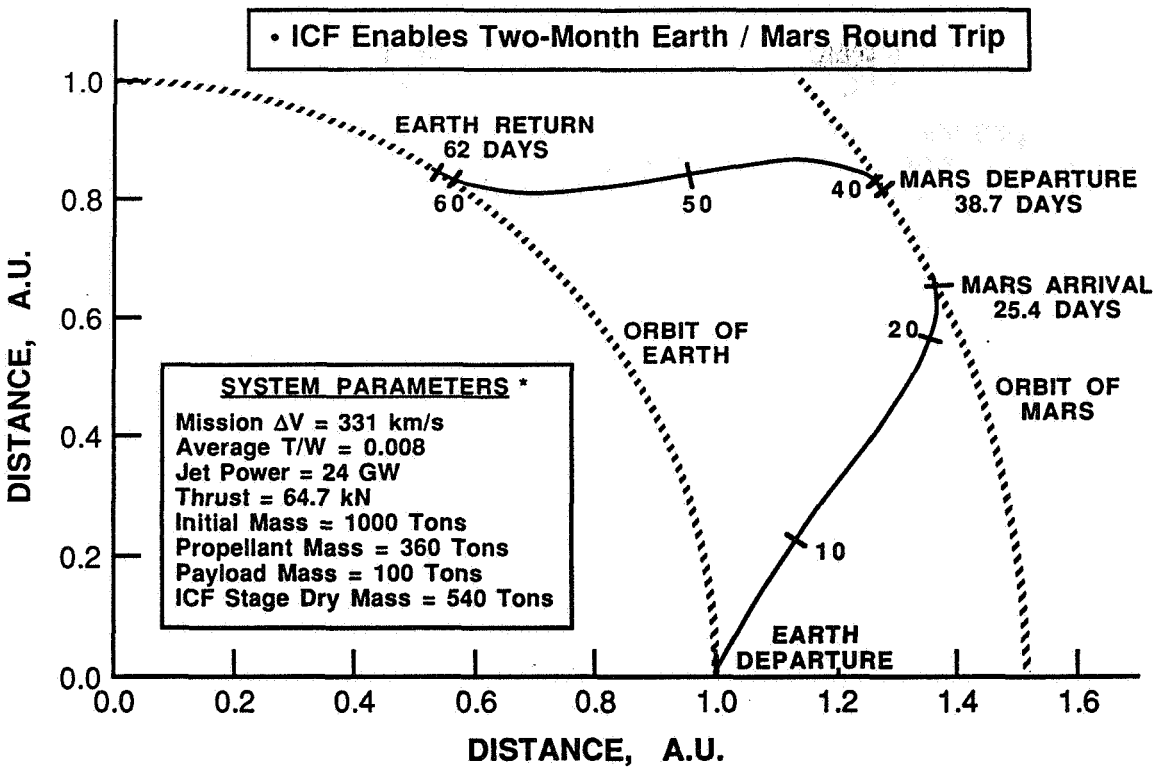

* Based on Joint JPL, LLNL, ETEC, JSC Study (VISTA ICF Concept)

JPL PENN STATE ANTIMATTER-CATALYZED MICRO-FISSION/FUSION PROPULSION

Concept Description

- Uranium (or Pu) enriched DT (or D-He3) pellet is compressed (by ions, lasers, etc.)
- At the time of peak compression, the target is bombarded with a small number (~10^8) of antiprotons to catalyze fission
- The fission energy release triggers a high-efficiency fusion burn to heat the propellant

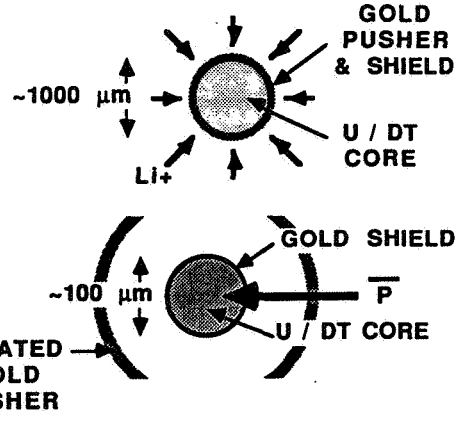

- The resulting expanding plasma is used to produce thrust

⇨

- Use a small amount of antimatter - an amount that we could produce with existing technology and facilities
- Retain mission benefits of "conventional" ICF
  - Potential benefits of "easier" drivers / aneutronic fuels

JPL

SUMMARY

- Current APC program contains a mix of near-term to far-term concepts in both cooperative and directly-supported university tasks

APPLICATION	COOPERATIVE	DIRECT-SUPPORT
Near-Term	C60 -Ion	Long-Life EP (Princeton)
Mid-Term	Li-LFA	
Far-Term		Fusion (PSU, LPP)

- Plans are to continue current activities and add (contingent on funding):
  - Transition from modeling to demonstration of LPP dense plasma focus thruster
  - Begin evaluation of alternate fusion driver / confinement concepts
  - Scale Princeton U. adv. long-life pulsed-Xe plasma thruster to micro-size

427170
Pgs 3

N95-70883

Magnetobraking: Use of Tether Electrodynamic Drag for Earth Return From Mars

Geoffrey A. Landis
NYMA, Inc.
NASA Lewis Research Center 302-1
21000 Brookpark Rd.,
Cleveland, OH 44135
(216) 433-2238
e-mail: GLANDIS@LERC.NASA.GOV

EXTENDED ABSTRACT

It has often been proposed that a vehicle returning from Mars will use aerobraking in the Earth's atmosphere to dissipate hyperbolic excess velocity to capture into Earth orbit. Here a different system for dissipating excess velocity without expenditure of reaction mass, magnetobraking, is proposed [1].

Magnetobraking uses the force on an electrodynamic tether in the Earth's magnetic field to produce thrust. An electrodynamic tether is deployed from the spacecraft as it approaches the Earth. The Earth's magnetic field produces a force on electrical current in the tether. If the tether is oriented perpendicularly to the Earth's magnetic field and to the direction of motion of the spacecraft, force produced by the Earth's magnetic field can be used to either brake or accelerate the spacecraft without expenditure of reaction mass. The peak acceleration on the Mars return is 0.007 m/sec^2, and the amount of braking possible is dependent on the density and current-carrying capacity of the tether, but is independent of length. A superconducting tether is required. The required critical current is shown to be within the range of superconducting technology now available in the laboratory.

Since energy is produced as the spacecraft velocity decreases, no on-board power source is required. A difficulty in magnetobraking is dissipating the energy produced. As the spacecraft approaches the Earth, the magnetic field increases and the power produced by the tether increases, reaching a maximum of about 800 W per kilogram of spacecraft mass at closest approach. If the tether current is decreased during closest approach, this peak can be reduced, at the cost of reducing the braking effectiveness.

The energy produced as the spacecraft crosses the Earth's magnetic field can be used, for example, to drive an electric-propulsion engine such as an ion engine or a pulsed-inductive thruster. The power densities produced by an electrodynamic tether in the Earth's magnetic field can be orders of magnitude higher than power densities produced by other means, and hence extremely effective electric propulsion is possible. Used together, an electrodynamic tether and electric propulsion could be the most effective solution for braking a returning Mars vehicle.

General principles of electrodynamic tethers are discussed in many references [2-5], and will not be reviewed here. There have been several demonstrations of tether operation in space. The experiment TSS-1 ("Tethered Satellite System-1), although it did not deploy to the full length, demonstrated controllability of a tether in space in the most critical regime of short tether lengths as well as verifying the VxB voltage expected by the conducting tether perpendicular to the Earth's magnetic field. The Delta-launched SEDS-1 ("Small Expendable Deployer-1") demonstrated full deployment using a simple friction-braked reel. The follow-on experiment demonstrated the plasma-contactor and the principle operational features of electrodynamic tether. Thus, all the required principles of tether technology have been demonstrated in orbit.

The calculation of the force on the magnetobraking tether is straightforward. (A more complete analysis can be found in the complete paper [1]. The force produced on a tether by the Earth's magnetic field is:

$$F = ILxB \tag{1}$$

where L is the length of the tether, I the current, and B the magnetic field. The Earth's magnetic field at a distance r from the surface can be expressed as:

$$B = B_0(R_e/r)^3 \tag{2}$$

R_e, the radius of the earth, is $6.4 \cdot 10^6$ m. The surface field B_0 is:

$$B_0 = 35\ \mu\text{Tesla}\cos(\lambda) \tag{3}$$

where λ = latitude from magnetic equator. Here we will assume that the spacecraft comes in along the magnetic equator, and hence $\lambda = 0$.

The values of current density and density will depend on the material used. The new "high temperature" (HT) superconductor materials are less well developed technically, but can be operated at temperatures of 77°K and higher, allowing the possibility of cooling by passive means in space. Superconductors are characterized by a maximum current density, known as the critical current. This is a function of the applied magnetic field and the temperature.

The most important value is the current density which has been obtained from material in the form of wires. $YBa_2Cu_3O_{7-x}$ (referred to as YBCO) is the most well-developed of the HT superconductor materials. In wire form, YBCO can be purchased with a critical current density (at 73°K) of 1000 A/cm^2. The density ρ of YBCO is 6.3 gr/cm^3. A somewhat less developed HT superconductor, Bi 2223 ($Bi_2Sr_2Ca_2Cu_3O$), can be purchased in strip form with a critical current density of 3500 A/cm^2 ($J = 3.5 \cdot 10^7$ amps/m^2) at 77°K. For currently available Bi 2223 superconductor strip, the specific current density LI/m ($=J/\rho$) is $5.5 \cdot 10^3$ amps-meters/kg. This is below the minimum specific current density needed for magnetobraking. Thus, high temperature superconducting materials now available in wire or strip form will not suffice for magnetobraking

However, both the achievable current densities and the technology for making HT superconductors in wire form is advancing rapidly. It is plausible that current densities now achieved in bulk material may in the near future be achievable in material manufactured into wires. At 77 °K, bulk YBCO has achieved currents over 10^8 amps/m^2. Other superconductor materials

have even higher critical currents. Critical current (at 77K) for HoBaCuO is $3 \cdot 10^{10}$ amps/m^2. If the HoBaCuO material could be made into wire form, it would have a specific current density of $4 \cdot 10^5$ amp-meter/kg, which is quite sufficient to achieve magnetobraking. To this mass, of course, would have to be added other elements of the system, including a method of handling the power produced, plasma contactors, cooling systems, and structural elements.

In summary, the current densities required for magnetobraking are higher than those achieved in wire form today, but within levels which are technologically achievable.

Other Applications

The concept of magnetobraking is not limited to Mars return applications. It can also be used during a gravity assist in the Earth's magnetic field, either to produce thrust, to change the orbital plane, or to add magnetic force to the gravity force in a magnetically-enhanced gravity assist..

Jupiter is a much better planet for electrodynamic tether use, with a stronger magnetic field (12 B_e) and higher radius (11.2 R_e). Magnetobraking could be used to capture into Jupiter orbit a probe to the Jovian moons; once captured, the electromagnetic tether could be used as a propulsion system throughout the Jupiter magnetosphere [6]. Alternatively, used in reverse, a magneto-gravity-assist could be used to propel a probe to Saturn or beyond.

Finally, a deep-space or interstellar probes could use a magneto-assist in the Sun's gravity field. By making a ΔV maneuver deep in the sun's gravity well, considerable leverage of the ΔV is produced.

References

[1] G.A. Landis, "Magnetobraking for Earth Return Vehicles," to be published, *Acta Astronautics*.

[2] P.A. Penzo and P.W. Ammann, eds., *Tethers in Space Handbook, Second Edition*, prepared by SRS Technologies for the NASA Office of Space Flight, under contract NASW-4341, May 1989.

[3] *Tethers in Space: Toward Flight* ; AIAA, Washington D.C., May 1989.

[4] G. von Tiesenhausen, ed., *The Role of Tethers on Space Station, NASA Technical Memorandum TM-86519,* Oct. 1985.

[5] L. Guerriero and I. Bekey, eds., *Space Tethers for Science in the Space Station Era,* proceedings of a conference in Venice, Italy, Oct. 1987, Societa Italiana di Fisica Conference Proceedings Volume 14, Bologna, Italy, 1990.

[6] S.B. Gabriel, R.M. Jones and H.B. Garrett, "Alfven Propulsion at Jupiter," in L. Guerriero and I. Bekey, eds., *Space Tethers for Science in the Space Station Era,* 217-229.

LOW COST BOOSTER AND HIGH PERFORMANCE ORBIT INJECTION PROPULSION EXTENDED ABSTRACT

N95-70884
42717
Bs 8

R. L. Sackheim
TRW Space and Electronics Group

Introduction and Background

Space transportation is currently a major element of cost for communications satellite systems. For every dollar spent in manufacturing the satellite, somewhere between 1 and 3 dollars must be spent to launch the satellite into its initial operational orbit. This also makes the weight of the satellite a very critical cost factor because it is important to maximize the useful payload that is placed into orbit to maximize the return on the original investment. Most communications satellites in use today operate from geosynchronous orbit. Since most of the launch vehicles currently available (e.g., Delta, Atlas, Ariane, Long March, Titan, etc.) insert these satellites into a geosynchronous transfer orbit (GTO), an apogee kick propulsion system must be included on-board the satellite to provide the additional energy required to achieve the final operational geosynchronous orbit (GEO). The satellite apogee propulsion system (APS) using propulsion technologies that are available today is a major fraction of the cargo weight carried into GTO by the current family of launch vehicles. Additional propulsion capability must also be provided by the satellite if there are significant station keeping (maintaining longitude and latitude positioning) requirements for the communication mission to provide the specified earth coverage. It seems apparent then, that tremendous economic advantage for satellite communications systems can be gained from improvements in two key highly leveraged propulsion areas. The first and most important economic improvement can be achieved by significantly lowering the cost of todays launch vehicles. The second gain that would greatly benefit the communications satellite business position is to increase both the useful (payload) weight placed into orbit and the revenue generating lifetime of the satellite on-orbit.

The point of this paper is to first explain that these two goals can best be achieved by cost reduction and performance increasing advancements in rocket propulsion for both the launch vehicle and for the satellite on-board apogee insertion and on-orbit velocity control systems. Let us first deal with low cost propulsion leverage on low cost launch vehicles. It has been determined in previous studies that the rocket engines typically comprise 40 to 50% of current expendable launch vehicle (ELV) costs[1]. The next most expensive elements are the vehicle structure including the propellant tankage, followed by the pressurization and fluid feed systems. Because of the high leverage of the rocket engine cost on the launch vehicle cost, it was found in previously reported studies by McDonnell Douglas Aerospace (MDA)[1,2] and TRW that the most cost effective engine for ELVs would be a fundamentally low cost design that operated at low pressure (< 1000 psia); incorporated hardware elements specifically designed for low cost such as simple and inherently stable injectors with passively cooled thrust chambers; and that also relied upon a simple high pressure gas feed system[3]. However, it was later determined by MDA that for larger vehicles, a purely gas-pressurized feed system would tend to increase costs because of the weight and complexity of the high pressure propellant tanks and the very large gas pressurization feed system. A low cost alternative to heavy and complex pure gas pressure feed systems was found to be the use of simple low pressure, fluid film bearing turbopump assemblies that were stage mounted as part of the low cost vehicle design. A team of MDA, TRW and Allied Signal Aerospace was then formed to conduct some very preliminary design and development activities (on independent company IR&D funds) to establish and verify this low cost launch vehicle design concept.

For the orbit insertion and velocity control phases of the communications satellite mission the real pay off comes from the opposite end of the propulsion technology spectrum. Here, as illustrated in Figure 1, the real pay off comes from high performance that minimizes the on-board consumables to maximize the useful payload fraction in orbit. To this end, TRW is working to advance two key spacecraft propulsion technologies. These are advanced liquid apogee engines to increase specific impulse above 330 seconds and very high performance electric propulsion systems that, under the right circumstance, can drastically reduce the weight of propellant for both orbit raising to GEO and for subsequent on-orbit maneuvering.

To appreciate the discussion that follows, it is important to recognize that for a spacecraft integral apogee propulsion system, specific impulse (ISP) is a very important parameter in communications satellite design, because one second of ISP is worth about 10 to 14 lb of spacecraft weight reduction. Depending upon the specific satellite design, some commercial communications manufacturers have stated that each pound saved then will reduce initial satellite cost by about 10,000 to 20,000 dollars. On the other hand, to achieve low cost expendable launch vehicles, rocket propulsion performance is not a key driver, but it is critically important to reduce the cost of the most expensive vehicle hardware elements, namely the rocket engines, structure and fluid systems. The remainder of this paper will discuss these specific points in more detail.

Space Transportation Cost Influence Factors to Reduce Costs

The emphasis in the past to reduce expendable launch vehicle costs has been to reduce gross lift off weight (GLOW). The perception was that if the design team can minimize GLOW by maximizing performance, then the launch vehicle cost will be minimized by some significant number of dollars per pound of vehicle weight saved. Furthermore, as reported in Reference 1, if one examines the

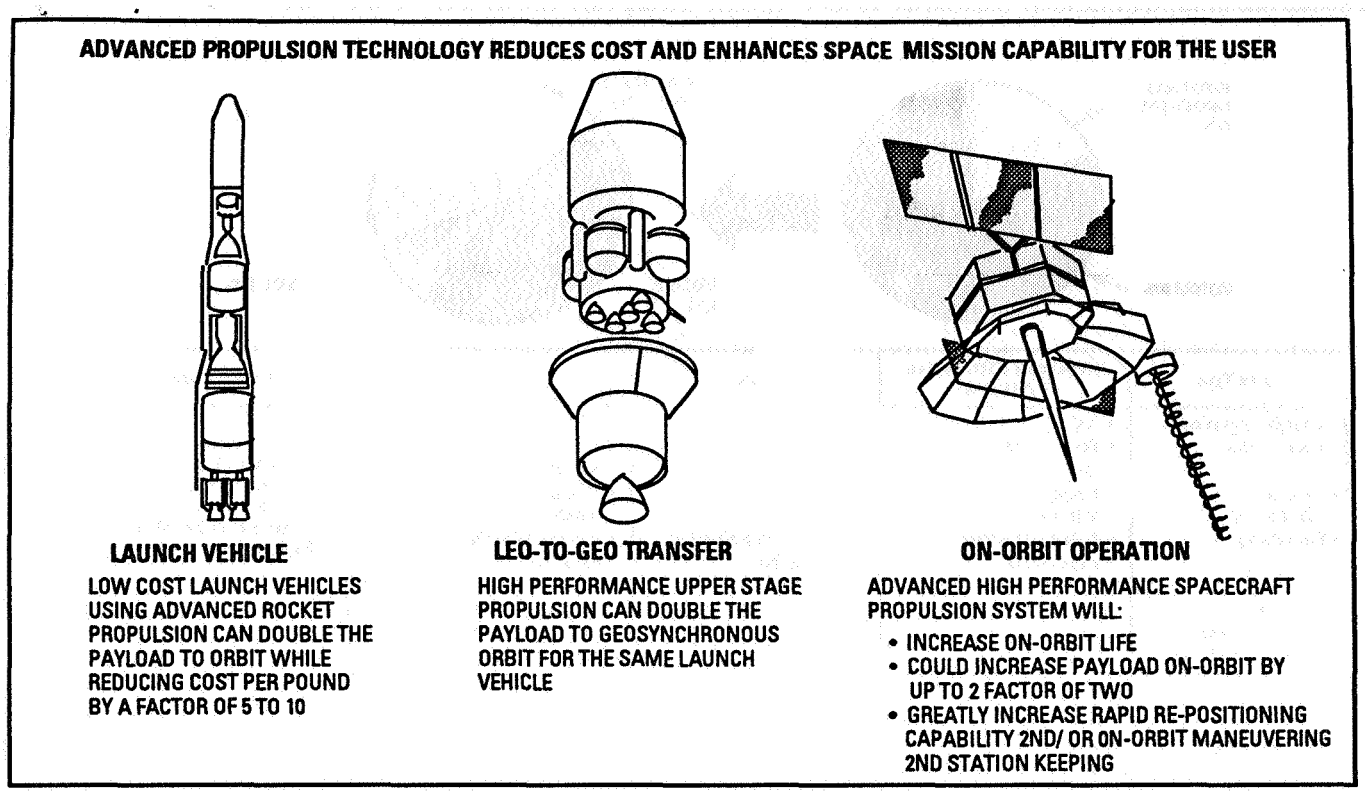

Figure 1. Integrated Rocket Propulsion Advancements for Efficient Space Transportation

total cost of a launch, it is apparent that the vehicle hardware is 80% of the cost while flight operations account for only 20% (Figure 2). This again would tend to substantiate the argument that minimum GLOW equals minimum launch vehicle cost. However, one has to only examine what makes up the vehicle cost to find out that half the cost is in the engine, a third of the cost the structure, and the remainder of the cost is the fluid systems and avionics. Of this grouping, only the structure at 30% has any direct cost relationship to its weight. Its cost per pound, however, can vary greatly depending on the type of structure employed. For example, isogrid structures are complex and cost about $400/lb while monocoque structures cost less than $100/lb. Vehicles designed with expensive structures place a premium on achieving maximum engine performance in order to reduce structural cost. Use of low cost structures, on the other hand, permit relaxed engine performance requirements. Thus, a vehicle designed with a simple low cost structure benefits not only from the reduced structural cost, but also from reduced engine costs.

Other vehicle components are sophisticated systems and there are many other factors that can drive up the cost. In the major contributor, the rocket engine, cost is driven mainly by chamber pressure and complexity. Very high pressure engines tend to have extremely complex cycles and mechanisms. The very high costs for these high pressure engines are related to the fact that they rely upon integral, very sophisticated turbopumps with complex power cycles such as expander or staged combustion, where one or both of the high pressure propellants is used in some form to regeneratively cool the combustion chambers. These high costs are not only driven by the many precision parts and components of the various subsystems, but are also caused by their interrelationship that adds to engine complexity and lowers reliability.

Shown in Figure 2 is a simple comparison of four LOX/LH_2 engines. There's the current state of the art design which is the reusable SSME that is recognized as an expensive and complex engine. The next most complex engine design concept is the STME which still operates at relatively high chamber pressure and utilizes a regeneratively cooled combustion chamber with high pressure integral turbopumps. The third most costly engine is the French Vulcain where the French did extended studies trying to minimize the cost of their engines. This engine design reduces the chamber operating pressure considerably and simplifies the combustion and cooling cycle. However, it still uses a regeneratively cooled combustion chamber. The fourth engine, which is TRW's ultra low cost design, goes to the other extreme. It operates at minimum chamber pressure and separates the turbopump from the engine so that it can function as an independent system and can be stage mounted. It has a very simple injector concept with a passive ablative cooled chamber so that it is a truly inexpensive, expendable engine. This design is estimated to be at least an order of magnitude less expensive than the other American engines and one-fifth the cost of the French engine. Also with the much simpler TRW engine and Allied Signal turbopumps, there is a significantly lower development and qualification cost.

There is some question as to why the ultra low cost engine has to be low pressure. One of the answers is that

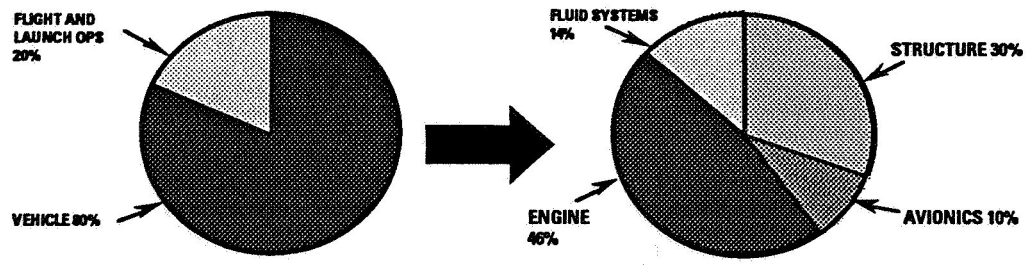

Engine Type	TRW Engine (TRW Engine & ASE TPA)	STME	SSME	French Vulcain
• Chamber pressure • Power cycle • Injector • TCA cooling • Reusability	• 300 psi • Stage mounted boost pump • Simple single pintle injector • Ablative chamber • Expendable	• 2,250 psi • Gas generator and turbo pump • Complex multi-element injector • Regenerative chamber • Expendable	• 3,260 psi • Engine mounted turbopumps and staged combustion • Complex multi-element injector • Regenerative chamber • Reusable	• 1,470 psi • Engine mounted gas generator & turbopump • Complex multi-element injector • Regenerative chamber • Expendable
Manufacturing comparison (parts, operations, welds, etc.)	82	2565	7417	Unknown
Cost/unit, $M	2	>14	67	10
Development/qual cost	180 M	>1B	>3B	Unknown
Thrust $_{vac}$ (lb_f)	480,000	650,000	512,000	202,000

R1M 93.0226.03

Figure 2. Simple Engine = Low-Cost Reliable Propulsion = Low-Cost Reliable Launch Vehicle

the low pressure ratio enables a simplified turbopump design which is a major cost reduction factor. The low pressure operation also significantly lowers the heat flux to the thrust chamber throat which then allows the use of a castable ablative cooled combustion chamber which provides major reduction in engine costs. As shown in Figure 3, the most important design region for low cost engines is in the operating chamber pressure ranges from 300 to 1000 psi. The push to go to 1000 psi chamber pressure is from the upper stage application driven requirement of engine nozzle envelope. Current studies have shown the 300 psi chamber pressure is a cost optimum design condition for the first stage engines where nozzle exit diameter is usually not a driving factor. In the case of upper stage engines, the nozzle in many cases is truncated to fit in a given envelope and, therefore, some nozzle performance is lost. The overall combustion efficiency of these very low pressure engines is nearly the same as that of the high pressure engines. There is a very small increase in performance due to the pressure level. Most of the performance difference between the high pressure and the low pressure engines is in the fact that a higher area ratio nozzle can be packaged in a given envelope for the higher pressure engines. The low cost engines can be made to be reusable at most chamber pressures with the incorporation of internal cooling ducts or regenerative chamber technology. But both of these cooling techniques will significantly affect cost. The Allied Signal foil bearing pump and a TRW pintle injector assembly are already reusable as currently designed for the ultra low cost configuration.

Baseline MDA/TRW/Allied Signal Ultra Low Cost Launch Vehicle Design Concept Using Low Cost Propulsion

Based upon the results of recent joint in-house studies, the MDA/TRW/Allied Signal team has established an ultra low cost launch vehicle design concept. This concept consists of two stages; each using LO_2/LH_2 propellants, simple monocoque aluminum tanks and structure. A low cost TRW pintle-injector thrust chamber using passive ablative cooling is used for each stage. The thrust chambers for each stage are fed by Allied Signal foil bearing, turbopumps that are mounted on the stage structure and driven by a simple gas generator power cycle. For Delta-class payload capability, the first stage is powered by either a single 750 K lb thrust engine or two 400 K lb thrust engines. The second stage engine thrust is 50 to 60 K lb (vacuum). Increased payload capability can be provided by adding either solid or liquid propellant strap-on boosters to the core vehicle. The liquid strap-ons in this case, would be built from core vehicle components, giving a modular family of ultra low cost vehicles.

The TRW ablatively cooled pintle injector thrust chamber assembly is the key enabling technology making such an ultra low cost vehicle concept viable. The low chamber pressure (300 to 1000 psia) permits use of low cost, mold-in-place ablative materials and simplifies chamber design and manufacturing. This low cost passively cooled approach, however, results in propellants entering the chamber in a colder state than with the much more

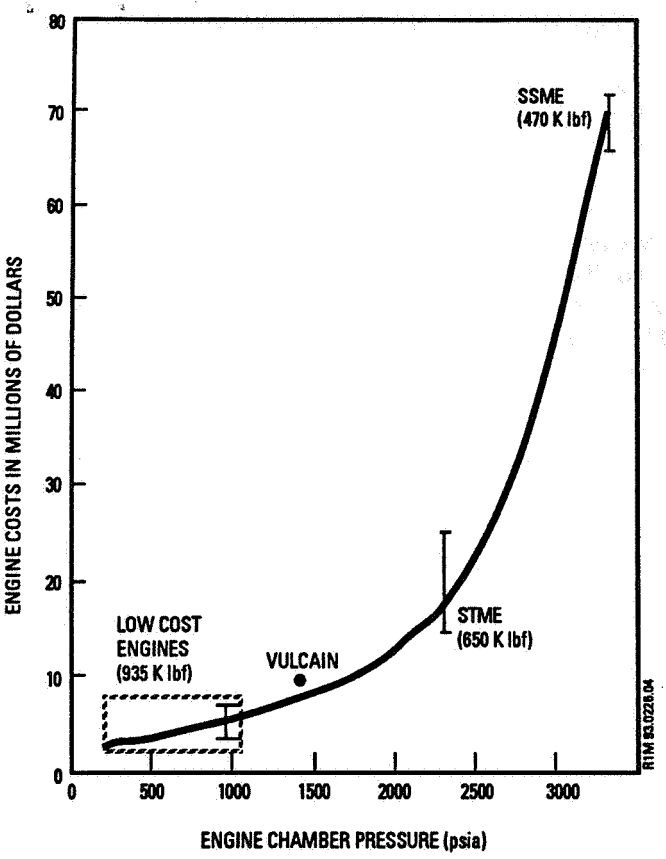

Figure 3. First Article Engine Costs

expensive regeneratively cooled chamber designs. In the case of LOX and LH_2 propellants, conventional injectors produce spontaneously unstable combustion at the LH_2 temperatures of interest. Use of the TRW pintle injector eliminates this problem, however, because of its inherently stable combustion characteristics.

This injector is a patented design exclusive to TRW rocket engines and has unique features that make the engine combustion characteristics different from those using other types of injector designs. Its many benefits include excellent combustion performance, efficient deep throttling, adaptability to low cost manufacturing, and high reliability. Approximately 200 pintle injector engines of various sizes and operating on a variety of propellants have been flown without a single in-flight failure. Also, in over thirty years of development, testing and production, TRW has never experienced combustion instability in any of its pintle injector engine designs. This has been true of engines operating over a range of thrust from 5 to 250,000 lb on earth-storable hypergolic propellants and a large number of smaller engines operating on a variety of propellants (21 combinations) in long duration-firing, pulsing (down to 2 msec) and deep throttling (as much as 19:1) modes. Operating chamber pressures have ranged from 10 to 3,500 psia.

The basic pintle injector concept is illustrated in Figure 4. It consists of a closed cylindrical element that projects into the combustion chamber and has ports machined into the cylindrical surface that allow the center propellant to flow radially into the chamber. The center propellant may be either oxidizer or fuel. The propellant port configurations typically range from discrete primary

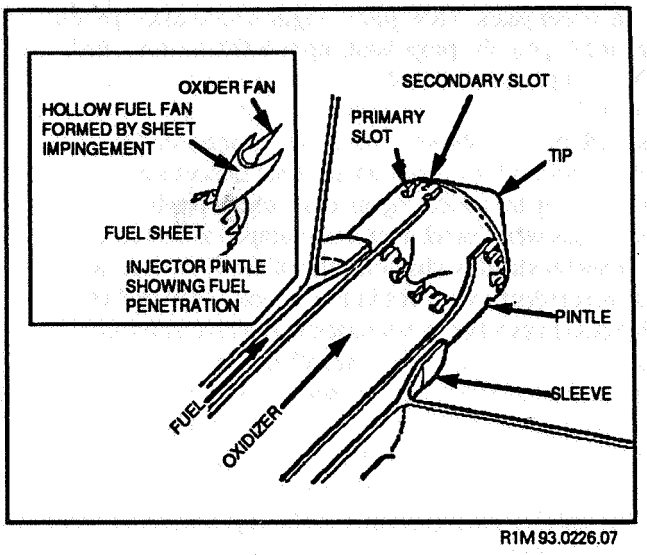

Figure 4. TRW Coaxial Pintle Injector Concept

and secondary jet slots to a continuous gap. Selection of a particular configuration is governed by a number of factors including the propellants to be used, the required combustion chamber wall thermal environment, desired combustion performance, and whether the injector is intended to operate in continuous flow, throttling, or pulsing modes.

The other propellant enters the chamber flowing axially along the exterior of the cylindrical element. Mixing of the propellants occurs where this axial-flowing cylindrical sheet meets the radial flow issuing from the central propellant slots.

The genesis of the pintle injector is traceable to the Apollo program. It provided a means to perform deep throttling, needed for a controlled descent to the lunar surface, while maintaining good stable combustion performance and mixture ratio control. Once Apollo got underway, TRW work on the pintle injector attracted NASA interest and resulted in its selection for the Lunar Module Descent Engine (LEMDE). LEMDE was an ablative-cooled, pressure-fed engine having a maximum thrust of 10,500 lb with a chamber pressure of 100 psia and a 10:1 throttling range operating on NTO/A-50 propellants. This engine proved to be very stable throughout the development, qualification and flight phases of the Apollo program. It successfully landed on the moon six times and saved the crew of Apollo 13.

In the mid 1970's, a fixed thrust variant of the LEMDE was produced and designated as the TR201. It flew 75 successful missions as the pressure-fed second-stage engine on the Delta launch vehicle. During the late 1960's and early 1970's, the basic LEMDE concept was scaled up to 250,000 lb thrust and operated on NTO/UDMH propellants. In addition, 50,000 lb thrust engines were operated on IRFNA/UDMH, LOX/RP-1 and LOX/Propane. Smaller engines having 3000 lb thrust were tested on FLOX/LCH_4, FLOX/GCH_4 and FLOX/(LC_2H_6 + LCH_4) propellants. In all cases, explosive disturbances purposely produced during tests, were well damped and no evidence of spontaneous instabilities were observed even under liquid/liquid injection conditions with cryogenic propellants.

In recent years, TRW pintle engines have also operated on gelled hypergolic propellants up to 8,000 lb thrust and LOX/LH_2 up to 16,400 lb thrust. No spontaneous instabilities have been observed in either case. In the LOX/LH_2 tests, both propellants were injected at near normal-boiling point conditions for which conventional injectors are spontaneously unstable. Again, explosively produced disturbances were found to be well damped in this case. This inherent stability characteristic of the TRW injector is a major cost reduction benefit in that typical TRW rocket engine design practice is not concerned with combustion instability as an issue. This approach is justified since no pintle engine has had to employ stability enhancing features, such as baffles or acoustically resonant chambers which must undergo protracted and expensive empirical characterization and verification test programs. Because of these inherent stability characteristics, TRW engines can operate in low cost regimes not possible with engines using other types of injectors.

Allied Signal foil bearing turbopumps are particularly attractive for this low cost launch application because of their simplicity, low cost and robustness. The foil bearing is a series of overlapping metal foils which provides a self-energized hydrodynamic fluid film bearing of the same fluid being pumped (Figure 5). This type of bearing has a number of advantages as compared to ball bearings or hydrostatic bearings. Foil bearing turbopumps are expected to cost much less to develop and manufacture and be more reliable than the types of pumps currently used in rocket engine applications.

Status of Low Cost Space Transportation Propulsion Advancements at TRW

In recent years, TRW has established an active program, in cooperation with McDonnell Douglas, Allied Signal and NASA, to develop ultra low cost pintle injector engines operating on LOX/LH_2 propellants. In 1991, a TRW engine with a sea level thrust of 16,400 lb was successfully demonstrated at the NASA Lewis Research Center (LeRC) under a NASA Space Act cooperative test agreement. This engine demonstrated that a pintle injector engine can operate stably with excellent combustion performance with LOX/LH_2 propellant injected at near normal boiling point temperatures, typical of conditions envisioned for the low cost vehicle application.

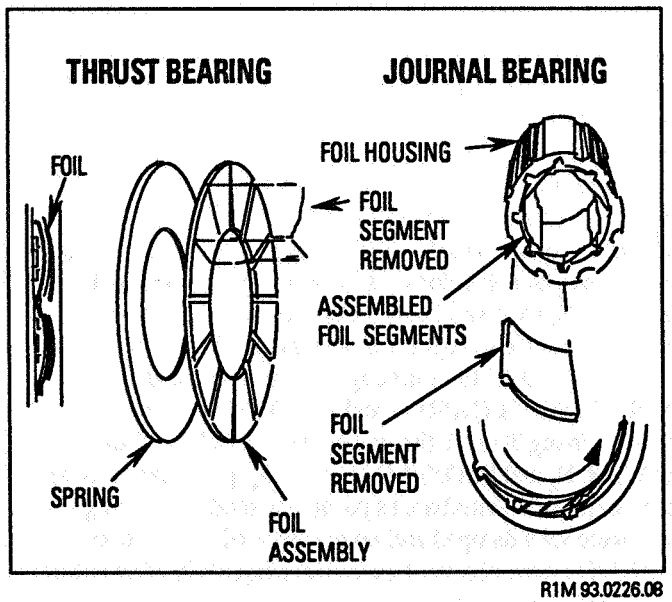

Figure 5. Allied Signal Foil Bearing Concept

Recently, a 40,000 lb sea level thrust (50,000 to 60,000 lb vacuum thrust) engine was, designed fabricated, and tested. This engine uses low cost molded-in ablative liners. An extensive series of tests have been sucessfully conducted at NASA LeRC. The results of these tests continue to demonstrate the technology required for an ultra low cost upper stage engine, as well as add to the data base for scaling the design up to much larger first stage engines.

With the successful completion of the 40,000 lb thrust engine tests at LeRC, TRW now plans to seek funding to scale the design up to 400,000 lb thrust. Fabrication and testing of this engine would follow, with the objective of demonstrating good combustion performance and stability in an engine size of interest for first stage applications.

High Performance Spacecraft Propulsion to Maximize Space Asset Payoff

Up to this point we have primarily focused on the economic impact of the earth to orbit launch phase of space transportation for communications satellites. The basic argument thus far has emphasized that launch providers must find realistic ways to drive the cost of their launch services way down to maintain the economic viability of space based communications systems. We have presented data that shows that the major cost driver for ELVs is the propulsion system with the majority of these costs coming from the rocket engines. The data presented in the preceding sections argues that the most effective (in fact the only way – if you believe history) way to reduce these costs is to design and build the lowest cost and least complex propulsion system consistent with acceptable reliability standards rather than to attempt to maximize performance. We will now change our focus to examine what factors influence the cost of the ELV cargo element itself to see if propulsion advancements can lower the cost of the fixed communications satellite asset on orbit.

Even if the launch vehicle cost could be driven way down, there is still plenty of room to increase the cost effectiveness of the cargo element launched into initial orbit. Depending upon where the earth-to-orbit launch vehicle injects its cargo, an additional velocity increment or ΔV (or orbit injection energy) will usually be required to achieve the operational orbit. In the case of GEO COMSATs, this additional energy usually provides for apogee circularization (or "apogee kick") and in some cases includes perigee raising augmentation energy. This ΔV energy can either be provided by an additional upper stage or by an integral propulsion system on board the satellite. The argument from this point forward now switches to maximizing the upper stage or on-board propulsion system performance to a level that is consistent with specific space system financial investments versus on-orbit revenue pay offs. The propulsion performance benefits will vary depending on the

customer/user system concept and the specific contract. It should be noted, however, that in almost all cases there seems to be significant pay off from increases in space propulsion system performance (again consistent with the specific customer contract provisions and constraints).

Additional orbit transfer stage propulsion system performance benefits will vary with the stage size, its specific purpose and use and the total value of the injected space asset. In the case of the on-board integral propulsion system, however, the economic benefits of performance improvements will tend to keep increasing in one way or another as long as the non-recurring and recurring costs do not become completely unaffordable. This is because about 40 to 60% of the spacecraft weight will be used for some combination of final orbit injection velocity and on-orbit velocity and attitude control. Obviously, if this fraction of the spacecraft weight could be reduced, then more of the weight would be available for revenue generating payload or longer life on-orbit.

The two basic approaches to improving space propulsion performance are either increasing the efficiency of existing chemical systems or the use of high performance, high power electric propulsion systems. TRW as well as many other companies is working to develop both of these technologies to realize the increased payload economic advantages discussed above.

Status of High Performance Spacecraft Propulsions Systems at TRW

Spacecraft propulsion systems for most of the past three decades have relied upon limited use of solid apogee kick rocket motors and earth storable liquid propellants, principally hydrazine as a monopropellant and nitrogen tetroxide-amine fuels as bipropellants. As shown in Figure 6, the technology level for these propellants and the systems in which they are used has continually progressed and been upgraded as spacecraft missions have changed. The introduction of the dual mode (N_2O_4-N_2H_4) system concept by TRW and others represents one of the last significant earth-storable propulsion system improvements available. The dual mode system utilizes a N_2O_4-N_2H_4 bipropellant liquid apogee engine for apogee circularization and insertion and catalytic thrusters plus either (depending on the system requirements and constraints) electrothermally heated monopropellant hydrazine thrusters (EHT), or gas-gas injection, N_2H_4-N_2O_4 after burner thrusters, or higher power arcjets (if high power is available) for attitude control and stationkeeping. The hydrazine fuel for the main engine and attitude control subsystem (ACS) is also integrated into the same tank or tanks for additional system weight advantage. TRW has developed, qualified, and flown a 100-lbf thrust (100 psia) N_2O_4-N_2H_4 apogee engine demonstrating 314.6 lbf-sec/lbm ISP. TRW is presently developing an advanced dual mode N_2O_4-N_2H_4, liquid apogee engine in the 328 to 330 lbf-sec/lbm ISP range at nominal thrust chamber pressure levels. TRW has also recently demonstrated 318 sec ISP with an N_2O_4/MMH liquid apogee class engine. Other improvements can also be achieved using higher engine operating pressures because of the potential for higher thrust coefficient levels, the enabling use of higher temperature materials, the reduced length and volume of the engine envelope, and the potential engine weight savings. It is also clear that the use of higher pressure engines is a good method for meeting smaller satellite volume and length constraints. The net benefit of higher operating storable propellant engines should be the capability to achieve about 335 seconds ISP with smaller and lighter LAEs than are currently available. TRW is currently working under contract to NASA/Lewis Research Center to develop a higher operating pressure liquid apogee engine to also gain this additional spacecraft performance benefit. In summary, TRW is working, under contract to NASA and other spacecraft prime contractors, on a family of advanced, high performance spacecraft apogee and velocity control engines. These engine technology advancements will use three basic building blocks to evolve in a logical sequential fashion to the maximum achievable performance levels for storable chemical rocket engines. These are higher temperature capability materials (currently coated rhenium) for thrust chambers, higher operating pressures (about 300 to 500 psia as compared to current levels of about 100 psia) and the use of a higher energy space storable oxidizer (liquid oxygen). Incorporation of these advanced technologies will ultimately result in a spacecraft engine that will be capable of operating at or above 350 seconds of ISP. This engine will enable either increases in payload fractions of 15 to 20% or a like reduction in the overall spacecraft weight, relative to todays operational spacecraft integral propulsion systems. These improvements will, in turn, contribute to much more profitable communications satellite systems.

Finally, it must be pointed out that electric propulsion (EP) technology also offers tremendous performance benefits for spacecraft and space transportation systems. The high thrust efficiency of electric systems compared to chemical propulsion can significantly reduce the amount of propellant required for the same operations. In addition, the high power that is inherent in electric propulsion spacecraft will actually enhance or enable many operational mission concepts that up to now have been considered to be out of reach because of the cost of high power systems just for these missions (without the propulsion savings). Advances in critical EP related

Spacecraft Propulsion Systems technologies over the last three decades now enable the near term use of these systems for high performance, high payload fraction, communications satellites.

Advances in materials, microelectronics, and spacecraft design tools have contributed to the near term development of electric propulsion spacecraft. Additional new spacecraft technologies that are now becoming available include high power, radiation resistant solar arrays, high power distribution and control, qualified electric propulsion subsystems, lightweight radiation hardened avionics, advanced structural and thermal materials, and fully autonomous guidance and control for orbit raising and on-orbit control of high power, high performance communications satellites.

Electric propulsion systems will soon be flying on both flight demonstration and fully operational spacecraft. These systems will be capable of operation at power levels from

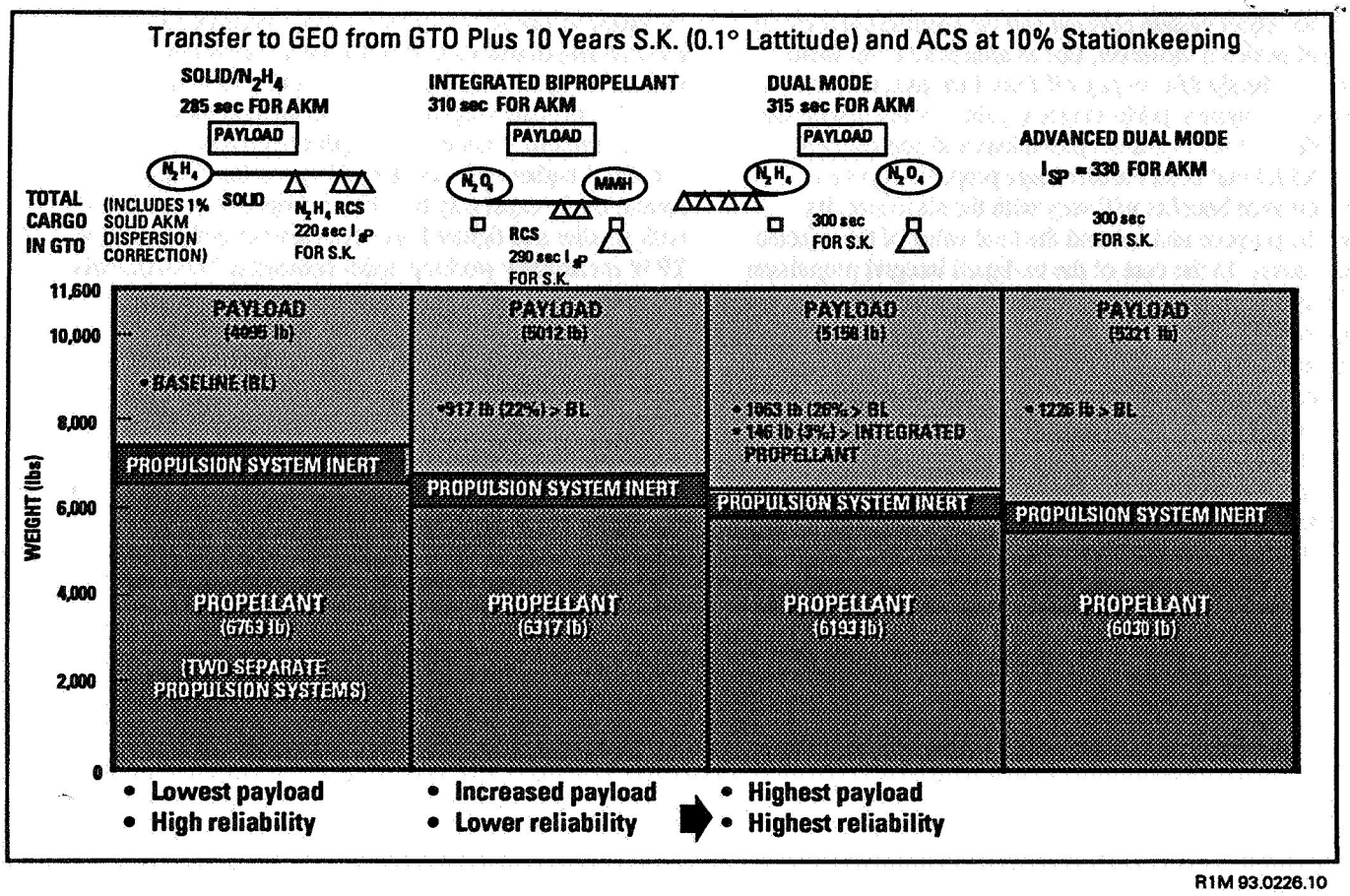

Figure 6. Comparison of the Evolutionary Performance Growth Spacecraft Propulsion Systems

several hundreds of watts to tens of kilowatts and will use either arcjets, ion thrusters or stationary plasma thrusters (SPTs). Specific impulse values will range from 500 seconds to 2000 to 3000 seconds, depending on the devices used. There is a drawback for some missions requiring very rapid "launch on demand" response, because it will take more time to reach the operational orbit using a low thrust electric propulsion orbit transfer system (typical trip times will take about six months from LEO to GEO, using 1,000 sec. ISP 20 to 30 KWe hydrogen arcjets). However a tremendous net savings could still be achieved in total communications system cost reductions. In simple terms, it has been shown that the use of an all electric propulsion orbit raising and on-orbit velocity control (positioning) system for high power communications satellites can result in almost twice the payload in operational orbit for about half the current or near term projected space transportation costs.[4]

Summary and Conclusions

This paper has presented information that clearly shows the influence of space transportation system performance and cost on the overall economics of space based communications systems. It has been pointed out that the space transportation system for communications satellites generally consists of three basic phases, which are: earth-to-orbit (launch vehicle); orbit raising to higher transfer orbits; and injection into, and maintenance in final operational orbit. Data has been presented to show that the major cost drivers for these three transportation phases are either the cost or the performance of the respective propulsion systems. The major point being made here is that the propulsion system economics must be viewed in two different ways. For the earth-to-orbit launch vehicle, low cost, simple, reliable and moderate performance propulsion system designs are far more cost effective than highly complex, ultra high performance designs. In fact, it is clearly shown that a major fallacy in past launch vehicle designs has resulted from repeated attempts to develop the highest performance, lightest weight rockets. This fallacy is a major reason for the relatively expensive launch vehicles that must be used for todays communications satellite systems. The only way to reduce the launch cost from the current $10,000 to $14,000 per pound to GTO level is to design a next generation of launchers that use a simple power cycle and lower operating pressure rocket engine with simple although somewhat heavier feed systems.

On the other hand, the relative cost to place any cargo into space will always remain high enough (even with the low cost innovations described herein) to demand the use of high performance spacecraft propulsion to maximize the fraction of cargo weight that is truly revenue generating, useful payload.

Therefore it is vitally important to develop the propulsion advancements described in this paper that will both dramatically, lower the cost of launch vehicles and maximize the useful payload fraction on-orbit for the required operational life times. The results of recent studies have been summarized to illustrate the specific economic advan-

tages of using ultra low cost, simple propulsion technology for low cost launch vehicles in conjunction with high performance upper stage and spacecraft integral propulsion systems for maximum value satellite payloads on-orbit.

References

1. J. P. Henneberry, F. J. Stoddard, A. L. Gu, and S. T. Thelander, "Low Cost Expendable Launch Vehicles." AIAA Paper 92-3433 presented at the AIAA/SAE/ ASME/ASEE 28th Joint Propulsion Conference and Exhibit, July 7 - 8, 1992, Nashville, Tennessee.

2. Carlson, C. R. and Simpson, J.S., "Low Cost ELV Technology Applicability to Spacelifters." AIAA Paper 93-4124 presented at the AIAA Space Programs and Technologies Conference and Exhibit, September 21 - 23, 1993, Huntsville, Alabama.

3. Fritz, D. E. and Sackheim, R. L., "Study of a Cost Optimized Pressure Fed Liquid Rocket Launch Vehicle," AIAA Paper No. 82-1108 presented at the AIAA/SAE/ASME 18th Joint Propulsion Conference, June 21 - 23, 1982, Cleveland, Ohio.

4. Sackheim, R. L. and Rosenthal, R., "Electric Propulsion: The Next Real Breakthrough in Space Transportation," IEPC-93-061, presented at the 23rd International Electric Propulsion Conference, September 13 - 16, 1993, Seattle, Washington.

427177
Pgs 13

N95- 70885

Strutjet-Powered Reusable Launch Vehicles

A. Siebenhaar and M.J. Bulman
Aerojet
Sacramento, California

S.E. Sasso and J.A. Schnackel
Martin Marietta
Denver, Colorado

(text follows)

INTRODUCTION

Martin Marietta and Aerojet are co-investigating the feasibility and viability of reusable launch vehicle designs. We are assessing two vehicle concepts, each delivering 8000 lb to a geosynchronous transfer orbit (GTO). Both accomplish this task as a two-stage system. The major difference between the two concepts is staging. The first concept, the two-stage-to-orbit (TSTO) system, stages at about 16 kft/sec, allowing immediate return of the first stage to the launch site using its airbreathing propulsion system for a powered cruise flight. The second concept, the single-stage-to-orbit (SSTO) system, accomplishes stage separation in a stable low earth orbit (LEO). These concepts distinguish themselves from other presently investigated concepts in three major aspects:

- First, the strutjet, a combined cycle engine system, avoids the extreme approaches of either all-rocket or all-airbreathing propulsion systems by combining the beneficial features of both systems in a logical and practical fashion such that significant specific impulse (Isp) gains are obtained without excessive engine weight. Strutjet-achievable mission average specific impulses are predicted to be 585 sec for the SSTO and 750 sec for the first stage of the TSTO system. Installed engine thrust-to-weight ratio is estimated at around 22:1. Corresponding values for an SSTO type conventional rocket engine are roughly 435 sec and 60:1 and for an SSTO NASP type propulsion system 700 sec and 15:1.
- Second, due to excellent Isp performance of strutjet-based systems, required propellant mass fractions are only 78 and 84 percent for TSTO and SSTO, respectively, and are within the present state of the art. In contrast, all-rocket SSTO mass fraction requirements are at least 90 percent.
- Third, thermal management of these vehicles can also be accomplished within the current state of the art because high-speed atmospheric operation is limited to Mach 8. This Mach number avoids severe vehicle heating conditions, which impose serious engineering challenges on the NASP X-30 vehicle and are typical for hypersonic atmospheric flight in the regime above Mach 8.

The enabling propulsion technology underlying both concepts is the Aerojet strutjet. This propulsion system combines ducted rocket, ram/scramjet, and pure rocket engine cycles into one compact engine. A strutjet operates in essentially four modes:

- As a ducted rocket during start and low-speed flight
- As a ramjet over the flight regime from about Mach 2.5 to 5
- As a scramjet from Mach 5 to 8
- As a pure rocket thereafter.

The strut, which gives this novel propulsion system its name, is the key element providing multiple operational functions such as compression of incoming air, inlet/combustor isolation, ram/scram fuel distribution and injection, and rocket thruster integration. Isp of this integrated engine is characteristic of airbreathing engines without the mass fraction penalty of having separate propulsion systems for different flight conditions.

SYSTEM BENEFITS OF THE STRUTJET PROPULSION

As Figure 1 illustrates, increases in specific impulse decrease the requirement for high propellant mass fraction, which is total propellant mass divided by takeoff mass of the vehicle without payload. Conventional chemical rocket-based SSTO systems require high mass fraction, about 90 percent, and, thus, depend on using cutting-edge materials and manufacturing processes. A propulsion system that offers higher specific impulse significantly reduces the need for such materials because lower mass fractions can still achieve viable solutions.

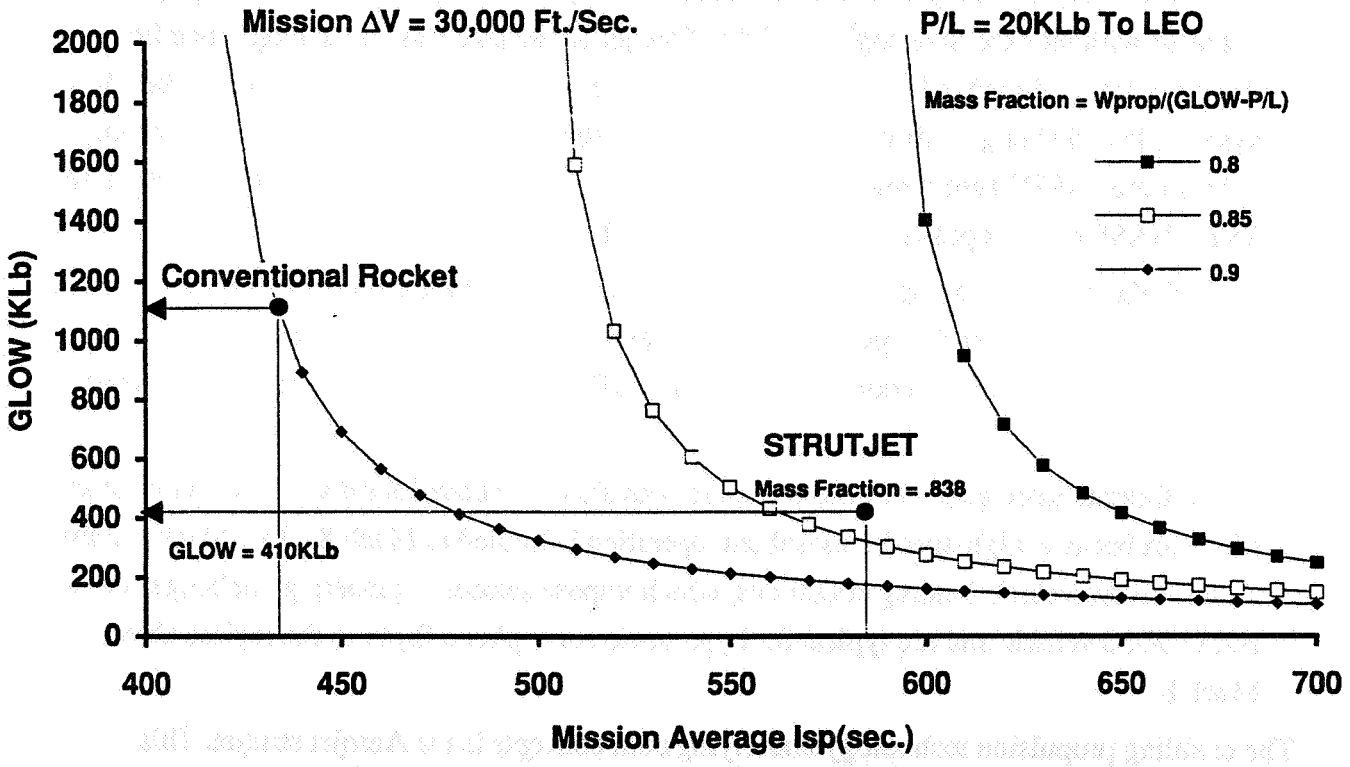

Figure 1. **Preferred Solution for SSTO: Strutjet**

Figure 1 also shows that the strutjet SSTO Isp/gross lift-off weight (GLOW) point lies to the right of the "knee" of the 85 percent mass fraction curve, whereas corresponding points for all conventional rocket SSTOs lie directly on the "knee" or on the steep portion of the 90 percent mass fraction line. This advantage is even more pronounced for the TSTO vehicle. Thus, suborbital separation of the second stage raises first-stage average mission Isp from 585 to 750 seconds. The locus of this vehicle on the corresponding Isp/GLOW plot is on the gentle

slope portion below the 80 percent mass fraction line. Being on the steep portion, at or above the "knee" of a critical system parameter curve, is not sound engineering practice because it indicates a risky design. A small loss in Isp causes a sharp rise in vehicle GLOW, which makes the concept or the mission unfeasible.

In contrast, loci of the strutjet-based vehicles on the Isp/GLOW chart indicate a large potential for future mass fraction improvement and afford a rather large degree of Isp insensitivity. Whereas strutjet vehicle GLOW is about one-third that of a conventional chemical rocket vehicle, its dry weight is about half. These drastically reduced weights and corresponding sizes benefit ground operation turnaround times and cost. Furthermore, the ability to use state-of-the-art materials and manufacturing processes can reduce development risk and cost of a strutjet-based launch vehicle.

Strutjet propulsion offers versatility to overall vehicle design. For vehicles studied to date, takeoff is configured vertically. A horizontal takeoff, however, with its relatively low takeoff weight, may be even more attractive because it reduces engine takeoff thrust substantially. This reduces the strutjet's rocket to ram/scramjet thrust ratio, which results in some small Isp gains and engine weight reductions. The biggest benefit, however, is that horizontal takeoff facilitates ground operations like payload integration and launch preparation. The strutjet is configured as a modular engine concept in which the number of modules used in a particular vehicle design can be varied to accommodate most payload and orbit requirements. The strutjet inlet is based on the well characterized strut compression inlet first introduced by NASA Langley Research Center.

The most significant benefit derived from this inlet is geometric contraction and isolation in a shorter length than conventional inlets. This leads to an engine that is easier to integrate into the vehicle, is lighter weight, has less drag, and absorbs less heat. The strutjet uses an aft-expanding nozzle concept, which has the advantage of altitude compensation and high expansion ratio. The pure airbreathing mode of the strutjet also enables the vehicle to cruise in the atmosphere like an airplane. This allows launching from a single launch site to accomplish orbit inclinations ranging from equatorial to polar. It also permits returning to launch site after second-stage separation. The former benefit opens up the possibility of eventually closing down one of the coastal launch sites, saving substantial recurring resources.

STRUTJET PROPULSION SYSTEM

The strutjet-combined cycle engine promises to revolutionize payload launch into space. This engine synergistically combines the best attributes of the high-performance oxygen/hydrogen rocket with the ram/scramjet engine. These integrated propulsion elements are contained within a single engine using common propellant feeds, cooling systems, and controls. The rocket provides the bulk of the thrust for takeoff and acceleration to ramjet takeover speed. The rockets

are contained in compact struts placed within the ramjet duct shown in Figure 2. The air drawn into the engine by the ejector effect at subsonic speeds and rammed in at higher speeds provides significant thrust augmentation during boost. The strut inlet uses efficient forebody

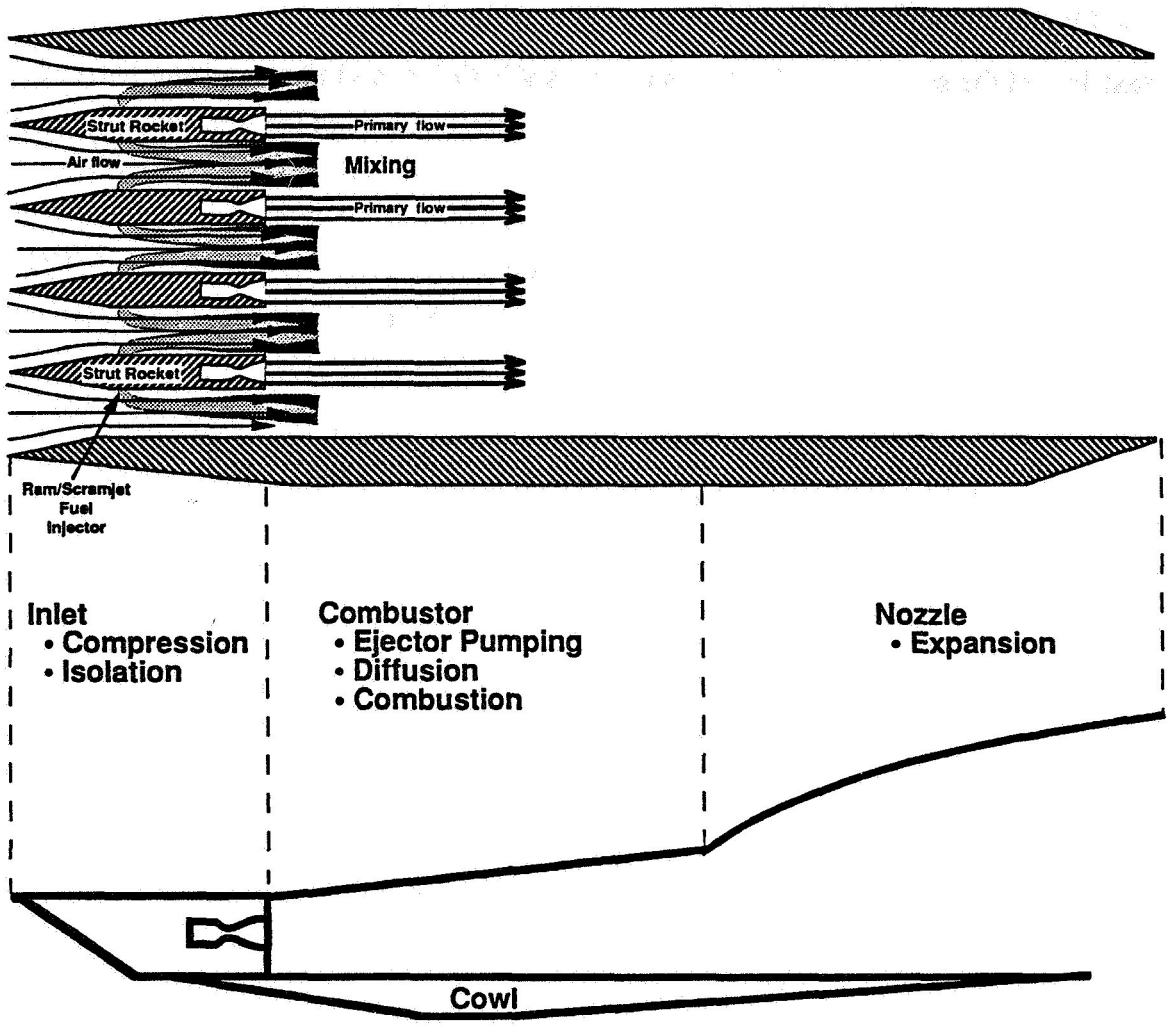

Figure 2. **Strutjet Combines the Best of Rocket and Ramjet Engines**

precompression together with strut compression, which is characterized by soft start, low spill drag, and good capture and recovery efficiencies. Initially, the fuel-rich rocket exhaust is sufficient to fuel air drawn into the engine. As the air mass flow increases with increasing speed, supplemental fuel is injected through ramjet injectors to maximize engine performance. Ramjet contribution occurs gradually starting at Mach 1 with full takeover at Mach 2.5. This transition provides the full benefit of the ramjet mode of operation with Isp approaching 3800 seconds.

Smooth transition from ram to scram mode has been demonstrated by Aerojet, as shown in Figure 3. Figure 4 shows the strutjet's Isp during a typical space launch mission. Aerojet's strutjet engine represents a significant departure from other airbreathing engine concepts, which

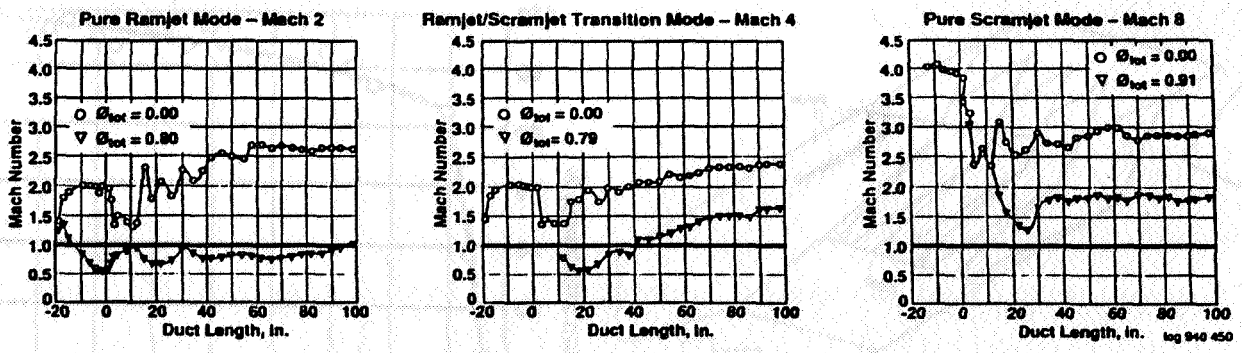

Figure 3. **Demonstrated Smooth Transition From Ramjet to Scramjet Operation**

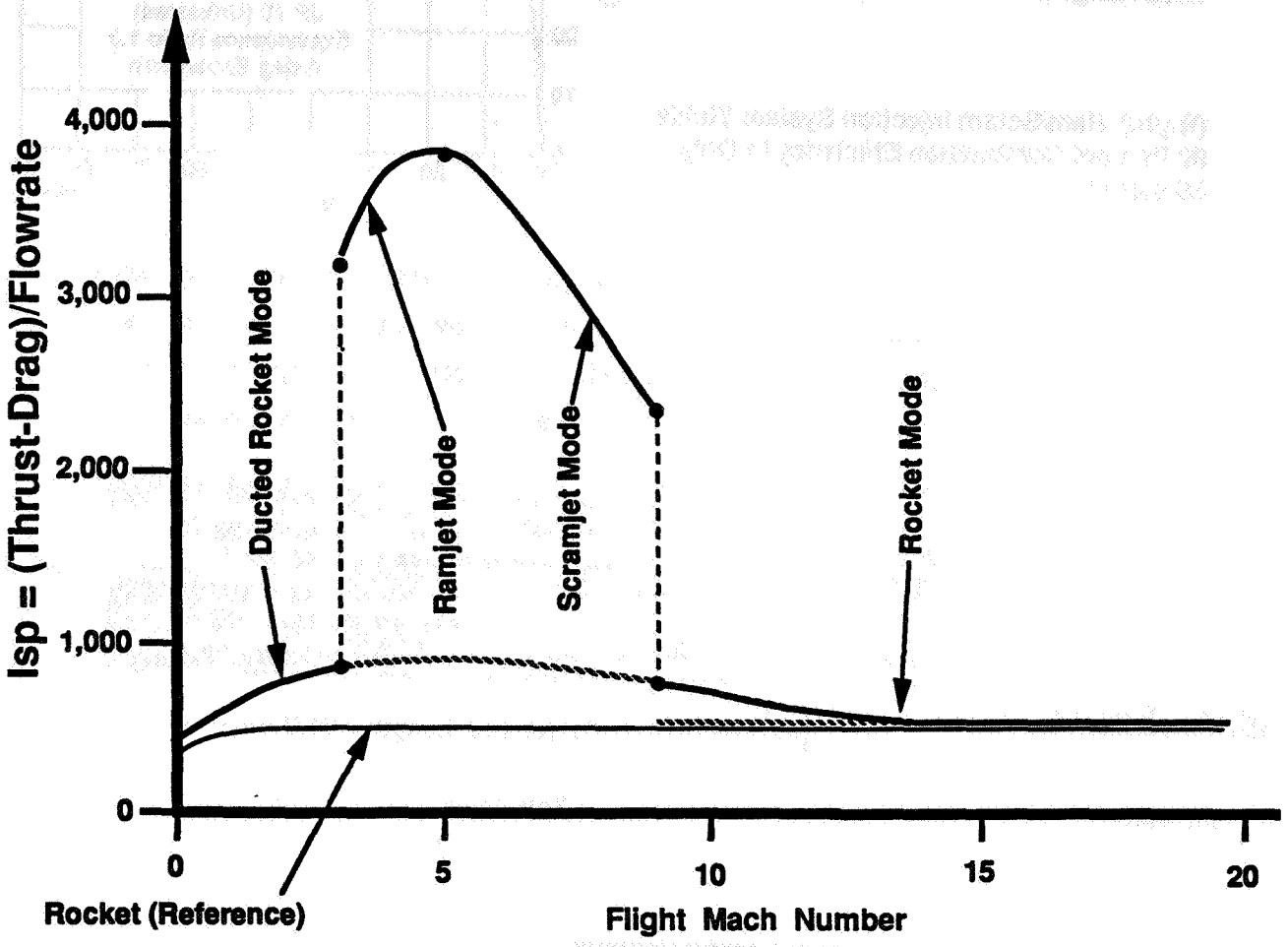

Figure 4. **Strutjet Engine Performs Significantly Higher Than Conventional LOx/LH_2 Rocket Engine**

are characterized by poor off-design inlet performance and heavy engine weight. The strut inlet operates well over a wide range of flight Mach numbers and contributes to a shorter, lighter engine. Figure 5 illustrates the strutjet inlet configuration. Struts also provide an ideal mounting place for ram/scram injectors. As shown in Figure 6, combustion efficiencies of 95 percent have

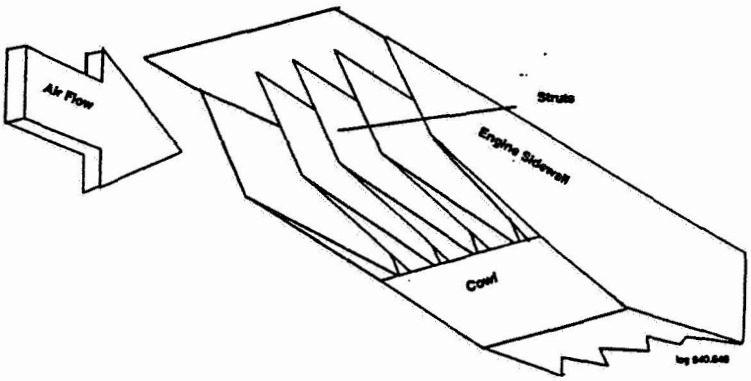

Figure 5. **Strut Compression Inlet Operates Over a Wide Range of Mach Numbers**

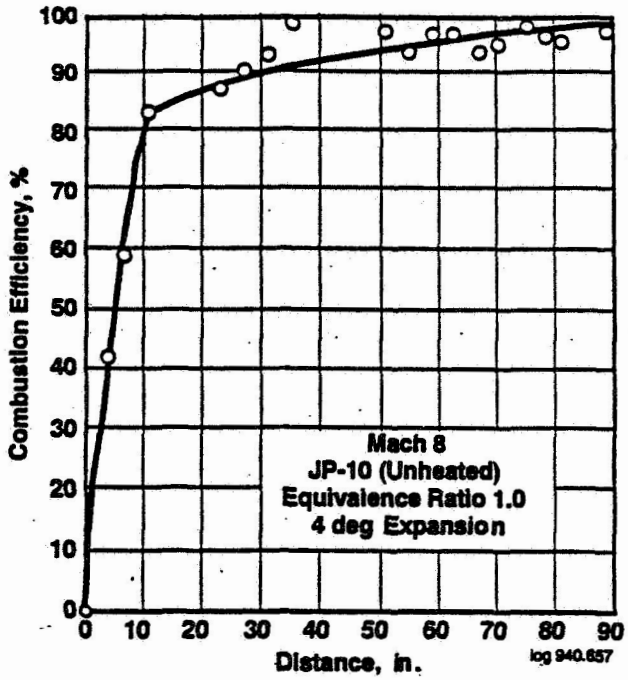

Figure 6. **(Right) Ram/Scram Injection System Yields 90 Percent Combustion Efficiency in Only 30 Inches**

been demonstrated with hydrocarbon fuels at Mach 8 conditions at high fuel equivalency ratios, where it is most difficult to burn efficiently. Figure 7 illustrates how strut-mounted injectors reduce the "mixing gap," thus allowing a significant reduction in combustor length and weight. Achievable installed strutjet engine thrust-to-weight ratios are estimated to be as high as 30:1.

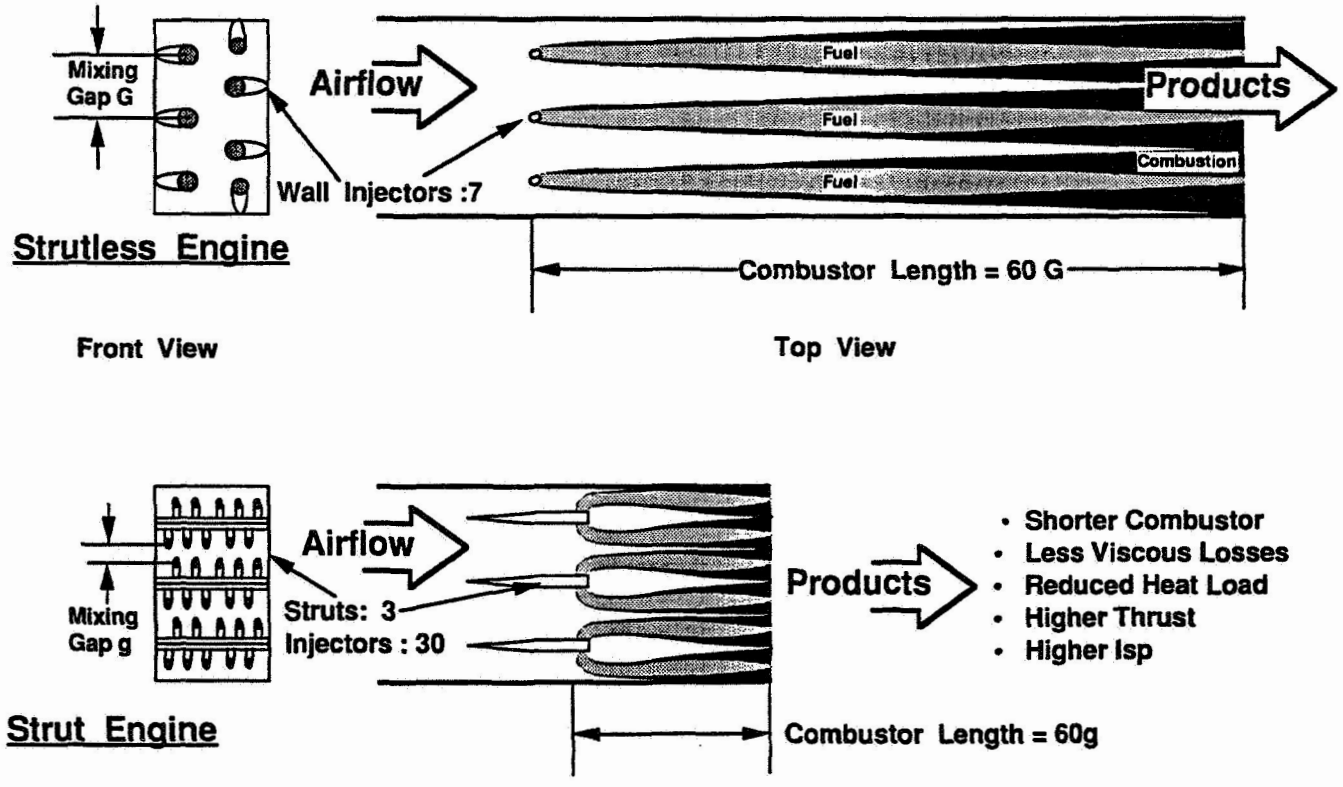

Figure 7. **Struts Enable Shorter and Higher Performing Engine**

TURBOMACHINERY

The turbomachinery, in particular the liquid hydrogen fuel pump, may be considered the Achilles heel of high-performance rocket engines. Unlike the conventional rocket engine, the strutjet provides high performance without relying on cutting edge turbomachinery technology, particularly advanced, high-stress, high-temperature materials. This in turn contributes significantly to increased reliability, extended life, and reduced cost of the strutjet engine.

The difference between the conventional rocket and the strutjet engines is manifested in the approach taken to achieve high performance. The mission average Isp of a conventional rocket-powered SSTO vehicle is strongly dependent on the vacuum Isp. Vacuum Isp is improved by using a high-area-ratio nozzle. If a fixed nozzle is used, the area ratio is the same at takeoff and during vacuum flight. Thus, the maximum fixed area ratio that can be used is determined by incipient nozzle flow separation at sea level. Nozzle flow separation occurs when nozzle exit pressure falls below 20 to 30 percent of the back pressure. High chamber pressures thus allow a higher area ratio without separation. Thus, conventional rocket engines typically operate at high chamber pressure, 3000 psi or more at takeoff, to permit an area ratio around 60:1. High chamber pressures place high demands on turbo pump discharge pressure and increase turbopump power level. This, in turn, produces unacceptable bleed losses if a gas generator cycle were used because overboard dump of the turbine drive gas would reduce mission average Isp more than the high area ratio would gain. Using the staged combustion cycle improves performance, but further increases required pump discharge pressure to provide the required pressure ratio across the turbine. This added cycle pressure can be partially mitigated by raising turbine inlet temperature. Fuel pump discharge pressures of 7000 to 8000 psi and turbine inlet temperatures on the order of 1700 °R are typically required for a staged combustion cycle engine with a 3000-psi chamber pressure.

In contrast, the strutjet can achieve high vacuum Isp at a chamber pressure of only 2000 psi because vacuum area ratio is determined by the large airbreathing nozzle exit, providing an area ratio of about 500:1. At takeoff, area ratio, which is set by the nozzle in the strut rocket, is typically on the order of 40:1. By definition, the strutjet engine has two distinct nozzle area ratios. Also, it can use a gas generator cycle that limits hydrogen pump discharge pressure to only about 3000 psi. The low required pumping power and available turbine pressure ratio allow low turbine inlet temperatures of about 1000 °R. Afterburning the fuel-rich turbine exhaust gases with the drawn-in or rammed-in air of the ducted rocket increases the Isp contribution of the exhaust gas from 200 sec for a conventional overboard dump to about 1000 seconds. In

summary, demands on the strutjet fuel turbopump are significantly reduced relative to the conventional rocket as shown below:

	Rocket	Strutjet	Reduction, %
Chamber Pressure, psi	3000	2000	33
Fuel Pump			
Discharge Pressure, psi	7000	3000	57
Turbine Inlet Temperature, °R	1700	1000	41
Turbine Tip Speed, rpm	2000	1700	15
Rotational Stress, %	100	72	28

As shown in Figure 4, during ascent from sea level to ramjet takeover and from scramjet cut-off to orbital insertion, the engine operates in the "ducted rocket" mode using drawn-in or rammed-in air to enhance thrust through mass flow increase and afterburning residual rocket fuel. During this mode, the engine's fuel side is powered by a fuel-rich gas generator exhausting into the ram/scram duct through dedicated injectors. The oxygen side is powered by an oxidizer-rich staged combustion cycle. In contrast to the hydrogen side, stage combustion on the oxygen side does not impose a technical challenge since oxygen, being a high density fluid, can be pumped to the required pressure levels with relative benign shaft speed. Full-flow oxygen-rich preburner technology has become available from Russia, providing the advantages of reduced turbine temperature and elimination of the interpropellant seals needed for fuel-rich gas-driven oxygen pumps. Figure 8 illustrates the engine cycle during the ducted rocket mode of operation. During pure airbreathing modes, the engine's entire oxygen feed system is inactive. As shown in

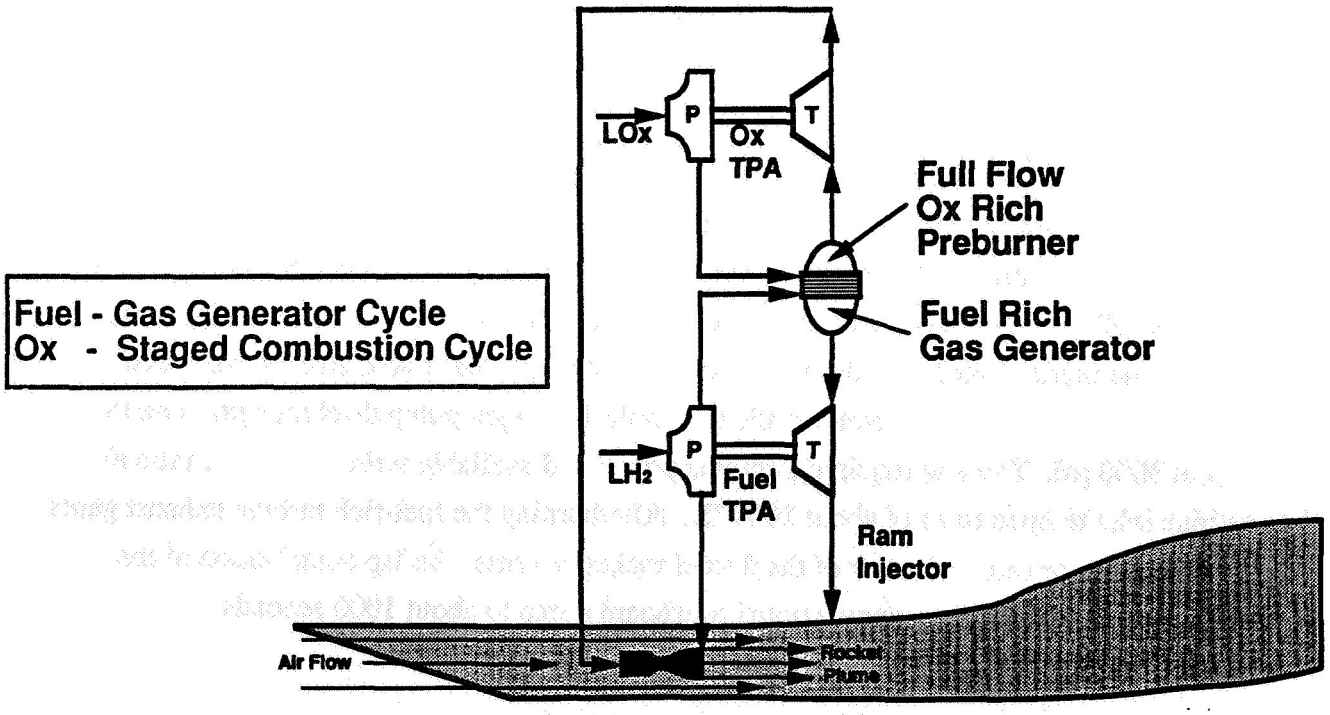

Figure 8. **Ducted Rocket Mode Provides High Thrust for Takeoff and Ascent**

Figure 9, the fuel side operates now in a benign expander cycle mode using heat available from required cooling of the engine structure. Figure 10 illustrates the location of these various operating modes on the fuel pump map.

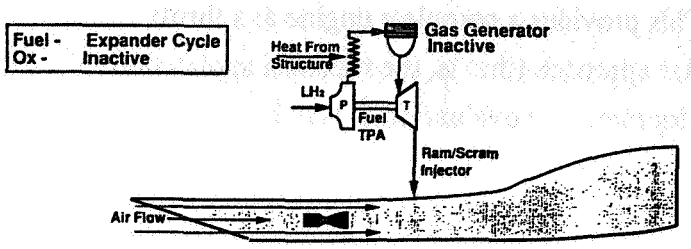

Figure 9. **Ram/Scramjet Modes Provide High Isp for Acceleration From Mach 2.5 to 8**

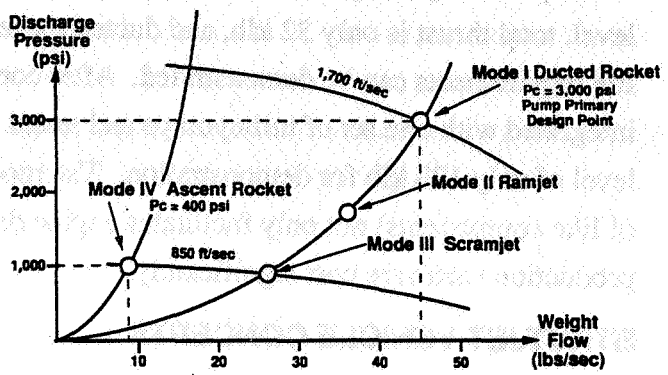

Figure 10. **Variable-Speed Hydrogen Turbopump Operates at Four Power Levels**

ENGINE ARCHITECTURE

As will be shown later, a typical TSTO vehicle that delivers 8000 lb of payload to an LEO orbit has a GLOW of 340,000 pounds. Figure 11 shows the top-level architecture of the strutjet propulsion system for this application. Takeoff thrust at 512 klb provides a comfortable thrust-

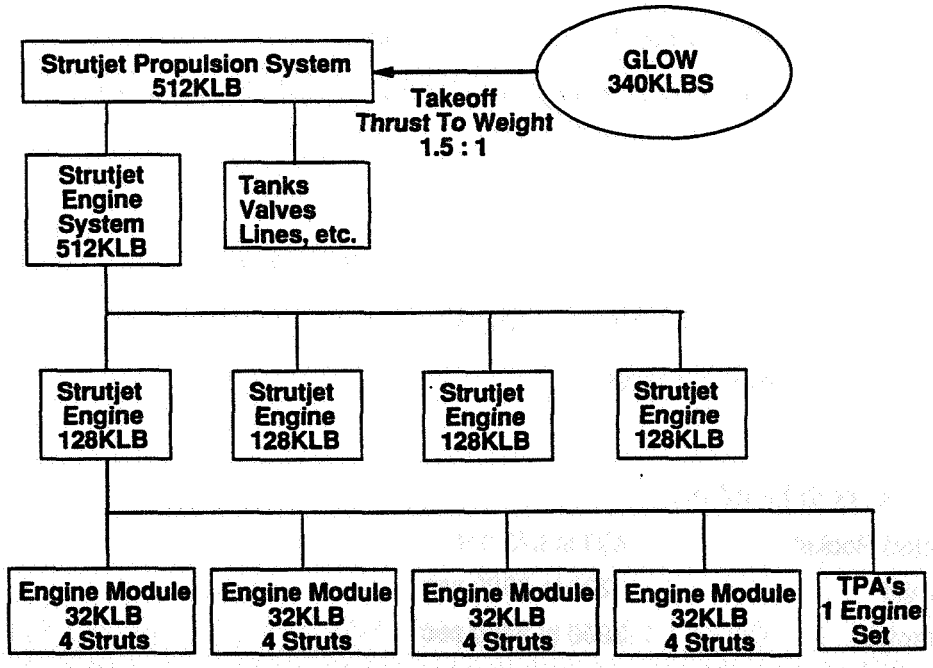

Figure 11. **Typical Strutjet Engine System Architecture**

to-weight ratio of 1.5 for net vehicle acceleration and engine out capability. The overall engine system integrates four self-contained strutjet engines each consisting of four engine modules and one turbopump set. Each module is provided 32 klb of thrust and consists of four struts delivering 8 klb thrust.

This concept is very flexible in terms of engine-vehicle integration and in flight operation. Also, it lends itself to a very logical and low-cost development approach. First, thrusters are being developed and packaged into one strut. Then, four struts are evaluated as a module. At this level, total thrust is only 32 klb, and ducted rocket and ram/scramjet performance, weight, and life requirements can be demonstrated. After completing these tests, four engine modules are integrated with one set of turbopumps and tested. This provides a complete engine at a thrust level of only 128 klb for demonstration. The modular approach (that is, the repeated application of like components) not only facilitates engine development and evaluation, it also lowers production hardware cost significantly.

STRUTJET VEHICLE CONCEPTS

In late 1993, Martin Marietta conducted an extensive analysis to determine which launch vehicle configurations have the highest potential for meeting requirements for a launch system delivering 8000 lb to GTO. Results of this analysis showed that two of the reusable candidates that best met the requirements were a single-stage-to-LEO launch vehicle (SSTO) with an upper stage to GTO and a two-stage-to-GTO launch vehicle (TSTO). Both concepts use a strutjet propulsion system on the reusable first stage of the vehicle and an expendable upper stage. Common to both vehicle configurations are the following attributes:

- Vertical takeoff/horizontal landing of reusable first stage
  - Good takeoff and low-speed acceleration provided by ducted rocket system
- Expendable second stage
  - SSTO concept : staged at LEO
  - TSTO concept : staged at 16 kft/sec; first stage returns to launch site
- Potential for single launch site for all inclinations
- High mission average specific impulse
  - SSTO : 585 sec
  - TSTO: 750 sec, both based on:

Ducted Rocket	400 to 675 sec
Ramjet	3200 to 3800 sec
Scramjet	3800 to 2400 sec
Pure Rocket	470 sec

- Lower takeoff and dry weights than conventional rocket vehicles
  - GLOW reduction-strutjet/chemical rocket: 410 klb/1100 klb ≈ 1/3
  - Dry weight reduction-strutjet/chemical rocket: 63 klb/110 klb ≈ 1/2

- Airbreathing operation to only Mach 8
  - Manageable aero heating environments
  - Testable with today's facility capabilities
- Available material technologies for engine and vehicle
- Large potential for future payload growth and cost reductions
  - Isp increase through airbreathing operation at higher than Mach 8
  - Mass fraction improvement through advanced materials
- Single propellant combination for all operational modes, LOX/LH_2.

Figure 12 illustrates the design of the SSTO concept. The TSTO vehicle concept, also shown, is similar in design with the first stage smaller and the second stage larger, requiring two RL-10A4

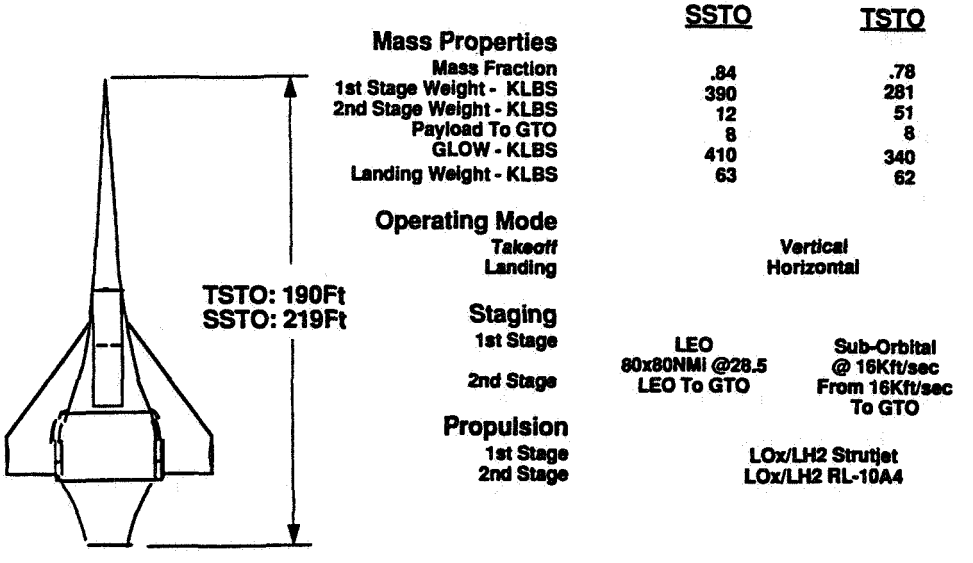

Figure 12. **Strutjet-Powered Vehicles for SSTO and TSTO**

engines. The first stage of the TSTO vehicle includes fuel to return to the launch site. Trajectories for the reusable launch vehicles are shown in Figure 13 for SSTO and in Figure 14 for TSTO. Both trajectories, after a short rocket-powered vertical rise, execute a pitchover phase to enable airbreathing capability until Mach 8. When a flight speed of Mach 8 is achieved the airbreathing modes are terminated, and the vehicles pitch up into a steeper ascent trajectory under pure rocket power. As shown in Figure 13, orbit insertion of the SSTO vehicle occurs at a down range of about 1,000 nmi. In contrast, as shown in Figure 14, second stage deployment occurs at a downrange of about 400 nmi. The first stage then follows with a ballistic trajectory to an altitude of about 300,000 ft, descends and turns unpowered, restarts the ramjet at about 1400 nmi downrange, and cruises back to the launch site at an altitude of 100,000 ft and a flight speed of Mach 5.

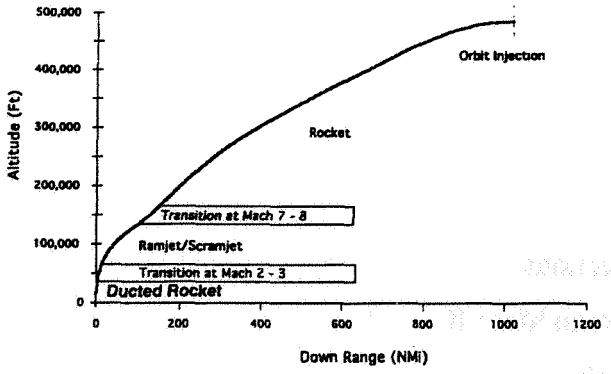

Figure 13. **SSTO: Trajectory of Reusable Strutjet-Powered Vehicle**

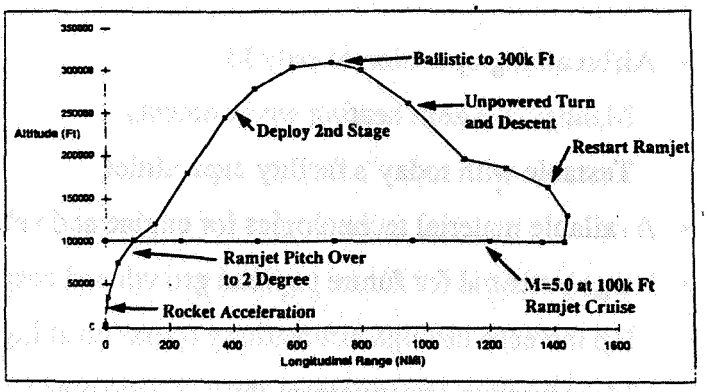

Figure 14. **TSTO: Trajectory of Reusable Strutjet-Powered First Stage**

SUMMARY AND CONCLUSIONS

For the reference mission, delivery of 8000 lb to GTO, two vehicle concepts are defined: an SSTO with an expendable second stage and a TSTO with stage separation at about 16 kft/second. Both systems are significantly lighter in takeoff and dry weight, 67 and 50 percent respectively, than their conventional rocket counterparts.

Design of an SSTO launch system is extremely sensitive to the performance of the propulsion system. Using existing or upgraded conventional chemical rocket propulsion systems results in vehicle designs that are not compatible with sound engineering practices due to their high sensitivity to system Isp and inert weight growth. These sensitivities can be brought down to levels that are consistent with today's practices if a combined cycle engine like Aerojet's strutjet is used. The strutjet is a propulsion system that, due to its possible mission average Isp of 585 to 750 sec and a relatively high engine thrust-to-weight ratio of about 22, enables using state-of-art material technology.

The strutjet is a rugged engine design using state-of-the-art materials and manufacturing processes. Fundamental operating conditions of the engine, like ducted rocket performance and ram-to-scramjet transition, have been demonstrated by test or can be derived reliably from existing data. Test data are available for inlet aerodynamic performance and thermal management of strut leading edges, rocket chambers, and ram duct engine sidewalls and panels. Strut injectors have been proven successfully for hydrocarbon fuels; similar results for hydrogen fuel are expected.

Next steps in developing this promising space launch concept center around additional component design, fabrication and ground tests, an overall engine design, fabrication and free jet test. Subsequent subscale flight tests will demonstrate the governing principals of this propulsion concept and its scalability to a full operational engine and vehicle.

427179
Pgs 3

N95- 70886

TECHNOLOGY NEEDS FOR SINGLE STAGE TO ORBIT PROPULSION

S. Stoyanof and J. Monk
NASA Marshall Space Flight Center
Huntsville, Alabama

INTRODUCTION

Propulsion Technologies

NASA's Reusable Launch Vehicle (RLV) Propulsion Technologies Program includes maturation and demonstration activities supporting a variety of propulsion system concepts. The primary emphasis of this program is to identify and mature the technologies required to enable the development of the optimum main propulsion system (MPS) for RLV applications. By applying a methodical approach to the maturation process, through use of subscale system and subsystem validation testing and, where appropriate, engine system level technology demonstrations, the development cost of the RLV MPS will be substantially reduced. The major building blocks of this approach are Engine Systems and MPS Subsystem Demonstrators, Supporting Component Technologies, and Russian Technologies, and are described below.

PROGRAM SPECIFICS

Engine Systems and MPS Subsystem Demonstrators

The key technology capability that historically has not been demonstrated prior to concept selection has consistently been the engine system. Demonstration of key technologies at the engine system and MPS subsystem level will provide the understanding required to make an informed concept selection prior to initiation of the full-scale development of the engine system. Adequate system-level technology demonstration will greatly reduce the cost and risk of the development program.

Engine Systems

Operability is one of the most critical requirements for an RLV propulsion system. Test-bed engines provide a cost effective, practical approach to 1) the development of operability schemes, 2) a means for exploration of engine control concepts, and 3) a tool for the exploration of system simplification. In addition, the demonstration engine concept provides the capability to generate an improved set of derived requirements - individual component requirements, engine system requirements, and operability requirements. The test-bed engine system will permit

extrapolation of requirements from demonstrated conditions to the desired design point. Combined with the other technology demonstrations, this process will develop design data bases, correlate test data with predictions, and anchor analysis models and codes. The most promising engine system concepts are included in the initial phase of the demonstration program, which includes the SSME-derived bell annular tripropellant engine and the Russian RD-0120 derived tripropellant engine.

Subscale MPS Test-Bed

The primary function of the subscale MPS test-bed is to assess the capability of competing MPS concepts to meet performance and operability requirements of the RLV program. The ability to assess propulsion system integration issues early in the design/development process is key to controlling costs. In addition, accurate definition of derived requirements is critical to the successful execution of the full-scale development program. The subscale MPS subsystems test-bed will permit extrapolation of requirements from demonstrated conditions to the desired design point.

Integrated Propulsion System Test-Bed

A subscale integrated propulsion systems test-bed will assess the capability of a fully functional, integrated RLV propulsion system to achieve the desired performance and operability goals. The demonstrator consists of RP-1, LO_2, and LH_2 tanks, propellant feed system, pressurization system, propellant loading system, propellant conditioning system, vehicle health management, tank support structure, and thrust structure. These components are installed into a fully integrated ground test facility which will provide maximum flexibility for testing advanced system components.

Integrated Auxiliary Propulsion System Test-Bed

One key approach toward implementing operability into the propulsion system design is to use common propellants (O_2/H_2) for all propulsion and power functions on the vehicle; including the main propulsion, auxiliary propulsion and reaction control thrusters, auxiliary power unit (APU), thermal control system, and fuel cells. A liquid/gas conversion (LGC) system will be designed and built to take the LO_2/LH_2 from the main propellant tanks, pressurize and vaporize the cryogen to warm high-pressure gas, and supply the RCS thrusters. An LGC system, compared to an all-gas RCS, will provide a significant weight/volume savings. A Russian O_2/H_2 APU will provide the needed hydraulic power without penalizing the main engine power balance. The propellant conditioning LGC subsystem and the APU will be integrated into a

workhorse pallet which will be fully tested for function, operability, and performance in preparation for future integration into the Delta Clipper-Experimental Advanced (DC-XA) demonstrator vehicle for ground/flight testing that will serve to further mature these technologies.

Supporting Component Technologies

The primary objective of the RLV Propulsion Technology Program is the maturation and demonstration of engine system and MPS subsystem technologies. However, there are additional component technologies that support the LO_2/LH_2 and LO_2/LH_2/RP-1 engine system concepts that require early technology development. These technologies include the demonstration of the performance and manufacturing processes of modular combustion chamber concepts and design, fabrication, and testing of oxidizer-rich LO_2/LH_2 preburners, oxidizer-rich LO_2/RP-1 preburners, and testing of candidate turbine drive system materials.

Russian Technologies

Recent data on the technological capabilities of the former Soviet Union are being evaluated for application in the RLV Program. The Russian propulsion systems make extensive use of oxygen rich combustion to improve the efficiency of their engines. The transfer and understanding of this technology could provide significant returns for successful incorporation into U.S. propulsion systems. In addition to the oxygen-rich technologies, there are Russian manufacturing methods/techniques and materials that have been evaluated and selected for inclusion in the initial phase of the RLV Program. In addition to existing technology, the Russians are currently working on development of a tripropellant derivative of the venerable RD-0170 engine.

427180
Pg 5

N95-70887

LOX DROPLET VAPORIZATION IN A SUPERCRITICAL FORCED CONVECTIVE ENVIRONMENT

Chia-chun Hsiao and Vigor Yang
Propulsion Engineering Research Center
Department of Mechanical Engineering
The Pennsylvania State University
University Park, PA 16802

SUMMARY:

A systematic investigation has been conducted to study the effects of ambient flow conditions (i.e. pressure and velocity) on supercritical droplet gasification in a forced-convective environment. The model is based on the time-dependent conservation equations in axisymmetric coordinates, and accommodates thermodynamic nonidealities and transport anomalies. In addition, an efficient scheme for evaluating thermophysical properties over the entire range of fluid thermodynamic states is established. The analysis allows a thorough examination of droplet behavior during its entire lifetime, including transient gasification, dynamic deformation, and shattering. A parametric study of droplet vaporization rate in terms of ambient pressure and Reynolds number is also conducted.

TECHNICAL DISCUSSION:

Many liquid-fueled combustion systems (such as diesel engines, ramjets, gas turbines and liquid rockets) are designed to deliver fuel and oxidizer into a pressurized chamber through atomizers which break the liquid fuel and form a large number of droplets. These droplets then undergo a series of vaporization, breakup, and mixing process to form fuel-oxidizer mixture for reaction. Modern combustor designs even extend the chamber operational condition into regimes well above the thermodynamic critical points of fuels for better performance. Information regarding droplet trajectory, breakup criteria, and gasification rate in a supercritical convective environments becomes crucial.

Although several studies have been conducted to investigate the characteristics of droplet vaporization in supercritical conditions (Hsieh *et al.*, 1991; Shuen *et al.*, 1992; Yang *et al.*, 1994), effects of ambient convective flow on droplet behavior have not yet been addressed. The purpose of the present work is to conduct a systematic investigation into supercritical droplet vaporization in a forced-convective stream. The formulation starts with the time-dependent conservation equations of mass, momentum, energy, and species concentration in axisymmetric coordinates for both droplet interior and ambient gases. Full account is taken of thermodynamic non-ideality and transport anomaly during the droplet phase transition from the subcritical to supercritical state. In addition, a unified property evaluation scheme based on the BWR equation of state and extended corresponding-state technique is established to predict fluid thermophysical properties. The governing equations and associated boundary conditions are solved numerically using an implicit finite-difference scheme with a dual time-stepping integration scheme.

In the first part of this study, a series of calculations has been carried out to study liquid oxygen (LOX) droplet gasification in a hydrogen stream at different pressures and Reynolds numbers. Detailed velocity and thermodynamic properties contours have been studied thoroughly. Secondly, a parametric study is conducted to establish correlations for droplet lifetime, gasification rate, and drag coefficient as functions of ambient pressure, temperature, droplet diameter and Reynolds number.

Governing Equation

The flow under consideration is laminar and axisymmetric. If body forces, viscous dissipation, and thermal radiation are ignored, the conservation laws can be written in the following form.

Mass:

$$\frac{\partial}{\partial t}\iiint \rho dV + \iint \rho u_j dA_j = 0. \tag{1}$$

Momentum:

$$\frac{\partial}{\partial t}\iiint \rho u_i dV + \iint \rho u_i u_j dA_j = \iint \tau_{ij} dA_j. \tag{2}$$

Energy:

$$\frac{\partial}{\partial t}\iiint \rho e dV + \iint \rho e u_j dA_j = \iint \tau_{ij} u_i dA_j - \iint (q_T)_j dA_j. \tag{3}$$

Species Concentration:

$$\frac{\partial}{\partial t}\iiint \rho Y_l dV + \iint \rho Y_l u_j dA_j = -\iint (q_{M,l})_j dA_j. \tag{4}$$

where

$$\tau_{ij} = -p\delta_{ij} + 2\mu e_{ij} - \frac{2}{3}\mu(\nabla \cdot u)\delta_{ij}.$$

Standard notations in fluid mechanics and thermodynamics are used in (1)-(4). The specific total energy e at a given pressure is defined as

$$e = \sum_{l=1}^{N} Y_l (h^0_{f,l} + \int_{T_{ref}}^{T} C_{p,l} dT) - \frac{p}{\rho} + \frac{u_i u_i}{2},$$

where the index N represents the number of species considered, Y_l the mass fraction of species l, and T_{ref} the reference temperature for enthalpy of formation. Fick's and Fourier's laws are used to approximate the species and thermal diffusion in Eqs. (3) and (4), respectively.

Property Evaluation

An extended corresponding-state principle, which requires only critical constants and Pitzer's acentric factor for each component, is used to predict properties over the entire range of fluid p-v-T states for a mixture. The basic idea of the corresponding state model is relatively straightforward. It is assumed that the configurational properties of a single-phase mixture can be adequately represented by those of a hypothetical pure fluid. The properties of this hypothetical pure fluid are then evaluated via corresponding states with respect to a given reference fluid. The extended corresponding-state theory using shape factors and mixture combining rules can satisfactorily predict the thermodynamic properties of mixtures from an equation of state of the reference substance. Meanwhile, transport properties are expressed as a function of density and temperature through conformal mapping to the reference fluid. For accurate property prediction, it is desirable to have an equation of state that accurately represents the p-v-T behavior of a mixture.

In the present study of multicomponent droplet dynamics at supercritical conditions, a generalized BWR equation of state is used to predict both gas and liquid phase behavior of the reference fluid.

$$p = \sum_{n=1}^{9} a_n(T)\rho^n + \sum_{n=10}^{15} a_n(T)\rho^{2n-17} e^{-\gamma\rho^2} \tag{5}$$

where γ is 0.04, and the functional coefficients $a_n(T)$ vary with the reference fluid. This equation of state must be solved iteratively to obtain the density of the reference fluid. The density of the mixture is then obtain through an extended corresponding-state method.

$$\rho = \frac{\rho_0[T/f_{m,0}, p(h_{m,0}/f_{m,0})]}{h_{m,0}} \tag{6}$$

Enthalpy, internal energy, entropy, fugacity, etc., are important thermodynamic properties, which can be related to engine operating variables such as temperature and density. The heat capacity of a mixture can be expressed as the sum of the ideal gas heat capacity at the same temperature and composition plus a residual heat capacity (Leach, 1967)

$$C_p = C_p^0 + \Delta C_p \tag{7}$$

where ΔC_p is most conveniently determined by

$$\Delta C_p = T \int_\infty^V (\frac{\partial^2 p}{\partial T^2}) dV - \frac{T(\partial p/\partial T)_V^2}{(\partial p/\partial V)_T} - R$$

Viscosity coefficient for a mixture fluid can be reproduced using a two-shape-factor corresponding-state method with correction for mass and size difference.

$$\mu_{mix}(\rho, T, \{x_a\}, \{m_a\}) = \mu_0(\rho_0, T_0) F_\mu + \Delta\mu^{ENSKOG} \tag{8}$$

where

$$F_\mu = \left(\frac{M_m}{M_0}\right)^{1/2} f_{x,0}^{1/2}\ h_{x,0}^{-2/3}$$

Here M_m is the molecular weight of the mixture. A relatively simple correction taken from the Enskog hard sphere theory is used with the predictions. The function corrects for deviations in mass mixing rules at low densities, and for differences in molecular size.

$$\Delta\mu^{ENSKOG} = \mu_{mix}^{ENSKOG}(\{\rho\sigma_a^3\}, \{x_a\}, \{m_a\}) - \mu_x^{ENSKOG}(\rho\sigma_x^3, m_x) \tag{9}$$

The Enskog model (1954) has been solved for a multicomponent mixture of hard spheres by Tham and Gubbins (1971) and is used to calculate μ_{mix}^{ENSKOG} and μ_x^{ENSKOG}.

Ely and Hanley proposed an expression for thermal conductivity which can be divided into three contributions,

$$\lambda = \lambda'(\rho, T) + \lambda''(T) + \Delta\lambda_{crit}(\rho, T) \tag{10}$$

The first term on the right-hand side is caused by the transfer of energy from purely collisional or translational effects and can be calculated via the corresponding-state method. The second term in Eq. (10) is due to the transfer of energy via internal degrees of freedom. This is independent of density and may be evaluated by the modified Eucken correlation with an empirical mixing rule for polyatomic gases. Modern theory of transport phenomena (Sengers,1971,1972) predicts an infinite thermal conductivity at the pure fluid critical point and a large enhancement of thermal conductivity in the vicinity of the critical point. The third term in Eq. (10) accounts for this phenomenon and is a function of temperature and density.

RESULTS:

The theoretical model described in the preceding sections has been applied to LOX droplet vaporization in a hydrogen stream at different pressures (100, 200 and 400 atm) and Reynolds numbers ($60 - 250$). A LOX droplet with initial temperature of 100 K and introductory diameter of 100 μm is injected into the 1000 K hydrogen stream. Part of the heat transferred from the gas phase goes into vaporizing droplet, while the remainder goes into heating the droplet interior. Since the critical mixing temperature of oxygen is 154.6 K at 1 atmosphere and decreases with increasing pressure, the droplet becomes supercritical almost instantaneously upon introduction to the hydrogen gas at the supercritical pressure levels of interest (100, 200 and 400 atm). Once this occurs, the enthalpy of vaporization and surface tension vanish, leaving an essentially continuous medium with no abrupt phase change in the vaporization process. Although the interior region of the droplet remains at the liquid state with a subcritical temperature distribution, the medium attributes (ρ, p, T and thermophysical properties) vary continuously between the liquid core and ambient gases with no distinct liquid surface as exists for a droplet in a subcritical environment. As a result, a single-phase analysis is used to treat the droplet interior and ambient gases simultaneously as one fluid. Since there is no discontinuity, the surface of the droplet is defined as the surface at which the temperature attains the value of the critical mixing temperature.

Density contours with streamline patterns are shown in Fig. 1 for the 5 m/s ambient flow case considered here. A recirculating flow in the wake of the droplet occurs as a result of the shear force between liquid oxygen and the surrounding gases. For the higher Reynolds number case (15 m/s), droplet shattering is seen, as shown in Fig. 2. The convective flow penetrates through the liquid phase, breaking the droplet into two parts - the core disk and the surrounding ring. The wake region, however, is convected away from the droplet due to the diminishing shear flow between gas and liquid phases. In both of these supercritical cases, no discernible flow circulation is found in the droplet interior, in contrast to the Hill's vortex found in low-pressure cases.

Time variations of droplet residual mass at different pressures and velocities are shown in Figs. 3 and 4. When droplet surface reaches critical condition, no sharp boundary between gas and liquid phases exists. The entire flow field becomes a continuous medium. Under this condition, droplet vaporization is best characterized by the droplet residual mass which is confined by a surface with critical mixing temperature. Results show that high Reynolds number favors droplet evaporation. In a stronger convective flow (15 m/s), droplet tends to deform and as such increases contact surface with ambient flow, while the ambient stream convects the gasified oxygen downstream and enhances both thermal and species diffusion. Figures 5 and 6 show the time variations of droplet moving velocity. The first derivative of these curves can be used to calculate droplet acceleration. Drag force defined by Newton's second law can be obtained by multiplying acceleration of center of gravity with its mass.

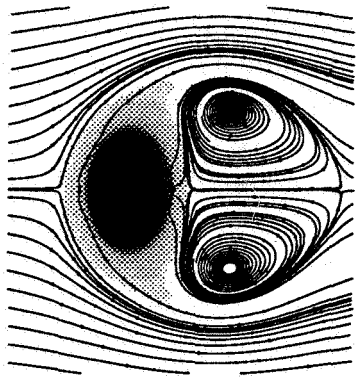

Figure 1: Density Contours and Streamlines at $t = 176\mu s$, LOX/H_2 System, $D_0 = 100\mu m$, $p_\infty = 100$ atm, and $U_\infty = 5m/s$.

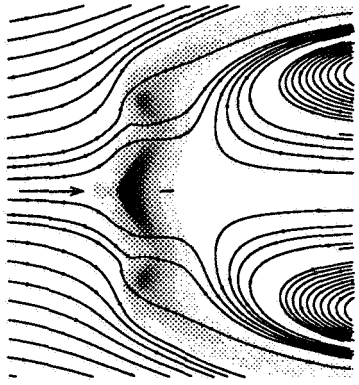

Figure 2: Density Contours and Streamlines at $t = 176\mu s$, LOX/H_2 System, $D_0 = 100\mu m$, $p_\infty = 100$ atm, and $U_\infty = 15\ m/s$.

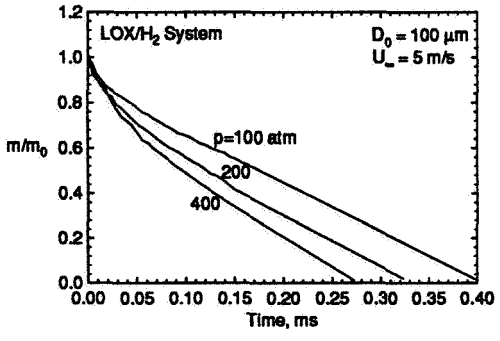

Figure 3: Time Variations of Droplets Residual Mass at Various Pressures, LOX/H_2 System, $D_0 = 100\mu m$, and $U_\infty = 5\ m/s$.

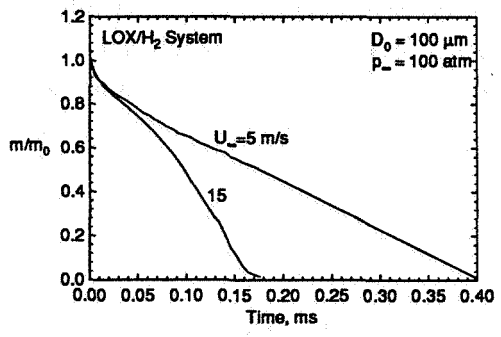

Figure 4: Time Variations of Droplet Residual Mass under Various Convective Velocities, LOX/H_2 System, $D_0 = 100\mu m$, and $p_\infty = 100$ atm.

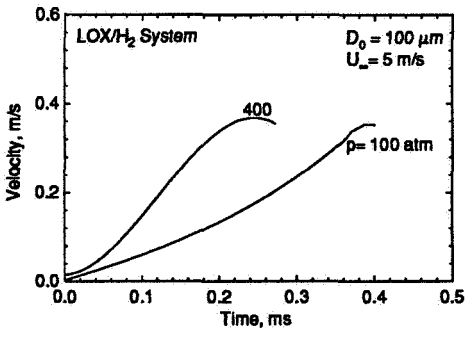

Figure 5: Time Variations of Velocity of Center of Gravity for Oxygen at Various Pressures, LOX/H_2 System, $D_0 = 100\mu m$, and $U_\infty = 5\ m/s$.

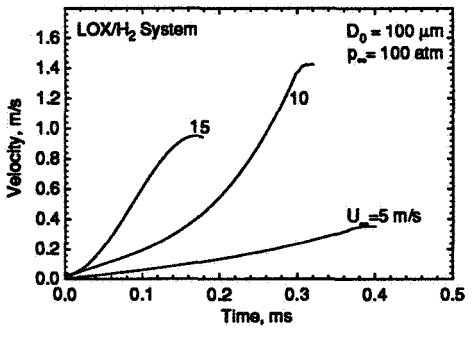

Figure 6: Time Variations of Velocity of Center of Gravity for Oxygen under Various Convective Velocities, LOX/H_2 System, $D_0 = 100\mu m$, and $p_\infty = 100$ atm.

Pg 9 427182

N95- 70888

SHADOWGRAPHY OF TRANSCRITICAL CRYOGENIC FLUIDS

R. D. Woodward and D. G. Talley
USAF Phillips Laboratory
OLAC PL/RKFA
Edwards AFB, CA 93524

T. J. Anderson and M. Winter
United Technologies Research Center
East Hartford, CT 06108

SUMMARY/OVERVIEW:

The future of liquid-rocket propulsion depends heavily on continued development of high pressure liquid oxygen/hydrogen systems that operate near or above the propellant critical states; however, current understanding of transcritical/supercritical injection and combustion is yet lacking. The Phillips Laboratory and the United Technologies Research Center are involved in a collaborative effort to develop diagnostics for and make detailed measurements of transcritical droplet vaporization and combustion. The present shadowgraph study of transcritical cryogenic fluids is aimed at providing insight into the behavior of liquid oxygen or cryogenic simulants as they are injected into a supercritical environment of the same or other fluids. A detailed history of transcritical injection of liquid nitrogen into gaseous nitrogen at reduced pressures of 0.63 (subcritical) to 1.05 (supercritical) is provided. Also, critical point enhancement due to gas phase solubility and mixture effects is investigated by adding helium to the nitrogen system, which causes a distinct liquid phase to re-appear at supercritical nitrogen pressures. Liquid oxygen injection into supercritical argon or nitrogen, however, does not indicate an increase in the effective critical pressure of the system.

DISCUSSION:

Background and Objectives

To meet today's requirements for greater economy, efficiency, and reliability in space and launch propulsion, there exists a need within the liquid-rocket-propulsion community to better understand and predict mechanisms related to combustion performance, chamber wall and injector faceplate heat transfer, and combustion instabilities. This is particularly true in high pressure systems in which the fuel or oxidant (liquid oxygen in rocket propulsion systems) is injected at supercritical pressures but initially at a subcritical temperature. The propellant then undergoes a transition to a supercritical state as it is heated and burned in the combustion chamber—the so-called transcritical process. Compared with the subcritical case, transcritical and supercritical injection and combustion remain relatively poorly understood.

There are a number of differences from the subcritical case that need to be addressed. Gas/liquid density ratios are near unity, so the quasi-steady gas phase assumption commonly employed in subcritical studies is no longer valid. The equilibrium "wet bulb" condition may also not exist. Thus transcritical droplet vaporization/combustion is a fully unsteady phenomenon. The computation of properties becomes significantly more complicated in that properties such as diffusion coefficients become functions of pressure as well as temperature, and the solubility of the gas phase in the liquid phase increases significantly. The latter effect can mean that the effective critical pressure of the soluble mixture can be several times the critical pressure of the pure phase. Other property anomalies can lead to singular behavior near the critical condition. For instance, the burning rate has been observed to reach a maximum near the critical pressure, and the potential to couple with combustion instabilities may be increased. The surface tension also vanishes, potentially leading to significantly different droplet deformation and breakup mechanisms. These latter mechanisms can be particularly important because they have a direct effect on mixing.

Past experimental studies of transcritical droplet processes have been mostly limited to global measurements such as the variation of droplet lifetimes and burning times as a function of pressure [1-4]. While useful, these provide an incomplete picture of the transport and breakup mechanisms that can contribute to mixing and the potential to couple with combustion instabilities. On the other hand, the theoretical understanding of transcritical droplet vaporization, combustion, and breakup has advanced significantly in recent years due to the introduction of new models [5,6]. However, these remain unverified experimentally. The objective of work ongoing at the Phillips Lab and United Technologies Research Center (UTRC) is to provide detailed measurements of transcritical droplet flow fields and temperature and composition profiles that can be used to validate these models, as well as to develop semi-empirical correlations for direct use in comprehensive engine design codes.

Detailed measurements of droplet flow fields and temperature and composition profiles are believed to be feasible through a combination of 1) precise control of the droplet generation process to achieve repeatable, mono-sized droplets, and 2) incorporation of innovative droplet diagnostic techniques that have recently been developed [7-9]. Since the primary application at the Phillips Laboratory is rocket propulsion where the transcritical fluid is typically liquid oxygen (LOX), a piezoelectric droplet generator has been developed which is capable of producing a monodisperse stream of cryogenic droplets at high pressures. In the other arena, advanced droplet diagnostics have been under development for a number of years under AFOSR and Phillips Laboratory funding by several researchers [7-9]. These have been limited almost exclusively to subcritical droplets. Application of these and other techniques is currently being evaluated in a collaborative effort with UTRC. At present, Raman imaging appears attractive at high pressures due to the increased signal from the high molecular number density, and can potentially provide both species and temperature measurements. As part of the collaborative effort, a preliminary study of Raman imaging of LOX droplets at high pressures has been performed at UTRC facilities. The shadowgraph study emphasized in this paper was conducted in support of that effort and was aimed at understanding some of the practical issues involved before extensive application of the advanced diagnostic techniques.

Cryogenic Droplet Generation

The cryogenic droplet generator is supplied with high-pressure gaseous oxygen (or nitrogen) that is condensed within an annular liquid nitrogen heat exchanger. The main droplet generator components include a 7 micron filter, a cylindrical piezo-electric crystal (piezo), and a 127 μm (.005") diameter sapphire orifice. With electrical excitation, the piezo transmits an oscillatory disturbance to the condensed oxygen. In cryogenic operation, the device has been run in an augmented Rayleigh breakup mode for creating a droplet stream. A low-speed LOX jet is established at the droplet generator exit, then the piezo excitation is adjusted to augment the natural frequencies of the jet breakup. By altering the driving frequency and the flowrate, droplet size and spacing can be controlled. Typical LOX droplet sizes are 100 to 300 microns with inter-droplet spacing of 2 to 10 diameters. The generator is installed in a high pressure vessel with optical access on four sides so that the droplet stream can be observed and various diagnostic techniques can be employed. Repeatable, mono-sized LOX droplet generation has been achieved at pressures to 1200 psig in a helium environment.

Figure 1 illustrates typical LOX droplet generation at two different helium pressure environments. Figure 1(a) shows a very steady droplet stream at a pressure of 200 psig. while Fig. 1(b) shows a less steady, vigorously vaporizing stream at 1000 psig. The vaporization produces an unsteady oxygen-rich wake around each droplet that interacts with following droplets, perturbing the droplet stream trajectory. The field of view depicted in these figures is approximately 13 mm. These images were taken with a standard video-rate television camera illuminated by a

synchronized strobe pulse. All subsequent shadowgraph images used the same synchronized strobe lighting, but were recorded with an 8-bit intensified/gated camera that was setup for oxygen Raman imaging experiments.

It was uncertain if a reasonably consistent stream of LOX droplets could be generated at high pressures (above the critical pressure for pure oxygen) in for example a helium environment or at what point any apparent transcritical behavior would be observed. (Due to enhanced solubility of the gas phase in the liquid phase at high pressures and the corresponding mixture properties, transcritical effects may not be exhibited in binary systems until a chamber pressure up to several times that of the pure phase is reached.) As seen in Fig. 1(b), a fairly coherent and repeatable stream was produceable although not a trivial feat. Several effects related to the high pressure (high density) conditions were observed, e.g., enhanced vaporization (due to enhanced heat transfer) and increased droplet drag and thus noticeable droplet displacement and asphericity. Despite the high pressure effects noted, no phenomena directly attributable as supercritical behavior were observed.

Keep in mind that the temperature in the pressure vessel was typically in the range of 250-273 K, and so was always well above the critical temperature of oxygen. (See Table 1 for critical states of the propellants and simulants of interest here.) The droplet generator cooling jacket was continuously replenished with LN_2 at approximately 1 atm, and thus the initial droplet temperatures can be assumed to be near the normal boiling point of nitrogen (77 °K).

Transcritical Behavior

To understand better what could be defined as transcritical or supercritical behavior, it was decided to investigate, in a non-rigorous, macroscopic manner, the behavior of a pure substance as it transitions to supercritical conditions. Thus, experiments were conducted with transcritical injection of liquid nitrogen (LN_2) into gaseous nitrogen.

Figure 2 depicts a series of shadowgraph images of LN_2 injected through the droplet generator into gaseous nitrogen at reduced pressures (P_r, normalized by the critical pressure of N_2) of 0.63 to 1.05. In Fig. 2(a), at the subcritical chamber pressure of 300 psig ($P_r = 0.63$) a relatively coherent droplet stream can be produced. At the comparatively high density in this pressurized nitrogen environment, the character of the droplet stream is similar to that of the higher pressure LOX into helium stream shown in Fig. 2(b). At the higher subcritical pressure of 400 psig, Fig. 2(b) indicates that the droplet stream is no longer controllable. Rayleigh breakup, enabling production of a repeatable droplet stream, occurs when capillary forces are dominant. The higher Weber number environment, resulting from the higher ambient density and reduced surface tension near the critical point, changes the breakup mode to a regime where aerodynamic forces are significant and where droplet generation is unpredictable. Also, note that sporadic large drop production is simultaneously occurring at chamber pressures above 300 psig due to the condensation of gaseous nitrogen at the top of the chamber in the vicinity of the cold droplet generator exit. These droplets fall in a region close to and sometimes interspersed with the droplets exiting the generator orifice.

At pressures only slightly greater than that of Fig. 2(b) while operating under similar conditions, all signs of liquid structures disappeared. On the other hand, it was discovered that if the droplet-producing gas supply as well as the piezo were turned off, large liquid structures could be sustained at higher pressures. It might be surmised that at pressures close to the critical point, surface tension may be so low that any liquid structures of recordable size are destroyed by even the slightest flow perturbations to the point where essentially instantaneous vaporization occurs. Thus to continue the investigation while approaching the critical pressure, the mode of operation consisted of allowing condensed nitrogen to gravity feed through the droplet generator. However, under these conditions, it became uncertain whether the liquid nitrogen structures observed were originating in the droplet generator and "oozing" through the orifice essentially free of capillary

forces, or if they were originating in the chamber as condensation from the cold walls of the droplet generator housing.

Figure 2(c), at pressure nearing critical ($P_r = 0.96$), depicts a buoyancy-driven LN_2 flow that consists more of "stringy," ligament-like structures than droplets. Apparently large deformations result from small disturbances, and with insufficient surface tension to effectively reshape the liquid globs and pinch ligaments into drops, many strange-shaped liquid structures emerge. Also note that the surfaces of these structures appear somewhat fuzzy, as one might expect as critical conditions are approached.

Even closer to critical pressure ($P_r = 0.98$), Fig. 2(d) shows the same type of globular liquid structures except of much smaller characteristic dimension and with fuzzier interfaces. The liquid near the droplet generator exit especially is beginning to look cloud-like as it nears transition through the critical point. Farther downstream much of the liquid has vaporized.

At the critical pressure ($P_r = 1$), most shadowgraph visualizations indicated the presence of no liquid structures. Generally, density gradients/fluctuations were quite evident in the images. Sporadically one or two small globs with surface features would appear. As shown in Fig. 2(e), at slightly supercritical pressure ($P_r = 1.05$), small, cloud-like plumes of transcritical liquid could be seen entering the chamber occasionally. This was true also at pressures well above critical. Note that the pressure measurements quoted here are not extremely accurate (~±2% of critical pressure). Also recall that injection occurs initially at temperatures well below critical so that even at supercritical pressure, liquid could and should exist prior to heating to a critical state.

With mixture property effects on criticality in mind, a quick experiment was conducted to investigate the effect of adding a small amount of helium to the LN_2/nitrogen system since it was observed that LOX droplets could survive in a supercritical helium environment of at least $P_r = 1.7$ (based on pure O_2 critical pressure). With the nitrogen system at a slightly supercritical state ($P_r = 1.05$) and thus with no well-defined liquid structures present, a small flow (fraction of a gram per minute) of helium was introduced into the bottom of the chamber. Within a minute or two and before a noticeable increase in chamber pressure, the helium diffused throughout the chamber, apparently mixed with the injected nitrogen, and caused liquid structures with distinct surfaces to re-appear. (See Fig. 3(a).) Thus, the solubility of the helium into the nitrogen resulted in mixtures that were below the critical mixing point. Helium was allowed to continue flowing into the chamber for several minutes until a chamber pressure of 600 psig ($P_r = 1.26$) was reached. Total quantity of helium added was about 1 gram (to about 35 grams of N_2). Figure 3(b) illustrates the result: a stream of fairly spherical LN_2 droplets with well-defined surfaces.

Obviously, the solubility of helium into LN_2 (or hydrogen into LOX in the real case) at high pressures affects the way vaporization and mixing occur. However, what about larger molecular weight species? To broaden the picture, a few experiments were conducted with LOX into argon and into nitrogen. Both the LOX/Ar and LOX/N_2 systems appeared to experience transcritical effects very near the critical pressure of pure oxygen, i.e., no critical point enhancement due to gas phase solubility and mixture effects was observed. Thus, is critical point enhancement dependent on the size of the gas phase molecules? (If gas phase molecules are small enough to fill gaps in the clusters of the larger liquid molecules and hence provide additional molecular forces, would this be a mechanism to keep the cluster intact beyond the pure phase critical point?) Also, what effect do combustion products have in this scenario?

REFERENCES:

1. Faeth, G.M. Dominicis, D.P. Tulpinsky, J.F., and Olson, D.R., "Supercritical Bipropellant Droplet Combustion," *Twelfth Symposium (International) on Combustion,* The Combustion Institute, pp. 9–18 (1969).
2. Sato, J., Tsue, M., and Kono, M., "Effects of Natural Convection on High Pressure Droplet Combustion," *Comb. Fl.* 82: 142–150 (1990).

3. Natarajan, R., and Brzustowski, T.A., "Some New Observations on the Combustion of Hydrocarbon Droplets at Elevated Pressures," *Comb. Sci. and Tech.* 2: 259–269 (1970).
4. Sowles, R.E., "An Experimental Study of Carbon Dioxide Droplets Falling Through Inert High Pressure High Temperature Environments," Ph.D. Thesis, University of Wisconsin (1973).
5. Yang, V., Lin, N.N.,and Shuen, J.S., "Vaporization of Liquid Oxygen (LOX) Droplets in Supercritical Hydrogen Environments," *CST* 93-01-06 (1993).
6. Delplanque, J.-P., and Sirignano, W.A., "Numerical Study of the Transient Vaporization of an Oxygen Droplet at Sub- and Supercritical Conditions," *Int. J. Heat Mass Transfer* 36: 303–314 (1993).
7. Winter, M., "Droplet Slicing Measurements of Internal Circulation," 31st AIAA Aerospace Sciences Meeting & Exhibit, Reno, NV, paper 93–0900 (1993).
8. Winter, M., and Melton, L., "Fluorescent Diagnostics and Fundamental Droplet Processes," AFOSR Contractors Meeting in Propulsion (1994).
9. Chang, R.K., "Nonlinear Optical Spectroscopy of Multicomponent Droplets," AFOSR Contractors Meeting in Propulsion (1994).

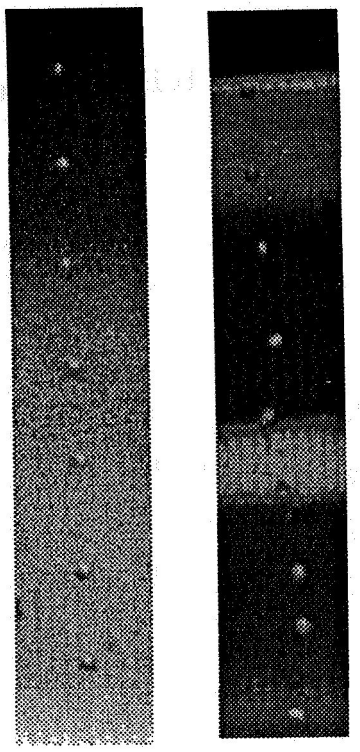

(a) (b)

Figure 1. LOX droplet generation into helium at (a) 200 and (b) 1000 psig

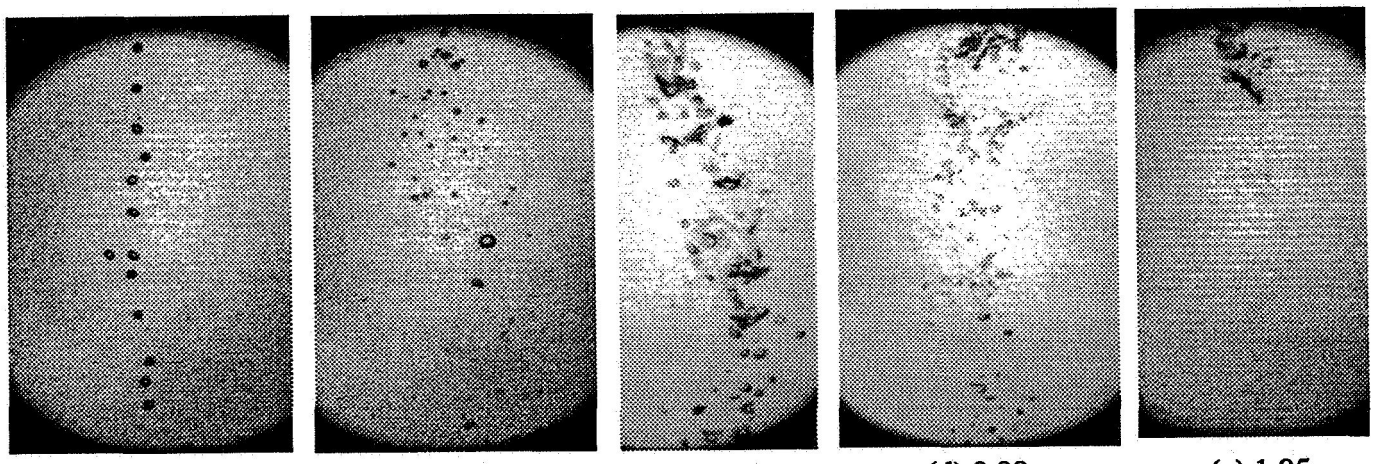

P_r: (a) 0.63 (b) 0.84 (c) 0.96 (d) 0.98 (e) 1.05

Figure 2. Shadowgraphs of liquid nitrogen injection into high pressure gaseous nitrogen

Figure 3. Effect of helium introduction into the supercritical nitrogen/nitrogen system (a) immediately, 500 psig (b) after several minutes, 600 psig

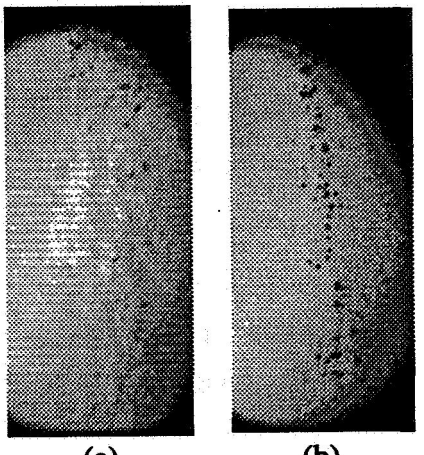

(a) (b)

Table 1.	H_2	He	N_2	O_2	Ar
Critical Pressure (atm)	13	2.336	34	50.5	48.8
Critical Temperature (°K)	33.15	5.2	126.25	154.65	150.75
Molecular Weight	2.016	4.003	28.016	32.000	39.94

N95-70889

HIGH ENERGY LASERS AS A STABILITY RATING DEVICE

427184
8 1

Kevin J. Breisacher and Larry Liou
NASA Lewis Reasearch Center
Cleveland, Ohio

Summary

A very cursory test program was performed to evaluate the feasibility of using a 100W CO_2 laser to initiate resonant oscillations in a test combustor. GOX/RP-1 were selected as propellants due to the absorption characteristics of RP-1 and due to test facility capabilities. Very low amplitude oscillations were initiated during laser pulsing that correspond to the first longitudinal mode of the test engine.

Discussion

Typically, the stability of liquid rocket engines is determined by "bomb" testing in which pyrotechnic devices are detonated inside a firing engine in hopes of exciting resonant oscillation modes. Bomb testing is expensive and tends to damage hardware. There is no well defined procedure for determining the size and location of the bomb needed to excite an oscillation. Bombs by their nature expend their energy exciting a broad band of frequencies, and do not necessarily provide an answer to the question of how a combustor responds to an oscillation at a particular resonant frequency. Other pulsing techniques such as pulse guns and sirens typically suffer from placement, cost, and inertial coupling considerations and thus are seldom used.[1] Using a laser as a stability rating device has some potentially attractive features. Recently, by piggybacking on the tail end of another test program,[2] we were able to perform a brief assessment of the feasibility of using a high energy laser as a stability rating device for a test combustor.

The pulsing system used in the experiment consisted of a laser and beam-steering optics. The optical setup is shown in Figure 1. A CO_2 laser was used with a wavelength of 10.6 microns and a beam diameter of 4 mm. A CO_2 laser was selected for several reasons. RP-1 absorbs strongly at 10.6 microns. CO_2 lasers are able to provide high energy pulses at repetition rates matching the frequency range of interest for combustion instabilities. Finally, CO_2 lasers are relatively inexpensive. The laser could be pulsed at a rate from 2kHz to 10 kHz with a 50% duty cycle. Pulse energies ranged from 32 mJ to 17 mJ per pulse at 2 and 5

kHz repetition rates respectively. The beam steering optics in the order traversed by the beam included a periscope, a 45 mirror, and a focusing lens. The periscope raised the beam to the level of the test engine. The focal length of the focusing lens used was 10 cm. Absorption was chosen as the energy deposition technique due to the optcal properties of RP-1 and to the high cost of the optics (large focusing lenses) needed to create a laser spark.

The test engine used in the experiment consisted of a windowed combustor section, an injector, a torch ignitor, and a heat sink nozzle (Figure 2). The combustion chamber accomodates up to four optical windows. The windows were made of coated zinc selenide for maximum transmission at 10.6 microns. Typically, only one zinc selenide window was used and the remaining window openings were fitted with metal blanks. The zinc selenide windows maintained the integrity of the chamber although significant cracks were visible at the conclusion of testing. The injector consisted of four GOX on RP-1 impinging triplet elements. The torch ignitor fired radially into the chamber. Initially, the ignitor was placed near the injector face but was moved downstream (just before the contraction section) in an effort to achieve more steady combustion. A GN_2 purge was applied at the window surfaces in the direction of the propellant flow to provide cooling. The chamber was equipped with a static pressure transducer to measure chamber pressure and a single high frequency piezoelectric tansducer for measuring any induced pressure oscillations.

The length of the engine from the injector face to the throat was 8.88" and the chamber diameter was 2.06". This length combustor would have a first longitudinal mode of 2622 Hz assumming perfect mixing and equillibrium chemistry. The combustor was operated at a mixture ratio of from 1.7 to 2.5. The nominal chamber pressure was 70 psi. Unfortunately, it was difficult to maintain a steady chamber pressure during a run with the given hardware setup and there was insufficient time to remedy the problem. Due to the limited time available for testing, it was decided to attempt to initiate oscillations with the laser despite the unsteadiness in chamber pressure. During a test, the laser pulsing was usually initiated half way through a run. The laser pulsing was initiated by sending a TTL signal to a wave generator that sent a waveform to the CO_2 laser that drove at it a 50% duty cycle at a pre-set frequency. The beam was focused at a point 2.5" downstream of the injector face and about 3/4" inside the chamber. Due to the setup of the test stand , it was not possible to move the focal point closer to the injector face.

Attempts were made to drive the engine at various frequencies (2600 Hz, 3000 Hz, 5000 Hz, 5200 Hz). The variation of energy delivered versus frequency is given below (measured just before transmission through the zinc selenide window into the combustor):

Frequency (Hz)	Power with Wavetek (W)	Power with CA 48 (W)
2000	60	
3000	65	
4000	66	
5000	67	85
6000	65	
7000	65	

The variation in power with frequency is fairly flat. The energy output of the laser peaks at 5000 Hz due to a resonance in its plasma tube. The lower power level obtained with the Wavetek signal generator at 5000 Hz is probably due to an impedance mismatch. The CA-48 was used for all testing at 5000 Hz.

No chamber pressure oscillations were recorded except when the driving frequency was 5000 Hz. When the CO_2 laser was driven at 5000 Hz, pressure oscillations at 2380 Hz were consistently recorded (Figures 3a and 3b). The amplitude of these oscillations were 2 - 2.5 psi (3% of Pc). These oscillations had a characteristic beat frequency of 125 Hz. This beating may be occurring due to the 1L oscillation (2380 Hz) going in and out of phase with the effective driving of the laser at 2500 Hz. It is interesting that no oscillations were observed when the laser was pulsed at 2600 Hz. The energy per pulse is almost double that at 5000 Hz when oscillations were observed. However, the total energy delivered at 5000 Hz is 35% higher than at 2600 Hz. Obviously, more work needs to be done to assess the feasibility of using lasers as a stability rating device. In particular, the sensitivity of the response of the combustor to the location of the focal point of the laser needs to be explored.

References

1) "Liquid Propellant Rocket Combustion Instability", NASA SP-194, 1972.

2) L. Liou, "Laser Ignition in Liquid Rocket Engines", AIAA-94-2980, 30th Joint Propulsion Conference, June 1994.

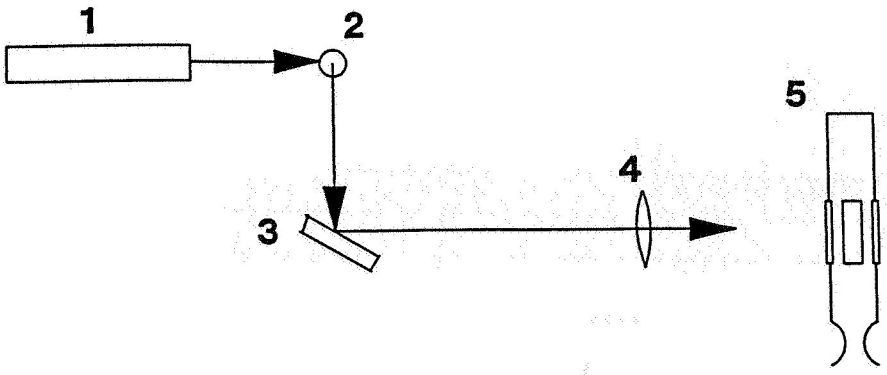

1. CO2 Laser
2. Periscope
3. 45 - degree mirror
4. Focusing lens
5. Test combustor

Figure 1. - Optical Setup

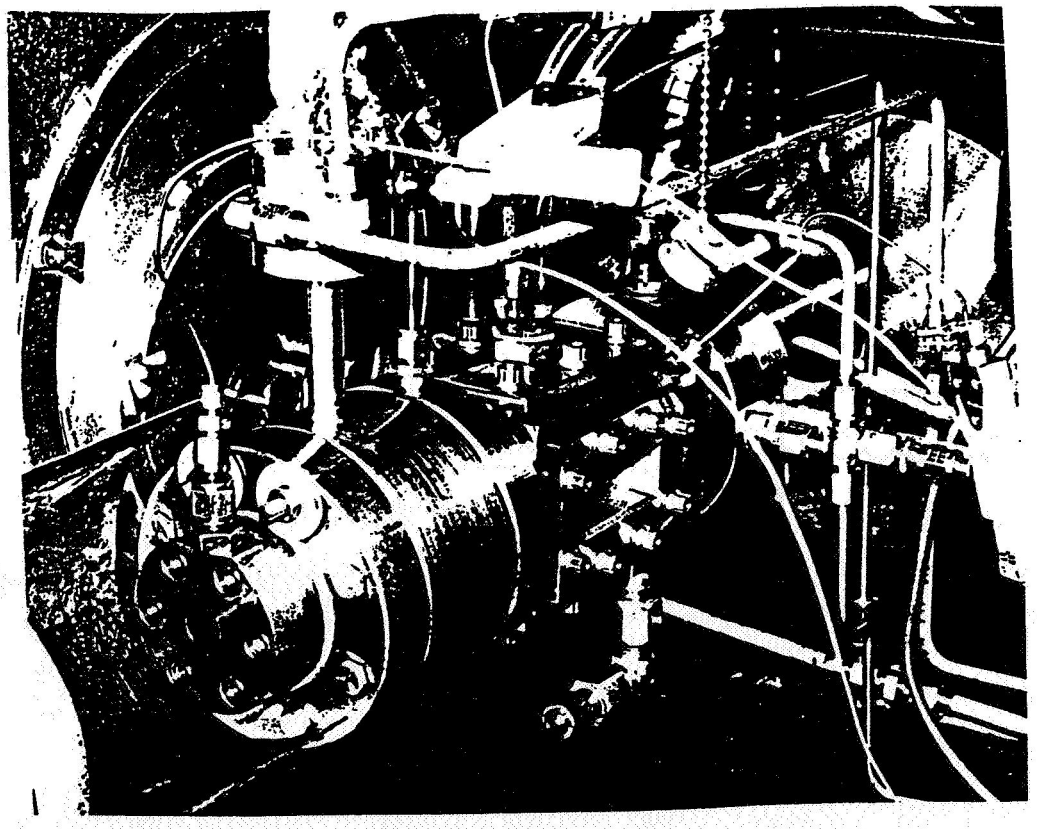

Figure 2. - Test Combustor

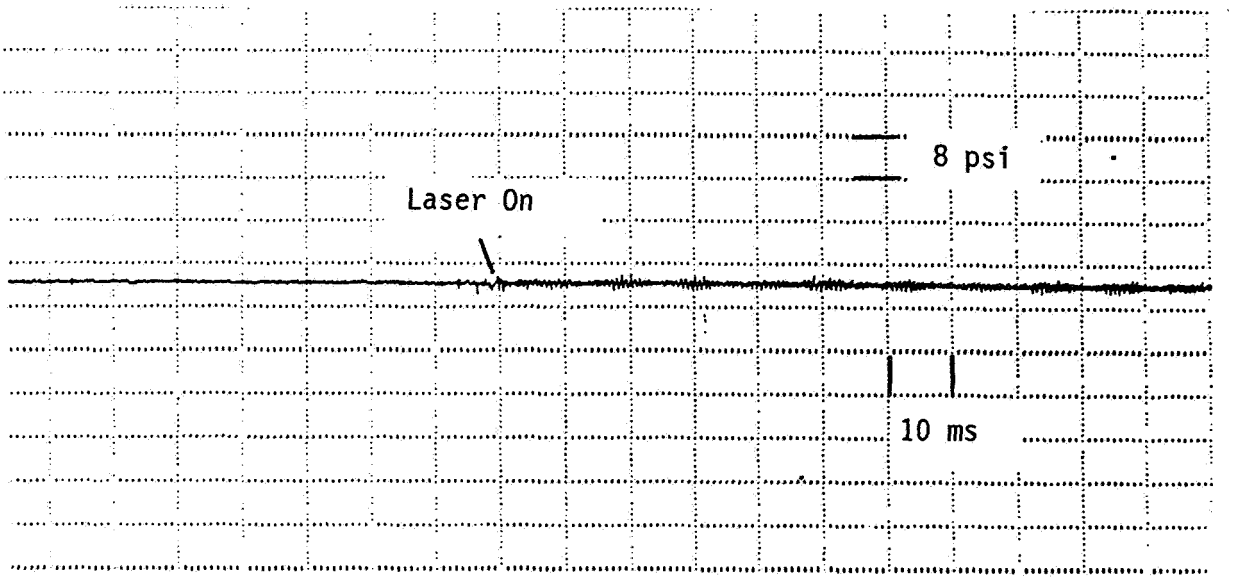

Figure 3a. - Pressure Trace

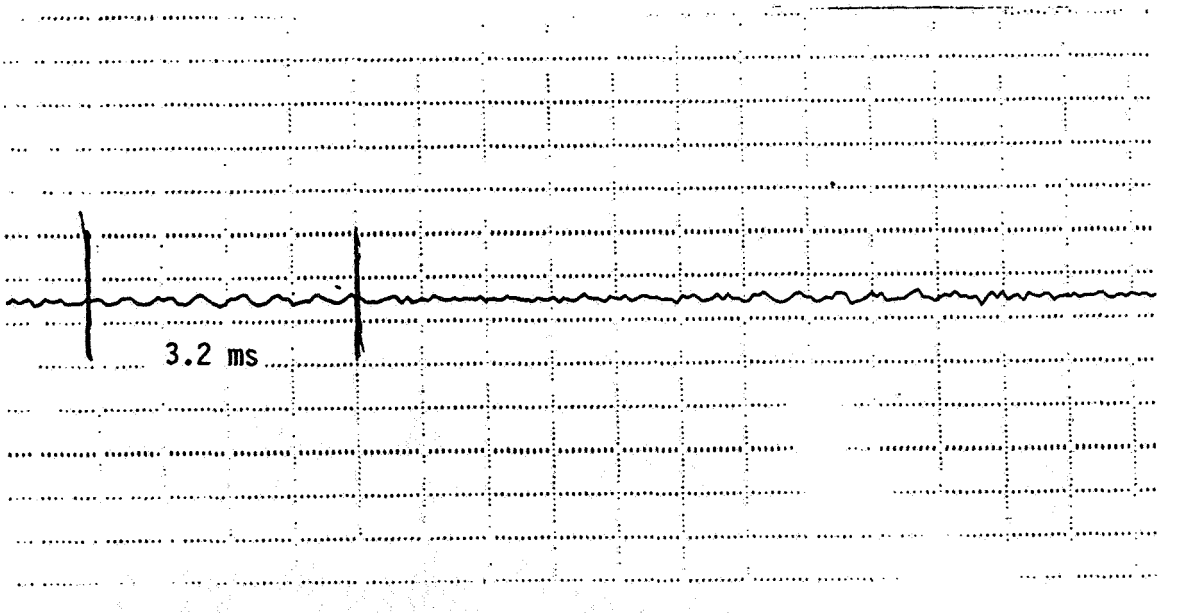

Figure 3b. - Expanded Pressure Trace

Pgs 5 427186

N95-70890

A Laser-Based Sizing/Velocimetry Technique to Investigate the Secondary Atomization of Aluminum Gel Propellants

D. C. Mueller and S. R. Turns
Propulsion Engineering Research Center
and
Department of Mechanical Engineering
The Pennsylvania State University
University Park, PA 16802

SUMMARY:

A laser-based, forward-scatter diagnostic technique, employing a single laser sheet, has been developed to simultaneously measure the size and velocity of individual 10-150 μm droplets in a dilute polydisperse droplet stream (<1000 particles/cc) and to detect the presence of burning aluminum in these same droplets. Spectral emission from aluminum vapor in the 390-400 nm wavelength region is used as an indication of burning aluminum. The technique utilizes a 4-mm uniformly illuminated probe volume, eliminating trajectory-dependent particle sizing and size-dependent system detection bias. Particle sizing is based on a correlation of particle size with near-forward scattered light intensity. Calculations show average particle sizing variation to be within 3.5% over the expected range of refractive indices. Calibrations using a range of optical pinholes (10-100 μm) were used to verify the above sizing correlation.

DISCUSSION:

Recent theoretical rocket performance studies indicate that aluminum gel propellants, consisting of very fine solid particles suspended in a gelled liquid propellant, may offer increases in engine specific impulse and/or propellant density over conventional liquid propellants.[1-3] Increased propellant combustion times and condensed Al_2O_3 particles in the flowfield, however, may result in sufficient performance losses to eliminate the potential performance gains of aluminum gel propellants.[4] One potential mechanism for reducing these losses is to burn smaller droplets, but the viscous nature of gel propellants may make fine gel atomization difficult to achieve. Fortunately, secondary atomization, in which a droplet spontaneously shatters into a number of smaller droplets due to an internal vaporization of the liquid carrier, may produce the desired small droplets.

Previous research on secondary atomization,[5-7] however, has focused primarily on large droplets (200-1200 μm), while practical applications will require smaller droplets (10-150 μm).

Since small-droplet secondary atomization may differ from that of large droplets, primarily due to a difference in the number of aluminum particles present in a given droplet,[8] we are currently investigating the combustion of aluminum/hydrocarbon gel droplets in the range of practical interest (10-150 μm). One objective of the present investigation is to develop non-intrusive diagnostic techniques to study the combustion of 10-150 μm diameter gel droplets. In light of this objective, a laser diagnostic technique, based on near-forward Mie scattering, has been developed to measure the size and velocity of individual droplets in a dilute stream of burning gel droplets and to detect the presence of burning aluminum in these same droplets.

A problem inherent to laser-based sizing systems is the Gaussian distribution of the laser-beam intensity in the radial direction. In a typical system, the probe volume spans the entire beam cross-section, making probe volume illumination non-uniform and scattered light intensity dependent on trajectory through the probe volume. Since particle size is correlated with scattered light intensity, measured particle size in a single-beam system is dependent on trajectory in addition to actual size.[9] In a two-beam laser system, particle trajectory does not play a role in determining measured particle size since a second, coaxially aligned, smaller-diameter beam is used to limit the probe volume to a uniform-intensity region near the center of the sizing beam.[10] In both single and two-beam systems, non-uniform probe volume illumination yields a probe volume cross-sectional area that increases with increasing particle size.[10] Consequently, a system detection bias is introduced, in which smaller particles are underrepresented. While the above phenomena can be corrected for in post-collection processing,[9-11] the material refractive index must be known or constant, and in the case of a single-beam system, all particles must have approximately the same velocity.[9]

Since the shape and refractive index of a gel droplet change as the droplet burns (i.e., Al particle/hydrocarbon → Al particle agglomerate → molten Al → Al_2O_3) and particle velocity may vary significantly because of secondary atomization, the post-collection processing mentioned above can not be employed. Therefore, our system is designed such that the probe volume is uniformly illuminated by a horizontal laser sheet. While this technique eliminates uncertainties associated with a non-uniformly illuminated probe volume, the burning droplet stream and the horizontal slit control the probe volume dimensions, limiting the technique to narrow-diameter droplet streams.

A schematic of the diagnostic system and droplet burner is presented in Fig. 1. In brief, a 1.1-mm diameter He-Ne laser beam (Spectra-Physics 124B) is passed through a 750 mm focal length plano-convex spherical lens (L1, Oriel 40815) and a 19 mm focal length plano-convex cylindrical lens (L2, Newport CKX019), producing a horizontal laser sheet over the burner. This sheet has a calculated $1/e^2$ thickness of 550 μm and a width of 36 mm at the focal point of the lens combination. Gel droplets passing through this sheet scatter light which is collected in the

near-forward direction and collimated by a 350 mm plano-convex spherical lens (L3, Oriel 40800), which has a strip of flocking material across its center to block direct laser light. An adjustable aperture (A1, Newport ID-1.5) is used to limit the total light collection angle. The collimated light passing through this aperture is then focused on a 200 μm horizontal slit (S1) by a second 350 mm lens (L4, Oriel 40800). Light passing through this slit is recollimated by a 50 mm plano-convex lens (L5, Oriel 41340) and is separated into two components by a beam splitter cube (BS1, Melles-Griot 03-BSC-009). The first component, used for particle sizing, is refocused through a second 50 mm spherical lens (L6, Oriel 41340), passes through a 632.8 nm line filter (F1, Oriel 52720), two optical diffusers (not shown, Oriel 48010) and enters a photomultiplier tube (PMT) (Hamamatsu R928) where the particle sizing signal is generated. The second component, used to detect aluminum combustion, passes through a 400-nm narrow bandpass filter (F2, Oriel 53800) and enters a second PMT (Hamamatsu R928) to produce the aluminum combustion signal. A detailed discussion of the aluminum combustion system can be found in prior work.[12] A two-channel 20 MHz A/D acquisition board (Rapid Systems 2040) is used to collect the above signals, which are then analyzed using a personal computer.

In general, Mie scattering intensity is highly sensitive to both particle shape and refractive index, making a correlation between scattered light intensity and gel particle size difficult to achieve. Light scattered in the near-forward direction, however, is relatively insensitive to shape and refractive index[13] and can be accurately correlated with particle size over a range of refractive indices. In order to obtain a good sizing correlation, defined as a monotonic function with good insensitivity to refractive index, a parametric study of light collection geometry was conducted. From this study and a consideration of system physical limitations, the scattering response for light collected at a 1.95° angle from the forward direction and over an angle of 1.72° was found to yield the best response. This collection geometry corresponds to a flocking strip thickness of 2 mm and an aperture (A1) diameter of 32 mm.

The series of lines in Fig. 2 shows normalized scattering intensity as a function of particle size for various anticipated material refractive indices calculated using Mie theory. From this plot it is evident that refractive index variations should affect particle sizing in the 10-125 μm range by at most 12% since the range of refractive indices employed here represents a worst-case scenario. In addition, a range of optical pinholes, which scatter light in the forward direction in the same manner as equivalent particles, were used to verify that the system scattering response matches the theoretical sizing correlation. These measurements demonstrate excellent agreement between the calculated correlation and actual system response. The optical pinholes were also used to verify the uniformity of probe volume illumination.

Figure 3 is a plot of maximum normalized system response as a function of horizontal pinhole location for a number of different size pinholes. From this plot it can be seen that worst-

case probe volume response is within 7.5% of maximum in the center 2 mm of the probe volume and 19% for the entire volume. Since virtually all particles will pass through the center 2 mm, the uniformity is quite good. In addition to providing accurate single-particle sizing, the system must be able to perform in a reasonably dense spray without interference from other particles, since signals generated by more than one particle must be rejected. The probability of only one particle being in the probe volume was calculated using a Poission distribution and was found to be reasonable (>50%) for particle number densities of 1000 particles/cc or less.[14]

In summary, the above results indicate that the diagnostic system is performing as expected and should provide accurate particle sizing/velocimetry measurements in a dilute burning droplet stream over a range of material refractive indices. In addition, a uniformly illuminated probe volume is employed to reduce particle size distribution uncertainties associated with a changing material refractive index and/or particle velocity, making this an ideal technique for investigating the secondary atomization of aluminum gel propellants.

REFERENCES:

1. Palaszewski, B., "Advanced Launch Vehicle Upper Stages Using Liquid Propulsion and Metallized Propellants," NASA Technical Memorandum 103622, Oct., 1990.
2. Zurawski, R. L., and Green, J. M., "An Evaluation of Metallized Propellants Based on Vehicle Performance," AIAA Paper 87-1773, June-July 1987.
3. Yatsuyanagi, N., Sakamoto, H., Sato, K., Ono, F., Tamura, H., and Moro, A., "Combustion Characteristics of Metallized Hydrocarbon Fuels," 17th International Symposium on Space Technology and Science, Tokyo, Japan, May 1990.
4. Mueller, D. C., and Turns, S. R., "A Theoretical Evaluation of Secondary Atomization Effects on Engine Performance for Aluminum Gel Propellants," AIAA Paper No. 94-0686, presented at AIAA 32nd Aerospace Sciences Meeting and Exhibit, Jan. 10-13, 1994, Reno, NV.
5. Takahashi, F., Heilweil, I. J., and Dryer, F. L., "Disruptive Burning Mechanism of Free Slurry Droplets," *Combustion Science and Technology*, Vol. 65, 1989, pp. 151-165.
6. Lee, A., and Law, C. K., "Gasification and Shell Characteristics in Slurry Droplet Burning," *Combustion and Flame*, Vol. 85, 1991, pp. 77-93.
7. Wong, S.-C., and Turns, S. R., "Disruptive Burning of Aluminum/Carbon Slurry Droplets," *Combustion Science and Technology*, Vol. 66, 1989, pp. 299-318.
8. Mueller, D. C., and Turns, S. R, "Some Aspects of Secondary Atomization of Aluminum/Hydrocarbon Slurry Propellants," *Journal of Propulsion and Power*, Vol. 9, May-June 1993, pp. 345-352.
9. Holve, D. J., and Self, S. A., "Optical Particle Sizing for In Situ Measurements- Part 1", *Applied Optics*, Vol. 18, May 1979, pp. 1632-1645.
10. Wang, J. C., and Hencken, K. R., "In Situ Particle Size Measurements Using a Two-Color Laser Scattering Technique," *Applied Optics*, Vol. 25, March 1986, pp. 653-657.
11. Holve, D. J., and Self, S. A., "Optical Particle Sizing for In Situ Measurements- Part 2", *Applied Optics*, Vol. 18, May 1979, pp. 1646-1652.
12. Mueller, D. C., and Turns, S. R., "Ignition and Combustion of Metallized Propellants- Semi-Annual Report (Jan.-June 1991)," NASA-Lewis, Grant No. NAG 3-1044.
13. Bohren, C. F., and Huffman, D. R., Absorption and Scattering of Light by Small Particles, John Wiley & Sons, New York, 1983.
14. Mueller, D. C., an Turns, S. R., "Ignition and Combustion of Metallized Propellants- Annual Report (Jan.-Dec. 1993)," NASA-Lewis, Grant No. NAG 3-1044.

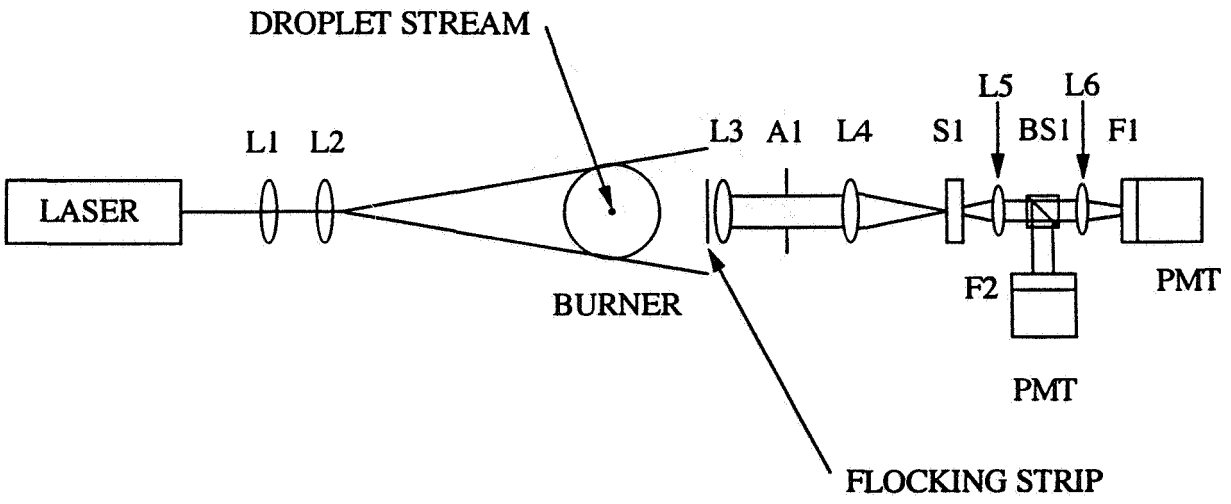

Figure 1. Schematic of the laser diagnostic technique.

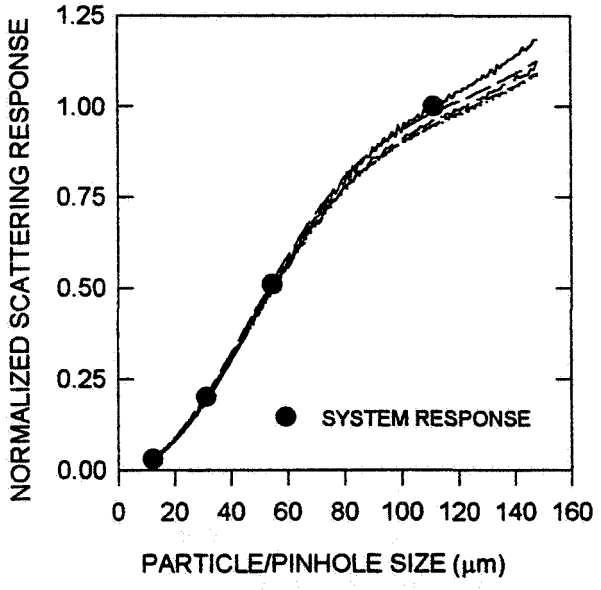

Figure 2. Calculated normalized scattering intensity and actual system response as functions of particle/pinhole diameter.

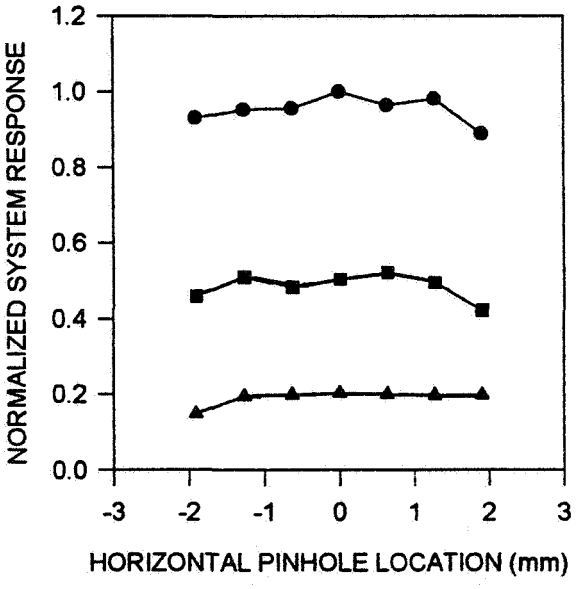

Figure 3. Normalized system response as a function of optical pinhole horizontal position in the probe volume for several pinhole sizes. (● - 111 μm, ■ - 55 μm, ▲ - 31 μm)

427189
Pg 5
N95-70891

Metallized Gelled Propellants: Oxygen/RP-1/Aluminum Combustion Experiments

Bryan Palaszewski
NASA Lewis Research Center
Mail Stop SPTD-2
21000 Brookpark Road
Cleveland, OH 44135

SUMMARY

A series of combustion experiments using metallized gelled liquid propellants were conducted. These experiments used a small 30- to 40-lb_f thrust engine composed of a modular injector, igniter, chamber and nozzle. The fuels used were traditional liquid RP-1 and gelled RP-1 with 0-wt %, 5-wt%, and 55-wt% loadings of aluminum and gaseous oxygen was the oxidizer. Ten different injectors were used during the testing: 6 were for the baseline O_2/RP-1 tests and 4 for the gelled fuels. Relatively high C-star efficiencies were obtained with gelled RP-1 (0-wt% RP-1/Al) and metallized 5-wt% RP-1/Al over the O/F range tested: 90-98%. A peak of 98% efficiency was reached with ungelled O_2/RP-1 and up to 95% efficiency was obtained with gelled RP-1/Al (55-wt% Al). Injector erosion was evident with the 55-wt% testing, while there was little or no erosion seen with the gelled RP-1 with 0 and 5-wt% Al. A protective layer of gelled fuel formed in the firings that minimized the damage to the rocket injector face. This effect may provide a useful technique for engine cooling.

Introduction

Metallized gelled propellants have been studied analytically and experimentally for over 60 years[1]. The historical work has focused on the benefits of high specific impulse, high density, and safety[2, 3, 4, 5, 6]. Current non-NASA uses for these propellants may lie in tactical and strategic missiles and aircraft ejection seats[3, 4, 5, 6]. Extensive work has been conducted with metallized-gelled Earth-storable propellants, such as hydrazine (N_2H_4), Inhibited Red Fuming Nitric Acid (IRFNA), and monomethyl hydrazine (MMH). However, these propellants are not planned for use in future NASA launch vehicles. To explore the potential of metallized-gelled fuels, NASA chose to pursue the propellant combinations that were more suitable to its future plans in the Metallized Propellant Program[7-14]. This program, at the NASA Lewis Research Center, has been conducting both experimental, analytical, and mission studies since 1987. This program's concentrated on

C-3.

O_2/RP-1 and O_2/H_2 propellant combinations and the issues related to using these gelled propellants with metal particle additives. Several mission studies have indicated that O_2/RP-1/Al can have significant benefits by increasing propellant density. Testing was therefore conducted with O_2/RP-1/Al propellants using gelled RP-1 with aluminum particles. Some of the results of that testing are summarized in this paper.

Purpose of Experiments

Rocket performance and heat transfer measurements were desired in this test program. During the combustion of metal particles, the two-phase flow creates a mismatch in the combustion time scale of the liquid droplets and the solid particles. The heat transfer measurements were envisioned so that some estimate might be made of the delay in ignition for the aluminum. Both baseline non-metallized propellants and various metal loadings with gelled RP-1 were used to compare the combustion temperature heat flux profiles of the different combustion environments.

Experimental Setup

All of the experiments were conducted in the Rocket Laboratories of NASA Lewis. The combustion testing was conducted in Cell 21 and Cell 14 was used for propellant mixing. Cell 21 is a test facility with a very flexible capability and many diverse propellants can be tested. Oxygen /hydrogen igniters flows, O_2/CO, O_2/Al and gelled-metallized propellants are some of the combinations that have been tested. Except for the RP-1 and RP-1/Al, all of the propellants in the cell are provided in gaseous form. The gases are O_2, H_2, and N_2. Nitrogen is used as a purge gas to protect the igniter and engine after engine shutdown. Both the O_2 and H_2 are provided from high-pressure trailers. The liquid RP-1 propellants are delivered to the engine using a pressurized tank attached to the cell. Gelled propellants are pressurized and fed using a piston-cylinder tank. Micro-Motion flow meters are used to determine the liquid flow rates while a series of orifices are used to control the gas flow rates. A TRADAR data acquisition system with up to 100 data channels is used.

Engine Hardware

Both heat sink and calorimeter experiments were conducted. The heat-sink combustion chamber has a 2.6-inch inside diameter and it is 6 inches long and the nozzle has a 0.6-inch diameter throat. A 22-channel cooling passage calorimeter chamber was used. The associated

calorimeter nozzle has 9 cooling channels. Numerous thermocouples are located in the cooling passages of the calorimeter combustion chamber. The injectors use a oxidizer manifold within the injector body and have a fuel dome set atop it. The injector elements are an O-F-O design and both four and eight element patterns were tested. During the testing, a wide range of oxidizer-fuel ratios (O/F) were investigated. The injectors were designed for an O/F range of 1.2-4.2 for O_2/RP-1 and 1.4-3.7 for O_2/RP-1/Al.

Fuel Preparation

Several types of gelled-metallized fuels with different metal loadings were investigated. All of the propellant mixing was conducted in Cell 14 of the Rocket Laboratories. When mixing, it is important to add the "dry" elements first: adding metal, then gellant, then fuel. A small amount of liquid surfactant, Tween 85, is also added to the high metal loading fuels. The gelled RP-1 was prepared with a 6.5 wt% gellant concentration. This gellant wt% was selected based on a series of gelling experiments in which a range of 1-10 wt% was used. With the 5 wt% RP-1/Al fuel, 5 wt% gellant was added and with the 55 wt% RP-1/Al, the gellant fraction was 3.5 wt%.

Engine Efficiency

Some preliminary results are presented here based on initial analyses of the test data. All of the results presented here are for the heat sink engine. The testing with the calorimeter engine is not yet completed, therefore no heat transfer data is presented. With the O_2/RP-1, the maximum Cstar efficiency occurred near a 3.0 O/F. With the gelled RP-1 (0-wt% RP-1/Al), the O/F for the maximum Cstar efficiency was nearly the same. Both demonstrated very high C-star efficiencies of up to 98%. Using O_2/RP-1/Al (5 wt% RP-1/Al) a 90-95 % Cstar efficiency was delivered. The efficiency curve had a very flat response, with no obvious peak in the curve. At a 55 wt% RP-1/Al loading, the Cstar efficiency peak occurred near 1.5-2.0 O/F.

Observations

Self-protection of injectors. During the testing with gelled RP-1 and the -wt% RP-1/Al, some residual propellant was found in the rocket chamber, coating the injector face and chamber walls. Once this thin layer was removed with a soft cloth, the metal surfaces exhibited minimal erosion. This is a marked contrast to the blackening of the O_2/RP-1 injector faces and injector-face erosion that occurred with the 55-wt% RP-1/Al. Am improved cooling technique might be

derived from this effect.

Metal agglomerations in the nozzle. When testing the 55-wt% RP-1/Al, metal agglomerations occurred in the nozzle. After 15, 2-second firings, the agglomeration had reduced the throat diameter from 0.6 inches to 0.45 inches. Several finger-like filaments extended out if the nozzle along its walls. This agglomeration was a hardened metal buildup that could not be easily removed. After taking the nozzle off the rig, the agglomeration could be chipped off with a chisel and once loosened, came off in large segments.

Conclusions

High efficiency combustion of gelled metallized propellants was realized with even simple 4- and 8-element triplet injectors. With gelled metallized fuels, C-star efficiencies of over 90 percent were achieved, with the highest efficiency for the 55 wt% RP-1/Al being 95 percent. Though the high metal loading, 55-wt% RP-1/Al, engine runs experienced some agglomeration and erosion difficulties, the 0- and 5-wt% tests ran well, with a high C-star efficiency, and demonstrated a self-protective layer of gelled propellants and combustion products.

Acknowledgements

I'd like to thank NASA Headquarters, Office of Advanced Concepts and Technology for their support of this work. Also, many thanks to Jim Zakany for his work as operations engineer for the rocket engine testing, Paul Molnar for his mechanical skills, and to J. P. for retiring from NASA.

REFERENCES

1) Sanger, E., Raketenflugtechnique, Berlin: R. Oldenberg, 1933, pp. 53.

2) Wells, W., "Metallized Liquid Propellants," Space/Aeronautics, Volume 45, June 1966, pp. 76-82.

3) Olson, T. and Setze, P., "Some Combustion Problems of High Energy Fuels for Aircraft," NACA Preprint, 1958, International Symposium on Combustion, pp. 883-893 and 7th International Symposium on Combustion, London and Oxford, Aug 28-Sept. 3, 1958.

4) Allan, B. and Chew, W., "A Review of Thixotropic Gels for Advanced Propulsion Systems," JANNAF Propulsion Meeting, CPIA Publication 602. Volume III, November 1993.

5) Arszman, J. and Chew, W., "TACAWS Propulsion Development Program," JANNAF Propulsion Meeting, CPIA Publication 602. Volume III, November 1993.

6) Trikha, A., Warren, S., and Peters, J., "Advanced Crew Escape Capsule Technologies Program," SAFE Association, Newhall, CA Proceedings, 1987, pp. 196-202.

7) Palaszewski, B. and Rapp, D., "Design Issues for Propulsion Systems Using Metallized Propellants," AIAA 91-3484, September 1991.

8) Rapp, D. and Zurawski, R., "Characterization of RP-1/Aluminum Gel Propellant Properties," AIAA 88-2821, July 1988.

9) Mueller, D. and Turns, S., "Some Aspects of Secondary Atomization of Aluminum/ Hydrocarbon Slurry Propellants," AIAA Journal of Propulsion and Power, Volume 9, Number 3, May-June 1993.

10) Wong, W., Starkovich, J., Adams, S., and Palaszewski, B., "Cryogenic Gellant and Fuel Formulation for Metallized Gelled Propellants: Hydrocarbons and Hydrogen with Aluminum," AIAA 94-3175, June 1994.

11) Palaszewski, B. and Powell, R., "Launch Vehicle Propulsion Using Metallized Propellants," AIAA 91-2050, June 1991.

12) Palaszewski, B., "Advanced Launch Vehicle Upper Stages Using Metallized Propellants," NASA TP-3191, presented at the JANNAF Propulsion Meeting, Anaheim, CA, October 3-5, 1990.

13) Palaszewski, B., "Lunar Missions Using Advanced Chemical Propulsion: System Design Issues," NASA Technical Publication (TP) -3065, AIAA 90-2341, July, 1990, also in AIAA Journal of Spacecraft and Rockets, May-June 1994.

14) Palaszewski, B., "Metallized Propellants for the Human Exploration of Mars ," NASA TP-3062, November 1990. Also, AIAA Journal of Propulsion and Power, Nov.-Dec. 1992.

427192
Pgs 5

N95-70892

FUNDAMENTAL PHENOMENA ON FUEL DECOMPOSITION AND BOUNDARY LAYER COMBUSTION PROCESSES WITH APPLICATIONS TO HYBRID ROCKET MOTORS

Kenneth K. Kuo, Y. C. Lu, Martin J. Chiaverini, George C. Harting
The Propulsion Engineering Research Center
The Pennsylvania State University
University Park, PA 16802

SUMMARY:

An experimental study on the fundamental processes involved in fuel decomposition and boundary layer combustion in hybrid rocket motors is being conducted at the High Pressure Combustion Laboratory of the Pennsylvania State University. This research should provide an engineering technology base for development of large scale hybrid rocket motors as well as a fundamental understanding of the complex processes involved in hybrid propulsion. A high pressure slab motor has been designed for conducting experimental investigations. Oxidizer (LOX or GOX) is injected through the head–end over a solid fuel (HTPB) surface. Experiments using fuels supplied by NASA designated industrial companies will also be conducted. The study focuses on the following areas: measurement and observation of solid fuel burning with LOX or GOX, correlation of solid fuel regression rate with operating conditions, measurement of flame temperature and radical species concentrations, determination of the solid fuel subsurface temperature profile, and utilization of experimental data for validation of a companion theoretical study also being conducted at PSU.

DISCUSSION:

Hybrid rocket systems offer several advantages over their liquid and solid rocket counterparts. First, hybrid rockets require only half as much feed system hardware as liquid propellant rockets, and therefore display improved reliability. Second, since they are much less sensitive to cracks and imperfections in the solid fuel grain, hybrids have safety advantages over solid propellant rockets. Third, hybrid rockets can be throttled for thrust control and maneuvering. In addition, solid fuels are safer for manufacture, transportation, and storage. From a performance standpoint, hybrid rockets have specific impulse similar to those of liquid and solid rocket motors.

The experimental hybrid rocket program at PSU has been established to study the fundamental fuel decomposition and reacting boundary–layer processes (see Fig. 1) which occur in actual hybrid rocket motors or motor analogs. Figure 2 shows a schematic diagram of the overall hybrid test rig, including motor analog, gas supply system, and ignition system. A computer code was developed to assist in the design of the test motor. The code used a time–dependent continuity

equation coupled with a chemical equilibrium code (CEC–76) to determine fuel regression rate, oxidizer–to–fuel mass ratio, chamber pressure, and gas temperature. Parametric studies were conducted to determine the effect of oxidizer flow rate, nozzle diameter, test time, and fuel composition on motor operating characteristics in order to meet the proper range of test conditions. Based upon the results of parametric studies and experience from previous experiments at Penn State, a windowed, 2–D hybrid motor was designed. Figure 3 shows a partial assembly drawing of the hybrid motor analog. The motor utilizes either two opposing fuel slabs or one fuel slab with an opposing inert slab and may operate with either gaseous or liquid oxygen as the oxidizer source. Interchangeable exit nozzles provide partial control of chamber pressure. The two sets of opposing windows can accommodate a variety of instrumentation and diagnostics for measuring fuel regression rate, gas velocity, flame temperature, and species concentrations. At this point, a large portion of the motor has been constructed.

The gaseous oxygen supply system shown in Fig. 2 consists of a main feed line and a nitrogen purge. Remotely operated ball valves initiate and terminate the flow of oxygen, while a critical flow venturi maintains a steady mass flux through the main line. An upstream thermocouple and pressure transducers located on either side of the venturi give a measure of the oxygen flow rate. The flow rate will be preset for each test. GOX and GN_2 filters prevent contamination of the system.

Based upon a literature search and comparative study of various ignition systems, an igniter was designed as shown in Fig. 2. The ignition system consists of a high–pressure gaseous oxygen/methane premixed torch and a solid–propellant pilot flame. The solid propellant strands are ignited electrically using nichrome wires connected to an AC transformer. Remotely operated solenoid valves control the flow of oxygen and methane. Check valves and vents prevent the contamination of the gas bottles and over pressurization of the system. Gaseous nitrogen is used to purge the ignition system after each test. The ignition system has been constructed and tested successfully with feed pressures up to 550 psig. It is expected that the GOX/CH_4 torch will ignite the fuel slabs and be shut off before the gas pressure in the motor exceeds a pre–specified critical pressure.

After a thorough literature search on spray injectors, a showerhead design was suggested for the LOX injector. This design employs multiple rows of pressure atomized jets aligned parallel to the fuel slab(s). This type of design has been well studied, and such an injector is relatively easy to manufacture. A prototype single–row injector was constructed and tested in an existing pressure chamber. Flow visualization studies using a video camera and a strobe light have been made to determine the break–up characteristics and degree of atomization of a water jet through the injector. This study is helpful in selecting the injector size for the pre–specified range of feed pressures.

A control panel for operating the hybrid motor, GOX supply line, and ignition system has been designed and assembled. The control panel will display a mimic diagram of the entire hybrid motor analog system, as well as switches to arm the GOX supply and ignition system, and to control the various remote valves and the solid propellant pilot flames. The tests will be automated using an IBM PC/AT computer and data acquisition and control board. The control program is currently being written and tested.

Several diagnostic techniques will be used to measure the properties of interest. The fuel regression rate will be deduced from images obtained by a high speed movie camera (HYCAM) coupled with a real–time x–ray radiography system. Radical species (such as OH) concentration and flame temperature will be measured as a function of longitudinal location using UV/visible absorption spectroscopy. Both static and dynamic pressures in the motor will be measured using pressure transducers.

The subsurface temperature of the solid fuel will be measured by an array of R–type fine–wire thermocouples which are embedded at pre–determined depths in the solid fuel slabs prior to testing. Several 25μm micro–thermocouples were manufactured, soldered to extension wires, and cast inside 0.25 inch diameter fuel plugs. Since the micro–thermocouples are easily damaged, it is expected that casting them inside small fuel plugs, then casting the plugs inside the fuel slab, will produce better results than simply inserting the thermocouples into the fuel while it is curing. Eight thermocouple–containing fuel plugs will be cast into each HTPB fuel slab.

In order to fabricate solid fuels with high quality and to achieve short curing time, several fuel curing tests were conducted using R–45M homopolymer from Elf Atochem and a curing agent of Isonate 143L (MDI) from Dow. Since R–45M has a hydroxyl value of about 0.73 meq/g and Isonate 143L has an amine equivalence of 144.3 g/eq, the weight of Isonate 143L used was approximately equal to 11% of the weight of R–45M (assuming an NCO/OH ratio of 1.05). The fuel curing time was about 8 hours, nearly an order of magnitude shorter compared to the combination of R–45M, IPDI curing agent, and dibutyltin dilaurate catalyst. Approximately 35 gallons of R–45M have been received from Elf Atochem to cast the fuel slabs for motor tests using HTPB fuel processed at the Penn State University.

In the above fuel curing process, a layer of Teflon release agent (obtained from the Miller–Stephenson company) was coated on the surface of fuel casting molds and allowed to dry thoroughly before fuel casting. After curing, the fuel slabs were easily removed from the molds. In the near future, the large fuel molds which will be used to cure fuel slabs for the tests, will be professionally coated with a Teflon release agent by Hitempco Southwest. As soon as the fuel casting molds and sample holders are complete the portion required by industrial companies will be shipped to NASA/MSFC or directly to the NASA designated companies.

Testing of the hybrid motor analog will commence after the motor and GOX supply system

have been completed. Table 1 shows the range of proposed test parameters. The first series of tests will utilize solid HTPB fuel and GOX. Later tests will use fuels supplied by industry. After all tests with GOX have been completed, the chamber will be moved into the Cryogenic Laboratory at the High Pressure Combustion Lab in order to use the existing LOX supply and control system for LOX/solid fuel tests.

Table 1. Range of Test Parameters

Solid Fuel Composition:	Baseline HTPB and NASA Fuels
Chamber Pressure:	300–900 psi
Oxidizer Flow Rate:	up to 1.5 lb/s
Initial Temperature:	70° F nominal
	35° F low
	90° F high

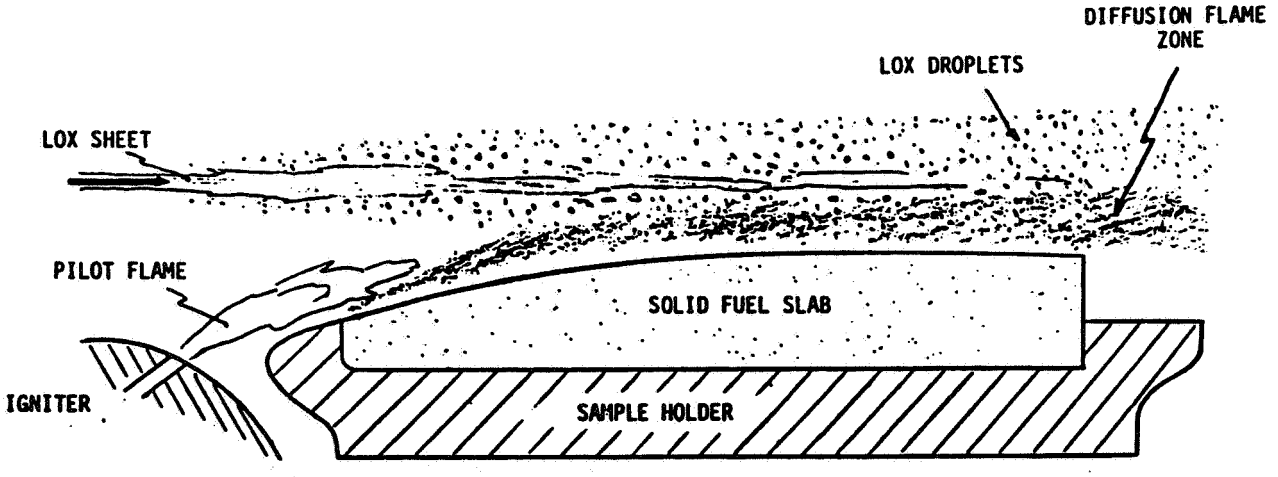

Fig. 1 Schematic Diagram of the Diffusion Flame Zone Adjacent to the Solid Fuel Slab

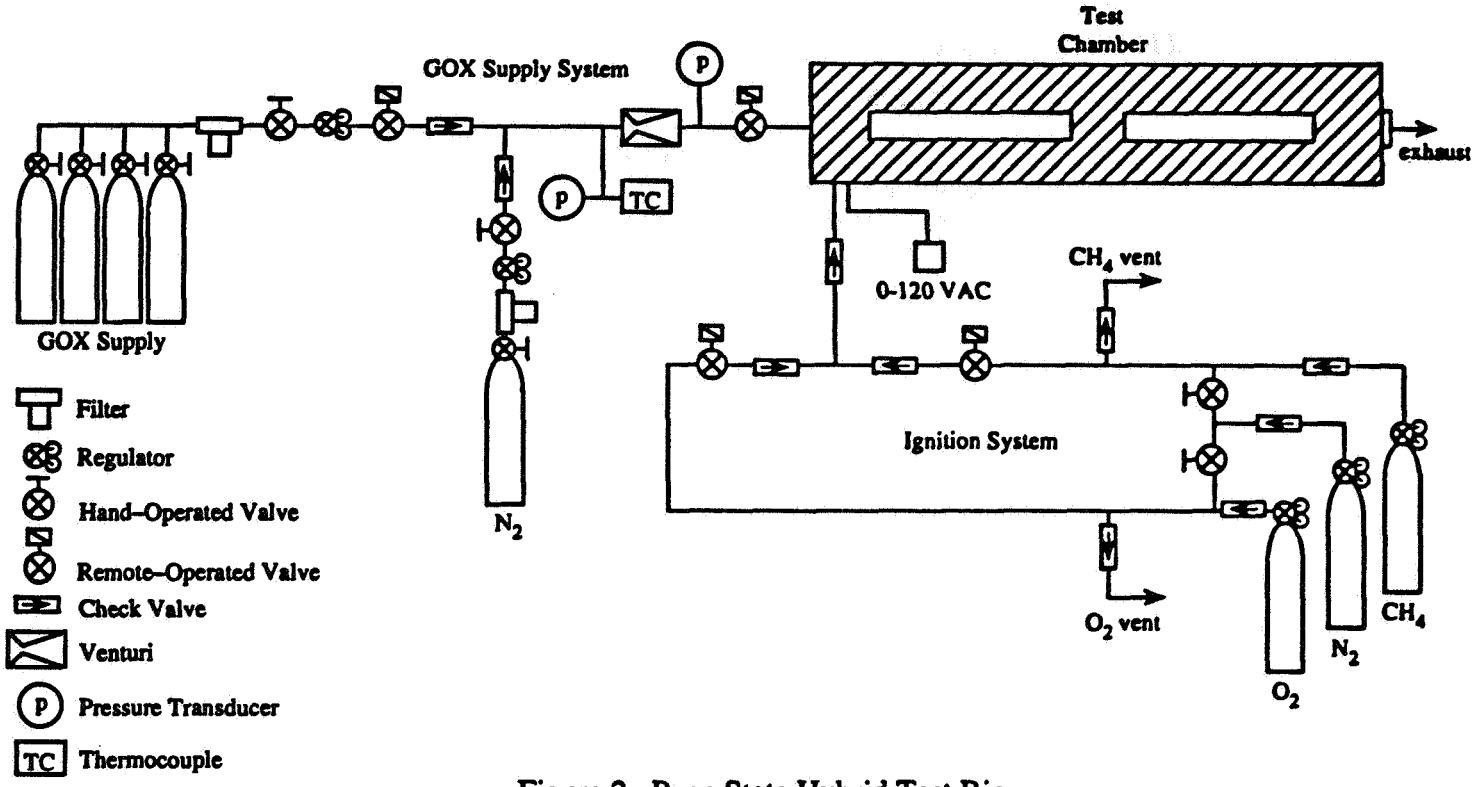

Figure 2. Penn State Hybrid Test Rig

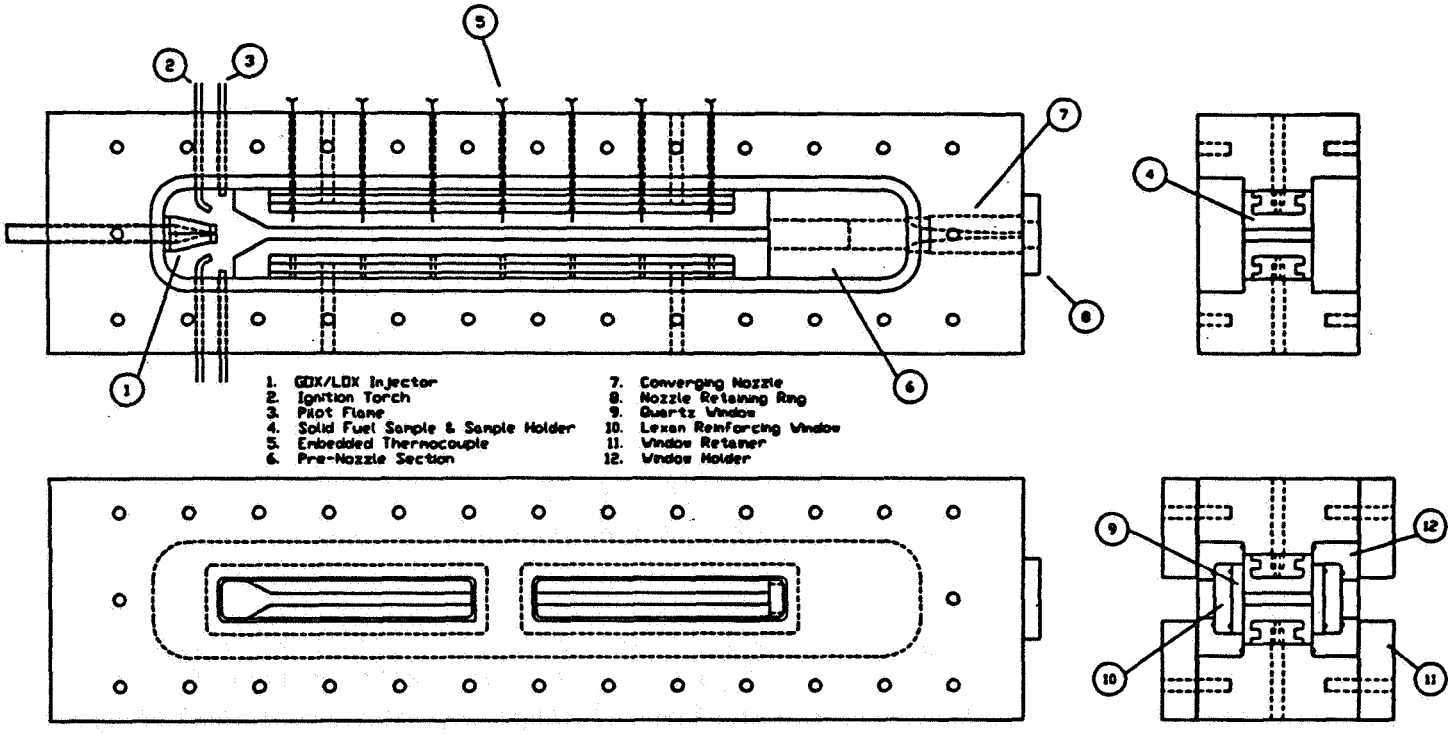

Fig. 3 - Partial Assembly Drawing of Hybrid Test Chamber

427196
P65 S

N95-70893

A HYDROGEN-OXYGEN ROCKET ENGINE COOLANT PASSAGE DESIGN PROGRAM (RECOP) FOR FLUID-COOLED THRUST CHAMBERS AND NOZZLES

Thomas M. Tomsik
NASA Lewis Research Center
Space Propulsion Technology Division
21000 Brookpark Rd., M.S. SPTD-2
Cleveland, Ohio 44135

SUMMARY

The design of coolant passages in regeneratively cooled thrust chambers is critical to the operation and safety of a rocket engine system. Designing a coolant passage is a complex thermal and hydraulic problem requiring an accurate understanding of the heat transfer between the combustion gas and the coolant. Every major rocket engine company has invested in the development of thrust chamber computer design and analysis tools; two examples are Rocketdyne's REGEN[1] code and Aerojet's ELES[2] program. In an effort to augment current design capabilities for government and industry, the NASA Lewis Research Center is developing a computer model to design coolant passages for advanced regeneratively cooled thrust chambers. The RECOP code incorporates state-of-the-art correlations, numerical techniques and design methods, certainly minimum requirements for generating optimum designs of future space chemical engines. A preliminary version of the RECOP model was recently completed and code validation work is in-progress. This paper introduces major features of RECOP and compares the analysis to design points for the first test case engine; the Pratt & Whitney RL10A-3-3A[3,4] thrust chamber (Fig 1).

MODEL DESCRIPTION

The RECOP model generates a preliminary design of tubular and milled channel coolant passages in regeneratively cooled thrust chambers given basic engine performance and geometry design constraints: thrust; chamber pressure; mixture ratio; expansion and contraction area ratio; characteristic chamber length; nozzle percent length; initial divergence and convergence half-angle; coolant flow path; coolant passage type; coolant inlet conditions; axial location of coolant inlet; hot-gas side wall temperatures; and chamber wall materials of construction. Output from the code provides information relevant to conducting detailed design and optimization studies of the engine: thrust chamber and nozzle dimensions and contour; wall heat flux; coolant pressure drop; coolant heat pick-up; coolant passage dimensions; combustion gas and coolant thermal and transport properties; and engine weight. A thrust chamber design schematic with typical dimensional requirements is shown in figure 2. The numerical procedure for the RECOP model is summarized in figure 3 and the main engine parameters computed by RECOP are listed below:

- Specific impulse and characteristic exhaust velocity (ODE)[5]
- Thrust chamber and coolant mass flow rate
- Thrust chamber and nozzle size and contour
- Combustion gas properties (ODE)
- Hot-gas side heat transfer coefficient and heat flux
- Coolant-side wall temperature and coolant total enthalpy
- Coolant transport and thermodynamic properties (GASP)[6]
- Coolant Reynolds and Mach number
- Coolant viscous and momentum pressure drop
- Coolant-side heat transfer coefficient and heat flux
- Coolant velocity by iteration until heat fluxes balance
- Final thrust chamber coolant passage dimensions
- Thrust chamber weight

Fundamental rocket engine performance and design equations[7,8] are used to compute thrust chamber size, throat diameter and chamber contour. The Rao method[9] generates the nozzle contour; a parabolic approximation for a Bell nozzle. There are options in RECOP for designing conical nozzles and entering nozzle coordinates specified in the form of a polynomial. The main calculation routine divides the engine into axial segments in the direction of coolant flow. The one-dimensional heat flux is calculated given the design hot-gas side wall temperature distribution. The Bartz equation provides the hot-gas side heat transfer coefficients. Starting at the coolant inlet a Newton-Raphson interative technique on the coolant-side provides heat transfer coefficients, coolant velocity and coolant passage dimensions. A solution is obtained at each axial station when the coolant-side heat flux is within a prescribed convergence tolerance.

There are five coolant flowpath configuration options available in the RECOP program: counter-flow; parallel-flow; split-flow; one-and-one-half pass; and series-flow. Insulating and gradated coating layers on the thrust chamber wall may be specified. RECOP is limited to engine designs ranging from 20 to 5000 psia chamber pressure, 2 to 12 mixture ratio and 2:1 to 1500:1 nozzle expansion area ratio. The preliminary version of RECOP was restricted to hydrogen/oxygen (H/O) and liquid hydrogen coolant primarily because of the availability of design information for H/O systems. Additional propellant combinations and coolant fluids will be incorporated into subsequent versions of RECOP. The program was written in FORTRAN-77 on a DEC-VAX computer; a PC version of the RECOP code is in the development phase.

RL10A-3-3A ANALYTICAL RESULTS

Figure 4 shows the RL10A-3-3A design parameters used in the RECOP code. Analytical thrust chamber contour results (Fig 5) agree with design coordinates from the injector face to an area ratio of about 8:1; the predictions are below design along the axial coordinates of the mid-nozzle region due to the Rao approximation. The hot-gas side design wall temperatures (Fig 6), hot-gas side

heat flux (Fig 7) and coolant static temperature profiles (Fig 8) all show good agreement with design information. The coolant static pressure results (Fig 8) deviate from the engine design data especially in the throat region. One reason for the large difference is that the "design" coolant static pressures shown in figure 9 were from a Pratt & Whitney analysis, but more importantly they contradict actual engine test data. Coolant pressure drop data from engine tests ranged from 260 to 280 psia; the RECOP code predicted a coolant pressure drop of 256 psia. Regarding coolant passage full-length tube geometry, a comparison of calculated tube height and width versus engine design points indicates good agreement (Fig 10). An overall comparison of RECOP with eighteen RL10A-3-3A design points showed that 39 percent of the predictions deviated from design by less than 1 percent; 33 percent were within 2 percent; and 28 percent were greater than 2 percent.

REFERENCES

1. Gerstley, J. G., "Advanced Hydrogen/Oxygen Thrust Chamber Design Analysis", NASA Contract Report NAS3-16774, Rocketdyne, Division of Rockwell International, Canoga Park, CA, Document No. ASR-73-170.

2. Taylor, C. E., "Expanded Liquid Engine Simulation (ELES) Computer Program", Vol 2, AFRPL-TR-85-055, Aerojet TechSystems Co., September, 1985.

3. Shubert, W. C., "Design Report for RL10A-3-3A Rocket Engine", NASA Contract NAS3-22339, Pratt & Whitney Report FR-15876, January 1982.

4. CPIA/M5 Liquid Propellant Engine Manual, Chemical Propulsion Information Agency, Unit 197, March 1992.

5. Gordon, S., McBride, B. J., "Computer Program for Calculation of Complex Chemical Equilibrium Compositions, Rocket Performance, Incident and Reflected Shocks, and Chapman-Jouget Detonations", NASA SP-273, Interim revision, updated version CET87, March, 1976.

6. Hendricks, R. C., Baron, A. K., Peller, I. C., "GASP - A Computer Code for Calculating the Thermodynamic and Transport Properties for Ten Fluids: Parahydrogen, Helium, Neon, Methane, Nitrogen, Carbon Monoxide, Oxygen, Fluorine, Argon, and Carbon Dioxide", NASA TN D-7808, Feb, 1975.

7. Huzel, D. K., Huang, D. H., "Design of Liquid Propellant Rocket Engines", NASA SP-125, 1967.

8. Sutton, G. P., "Rocket Propulsion Elements", 6th ed., John Wiley, 1992.

9. Rao, G. V. R., "Exhaust Nozzle Contour for Optimum Thrust", Jet Propulsion, Vol. 28, No. 6, pp 377-382, June, 1958.

FIG 1 : RL10A-3-3A ROCKET ENGINE

FIG 2 : REGENERATIVELY-COOLED THRUST CHAMBER AND NOZZLE CONTOUR

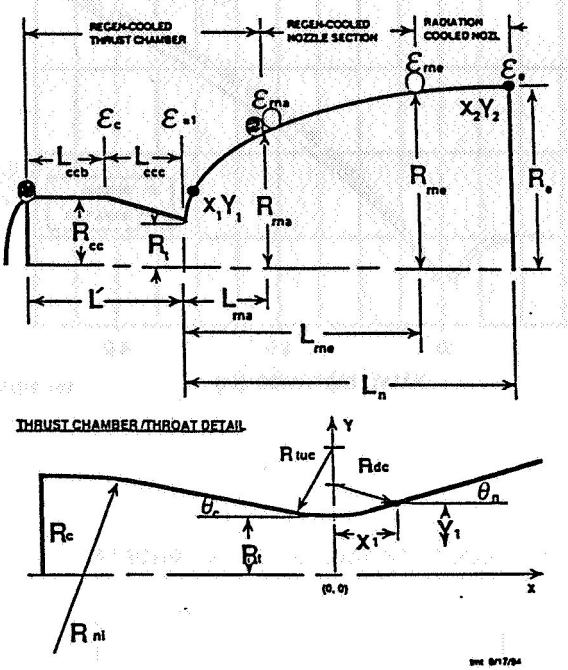

FIG 3 : COOLANT PASSAGE DESIGN CODE FLOW CHART

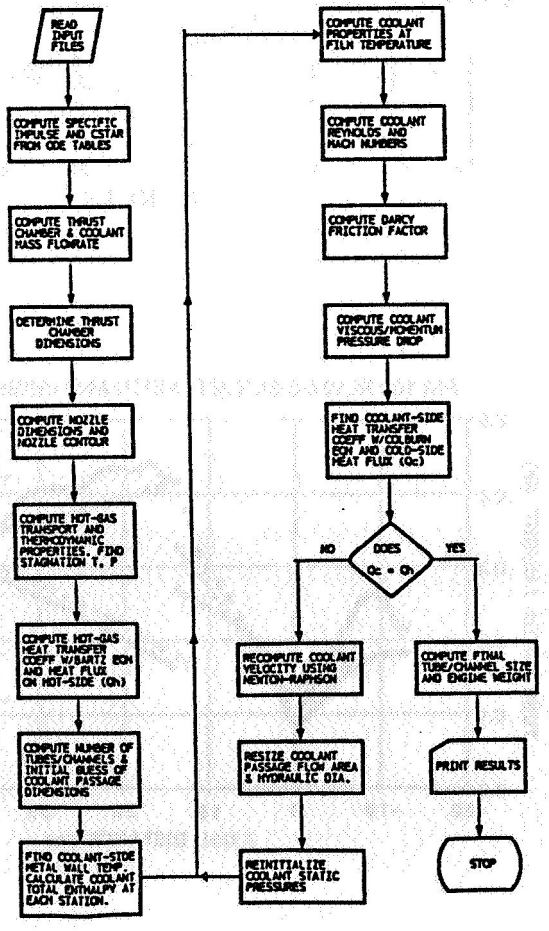

FIG 4 : RL10A-3-3A THRUST CHAMBER DESIGN INPUT PARAMETERS

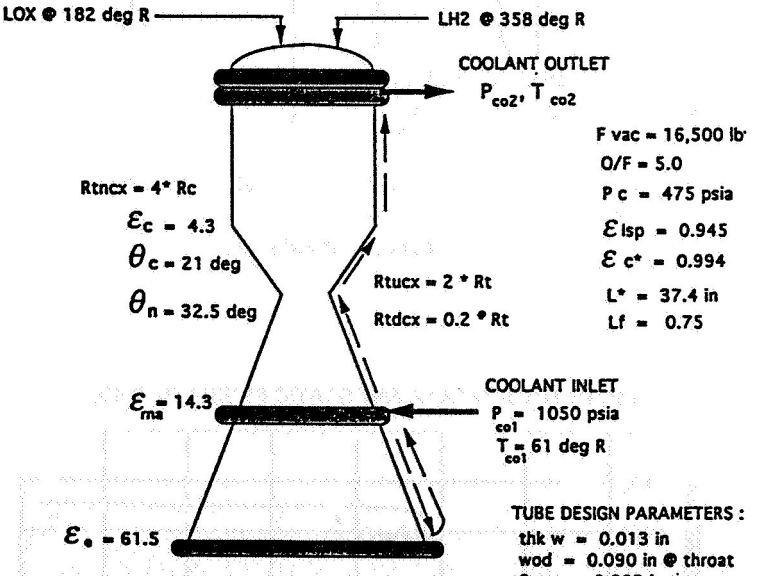

ONE AND ONE-HALF PASS (ICIRC = 4)
TUBULAR WALL CHAMBER / NOZZLE (IHXER = 3)
LH2 COOLANT FLUID (IFLUID = 1)

TUBE DESIGN PARAMETERS :
thk w = 0.013 in
wod = 0.090 in @ throat
Sgap = 0.002 in
Mtw 347 SS
thk jac = 0.070 in
ε rghns = 0.000046 in
θ_t = 150 deg

FIG 5 : RL10A-3-3A CHAMBER WALL RADIUS PROFILE

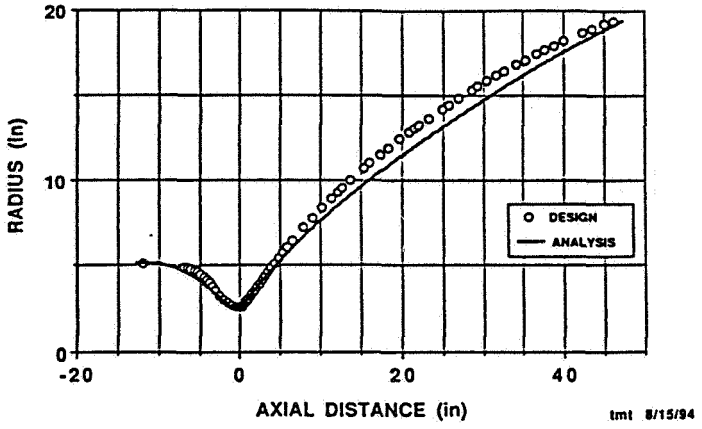

FIG 6 : RL10A-3-3A HOT-SIDE WALL TEMPERATURE PROFILE

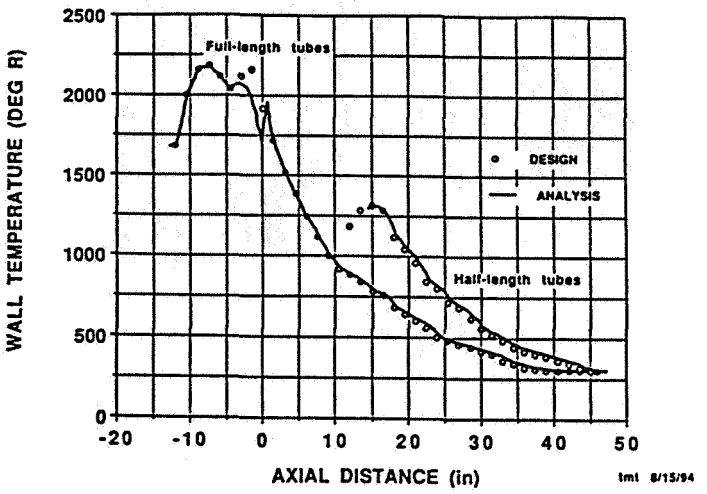

FIG 7 : RL10A-3-3A WALL HEAT FLUX PROFILE

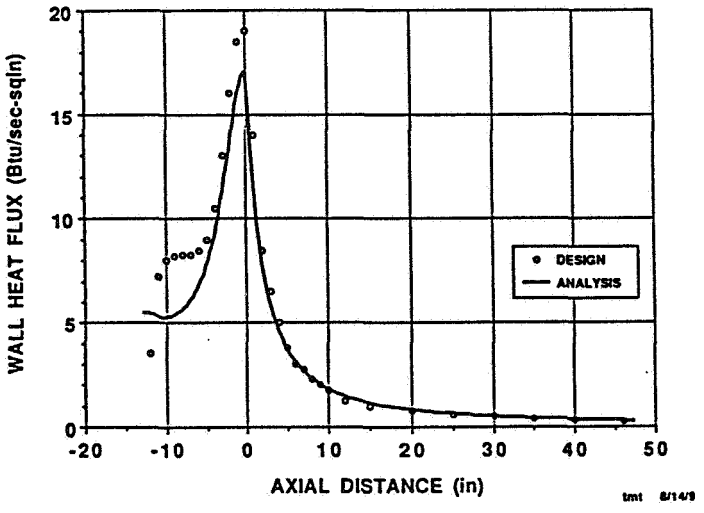

FIG 8 : RL10A-3-3A COOLANT STATIC TEMPERATURE PROFILE

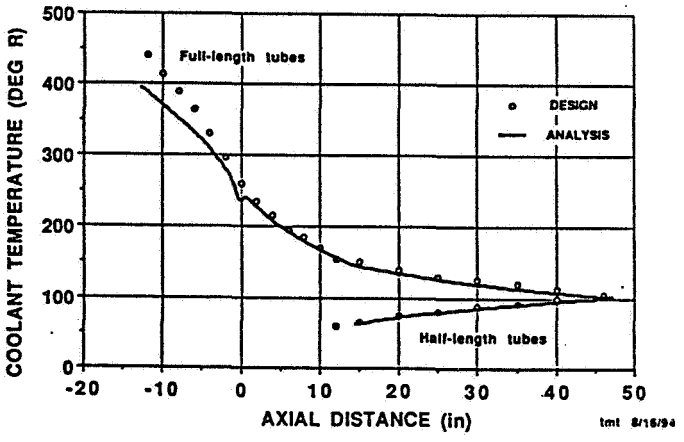

FIG 9 : RL10A-3-3A COOLANT STATIC PRESSURE PROFILE

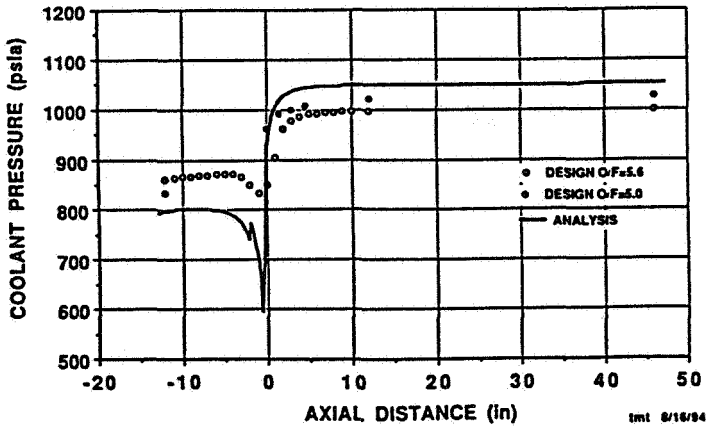

FIG 10 : RL10A-3-3A TUBE WIDTH AND HEIGHT PROFILE

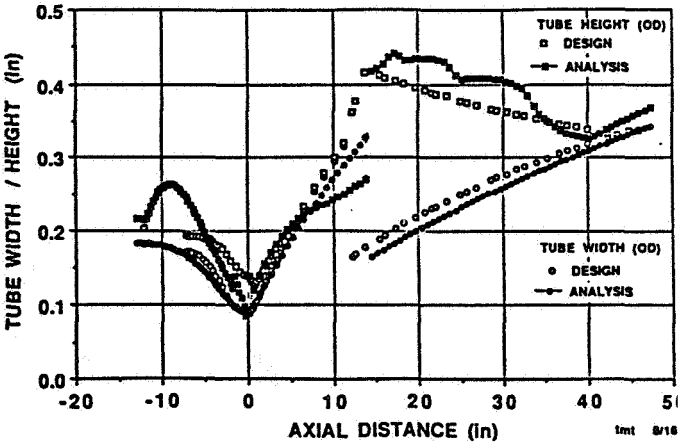

427198
B-4

N95-70894

The Least-Squares Finite Element Method for Low-Mach-Number Compressible Viscous Flows

Sheng-Tao Yu
NYMA Technology, Inc.
NASA Lewis Research Center

ABSTRACT

The present paper reports the development of the Least-Squares Finite Element Method (LSFEM) for simulating compressible viscous flows at low Mach numbers in which the incompressible flows pose as an extreme. Conventional approach requires special treatments for low-speed flows calculations: finite difference and finite volume methods are based on the use of the staggered grid or the preconditioning technique; and, finite element methods rely on the mixed method and the operator-splitting method. In this paper, however, we show that such difficulty does not exist for the LSFEM and no special treatment is needed. The LSFEM always leads to a symmetric, positive-definite matrix through which the compressible flow equations can be effectively solved. Two numerical examples are included to demonstrate the method: first, driven cavity flows at various Reynolds numbers; and, buoyancy-driven flows with significant density variation. Both examples are calculated by using full compressible flow equations.

INTRODUCTION

In this paper, low-Mach-number, compressible, viscous flows are of interest. Low-speed flows with significant temperature variations are compressible due to the density variation induced by heat addition. For example, a significant heat addition occurs in combustion related flow fields. Inside a chemical vapor deposition reactor, strong heat radiation also results in significant density variation. Although the flow speed is slow, one must employ the compressible flow equations to simulate such flows. However, it is well known that the conventional methods, which can handle high-speed compressible flows easily, fail miserably when applied to these low-Mach-number flows.

In the past, because of wide applications of the low-Mach-number flows, the issue of the efficiency and robustness of the calculations has been investigated. Most of the research, however, utilizes the finite difference and finite volume methods; few attempts have been made using the finite element methods. Conventional finite difference and finite volume methods in solving low-Mach-number flows can be divided into two categories: the pressure-based methods, and the density-based methods. The pressure-based methods have their root in the SIMPLE type algorithm. Essentially, a staggered grid has to be employed, i.e., the pressure and velocities are stored at different nodes. In addition, one usually has to employ a pressure correction equation (or other derived equation) instead of the original continuity

equation when solving the equation set. This approach, to some extent, is similar to the Galerkin mixed finite element methods for incompressible Navier Stokes equations. In the Galerkin mixed method, different elements have to be used to interpolate the velocity and the pressure in order to satisfy the LBB condition for the existence and stability of the discrete solution. Moreover, this approach results in an asymmetric, non-positive-definite coefficient matrix which can not be effectively solved by using iterative methods.

On the other hand, the density-based methods use the same nodes for the velocities and the pressure. Merkle et al. have successfully developed several density based methods for both low-Mach-number flows and all-speed flows. These methods are an extension of the computational schemes for high-speed, compressible flows. All these aerodynamic codes are designed based on the hyperbolic characteristic of the Euler equations; the viscous terms are effective only in a small portion of the domain and are interpreted as the damping of the numerical waves. When simulating low-Mach-number flows, however, the flow field is no longer dominated by the inviscid flow. The conventional aerodynamic codes encounter insurmountable slow-down. As a result, various treatments have been developed to enhance the efficiency. These treatments stem from preconditioning the jacobian matrices of the convective terms in the flow equations to improve their condition numbers. Usually, two steps are involved. First, according to Chorin, one adds a temporal derivative of pressure together with a multiplicative variable β, i.e., the pseudo-compressibility term, to the continuity equation. As a result, numerically viable time derivative terms exist in every equation even for flows at the low-speed (incompressible) limit. Consequently, based on the inviscid terms of the flow equations, the resultant equations become hyperbolic. And, a numerical method for a hyperbolic system can be employed to advance the system in time.

Since the transient solution is not of interest, one can enhance the computational efficiency by tuning up the propagation speed and damping effect of numerical waves so that the calculation can reach steady state faster. This is done by premultiplying a preconditioning matrix to the equation set. The eigenvalues of the convective-term Jacobian matrices are scaled to the same order of magnitude. Therefore, the stability of numerical waves is ensured and the time marching process is under control.

However, it is obvious that when low-Mach-number flows are of interest, the viscous terms play an important role and the flow system is elliptic. When using the preconditioning technique, one fabricates an artificial hyperbolic system in order to employ a time marching scheme to advance the system to a steady state. In other words, the preconditioning method is based on conditioning the inviscid part of the governing equations. For low speed flows, the viscous terms demand an implicit treatment due to the infinite fast characteristic speed. Therefore, as Merkle indicated that the real effect of the preconditioning matrix when using an implicit scheme is to eliminate the numerical stiffness caused by the approximate factorization. For unstructured grid solver, it is largely unclear what will be the effect of this type of preconditioning technique and certainly more study is needed.

In the finite element methods, fewer attempts have been carried out on calculating low-Mach-number

flows. For flow fields inside chemical vapor deposition reactors, Einset and Jensen developed a low-Mach-number formulation which was then solved by a Galerkin mixed method. In developing the low-Mach-number formulation, Einsted et al. proposed a correlation between the density and temperature based on the low-speed condition. The density in the governing equations was then replaced by the temperature. The equation set was solved by a mixed method which results in an asymmetric, non-positive-definite coefficient matrix. Einsted et al. inverted the matrix by the conjugate gradient squared (CGS) method and the generalized minimal residual (GMRES) method.

Because the low-Mach-number flows are closely related to the incompressible flows, it may be worthwhile to briefly review other treatments developed for the incompressible flows. On the finite difference setting, Chorin proposed to use a fractional step procedure to solve the incompressible flow equations. Later on, it was pointed out by Schneider et al. and Kawahara et al. that, by using the fractional step procedure, the restrictions imposed by the LBB condition for mixed formulation no longer apply. Various finite element schemes based on this procedure have been successfully developed and applied to incompressible flows using equal order interpolation. Other approaches, such as the Galerkin Least Squares method proposed by Hughes et al and Sampaio are shown to have similar effects. A wider interpretation of such schemes are described by Zienkiewicz and Wu. In addition, the fractional step procedure have been extended by Zienkiewicz and Wu to high speed compressible Navier-Stokes equations and shallow water equations

In this paper, a new formulation is proposed for the low-Mach number flows, in which the unknowns includes variables such as the vorticity, the pressure variation, and the divergence of velocity. With proper nondimensionalization, the magnitude of each term in the governing equations, which depends on the Mach number of the flow field, can be clearly discerned. As a result, a set of equations suitable for low-Mach-number flows is derived.

We employ the LSFEM as the numerical scheme to solve the low-Mach-number flows. This approach is an extension of the the LSFEM for incompressible flows which has been developed by Jiang et al. The LSFEM always leads to a symmetric, positive-definite matrix which can be efficiently inverted by an iterative scheme such as the conjugate gradient method. In the present paper, however, a direct solver is employed because the formulation and the feasibility of the LSFEM for low-Mach-number flows are of interest instead of the computational efficiency.

We present the governing equations to be solved by the LSFEM. In order to use simple C^o elements, we convert the second-order transport equations to first-order ones by introducing new variables into the equations. Then, the system of equations are nondimensionalized for low-Mach-number flows. In the paper, the implementation of the LSFEM is elaborated in detail. The temporal derivative terms of the flow equations are discretized by the Euler implicit method. Although, the transient solution is not of interest, the temporal derivative terms serves as a relaxation scheme for marching towards a steady state. The nonlinear terms are linearized by Newton's method. The discrete equations are formulated

in an increment form which is then solved by the LSFEM. In the last section, two numerical examples are presented: driven-cavity flows at various Reynolds numbers, and buoyancy-driven flows at various Rayleigh numbers. Both cases are calculated by using the compressible flow formulation.

Pgs 5 427199

N95- 70895

CONVERGENCE RATE ENHANCEMENT OF NAVIER-STOKES CODES ON CLUSTERED GRIDS

Kwang-Yoon Choi and George S. Dulikravich
Department of Aerospace Engineering, The Pennsylvania State University
University Park, PA 16802

SUMMARY

Our Sensitivity-Based Minimal Residual (SBMR) method which is based on our earlier Distributed Minimal Residual (DMR) method allows each component of the solution vector in a system of equations to have its own convergence speed. Our global SBMR method was found to consistently outperform the DMR method while requiring considerably less computer memory. Recently, we have developed and tested a new Line SBMR or LSBMR method and a Time-Step-Scaling (TSS) method that are even more robust and computationally efficient than our global SBMR method especially on highly clustered computational grids in laminar and turbulent flow computations.

Distributed Minimal Residual (DMR) Method

This method predicts an optimum amount of correction to each component of the solution vector by combining the information from several previous iteration levels. Each of the corrections obtained from the past iterations is multiplied by a different weighting factor and these weighting factors are determined so that they minimize the overall future residual. Although it is based on general Krylov subspace methods, the DMR method [1] differs from them by the fact that weighting factors are different from one variable to another in the system.

Global Sensitivity-Based Minimal Residual (SBMR) Method

The residual at a grid point depends on the solution vector **Q** at the neighboring grid points including the point itself. The sensitivity of residual R_m (m=1,2,3: number of equations) with respect to Q_k (k=typical neighboring points) is $\frac{\partial R_m}{\partial Q_k}$. That sensitivity can be determined from the finite difference equation used in the scheme. For a two-dimensional incompressible flow solved using Chorin's artificial compressibility method the solution vector is $\mathbf{Q} = \{p\ u\ v\}^T$. Suppose we have calculated the solution vector **Q** at iteration levels up to t+n where n is the number of regular iteration steps between two iteration levels. Then the change in the solutions between the iteration levels can be written as follows.

$$\Delta p_k = (p_k)^{t+n} - (p_k)^t \qquad \Delta u_k = (u_k)^{t+n} - (u_k)^t, \qquad \Delta v_k = (v_k)^{t+n} - (v_k)^t, \qquad (1)$$

Using the first two terms in a Taylor series expansion in artificial time direction, each residual for a two-dimensional system after n iterations will be

$$R_m^{t+n} = R_m^t + \left[\sum_k \frac{\partial R_m^t}{\partial p_k}\Delta p_k\right] + \left[\sum_k \frac{\partial R_m^t}{\partial u_k}\Delta u_k\right] + \left[\sum_k \frac{\partial R_m^t}{\partial v_k}\Delta v_k\right] \quad ; m=1,2,3 \qquad (2)$$

Similarly, future residual at t = (t+n)+1 can be approximated by

$$R_m^{(t+n)+1} = R_m^t + \left[\sum_k \frac{\partial R_m^t}{\partial p_k}\Delta p_k\right]\alpha_p + \left[\sum_k \frac{\partial R_m^t}{\partial u_k}\Delta u_k\right]\alpha_u + \left[\sum_k \frac{\partial R_m^t}{\partial v_k}\Delta v_k\right]\alpha_v \qquad (3)$$

Here, α's are the factors that multiply Δ's to estimate the future solution vector so that it minimizes the future residual. Then, $(p_k)^{(t+n)+1} = (p_k)^t + \alpha_p \Delta p_k$ with similar expressions for u and v [2,3,4,5].

Line SBMR (LSBMR) Method

The SBMR method calculates the same α's for the entire computational domain, which cannot represent optimum α's for both coarse grid regions and fine grid regions. Therefore, a natural conclusion is to allow α's to have different values in the clustered regions. A modified formulation (LSBMR) was developed [3,5] to allow these α's to have different values from one grid line to another. The LSBMR formulation will be explained using the two-dimensional, incompressible flow Navier-Stokes equations as an example. The system has three equations (rmax=3) and three unknowns (M=3), that are p, u and v. The acceleration coefficients for those unknowns are α_p, α_u and α_v, respectively. If the grid lines are clustered in the j-direction, then each j = constant grid line will be assigned its own set of three constant α's. The residual at a grid point (i,j) incorporates α's at the neighboring grid points plus the point itself. For the given Navier-Stokes system, this yields

$$R_r^{(t+n)+1} = R_r^t + \sum_{s=i-1}^{i+1}\left[\frac{\partial R_r^t}{\partial p_{s,j-1}}\Delta p_{s,j-1}\alpha_p^{j-1} + \frac{\partial R_r^t}{\partial p_{s,j}}\Delta p_{s,j}\alpha_p^{j} + \frac{\partial R_r^t}{\partial p_{s,j+1}}\Delta p_{s,j+1}\alpha_p^{j+1}\right]$$

$$+ \sum_{s=i-1}^{i+1}\left[\frac{\partial R_r^t}{\partial u_{s,j-1}}\Delta u_{s,j-1}\alpha_u^{j-1} + \frac{\partial R_r^t}{\partial u_{s,j}}\Delta u_{s,j}\alpha_u^{j} + \frac{\partial R_r^t}{\partial u_{s,j+1}}\Delta u_{s,j+1}\alpha_u^{j+1}\right]$$

$$+ \sum_{s=i-1}^{i+1}\left[\frac{\partial R_r^t}{\partial v_{s,j-1}}\Delta v_{s,j-1}\alpha_v^{j-1} + \frac{\partial R_r^t}{\partial v_{s,j}}\Delta v_{s,j}\alpha_v^{j} + \frac{\partial R_r^t}{\partial v_{s,j+1}}\Delta v_{s,j+1}\alpha_v^{j+1}\right] \qquad (4)$$

On each j = constant line, three values (M=3) of constant a's are determined so as to minimize the L-2 norm of the future global residual:

$$2\sum_{D}\sum_{r=1}^{3}\left(R_r^{(t+n)+1}\frac{\partial R_r^{(t+n)+1}}{\partial \alpha_p^j}\right)=0 \quad 2\sum_{D}\sum_{r=1}^{3}\left(R_r^{(t+n)+1}\frac{\partial R_r^{(t+n)+1}}{\partial \alpha_u^j}\right)=0 \quad 2\sum_{D}\sum_{r=1}^{3}\left(R_r^{(t+n)+1}\frac{\partial R_r^{(t+n)+1}}{\partial \alpha_v^j}\right)=0 \tag{5}$$

for j = 1, 2,· · ·, jmax. If jmax is the total number of j = constant grid lines, then substituting the equation (4) into (5) results in (jmax) x M algebraic equations for the same number of unknown optimum α's. For a given j = constant grid line when using central differencing in j-direction, α^j appears only in $R_m^{(t+n)+1}(i,j-1)$, $R_m^{(t+n)+1}(i,j)$ and $R_m^{(t+n)+1}(i,j+1)$. Therefore, we can see that the summation over the entire domain leaves the terms only with α^{j-2}, α^{j-1}, α^j, α^{j+1} and α^{j+2} summed along the j = constant line. Now we have

$$2\sum_{i=1}^{imax}\sum_{r=1}^{3}\left[R_r^{(t+n)+1}(i,j-1)\frac{\partial R_r^{(t+n)+1}(i,j-1)}{\partial \alpha_m^j}\right]+2\sum_{i=1}^{imax}\sum_{r=1}^{3}\left[R_r^{(t+n)+1}(i,j)\frac{\partial R_r^{(t+n)+1}(i,j)}{\partial \alpha_m^j}\right]$$

$$+2\sum_{i=1}^{imax}\sum_{r=1}^{3}\left[R_r^{(t+n)+1}(i,j+1)\frac{\partial R_r^{(t+n)+1}(i,j+1)}{\partial \alpha_m^j}\right]=0 \tag{6}$$

for j = 1,2,· · ·,jmax and m = p, u, v. In this example the simultaneous system of equations (6) yields a block penta-diagonal matrix equation for (jmax) x 3 optimum α's where each block is a 3 x 3 matrix. In the general case of a two-dimensional system having M partial differential equations, the block penta-diagonal system (6) will have blocks of size M x M. Superior performance of LSBMR is demonstrated for laminar (Fig. 1) and turbulent (Fig. 2) flows.

Time Step Scaling (TSS) Technique

A simple and efficient additional convergence acceleration technique called the Time Step Scaling (TSS) was developed [3,5] for the steady-state solution of the incompressible flow on highly-clustered grids. This technique can be considered as an extension of the local time-stepping so that time steps can be different for each equation and at each grid point. In the highly-clustered grid regions, the grid spacing in the direction of grid clustering is very small and it limits the magnitude of $\Delta\tau$ to be extremely small for stability reasons (time step is proportional to the square of the grid spacing). On the other hand, the Jacobian, J, becomes large in the clustered regions. However, the

product $J\Delta\tau$ is orders of magnitude smaller in the fine grid region than in the coarse grid region. Since the transient solutions are not of interest, one may desire to use larger time steps for some equations in the highly-clustered region for faster convergence. A close investigation of the convergence characteristics of each equation reveals that it is the slow evolution of pressure field in the fine-grid region which slows the overall convergence. Therefore, the time step for the continuity equation is scaled such that $J\Delta\tau$ in the clustered regions has the same order of magnitude as that in the coarse grid regions. To do this, the maximum value of $J\Delta\tau$ along the grid line in the direction of grid clustering is located and the time step at each grid point along this grid line is scaled as follows

$$\Delta\tau(i,j) = c\,\frac{1}{J(i,j)}\left(J\Delta\tau\right)_{max} \tag{7}$$

where $\Delta\tau(i,j)$ is the calculated time step without the TSS, $J(i,j)$ is the Jacobian, c is a user specified coefficient (typically 0.8) and $\left(J\Delta\tau\right)_{max}$ is the maximum value of $J\Delta\tau$ along the grid line considered. For highly-clustered grids, magnitude of $J\Delta\tau$ in the coarse grid region is orders of magnitude larger than that in the fine-grid region. The TSS technique was found to significantly accelerate the convergence when highly clustered grids are used (Figures 1 and 2).

REFERENCES

1. Lee, S. and Dulikravich, G. S., "Distributed Minimal Residual (DMR) Method for Acceleration of Iterative Algorithms," Computer Methods in Applied Mechanics and Engineering, Vol. 86, pp. 245-262, 1991.
2. Choi, K.-Y. and Dulikravich, G. S., "Reliability Enhancement of Navier-Stokes Codes Through Convergence Enhancement," NASA Propulsion Engineering Research Center Fifth Annual Symposium, University Park, PA, September 8-9, 1993, pp. 181-186.
3. Choi, K.-Y. and Dulikravich, G. S., "Convergence Acceleration of Iterative Algorithms Using a Sensitivity-Based Minimum Residual (SBMR) Method," 12th Workshop for CFD Applications in Rocket Propulsion, NASA MSFC, Huntsville, AL, April 19-21, 1994.
4. Choi, K-Y. and Dulikravich, G. S., "Global Sensitivity-Based Minimal Residual (GSBMR) Method for Acceleration of Iterative Convergence Rates," Proceedings of the 14th International Conference on Numerical Fluid Dynamics, Bangalore, India, July 11-15, 1994.
5. Choi, K.-Y., "Sensitivity-Based Minimum Residual Methods for Convergence Acceleration of Iterative Algorithms", Ph. D. dissertation, Department of Aerospace Engineering, The Pennsylvania State University, August 1994.

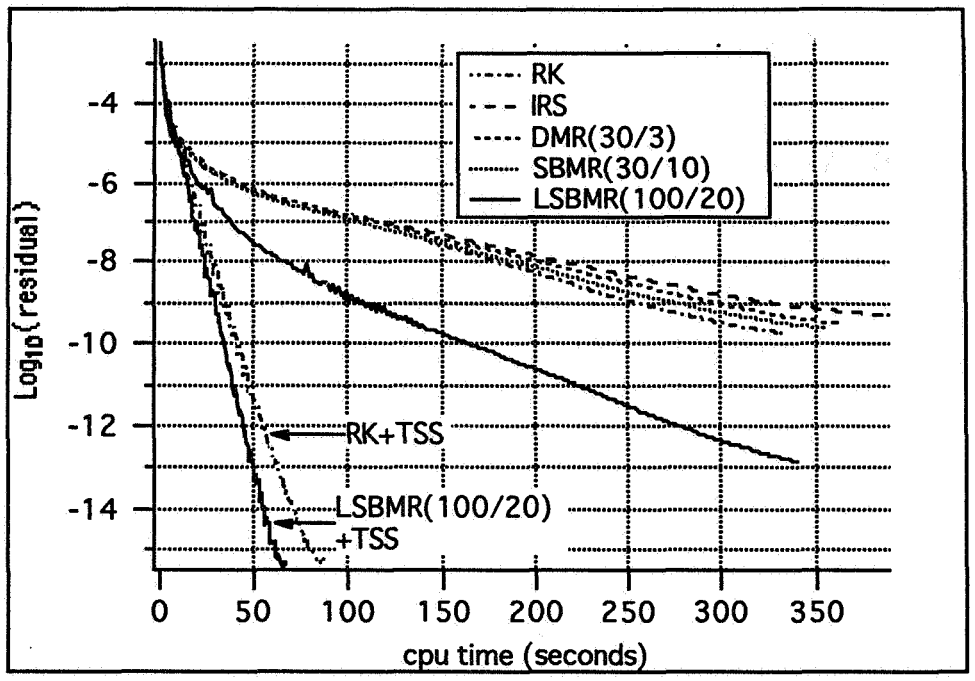

Figure 1 Convergence histories for a 2-D straight channel flow including the TSS technique. (L/H = 5, Re = 1600, 60x60 grid cells, $AR_{max} = 10^4$, $\beta = 5$, CFL = 2.8, von Neumann = 0.4)

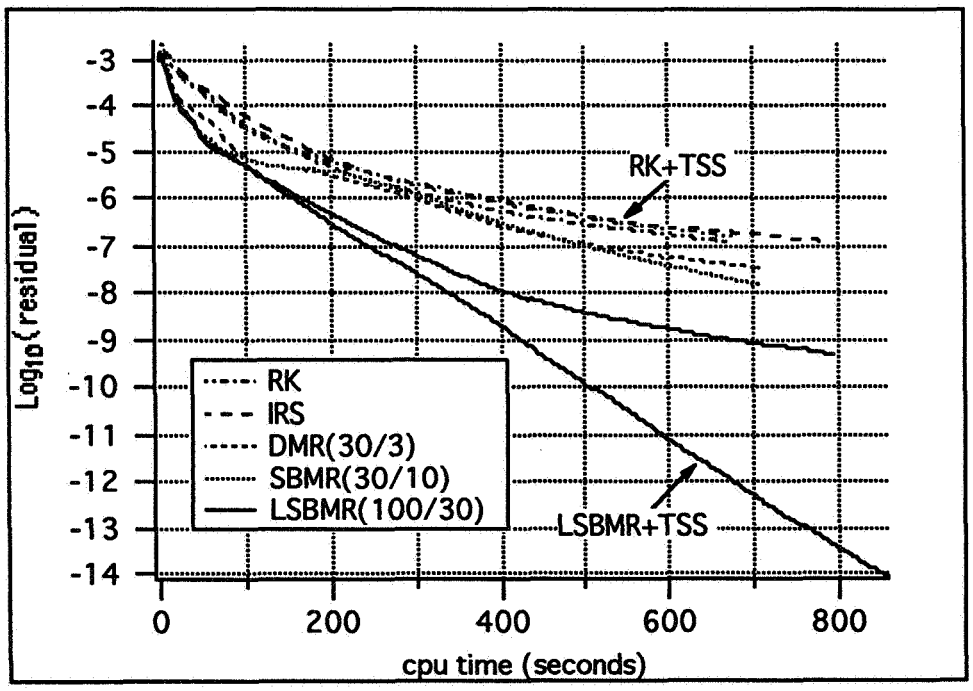

Figure 2. Convergence histories for a 2-D straight channel flow including the TSS technique. (L/H = 10, Re = 1.6×10^6, 60x120 grid cells, $AR_{max} = 10^4$, $\beta = 5$, CFL = 2.0, von Neumann = 0.4)

427202
Pgs 6 | N95- 70896

COMPUTATION FLUID DYNAMIC MODELING OF ROCKET BASED COMBINED CYCLE ENGINE FLOWFIELDS

Russell L. Daines* and Charles L. Merkle†
Propulsion Engineering Research Center
Department of Mechanical Engineering
The Pennsylvania State University

SUMMARY

Computational Fluid Dynamic techniques are used to study the flowfield of a fixed geometry Rocket Based Combined Cycle engine operating in rocket ejector mode. Heat addition resulting from the combustion of injected fuel causes the subsonic engine flow to choke and go supersonic in the slightly divergent combustor-mixer section. Reacting flow computations are undertaken to predict the characteristics of solutions where the heat addition is determined by the flowfield. Here, adaptive gridding is used to improve resolution in the shear layers. Results show that the sonic speed is reached in the unheated portions of the flow first, while the heated portions become supersonic later. Comparison with results from another code show reasonable agreement. The coupled solutions show that the character of the combustion-based thermal choking phenomenon can be controlled reasonably well such that there is opportunity to optimize the length and expansion ratio of the combustor-mixer.

INTRODUCTION

The use of multiple types of propulsion cycles is necessary for many hypersonic missions. The present paper addresses some of the flowfield characteristics that are encountered in a combined cycle concept for space launch that is based upon using a rocket engine as the fundamental element [1, 2]. This so-called Rocket Based Combined Cycle (RBCC) propulsion system is of interest for both single-stage-to-orbit (SSTO) and two-stage-to-orbit (TSTO) missions. A key feature is that it allows flight from take-off to orbit with a fixed geometry flow path.

An RBCC propulsion system is comprised of a rocket engine inside an air breathing engine as shown in Fig. 1. Both engines are integrated to operate as a single unit. The RBCC engine has the advantages of lift-off with pure rocket thrust, coupled with the ability to use inducted air as an oxidizer at lower altitudes, pure ram/scramjet performance at higher altitudes, after which it switches back to all rocket thrust after the vehicle is outside the atmosphere. This capability for capturing the oxidizer decreases the amount of stored oxidizer that is required which reduces take-off weight. Integrating the rocket and the air breathing engine also provides synergistic benefits that would not occur for the two units operating separately.

The ejector scramjet (ESJ) version of an RBCC engine operates in four modes: rocket ejector, ramjet, scramjet, and all-rocket mode. Each mode is used in the flight-speed regime where it is most efficient. A

*Graduate Research Assistant
†Distinguished Alumni Professor

major feature of the ESJ engine is that it operates with a fixed geometry flow path that provides a reduction in both the weight and complexity of the engine system as compared to a variable area flow path. In this fixed geometry flow path, the flow is thermally choked and accelerated supersonically by means of heat addition in a continuously diverging passage rather than a typical converging-diverging nozzle. Extensive research was conducted on rocket based combined cycle engines during the mid-1960's [3, 4], including the development and testing of both hydrogen- and hydrocarbon-fueled engines.

SOLUTION TECHNIQUE

The Favre-averaged, Navier-Stokes equations are solved in this modeling effort. To model the hydrogen-air reactions, an eighteen step, nine species reaction model is used. The specific heat, viscosity, and thermal conductivity of each species are calculated from fourth order polynomial curve fits. The binary diffusivity is calculated using Chapman-Enskog theory and the Lennard-Jones (6-12) potential. Mixture properties are determined using Wilke's mixing rule and appropriate averaging of binary diffusivities [5]. The q-ω turbulence model of Coakley [6] was also used. The temporal discretization of the Navier-Stokes equations is accomplished by means of an explicit, four-stage Runge-Kutta procedure, with the source terms in the species and turbulence equations being treated in a point-wise implicit manner to enhance numerical stability and convergence [7].

PROBLEM DESCRIPTION

The focus of the present paper is on modeling the mixing, combustion, and thermal choking processes in the diverging combustor of an RBCC engine operating in rocket ejector mode. The geometrical configuration is based on the axisymmetric ESJ engine of Congelliere *et al.* [3] and includes a slightly diverging "mixer" whose wall divergence angle is 0.5°, followed by a "nozzle" of divergence angle 1.75°. The end of the mixer and the beginning of the nozzle is defined as the point where the wall divergence angle increases. The computational domain includes the fuel injection, mixing, and combustion in the mixer and extends past the thermal choke point into the supersonic portion of the nozzle.

The upstream end of the computational domain corresponds to the location of the annular fuel injectors when the engine is in rocket ejector mode and represents the plane at which the fuel and oxidizer begin to mix. For clarity, references to mixer length will refer to the distance from this injection plane to the location where the duct wall angle changes. This length is varied parametrically, starting from a 45 cm base length, but for all computations, the combined length of the mixer and nozzle is 1 m. The inlet radius of the mixer is 6.35 cm. The oxidizer flow entering the mixer is assumed to be a well-mixed combination of air and completely combusted rocket exhaust. For the base case, the mass flow rate is set to the experimentally measured mass flow rate for a simulated free stream Mach number of 0.8. The static temperature is set at 1500 K. The computations are done for engine operation at the stoichiometric mixture ratio. Solutions are obtained on a $201x120$ grid.

Multi-species chemically reacting axisymmetric flow results are presented. The heat addition to the flow results from the mixing and combustion of fuel with the subsonic air stream coming from the mixer. This causes the heat addition and flowfield to be closely coupled, resulting in thermal choking that is dependent on the characteristics of the flow. A more detailed discussion of the results and comparisons with Congelliere's experimental measurements [3] are presented elsewhere [8].

RESULTS AND DISCUSSION

Representative results for the Mach number in the ESJ base case described above are given in Fig. 2. These results include both full flowfield contours and radial profiles at several axial locations. Specifically, profiles are shown for the mixer inlet (Plane A; x/L = 0.) and mid-plane (Plane B; x/L = 0.23), the end of the mixer and beginning of the nozzle (Plane C; x/L = 0.45), and for planes 75% (Plane D; x/l = 0.85) and 100% (Plane E; x/L = 1.0) of the way through the nozzle. The radial location in all profile plots is scaled by the local radius. For the solutions presented below the gaseous hydrogen is injected at 1100 K.

The Mach number contours in Fig. 2a show the two annular fuel streams at the mixer inlet. Reaction zones form on both sides of each fuel stream. The temperature in these reaction zones increases rapidly, while the air between the fuel streams remain at a relatively constant temperature. The Figure shows a more rapid initial increase in Mach number in the unheated flow than in the reacting flow. This difference, however, diminishes somewhat as the flow nears the sonic point, although the unheated flow still reaches Mach one at an axial location slightly upstream of the heated flow. The flow in the reaction region reaches the sonic velocity very near the mixer exit, where the wall angle increases. As the flow passes through the sonic point, it continues to accelerate to supersonic velocities. Mixing continues as the flow moves toward the exit, so that the flow Mach number is quite uniform at the nozzle exit except for a small region near the centerline where the flow is traveling at a higher Mach number. This is caused by the lower sonic speed at the centerline.

To complement the comparisons to experimental measurements refered to above and to further verify the predictions of the Runge-Kutta code, we compare the present predictions with those generated by the Finite Difference Navier Stokes (FDNS) code developed at NASA Marshall [9], which uses a pressure-based predictor-corrector algorithm. Mach number profiles at the mixer exit and nozzle exit, shown in Fig. 3, show that agreement between the codes is good. At the mixer exit the FDNS code predicts slightly lower Mach numbers near the wall and outer shear layer. At the nozzle exit, the near-wall discrepancy continues. The FDNS code also predicts less mixing in the bulk of the flow, resulting in a less uniform Mach number profile at the nozzle exit. Overall levels and shear region locations are in good agreement.

Grid adaption was applied to the original solution to better cluster the grid in high gradient regions of the flowfield and achieve better resolution of the shear layers without increasing the number of grid points. Here, the Self-Adaptive Grid Code (SAGE) [10] was used to adapt the grid. The Mach number profiles resulting from these two grids at the mixer exit, seen in Fig. 4, show that the adapted grid yields steeper gradients in the shear layers. Also there is a greater difference in the magnitudes of the peaks and troughs on the adapted grid, indicating less numerical diffusion than in the original solution. Finally, a tendency for the Mach number to overshoot near the centerline on the original grid is not present on the adapted grid.

To study the effects of fuel injection location, the combustor flow was calculated for mixer lengths of 15, 45, 65, 80, and 100 cm. The mixer wall angle was 0.5°. At the mixer exit for all but the 100 cm mixer, an additional length of duct was added with a wall angle of 1.75° to form the nozzle and bring the overall duct length to 100 cm. The centerline Mach number profiles for all five geometries are presented in Fig. 5. The axial locations of the centerline sonic point and the mixer exit are proximate for all but the longest mixer. The flow tends to choke at the location where the wall divergence angle increases if significant heat addition is continuing at that axial location. When significant heat addition has ceased prior to the mixer exit, as occurs in the 80 and 100 cm mixers, the location of thermal choking remains unchanged when the

mixer length is changed. In these cases, the subsonic flow upstream of the sonic point is not affected by the change in wall angle in the supersonic region. The subsonic flow is increasingly affected as the mixer length is shortened. In the 15 cm mixer, the flow in the subsonic region is significantly different from the flow in longer mixers. In this short mixer, the Mach number increases at a constant rate through the sonic point. In the other cases the Mach number increases more gradually at first then increases rapidly as the flow goes through the transonic regime. The increasing exit area of the ducts as the mixer is shortened and nozzle is lengthened allows the flow to expand more, increasing the exit Mach number.

As the simulated freestream Mach number increased in the experiments of Ref. 3, the mass flow rate into the engine and the stagnation pressure in the engine downstream of the inlet both increased. It should be noted that for all freestream Mach numbers in rocket ejector mode, the air flow was subsonic in the duct downstream of the inlet. Using the measured mass flow rates as inputs, calculations were performed over a range of vehicle flight speeds for a mixer length of 45 cm. Both the specific impulse and the thrust increase with increasing flight speed. The larger air flow rate allows a larger amount of fuel to be injected and burned, adding more energy to the flow. Overall, the Mach number contours for the different freestream Mach numbers do not vary significantly.

The extent of combustion increased with increasing vehicle velocity. This is indicated by an increased stagnation temperature at the mixer exit, shown in Fig. 6. The increased stagnation temperatures at higher freestream Mach numbers indicate a higher level of heat addition to the flow. The higher temperature regions are broader radially for the higher speeds, indicating that the mixing between the fuel and oxidizer is enhanced at these conditions. As the freestream Mach number increases, the air stream mass flow rate increases, so the mass flow rate of hydrogen fuel is also increased to maintain stoichiometric conditions. As this occurs, the velocity ratio between the fuel stream and the oxidizer stream increases. The increased shear velocity causes the flows to mix more rapidly. This trend of increasing combustion efficiency is opposite from the experimental results, which showed an initial decline in combustion efficiency as the freestream Mach number increased.

ACKNOWLEDGEMENTS

This work is supported by NASA Graduate Student Researcher Program Grant NGT-50884 through NASA Marshall Space Flight Center.

REFERENCES

1. Escher, W. and Schnurstein, R., AIAA Paper 93-1944, Monterey, CA, June 1993.
2. Foster, R., Escher, W., and Robinson,J., AIAA Paper 89-2294, Monterey, CA, July 1989.
3. Congelliere, J., Prevatte, N., and Lime, J., Rep. No. AFAPL-TR-67-118, The Marquardt Corp., May 1968
4. Odegaard, E. and Stroup, K., Rep. No. AFAPL-TR-66-49, The Marquardt Corp., October 1966
5. Yu, S., Tsai, Y., and Shuen, J., AIAA Paper 89-0391, Reno, NV, January 1989.
6. Coakley, T., AIAA Paper 83-1693, Danvers, MA, July 1983.
7. Weiss, J., Daines, R., and Merkle, C., AIAA Paper 91-3557, Cleveland, OH, September 1991.
8. Daines, R. and Merkle, C., AIAA Paper 94-3327, Indianapolis, IN, June 1994.
9. Wang, T., Computational Fluid Mechanics J., vol 1, no. 3, October 1992.
10. Davies, C. and Venkatapathy, E., Update to NASA Tech. Memo. 103905, March 1994.

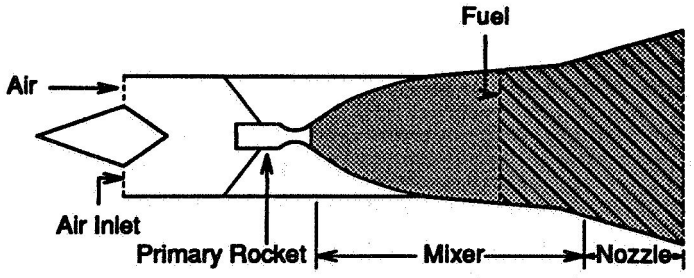

Figure 1: Schematic diagram of a generic RBCC engine. Reaction zone indicated by hatched region.

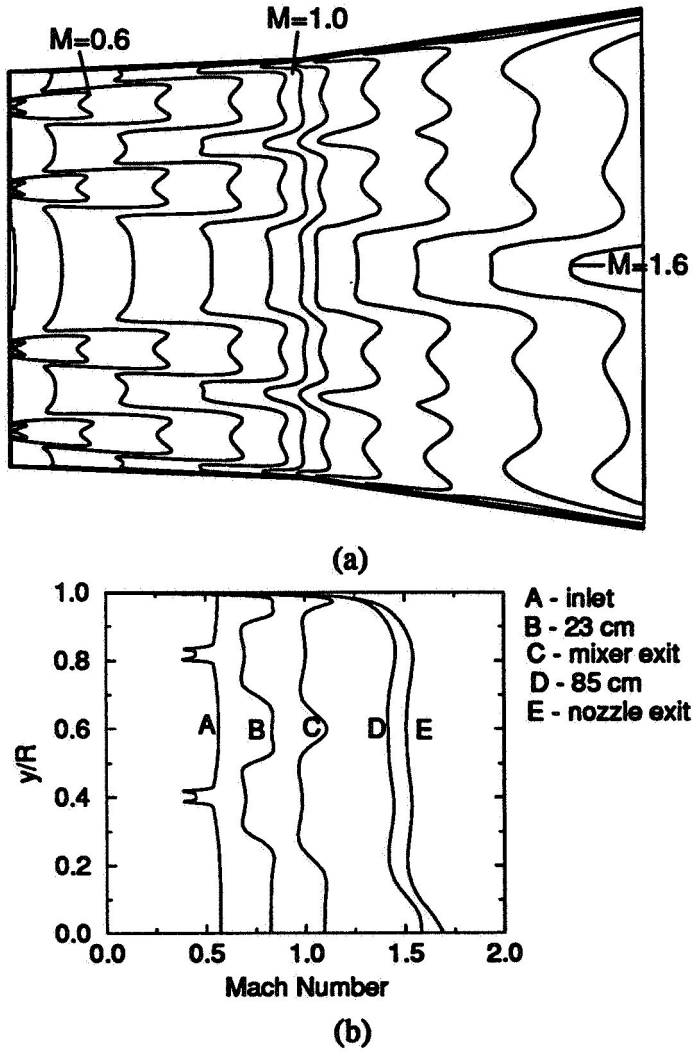

Figure 2: Mach number contours and radial profiles for axisymmetric reacting flow in a duct with a 45 cm mixer. Contour intervals are 0.1. Contour plot is shown here at a 5:1 radial aspect ratio for clarity of details.

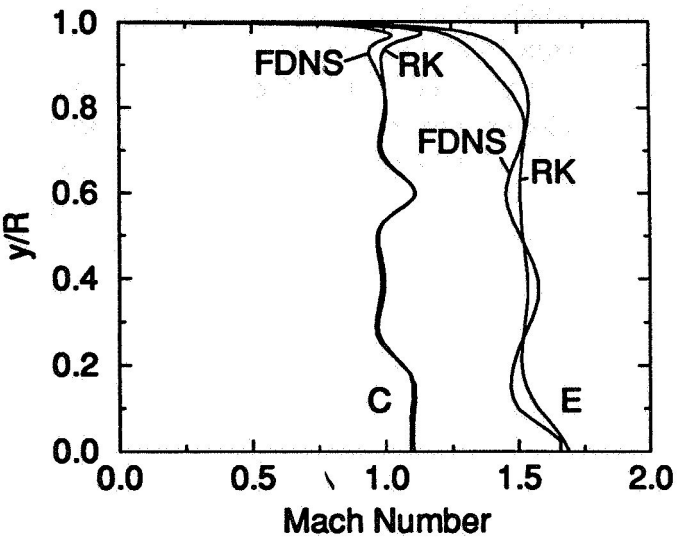

Figure 3: Radial Mach number profiles at the mixer exit (C) and the nozzle exit (E) from the Runge-Kutta and FDNS codes.

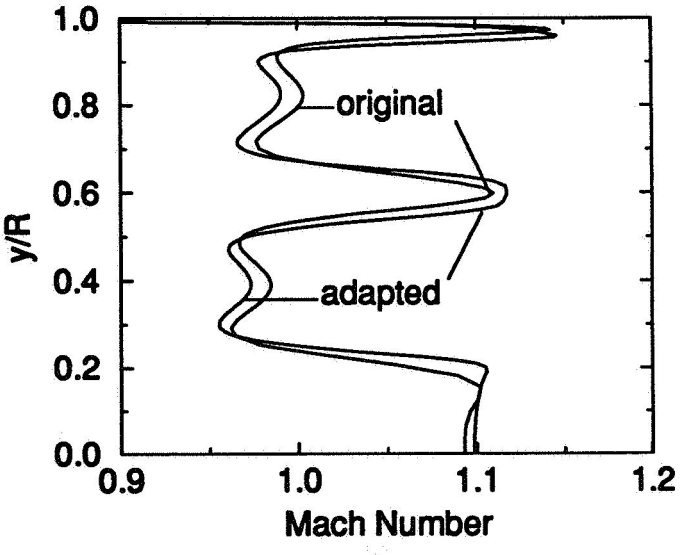

Figure 4: Radial Mach number profiles at the mixer exit on the original and adapted grids.

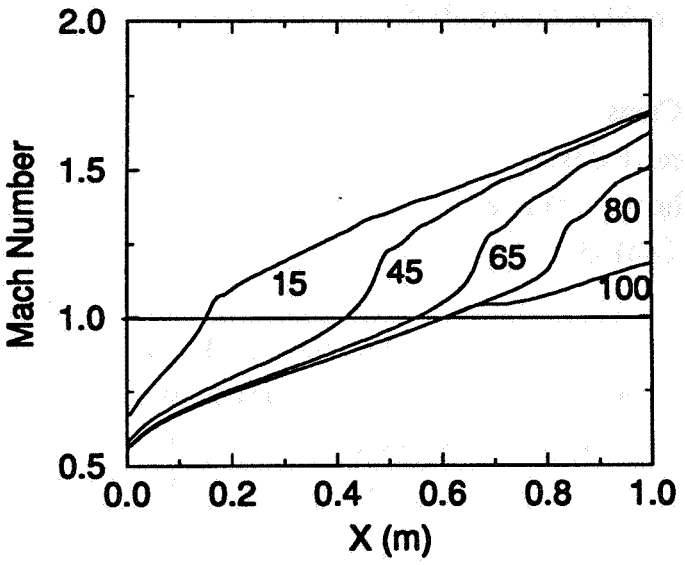

Figure 5: Centerline Mach number profiles for ducts with mixer lengths of 15, 45, 65, 80, and 100 cm. The straight line indicates the sonic point.

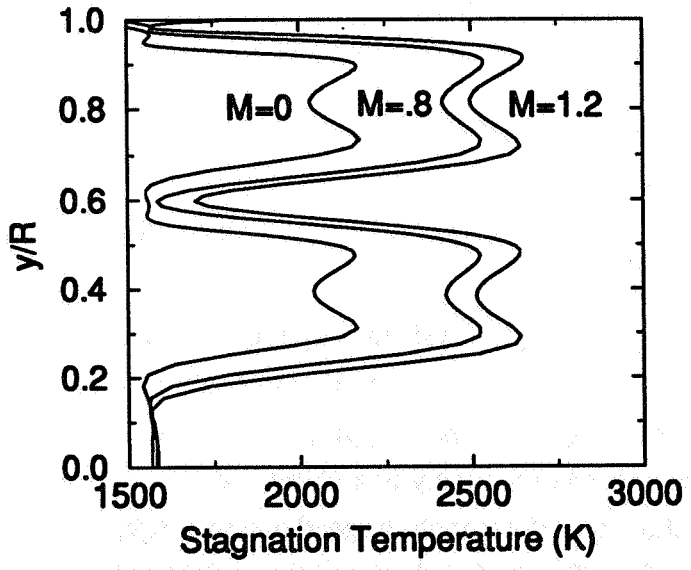

Figure 6: Mixer exit stagnation temperature profiles for varying freestream Mach numbers. Mixer length is 45 cm.

N95-70897

Multidisciplinary Propulsion Simulation Using the Numerical Propulsion System Simulator (NPSS)

42 720S
Pgs 1

Russell W. Claus
NASA Lewis Research Center
Interdisciplinary Technology Office
Cleveland, OH 44135

Implementing new technology in aerospace propulsion systems is becoming prohibitively expensive. One of the major contributors to the high cost is the need to perform many large scale system tests. The traditional design analysis procedure decomposes the engine into isolated components and focuses attention on each single physical discipline (e.g. fluid or structural dynamics). Consequently, the interactions that naturally occur between components and disciplines can be masked by the limited interactions that occur between individuals or teams doing the design and must be uncovered during expensive engine testing. This can pose serious problems for a highly integrated propulsion system, where tight coupling can produce unforeseen interactions having adverse effects on system performance. For example, the installation of an improved efficiency turbine into an existing engine can result in a re-balancing of the engine cycle with the consequence that the compressor is driven at a less efficient operating point, thereby reducing the total system performance as measured by specific fuel consumption (SFC) or some other system parameter. As a result, the introduction of advanced technology into design techniques that combine concurrent engineering and numerical simulation may provide a system design solution.

This overview will discuss a cooperative effort of NASA, industry, and universities to integrate disciplines, components, and high performance computing into a Numerical Propulsion System Simulator (NPSS). This integrated, interdisciplinary system analysis requires advancements in the following technologies: 1) interdisciplinary analysis to couple the relevant disciplines such as aerodynamics, structures, heat transfer, chemistry, materials, and controls; 2) integrated system analysis to couple subsystems and components at an appropriate level of detail; 3) a high performance computing platform composed of a variety of architectures, including massively parallel processors, to provide the required computing speed and memory; and 4) a simulation environment that provides a user-friendly interface between the analyst and the multitude of complex codes and computing systems that will be required to perform the simulations. This overview will review several research efforts to develop these technologies. The discussion will detail the "zooming" technique being employed to capture the relevant physics, the use of object-oriented programing, and progress in developing algorithms and applications for parallel computers.

N95- 70898

EFFECTS OF TRANSVERSE OSCILLATORY WAVES ON TURBULENT BOUNDARY LAYERS

427207
B1

Jonathan Matulevich and Harold R. Jacobs
The Pennsylvania State University
Department of Mechanical Engineering
University Park, PA

Studies of the interaction of unsteady (oscillatory) flows with the growth of a turbulent boundary layer on a flat plate have primarily dealt with an oscillatory component in the primary flow direction. Past studies of the 2-D flow have shown little or no increase in the time averaged heat transfer. The present paper deals with a steady axial and an oscillatory transverse flow. It is shown that for such flows the temporal variation for both the turbulent skin friction and heat transfer are such as to yield increased time averaged values.

427209
Gs 5

N95-70899

VALIDATION OF TWO-EQUATION TURBULENCE MODELS FOR PROPULSION FLOWFIELDS

Manish Deshpande[1], S. Venkateswaran[2], Charles L. Merkle[3]
Propulsion Engineering Research Center
Department of Mechanical Engineering
The Pennsylvania State University

Summary

The objective of the study is to assess the capability of two-equation turbulence models for simulating propulsion-related flowfields. The standard $k-\epsilon$ model with Chien's low Reynolds number formulation for near-wall effects is used as the baseline turbulence model. Several experimental test cases, representative of rocket combustor internal flowfields, are used to catalog the performance of the baseline model. Specific flowfields considered here include recirculating flow behind a backstep [1,2], mixing between coaxial jets [3] and planar shear layers [4,5]. Since turbulence solutions are notoriously dependent on grid and numerical methodology, the effects of grid refinement and artificial dissipation on numerical accuracy are studied. In the latter instance, computational results obtained with several central-differenced and upwind-based formulations are compared. Based on these results, improved turbulence models such as enhanced $k-\epsilon$ models as well as other two-equation formulations (e.g., $k-\omega$) are being studied. In addition, validation of swirling and reacting flowfields are also currently underway.

Technical Discussion

The k and ϵ transport equations are solved coupled to the the preconditioned Navier-Stokes equations. Preconditioning ensures that the system remains well-conditioned at all flow Mach numbers and Reynolds numbers, thereby providing uniform convergence under a wide range of conditions (Ref. [6,7] for details). Furthermore, convergence difficulties associated with strongly stretched grids, which are characteristic of turbulent flows, are mitigated by using the ADI algorithm with proper local time-stepping and preconditioning [6,7]. Several spatial discretization schemes such as second-order central-differencing and first- and third-order upwind differencing are used. When central-differencing is used, the presence of odd-even splitting and/or oscillatory solution behavior in the vicinity of steep gradients, sometimes necessitate the judicious addition of second-order dissipation through the use of switches or flux-limiters [8]. Oscillatory solutions, in particular, are frequently observed in turbulence computations and usually seem to be related to large-scale unsteady flow processes such as

[1]Graduate Research Assistant
[2]Research Associate
[3]Professor

vortex-shedding. Upwind schemes which possess inherent dissipative properties usually suppress such unsteady behavior and may therefore be regarded as more robust schemes.

Results and Discussion

The first test case discussed is the Driver-Seegmiller backward-facing step flow [1] shown in Fig. 1. The velocity contours (Fig. 2) indicate a recirculation length of $x/H = 5.7$, which is in agreement with other published computational results using the $k - \epsilon$ model (expt. value is 6.3). The results in Fig. 2 were obtained with third-order upwind-biased discretization of the convective terms. Interestingly, central differencing does not yield a converged solution with the velocity contours suggesting that the solution is unsteady. Addition of second-order dissipation [7] renders the solution steady. This unsteadiness was however not encountered with any of the upwind schemes studied. Figure 3 shows the velocity and μ_t profiles plotted against experimental data at several axial stations for the different discretization schemes. The central-differenced and third-order upwind schemes agree fairly well with each other, while the first-order scheme shows significant discrepancies in μ_t and under-predicts the recirculation length. Additionally, the results are well-predicted when third-order is used for the flow equations and first-order upwind is used for the turbulence equations. This result suggests that using first-order accuracy in the turbulence equations does not undermine the overall accuracy of the calculation.

A grid refinement study was performed for the backstep flow of Kim, Kline and Johnston [2]. Grid sizes of 91^2, 181^2 and 361^2 were used. The coarsest grid had 9 points within $y^+ = 10$. Fig. 4 compares the velocity and k profiles for the three levels of refinement for the third-order upwind scheme. As the figure shows, the coarsest grid differs significantly from the finer grids, especially in the region just downstream of the reattachment point. The two finer grids agree quite well with each other, implying grid-independence. Second-order central differencing, once again, indicated an unsteady solution even for the coarsest grid case unless additional dissipation was included.

The next case considered is the experiment of Johnson and Bennett [3], involving two co-flowing jets in a confined sudden expansion. Figure 5 shows the converged velocity contours for this case while Fig. 6 shows comparisons of velocity profiles obtained from central-differenced and upwind calculations plotted against experimental data. Overall agreement is quite good except at the centerline in the near-injector region.

The final test case presented here is the turbulent planar shear layer experiments of Chang *et al* [5]. In Fig. 7, comparisons of the velocity and k profiles are presented for the non-reacting case using third-order upwind for the convective terms. The computations were performed using inviscid wall boundary conditions at the upper and lower edges of the domain. The computations agree fairly well with the experiments in the upstream stations. However, in the downstream stations, there is growing discrepancy in the predicted k profiles. A similar discrepancy was observed in the calculations reported in Ref. 5 and may be related to the choice of wall boundary condition.

The above results demonstrate that accurate turbulent flow solutions may be obtained with the proper

choice of spatial discretization schemes. Several of the flowfields were observed to have convergence difficulties related to large-scale unsteadiness in the flowfield. Upwind-based schemes appear to be more robust in this regard, probably because of the dissipation that is inherent in these schemes. The results presented here will provide a baseline reference point for the selection of improved turbulence models for solving combustor-related flowfields. Additional calculations are underway for the computation of swirling and reacting flowfields.

Acknowledgements

This work was supported by Pratt & Whitney, West Palm Beach, Florida. The authors also wish to acknowledge Kevin Van Dyke and Andy Brankovic of Pratt and Whitney for their help in setting up some of the cases.

References

1. Driver, D. and Seegmiller, H., AIAA Journal, Vol. 23, No. 2, pp. 163-171.
2. Kim, J., Kline, S.J. and Johnston, J.P., J. Fluids Eng., Vol. 102, pp. 302-308, 1980.
3. Johnson, B. and Bennett, J., Proc. ASME Fluids Eng. Conf., Boulder, CO.
4. Chang, C.T., *et al*, AIAA 93-2381.
5. Lai, H.T., and Raju, M.M., AIAA 93-1773, 29th Joint Propulsion Conf., Monterey, 1993.
6. Buelow, P., Venkateswaran, S. and Merkle, C., AIAA 93-3367, Orlando, FL.
7. Venkateswaran, S., Proc. 14th Intl. Conf. on Num. Meth. in Fluid Dyn., Bangalore, India, 1994.
8. Jameson, A., AIAA 93-3359, Orlando, FL.

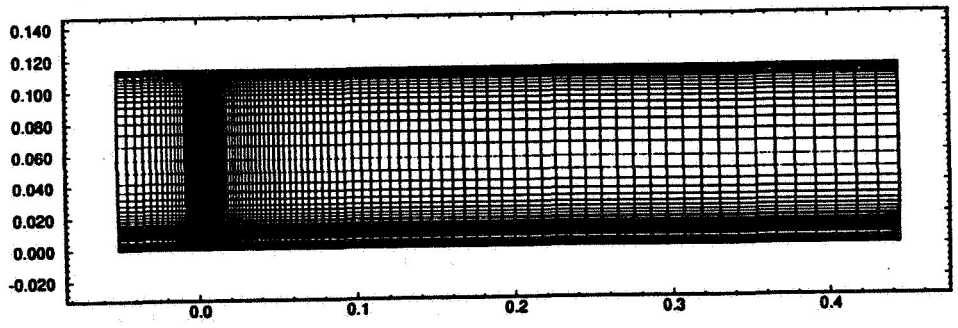

Figure 1: Computational Grid for Driver-Seegmiller Backstep Flow

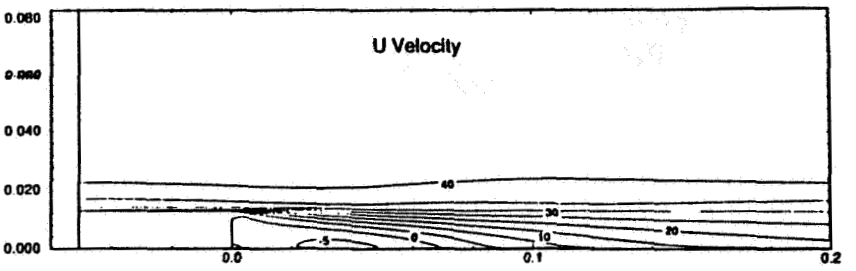

Figure 2: Velocity Contours for Driver-Seegmiller Backstep Flow

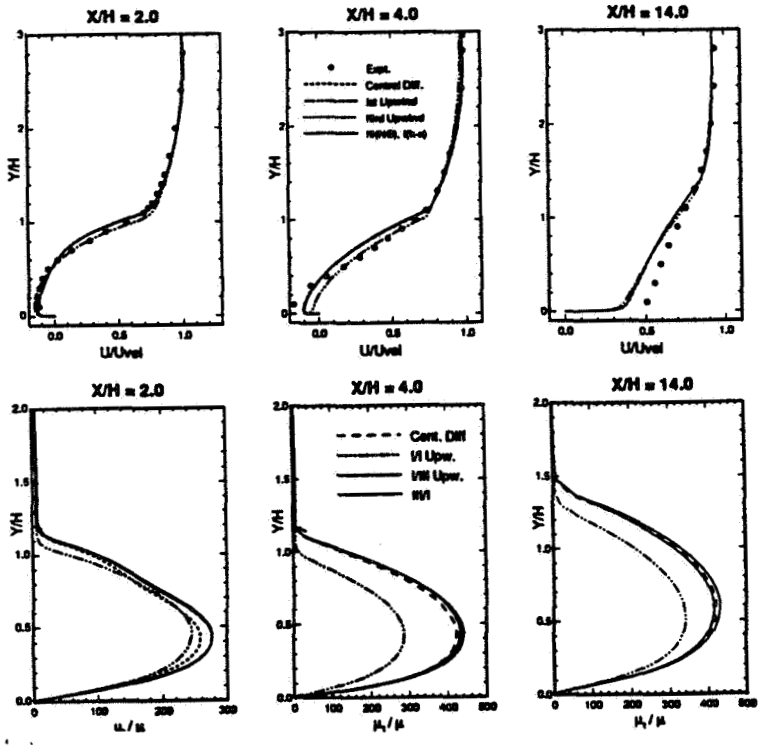

Figure 3: Velocity and μ_t profiles - Comparison between Schemes

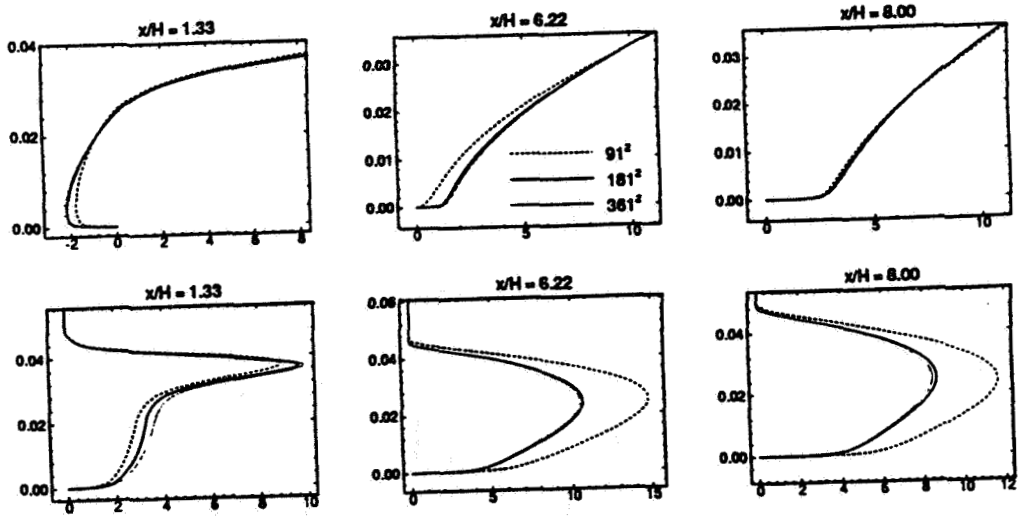

Figure 4: Velocity and k profiles for Kim *et al* backstep - Grid Refinement Study

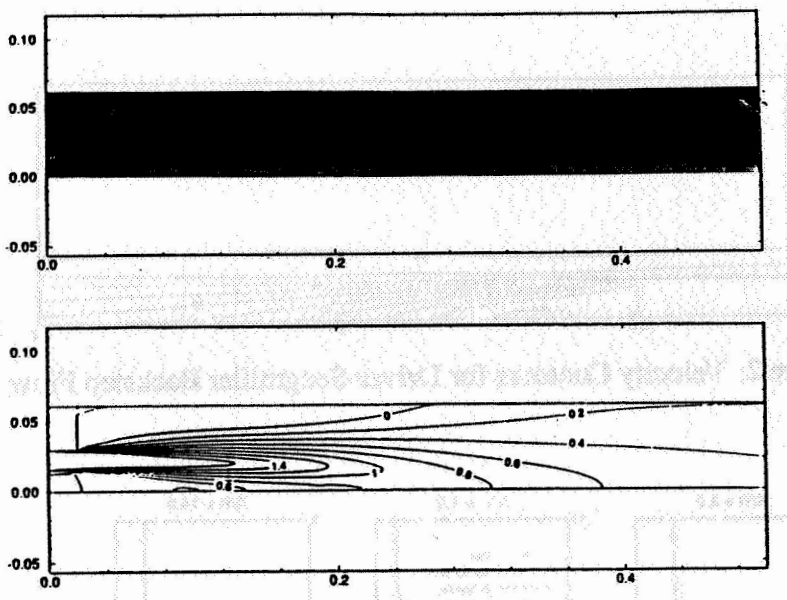

Figure 5: Computational Grid and Velocity Contours for co-axial jets.

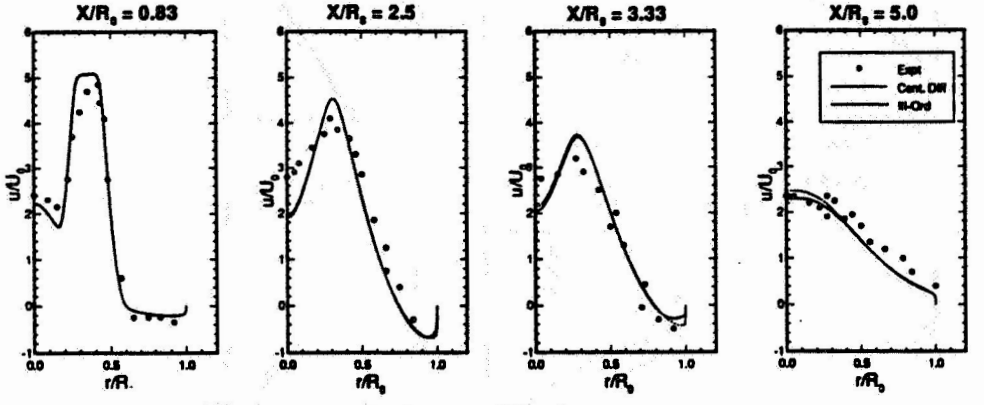

Figure 6: Velocity profiles for co-axial jets.

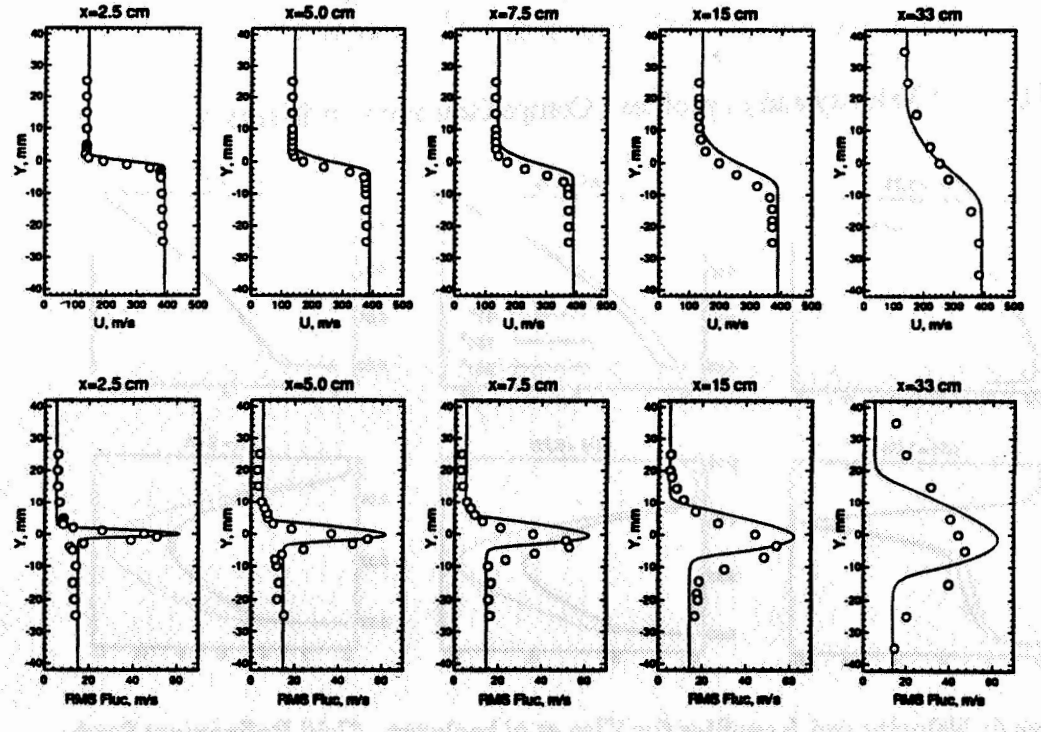

Figure 7: Velocity and k profiles for turbulent planar shear layer

427213 Pg 2 | N95-70900

A MODEL TO PREDICT THE CONDITIONS FOR LIQUID DROP BREAKUP AND THE RESULTANT MEAN FRAGMENT SIZE

K. L. Wert and H. R. Jacobs
Propulsion Engineering Research Center
and
Department of Mechanical Engineering
The Pennsylvania State University
University Park, Pa 16802-1413, U.S.A.

The potential significance of drop fragmentation in sprays and other propulsion-related multiphase flows has been noted in the literature [e.g., Caveny and Gany (1979) and Takagi et al. (1991)]. This has motivated recent experimental and theoretical works to: better understand the fundamental physics of drop breakup processes, and develop models of drop fragmentation suitable for use in multiphase flow codes. The works summarized below [Wert and Jacobs (1994) and Wert (1994)] aim to contribute to both sides of this two-pronged attack.

Development of a model to predict the deformation and conditions for fragmentation of a liquid drop was undertaken by Wert and Jacobs (1994). Though the development was tailored to distortion and breakup by aerodynamic forces (for Re ~ 100-1000), the model provides a framework for consideration of other drop breakup modes, e.g., collision induced breakup or fragmentation in a highly sheared flow. Two independent conditions for fragmentation were developed; one is specified in terms of a critical drop energy criterion, the other is based on stability theory. In agreement with the experimental data of Hsiang and Faeth (1992), Loparev (1975), and Hanson et al. (1963), both criteria predict that for a step change in relative velocity the critical Weber number (We_{crit}) is independent of Ohnesorge number (Oh) and approximately equal to 15 for $Oh < 0.03$. For $Oh > 0.03$ both criteria predicted an increase in We_{crit} with Oh, but the energy criterion overpredicts the rate of increase when compared with experimental observations. The predictions based on the stability criteria, however, show good agreement throughout the calculated Oh range. The unique derivation of the energy breakup criterion and its success in predicting We_{crit} for $Oh < 0.03$ would appear to support the conjecture that for drops that behave dynamically as though inviscid, the energy breakup criterion is the same regardless of the drop breakup mode in question. Additionally, both the energy and stability breakup criteria validate the use of a critical deformation criterion to predict aerodynamic breakup. However, the predictions of the stability model indicate that such a criterion

is an increasing function of Oh for Oh > 0.01.

A model was developed by Wert (1994) to predict the Sauter mean diameter of fragments produced in the bag and multimode drop breakup regimes (14 < We < 100). In these regimes the final breakup of liquid drops is viewed as resulting from the growth of capillary instabilities. The model links the time scale for drop breakup and the time scale associated with growth of the unstable waves. The instability scale is approximated from the results of linear stability theory for capillary waves on liquid cylinders. The drop breakup scale is based on correlations available in the literature for drops subjected to a rapid (relative to drop deformation time scales) rise in relative velocity. A constant of proportionality, deduced from the experimental data of Hsiang and Faeth (1992), is introduced. In the bag and multimode breakup regimes, the stability/time-based model offers a significant improvement in ability to correlate the data when compared with an equation proposed by Hsiang and Faeth (1992).

REFERENCES:

Caveny, L. H. and Gany, A., 1979. "Breakup of Al/Al_2O_3 agglomerates in accelerating flow fields," AIAA J., Vol. 17, No. 12, pp. 1368-1371.

Hanson A. R., Domich, E. G. and Adams, H. S., 1963. "Shock-tube investigation of the breakup of drops by air blasts," Phys. Fluids, Vol. 6, pp. 1070-1080.

Hsiang, L.-P. and Faeth, G. M., 1992. "Near-limit drop deformation and secondary breakup," Int. J. Multiphase Flow, Vol. 18, No. 5, pp. 635-652.

Loparev, V. P., 1975. "Experimental investigation of the atomization of drops of liquid under conditions of a gradual rise of the external forces," Izv. Akad. Nauk SSSR Mekh. Zhidkosti Gaza, Vol. 3., pp. 174-178.

Takagi, T., Fang, C. Y., Kamimoto, T. and Okamoto, T., 1991. "Numerical simulation of evaporation, ignition and combustion of transient sprays," Comb. Sci. and Tech., Vol. 175, No. 1-3, pp. 1-12.

Wert, K. L. and Jacobs, H. R., 1994. "A theoretical study of aerodynamic drop distortion and the conditions for drop breakup," Submitted for publication to J. Fluid Mech.

Wert, K. L., 1994. "A predictive equation for the mean fragment size resulting from aerodynamic-induced breakup in the bag and multimode regimes," Submitted for publication to Int. J. Multiphase Flow.

427215 Bs S

N95-70901

ANALYTICAL AND EXPERIMENTAL STUDIES OF IMPINGING LIQUID JETS

H.M. Ryan, W.E. Anderson, S. Pal and R.J. Santoro
Propulsion Engineering Research Center
and
Department of Mechanical Engineering
The Pennsylvania State University
University Park, PA 16802

SUMMARY:

Impinging injectors are a common type of injector used in liquid propellant rocket engines and are typically used in engines where both propellants are injected as a liquid, e.g., engines using LOX/hydrocarbon and storable propellant combinations. The present research program is focused on providing the requisite fundamental understanding associated with impinging jet injectors for the development of an advanced *a priori* combustion stability design analysis capability. To date, a systematic study of the atomization characteristics of impinging liquid jets under cold-flow conditions has been completed. Effects of orifice diameter, impingement angle, pre-impingement length, orifice length-to-diameter ratio, fabrication procedure, jet flow condition and jet velocity under steady and oscillating, and atmospheric- and high-pressure environments have been investigated. Results of these experimental studies have been compared to current models of sheet breakup and drop formation. In addition, the research findings have been scrutinized to provide a fundamental explanation for a proven empirical correlation used in the design of stable impinging injector-based rocket engines.

DISCUSSION:

An extensive series of detailed measurements, including sheet breakup length, drop size distribution and wavelength of apparent structures, were completed to delineate the atomization processes of two impinging water jets as a function of orifice diameter (d_o), impingement angle (2θ), pre-impingement length (l_j), length-to-diameter ratio (L/d_o), jet velocity (U_j) and jet flow condition [1, 2]. These tests were performed under ambient conditions, and the impinging injector used consisted of two precision-bore glass tubes that could be independently modified to obtain the desired geometry. This injector is referred to as the glass tube impinging injector throughout the text. Recent work has focused on evaluating the functional dependence of the measured variables (e.g., drop size) on an injector parameter, d_o/U_j, associated with an empirical correlation used for engine stability prediction. In addition, the measurement program has been expanded to include the effects of fabrication technique and chamber pressure on the impinging jet atomization process.

Finally, a finite difference model is being used to study the effects of jet disturbances and jet-jet interactions on incipient wave formation on the liquid sheet formed by two opposed impinging jets.

An empirical correlation, used by industry in the design of stable impinging injector-based rocket engines, relates the highest sustainable instability frequency to the injector parameter d_o/U_j (orifice diameter/injection velocity) [3]. According to the stability correlation, an increase in the injector parameter, d_o/U_j, leads to an increase in the frequency range over which the engine can operate stably. A general objective of this work is to develop a rational physical explanation for this successful empirical correlation; hence, the experimental results obtained with the glass tube impinging injector are analyzed with regards to the stability correlation. Specifically, the dependence of drop size distribution and atomization frequency on d_o/U_j is examined. It is important to keep in mind that the discussion to follow pertains to cold-flow atomization data, and that, ideally, the impinging jet atomization characteristics should be evaluated under high-pressure and combusting-flow conditions, which will be the next step undertaken in this research program.

The measured drop size number distribution, $f(d_D)$, is plotted as a function of drop size, d_D, and injector parameter, as shown in Fig. 1. The drop size distribution measurements were made using a Phase Doppler Particle Analyzer along the spray centerline (x=0) at an axial location (z) of 41 mm from the impingement point for an orifice diameter of 0.64 mm and an impingement angle of 60°. An increase in mean drop size is noted with increasing d_o/U_j, thus indicating that bigger drops may have a stabilizing effect. Notice that an increase in the injector parameter leads to broader distributions as well. Similar mean diameter and distribution shape trends are observed for different test cases (e.g., different radial positions and impingement angles).

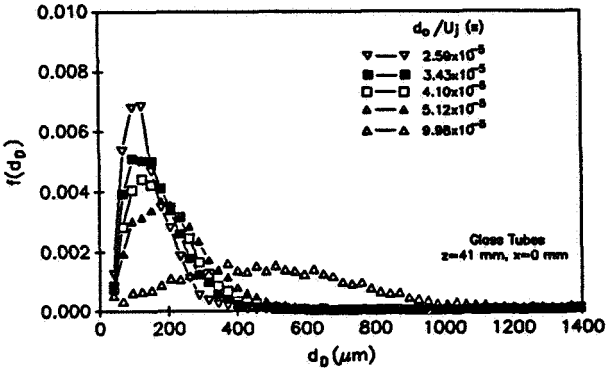

Fig. 1. The number distribution plotted as a function of drop size and injector parameter.

The functional dependence of the periodicity of ligaments detaching from the end of the impinging jet intact sheet on d_o/U_j was examined also. The measured separation distance between adjacent detaching ligaments was converted to an atomization frequency simply by dividing the jet velocity by the separation distance. The assumption that the detached ligament velocity is equal to the jet velocity needs to be substantiated. The calculated atomization frequency associated with the glass tube impinging injector is presented in Fig. 2, along with the highest sustainable combustion instability frequency predicted by the stability correlation. The dependence of the atomization frequency on d_o/U_j is quite similar to the highest sustainable combustion instability frequency;

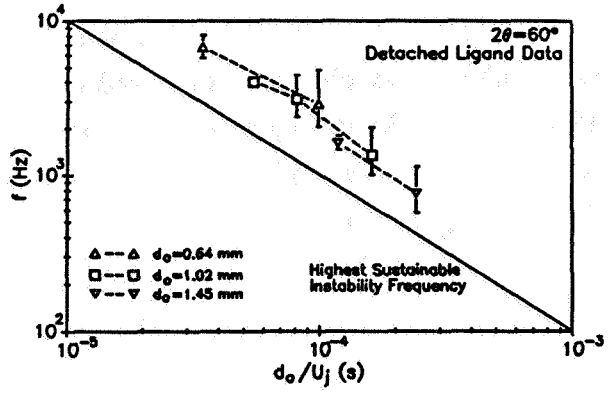

Fig. 2. A comparison between the calculated atomization frequency associated with the glass tube impinging injector and the highest sustainable combustion instability frequency predicted by the empirical correlation [3].

however, the calculated atomization frequency is approximately twice as great. The similar dependencies of maximum possible instability frequency and atomization frequency on d_o/U_j is significant in terms of periodic ligament formation being a key process in combustion instability phenomena.

In practical combustors, injector orifices and pre-impingement lengths are short, and chamber pressures are high. Consequently, a series of cold-flow atomization experiments were undertaken in which sheet breakup length and apparent disturbances on the liquid sheet surface were gauged as a function of jet velocity and chamber pressure for an electro-discharge machined (EDM) impinging injector having an orifice diameter of 0.51 mm, a length-to-diameter ratio and a pre-impingement length-to-diameter ratio of five, and an impingement angle of 60°. From instantaneous spray images, the intact sheet breakup length and the separation distance between adjacent disturbances on the sheet surface were measured.

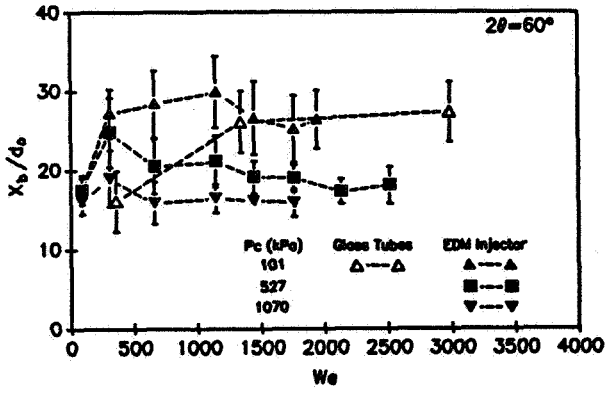

Fig. 3. Nondimensional breakup length as a function of Weber number, chamber pressure and injector type.

A plot of the nondimensional breakup length, x_b/d_o, as a function of Weber number, We ($=\rho_l U_j^2 d_o/\sigma$), is shown in Fig. 3. Each symbol in Fig. 3 represents an average of 17 individual breakup length measurements, while the bars represent the plus/minus standard deviation of those measurements. The breakup length decreases with increasing chamber pressure. In addition, for both the EDM as well as the glass tube impinging injector, the nondimensional breakup length is relatively insensitive to changes in We. Two differences between the glass tube impinging and the EDM injectors are the orifice length-to-diameter ratio and the pre-impingement length. The glass tube impinging injector L/d_o is 80 and l_j/d_o is 40, while the EDM injector L/d_o and l_j/d_o are both equal to five. In spite of these geometric differences between the two injectors, the measured nondimensional breakup lengths are comparable, especially at the higher Weber numbers.

Measurements of the separation distance between adjacent disturbances (disturbance wavelength) on the intact impinging jet sheet surface were made as a function of chamber pressure and injector type. As shown in Fig. 4, the measured disturbance wavelength is observed to be independent of both chamber pressure (up to 1070 kPa) and jet velocity (up to 19 m/s) for the EDM injector. Disturbance wavelength measurements for the glass tube impinging injector were independent of jet velocity (up to 18.5 m/s) as well; however, measurements were only made under ambient pressure conditions. At a pressure of 101 kPa, the measured disturbance wavelengths associated with the glass tube impinging injector are slightly larger than those measured for the EDM injector, which has a smaller orifice length and pre-impingement length as compared to the glass tube impinging injector.

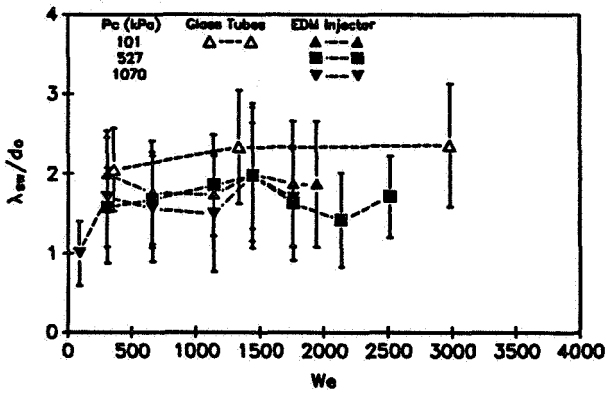

Fig. 4. Nondimensional surface disturbance wavelength as a function of Weber number, chamber pressure and injector type.

The formation of impact waves on the sheet surface emanating from the impingement point has been often observed and is a process which must be clearly understood for the development of an accurate mechanistic impinging jet atomization model. To specifically address this process, modeling efforts have centered on the use of a finite difference Navier-Stokes code (RIPPLE) [4] to investigate the effects of spatial and temporal jet flow oscillations on the primary breakup of the impinging jet fan into ligaments.

Directly opposed axisymmetric jets are chosen for study to simplify the analysis. Harmonic disturbances are imposed on each jet upstream of the impingement point to simulate jet instabilities. The imposed jet disturbances have a radial profile that is proportional to sin ($\pi r/d_o$), with the maximum axial velocity oscillation at the jet periphery being 5% of the mean jet velocity, U_j. The computed free surface contours for two cases, one in which a steady, flat velocity profile exists at both jet inlets, and the second case in which a sinusoidal velocity profile having a frequency of 1000 s^{-1} exists at both jet inlets, are shown in Fig. 5. For the unsteady jet case, the sheet disturbance frequency equaled the frequency of the imposed oscillation on the jet, and the resultant sheet is qualitatively similar to those experimentally observed. This model has some promise of clarifying the process of impact wave formation, and ongoing analytical work is focused on the most appropriate way to simulate pre-impingement jet oscillations.

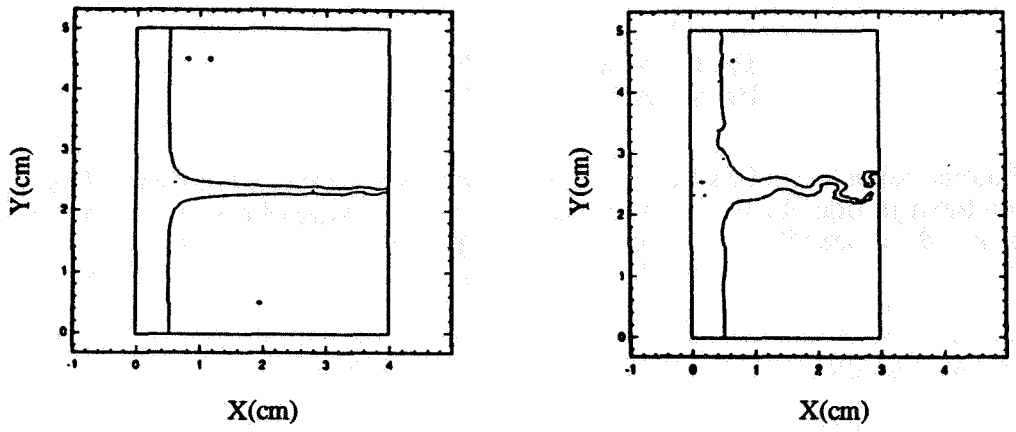

Steady Inlet Conditions

1000 Hz Oscillation

Fig. 5. Computed free surface contours for a steady jet inlet condition and an inlet condition with harmonic disturbances imposed on the jet. The top jet enters at the upper left hand corner with a mean velocity of -10 m/s and the bottom jet enters at the lower left hand corner with a mean velocity of 9.6 m/s. The jet diameter is 10 mm.

ACKNOWLEDGEMENTS:

The authors would like to acknowledge the support of the Air Force Office of Scientific Research, Air Force Systems Command, USAF, under grant number 91-0336, as well as the support of the Penn State NASA Propulsion Engineering Research Center under grant NAGW 1356. In addition, the technical information and feedback provided by the personnel of the Aerojet Propulsion Division is gratefully acknowledged.

REFERENCES:

[1] Anderson, W.E., Ryan, H.M., Pal, S. and Santoro, R.J., "Fundamental Studies of Impinging Liquid Jets," AIAA paper 92-0458, 30th Aerospace Sciences Meeting, Reno, NV, Jan. 6 - 9, 1992.

[2] Ryan, H.M., Anderson, W.E., Pal, S. and Santoro, R.J., "Atomization Characteristics of Impinging Liquid Jets," AIAA paper 93-0230, 31st Aerospace Sciences Meeting, Reno, NV, Jan. 11 - 14, 1993 (accepted for publication in Journal of Propulsion and Power).

[3] Anderson, W.E., Ryan, H.M. and Santoro, R.J., "Combustion Instability Phenomena of Importance to Liquid Bi-Propellant Rocket Engines," 28th JANNAF Combustion Meeting, San Antonio, TX, Oct. 28 - Nov. 1, 1991.

[4] Kothe, D.B., Mjolsness, R.C. and Torrey, M.D., "RIPPLE: A Computer Program for Incompressible Flows with Free Surfaces," Report LA-12007-MS, Los Alamos National Laboratory, Los Alamos, NM, April 1991.

42721 8 P3 1

N95-70902

FLUID PROPERTY AND OPERATIONAL EFFECTS ON SWIRL INJECTOR ATOMIZATION

G. B. Cox, Jr.
Pratt & Whitney/GESP
West Palm Beach, FL 33410-9600

Results of atomization tests of rocket injection elements are correlated in terms of the test fluid properties and the injection element operating conditions. The type of element modeled has a central, swirling liquid oxidizer flow; and a coaxial, axial gaseous fuel flow. Results of the correlations describe the effect of geometry, fluid properties, and operating conditions on liquid atomization. The ranges of test conditions allow reasonable extrapolation to actual high-pressure engine operating conditions. At such conditions, the swirl element should produce exceptionally finely-atomized and well-distributed spray for high combustion performance.

United Technologies Research Center (UTRC) completed a test program to measure fluid spray atomization, in terms of droplet size and droplet size distributions, for swirling-flow injection elements. Element sizes and dimensions covered ranges of dimensions representative of typical cryogenic (O_2/H_2) liquid rocket engine practice. Relevant dimensions include the element diameter, the tangential-entry metering slot length, and the coaxial fuel slot radial gap. Test fluids included water, simulated Jet-A, and Freon 113. These fluids cover ranges of properties which include or approach those of liquid oxygen. Gaseous nitrogen simulated the coaxial gaseous hydrogen fuel flow. A total of 159 separate test combinations covered wide ranges of fluid properties, and liquid and gas pressure drops, over ambient pressures ranging from atmospheric to approximately 420 psi. A UTRC-developed correlation described the dependence of droplet SMD on the various fluids and test conditions, but only to within an accuracy of +/- 30%.

The approach to developing an improved correlation involved correlating the droplet size data individually by injection element size. Within each element size, a systematic, multi-step process allowed the determination of individual fluid or operating condition effects on the spray SMD, prior to inclusion of the next effect. The final correlation for the large-diameter injection element correlated droplet SMD within a band of +/- 10%; for the smaller-diameter injection element, within +/- 15%.

Applying the results of the correlations to representative engine operating conditions, the revised correlations predict droplet sizes 12.5% of those predicted by the previous correlation. The effect of surrounding gas flow is two-fold: atomization is generally improved, but the effective spray angle is reduced. Thus, incrementally increasing the gas velocity will initially improve performance through finer atomization, but eventually will degrade performance through collapse of the spray cone and the resulting loss of inter-element mixing. More specific effects on spray droplet sizes include:

Droplet size is reduced by	Higher chamber density
	Increased gas/liquid momentum ratio
	Decreased liquid surface tension
	Deceased liquid density
	Increased $(\rho_{liq})\ (V_{gas})\ (D_{tube})/(\mu_{liq})$
	Increased liquid Δp

Viscosity effects are confined to smaller tubes or to very low liquid pressure drops. Atomization for the larger tube is more sensitive to the combustion chamber gas density than is the case for the smaller tube; however, atomization in the smaller tube is more sensitive to injection Reynolds number. Finally, the effect of momentum ratio on droplet size disappears for momentum ratios higher than 1.0.

427221 P5 3

N95-70903

THE EFFECTS OF TURBULENCE ON DROPLET DRAG AND SECONDARY DROPLET BREAKUP

Y.-H. Song, E. Coy, S. Greenfield, M. Ondas, T. Prevish, T. Spegar and D. Santavicca
Propulsion Engineering Research Center
Penn State University
University Park, PA 16802

OVERVIEW:

The objective of this research is to obtain an improved understanding of the behavior of droplets in vaporizing sprays, particularly under conditions typical of those in high pressure rocket sprays. Experiments are conducted in a variety of high pressure, high temperature, optically-accessible flow systems, including one which is capable of operation at pressures up to 70 atm, temperatures up to 600 K, gas velocities up to 30 m/sec and turbulence intensities up to 40%. Single droplets, 50 to 500 micron in diameter, are produced by an aerodynamic droplet generator and transversely injected into the flow. Measurements are made of the droplet position, size, velocity and temperature and of the droplet's vapor wake from which droplet drag, dispersion, heating, vaporization and breakup are characterized.

RESULTS:

The main results from this study[1,2] to date are the following:

1. Under laminar flow conditions, vaporization was found to reduce droplet drag, in quantitative agreement with the drag correlation of Chiang, Raju and Sirignano, as illustrated in Figure 1.
2. Under laminar flow conditions, droplet drag was not affected by unsteady curvilinear motion.
3. Under laminar flow conditions, unsteady curvilinear motion was found to result in small but non-negligible droplet lift ($C_L/C_D \approx 0.1$), but only at relatively high droplet Reynolds numbers ($20 < Re < 38$), as illustrated in Figure 2.

4. Turbulence was found to result in an apparent increase in droplet drag, however, this can be accounted for by an appropriate redefinition of the mean relative velocity, as illustrated in Figure 3.
5. Turbulence was found to result in an apparent decrease in the critical Weber number for secondary droplet breakup, however, this can be accounted for by an appropriate redefinition of the mean relative velocity.
6. The phenomenological nature of secondary breakup was observed to be fundamentally different in turbulent and laminar flows.
7. Under conditions of large relative droplet velocity typical of sprays, droplet dispersion increases with a t^3 dependence and not the t^2 dependence predicted by classical dispersion theory, as illustrated in Figure 4.

The research plan for this current year includes an extension of the study of the effect of turbulence on secondary droplet breakup to vaporizing conditions, the first demonstration of the use of Raman scattering to characterize droplets injected into supercritical environments, the completion of the calibration of the exciplex droplet thermometry technique and the demonstration of a vapor wake visualization technique for determining the phenomenological effect of turbulence on droplet drag and of acoustic waves on droplet vaporization.

REFERENCES:

1. Song, Y.-H. and Santavicca, D. A., "An Experimental Study of Drag and Lift Acting on Evaporating Droplets Following Curvilinear Trajectories in a Laminar Flow," submitted to *Combustion Science and Technology*.
2. Song, Y.-H. and Santavicca, D. A., "The Effect of Turbulence on Droplet Drag and Secondary Droplet Breakup," in preparation.

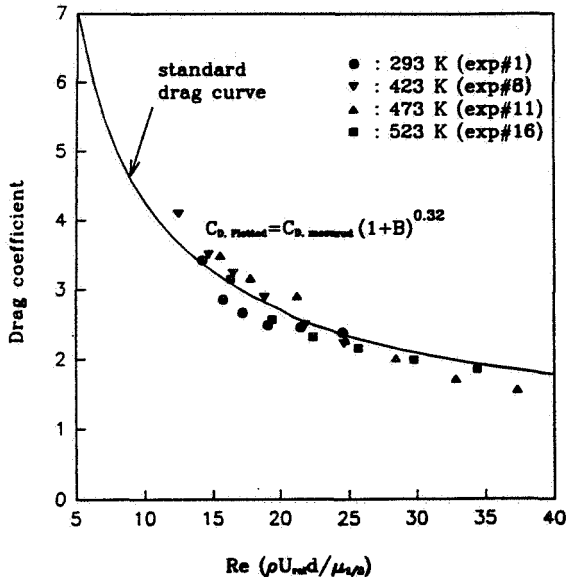

Figure 1. A comparison of the standard drag coefficient and the measured drag coefficient corrected to account for vaporization as proposed by Chiang, Raju and Sirignano.

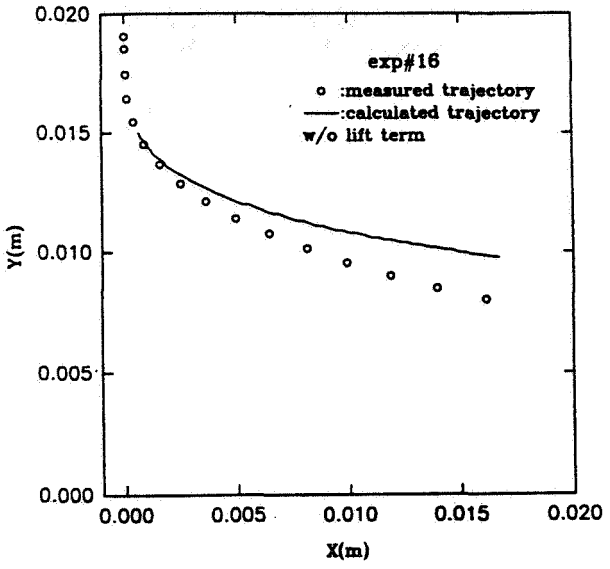

Figure 2. A comparison of the measured droplet trajectory and the predicted droplet trajectory calculated without lift.

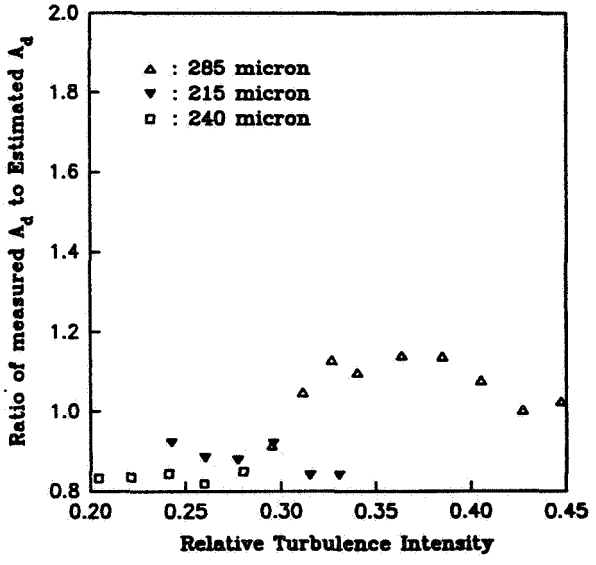

Figure 3. A comparison of the measured droplet acceleration and that calculated with the relative droplet velocity modified to account for gas velocity fluctuations.

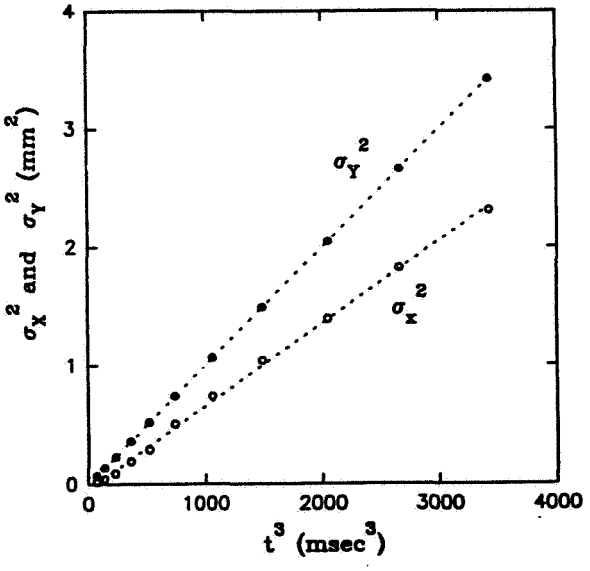

Figure 4. Measured droplet dispersion versus t^3.

427224
Pgs 5

N95-70904

SHEAR COAXIAL INJECTOR INSTABILITY MECHANISMS

C. Puissant†, T. Kaltz+, M. Glogowski+ and M. Micci*
Department of Aerospace Engineering & Propulsion Engineering Research Center
The Pennsylvania State University
University Park, PA 16802

OVERVIEW

There is no definitive knowledge of which of several concurrent processes ultimately results in unstable combustion within liquid rocket chambers employing shear coaxial injectors. Possible explanations are a detrimental change in the atomization characteristics due to a decrease in the gas-to-liquid velocity ratio, a change in the gas side injector pressure drop allowing acoustic coupling to the propellant feed system or the disappearance of a stabilizing recirculation region at the base of the LOX post. The aim of this research effort is to investigate these proposed mechanisms under conditions comparable to actual engine operation. Spray characterization was accomplished with flash photography and planar laser imaging to examine the overall spray morphology and liquid jet breakup processes and with a PDPA to quantify the spatial distribution of droplet size and mean axial velocity. A simplified stability model based on the Rayleigh criterion was constructed for the flow dynamics occurring within the chamber and injector to evaluate the potential coupling between the chamber and injector acoustic modes and was supported by high frequency measurements of chamber and injector pressure oscillations. To examine recirculation within the LOX post recess, velocity measurements were performed in the recess region by means of LDV. Present experiments were performed under noncombusting conditions using LOX/GH_2 simulants at pressures up to 4 MPa.

DISCUSSION

The laboratory injector used in these experiments was modeled after the injector element of the SSME fuel preburner and included two LOX post tip shapes, tapered and nontapered. Liquid nitrogen and gaseous nitrogen served as the principle simulants to liquid oxygen and gaseous hydrogen, respectively. Injector characterization was performed in an optically accessible pressure chamber. To evaluate the feasibility of laser Doppler velocimetry within the recess region of the injector, water and air were used but at reduced mass flow rates.

Spray Visualization Experiments

The effect of chamber pressure and gas mass flow rate on spray morphology was examined at liquid-to-gas mixture ratios of 0.78 and 1.57 with a liquid nitrogen mass flow rate of

† Adjunct Research Assistant, + Graduate Research Assistant, * Associate Professor

0.050 kg/s. Fig. 1 depicts the photographic results from three representative experiments using the planar laser imaging technique. As can be seen from Figs. 1a and 1b, increasing chamber pressure effects a contraction of the large scale liquid structures (liquid core and detached ligaments) and droplet flow regions observed downstream of the dense liquid structures. This trend would suggest an enhancement in the rate of liquid vaporization with increasing chamber pressure through a combined reduction in the latent heat of vaporization and liquid surface tension. In Fig. 1c the result of decreasing gas mass flow rate, or increasing mixture ratio, was a larger, more dispersed spray suggesting a strong influence of the gas mass flow rate on the atomization and vaporization of liquid nitrogen. In terms of droplet sampling with the PDPA, these reduced gas flow conditions are advantageous in that the dilute spray region is spread over a larger volume.

Additional tests were performed with the tapered LOX post using a stroboscope to visualize the spray. In general, the stroboscopic image provides more detail on the structure of the liquid core and detached ligaments than the laser sheet images but less information on the droplet flow region. Figs. 2a and 2b depict the structure of the jet issuing from the injector at sub- and supercritical pressures. Contradictory to the observed contraction of the spray with increasing pressure, the liquid core breakup length has increased for a supercritical chamber pressure ($P_c > 3.4$ MPa). This behavior may be attributed to the drop in relative velocity between the gas and liquid at very high chamber pressures, which may surpass any enhancements to liquid breakup due to increased gas density, or to the increase in droplet evaporation times observed in the supercritical region. Stroboscope tests with the nontapered LOX post under similar operating conditions revealed the same behavior for sub- and supercritical pressures but indicated little difference in spray morphology between the two LOX post designs.

Droplet Size and Velocity Measurements

Droplet size and velocity measurements were obtained at three mixture ratios, 2.2, 1.6 and 1.1, for a LN_2 mass flow rate of 0.072 kg/s. The effect of chamber pressure on droplet size and mean axial velocity was found to be negligible as is seen from tests B1 and B2 of Table 1. Interestingly, the number of droplets sampled during a fixed interval of the tests decreased dramatically with increasing chamber pressure due to the contraction of the spray at higher pressures and/or a change in optical alignment as a result of increased gas density. The results for tests B2 to B4 show an expected decrease in droplet mean axial velocity when moving radially outward in the spray and an increase in velocity when moving closer to the injector. Negligible change in droplet size as represented by D_{10} was observed for all three tests. The effect of decreasing mixture ratio is seen from tests B4, B5 and B6. Test B5 and B6, performed at the same location in the spray, show an increase in drop mean velocity with decreasing

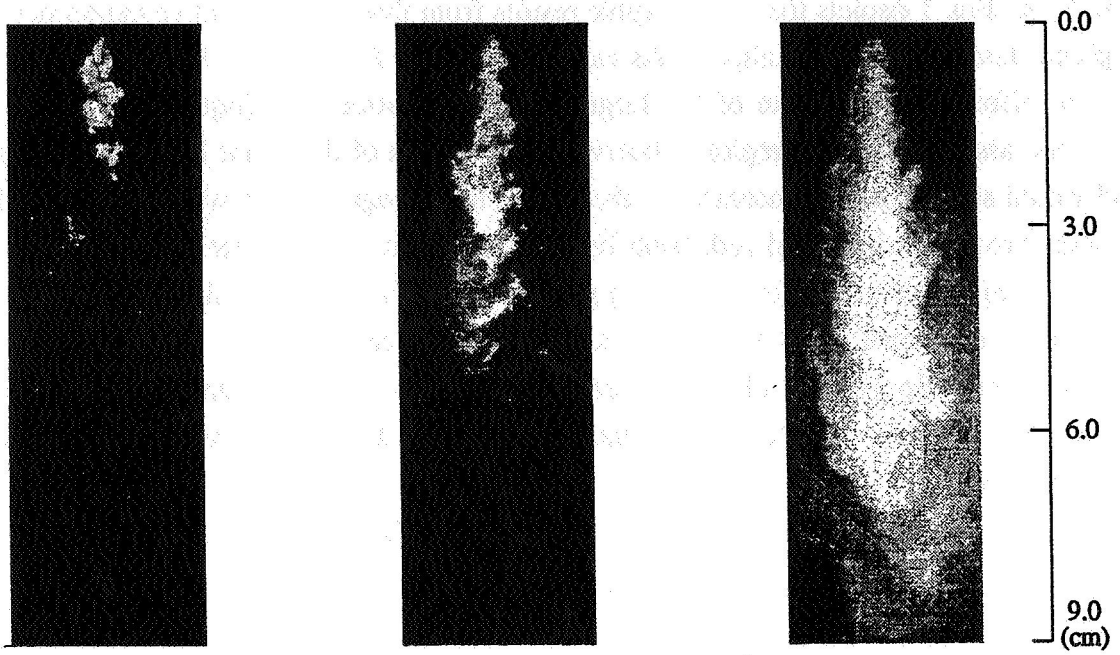

(a) 2.93 MPa (MR: 0.78) (b) 2.32 MPa (MR: 0.78) (c) 2.34 MPa (MR: 1.57)

Fig. 1 Effect of chamber pressure and mixture ratio on LN_2/GN_2 spray.

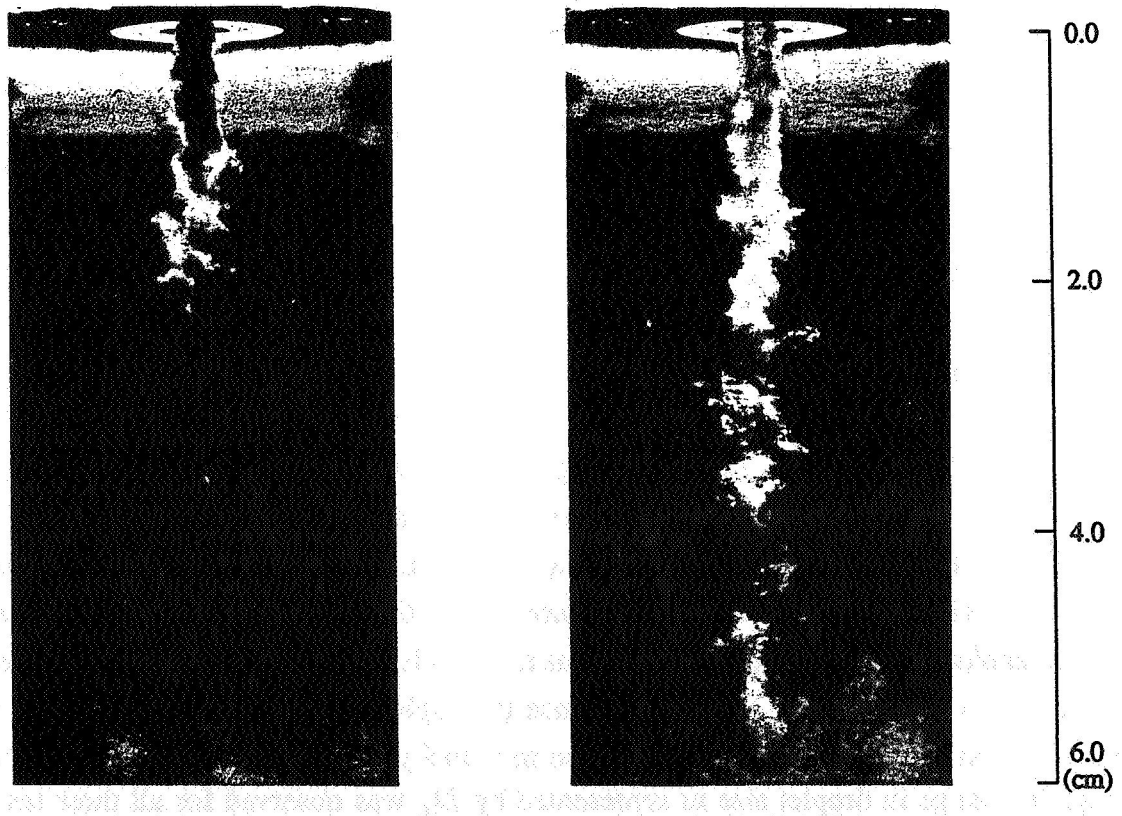

(a) 2.94 MPa (b) 3.97 MPa

Fig. 2 Stroboscope results for tapered LOX post at sub- and supercritical pressures (MR: 0.81).

Table 1. Operating Conditions and Droplet Size and Velocity Data for PDPA Tests.

Test No.	P_c (MPa)	$\dot{m}_l/\dot{m}_g$	U_g/U_l	Pos. (cm)		U_{drop} (m/s)	Droplet Size (μm)		No. Droplets
				Z	R		D_{10}	D_{32}	
B1	2.63	2.24	3.87	12	0	15.9	10.1	96.7	512
B2	2.40	2.19	4.20	12	0	14.4	11.2	97.3	2514
B3	2.37	2.15	4.30	12	0.5	9.3	12.9	91.6	375
B4	2.41	2.20	4.23	10	0	14.8	14.1	105.5	562
B5	2.45	1.60	5.74	10	0	20.8	7.5	110.3	151
B6	2.37	1.14	7.53	6	0	37.1	8.4	118.3	121

mixture ratio due to the higher gas exit velocity. The effect of mixture ratio on spray drop size is presented as the superposition of the three drop size distributions in Fig. 3. With increasing gas mass flow rate, or decreasing mixture ratio, the majority of droplets shift to smaller size ranges. The large difference between the arithmetic mean diameter and Sauter mean diameter listed in Table 1 arose from the bimodal size seen in Fig. 3. The small number of large droplets at the upper end of the size range, observed during all of the tests, may be due to remnants of the liquid core, coalesced small droplets or instrument misinterpretation of the collected signal.

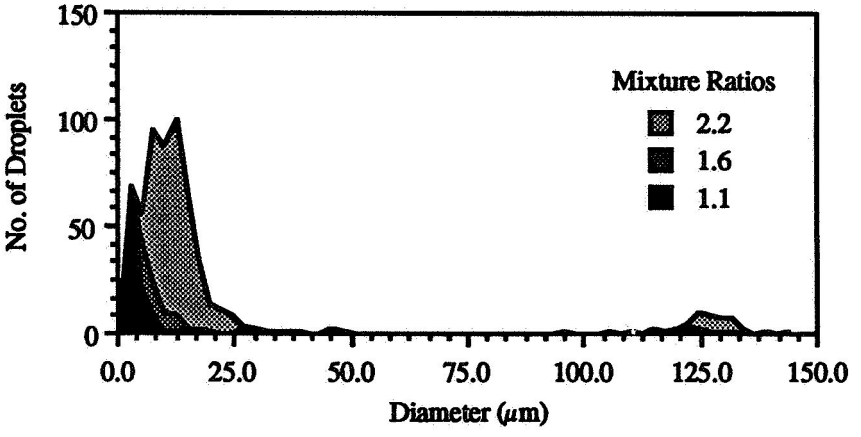

Fig. 3 Droplet size distribution for three oxidizer to fuel mixture ratios (P_C = 2.4 MPa).

Analytical Modeling

The injector response was calculated from the analytical model using only the processes of gas flow through the injector and the nozzle. The response was determined as a function of frequency and gaseous fuel temperature for the experimental conditions experienced during the cold flow LN_2/GN_2 experiments. During these experiments, high frequency pressure oscillations were measured in the chamber and the injector fuel plenum. Fig. 4 shows the injector response as a function of fuel temperature for several frequencies. It can be seen that at high frequencies the response is near zero, at intermediate frequencies the response is negative

and almost constant and at low frequencies the response becomes strongly positive as the fuel temperature decreases. The recorded high frequency pressure oscillations were spectrally analyzed to determine the frequencies and magnitudes of any acoustic oscillations within either the chamber or the injector fuel plenum. Oscillations at the same frequency in both the chamber and the plenum were found at two frequencies, 2000 and 5800 Hz. The calculated injector response at those two frequencies correlated well with the measured ratios of the pressure oscillation amplitude in the chamber to the amplitude in the plenum.

Recirculation Region

To permit LDV access to the recess region the injector was modified by inserting a Pyrex tube concentrically around the nontapered LOX post, such that the fuel annulus became a transparent boundary, 1.02 mm thick. Water was used as the LOX simulant and air for the gaseous fuel simulant. Measurements of mean axial velocity were taken inside the injector recess region as well as downstream of the injector. Downstream of the injector face only positive velocities were measured. Within the recess region several axial and radial scans revealed evidence of recirculation. Fig. 5 shows the droplet velocity near the center of the LOX post tip landwidth as a function of axial distance from the LOX post tip. The air flow rate was 1.8 g/s and the water flow rates were 1.9 and 4.5 g/s. It can be seen that the velocity drops to a negative value approximately 0.5 mm downstream of the LOX post base before becoming positive. Larger negative values of the velocity were observed for lower liquid flow rates. Thus, it appears that gas recirculation does exist in the recess region of a shear coaxial injector element and that the strength of the recirculation is a function of the operating conditions.

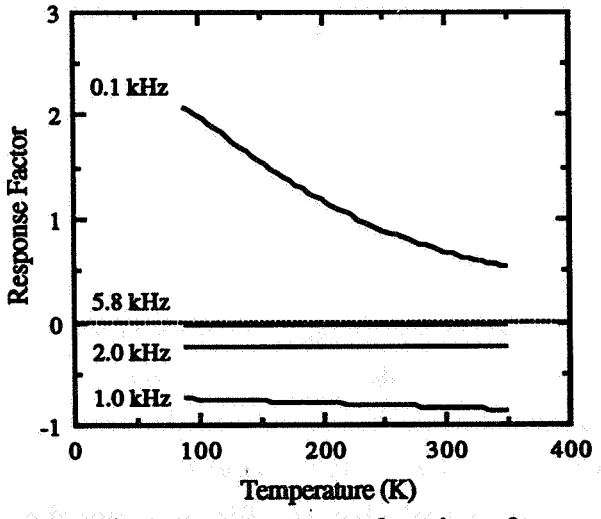

Fig. 4 Injector response as a function of gaseous fuel temperature for several frequencies.

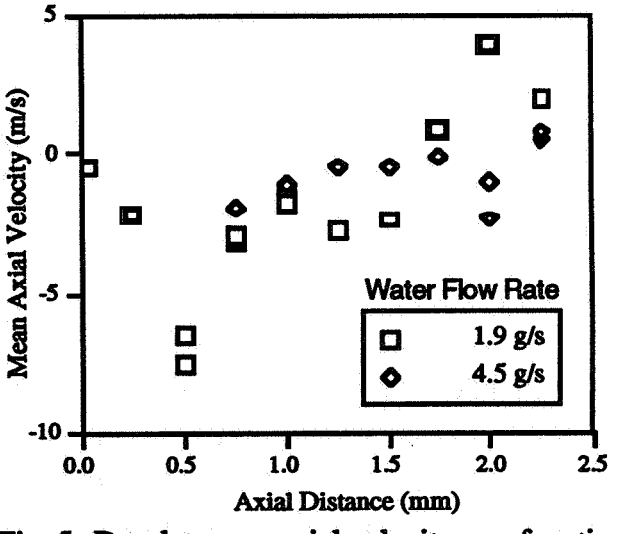

Fig. 5 Droplet mean axial velocity as a function of axial distance within the injector recess region.

427226
Pgs 5
N95-70905

ACOUSTIC EFFECTS OF SPRAYS

by
Maciej Z. Pindera and Andrzej J. Przekwas
CFD Research Corporation
3325 Triana Blvd.
Huntsville, AL 35805

1. INTRODUCTION

Since the early 1960's, it has been known that realistic combustion models for liquid fuel rocket engines should contain at least a rudimentary treatment of atomization and spray physics. This is of particular importance in transient operations. It has long been recognized[1,2] that spray characteristics and droplet vaporization physics play a fundamental role in determining the stability behavior of liquid fuel rocket motors.

This paper gives an overview of work in progress on design of a numerical algorithm for practical studies of combustion instabilities in liquid rocket motors. For flexibility, the algorithm is composed of semi-independent solution modules, accounting for different physical processes. Current findings are report and future work is indicated. The main emphasis of this research is the development of an efficient treatment to interactions between acoustic fields and liquid fuel/oxidizer sprays.

2. TECHNICAL DISCUSSION

2.1 General Approach

The presence of droplets and chemical reactions in the flow field is manifested as additional source terms in the gas-phase equation.

$$\frac{\partial \mathbf{U}}{\partial t} + \nabla \mathbf{F}_c + \nabla \mathbf{F}_d = \hat{\mathbf{S}}_{drop} + \hat{\mathbf{S}}_{chem} \tag{1}$$

where $\mathbf{U}$, $\mathbf{F}_c$ and $\mathbf{F}_d$ represent the conserved variables and convective and diffusive fluxes, respectively, and $\hat{\mathbf{S}}$ denotes the source terms. Modularity of the algorithm is insured by accounting for each effect separately using the method of fractional steps:

$$\frac{\partial \mathbf{U}}{\partial t} + \nabla \mathbf{F}_c = 0 \; ; \; \frac{\partial \mathbf{U}}{\partial t} + \nabla \mathbf{F}_d = 0 \; ; \; \frac{\partial \mathbf{U}}{\partial t} = \hat{\mathbf{S}}_{drop}(\mathbf{U}^*) \; ; \; \frac{\partial \mathbf{U}}{\partial t} = \hat{\mathbf{S}}_{chem}(\mathbf{U}^{**}) \tag{2}$$

The asterisks in the source terms represent evaluation using the results of the preceding calculation.

Second order accuracy is insured by using a Strang[3]-type operator splitting. Thus, if L_c, L_d, L_{drop}, and L_{react} denote individual operators which advance the solution through a time increment Δt, the solution at anew time lead can be expressed as:

$$\mathbf{U}^{n+2} = \left(L_c^{\Delta t}, L_d^{\Delta t}, L_{drop}^{2\Delta t}, L_{chem}^{2\Delta t}, L_{drop}^{\Delta t}, L_d^{\Delta t}, L_c^{\Delta t}\right)\mathbf{U}^n \tag{3}$$

Although the overall solution is explicit, each solution operator may be implicit as desired.

2.2 Gas Dynamics

Convective and diffusion equations are solved on a BFC grid using finite volume methodology. Convective fluxes are evaluated explicitly using high order characteristic based methods. Diffusive fluxes are evaluated in a central difference algorithm using the Heun and Crank-Nicholson schemes for time integration.

2.3 Source Terms

2.3.1 Chemistry: Early studies[4,5] of liquid rockets have indicated that at least at steady state the chemical time scales are several orders of magnitude smaller than time scales associated with the other combustion processes. For transient behavior the situation is not clear. Since chemistry calculations can be very expensive owing to the stiffness of the rate equations, a number of approaches for evaluation of chemical source terms are being tested. These include: direct solution of multi-step kinetics using solvers for stiff ODE's; lookup table based on source equation solutions; instantaneous kinetics based on ignition temperature.

2.3.2 Spray Production: Spray characteristics and droplet behavior are known to play a key role in determining stability behavior. Droplets are produced by disintegration of a liquid core injected into the combustor. Liquid core behavior is therefore expected to control the droplet and spray distribution. Role of injection mechanisms is illustrated in Figure 1 for two methods of introducing droplets into the computational domain. It is seen that considerations of liquid core behavior leads to a substantially different spray geometry.

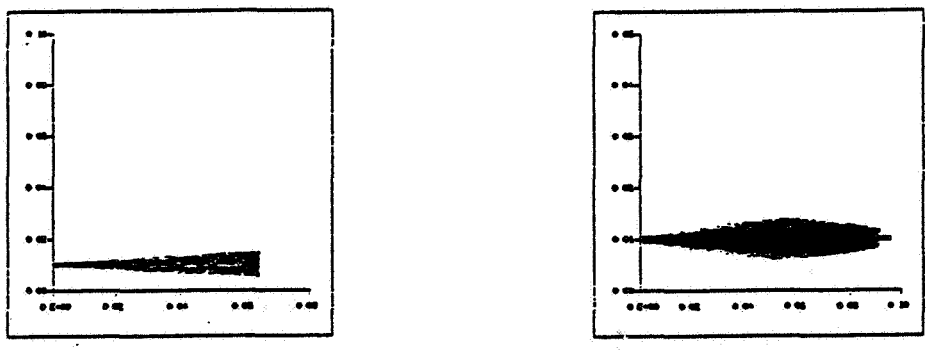

(a) (b)

Figure 1. Spray Shape Due to Two Modes of Injection (a) droplets injected individually from the left; (b) droplets injected from liquid core behavior calculations

Liquid Core: In the context of liquid rocket motors, atomization is typically achieved through breakup of liquid sheets and/or jets. This is true for impinging jets and shear-coaxial or swirl coaxial injectors. The common feature of such mechanisms is that before the breakup, the initial liquid stream has one dimension much smaller than the others: sheet thickness or the jet diameter. This disparity in dimensions is exploited by allowing the reduction in the problem dimensionality, essentially be constraining the fluid motion in the thin direction. This constraining is usually performed by integration of quantities such as velocity across the thickness conservation equations for mass, three momentum components and energy are:

$$\varphi + \varphi\left(u_x + u_y\right) = 0 \quad ; \quad \rho\varphi\dot{u} = -p_x + (\hat{p} - q)\beta_x - \bar{p}\alpha_x \; ; \; \rho\varphi\dot{v} = -p_y + (\hat{p} - q)\beta_y - \bar{p}\alpha_y \quad ;$$
$$\rho\varphi\dot{\lambda} = -\rho g\varphi - \hat{p} + q + \bar{p} \quad ; \quad \frac{1}{12}\rho\varphi\dot{\varphi} = \frac{p}{\varphi} - \frac{1}{2}(\hat{p} - q + \bar{p}) \qquad (4)$$

In the above equations the dot represents the material derivative. The surface tension q is a function of local liquid surface curvature. Position of top and bottom surfaces and the local thicknesses of the sheet are denoted by β, α and φ, respectively. The x,y,z velocity components are represented by u, v, and λ, respectively.

A simplified treatment of this system assuming small curvatures and axial pressure gradients has been tested for the case of a developing sheet in an axial acoustic field. The results are shown in Figure 2.

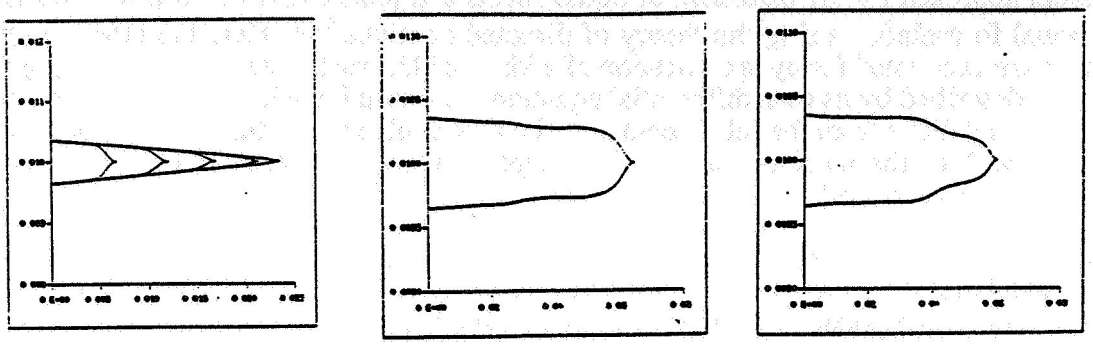

Figure 2. Liquid Sheet in an Acoustic Field; (a) time history of sheet development in a quiescent atmosphere; (b) snapshot of sheet geometry in an acoustic field; (c) snapshot of sheet geometry in an acoustic field with combustion

The figure shows that the simple model is capable of responding to interactions with highly transient gas-phase field.

In rocket engine combustion, transverse pressure oscillations are expected to be of particular importance. Experiments carried out at MSFC indicate that acoustic fields can significantly alter a sheet's geometry. Figure 3 shows some representative behavior of thin liquid sheets in a transverse acoustic field.

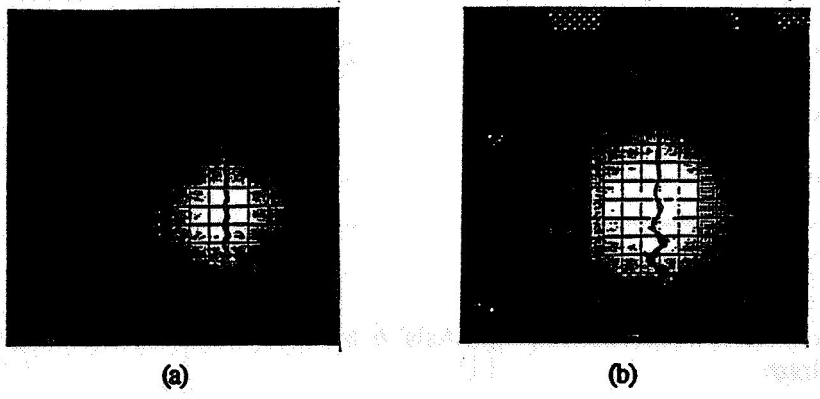

Figure 3. Shape of a Liquid Sheet Under Transverse Acoustic Oscillations at (a) 1218.54 Hz, 146 dB; (b) 748.34 Hz, 147.69 dB

The figure shows that proper frequency matching can result in severe sheet distortions. It is interesting to note that in this configuration, sheet deformation does not necessarily lead to increased droplet production. Computations are currently being conducted to simulate this behavior numerically using equation (4).

Sheet models obtained from 3-D considerations are inexact by definition, and their corresponding equations are not necessarily invariant under superimposed rigid body motions[6] (SRM). This is in contrast to the original 3D models which preserve such invariance. This is true from the constitutive as well as field equation point of view. This is of practical importance since invariance requirements may result in a different set of differential equations[7].

A different approach for the treatment of liquid sheets and jets involves an a-priori two and one-dimensional formulation using the theory of directed continua.[7-10]. Here the effects in the thin dimension are accounted for by specification of additional kinematic (vector) fields,directors, each of which is described by its own differential equation. Constitutive relations are also two and one-dimensional and differ from the full three-dimensional formulations in that they may depend on the medium as well as the local geometry. This approach for solution of liquid core behavior is currently being investigated.

Liquid core calculations are performed using the Jet Embedding technique. This involves a separate calculation of the liquid phase, using the gas-phase velocity temperature and pressure data. Gas-phase data is interpolated unto a separate liquid-core computational mesh.

Droplet Motion: Liquid core calculations are followed by droplet injection. In a current implementation, droplet dynamics include: viscous and quasi-steady heatup of motion are solved for each droplet. This model is capable of displaying interactions with acoustic waves, as shown in Figures 4 , 5, and 6. The figures show distortion of a spray by an axial acoustic wave (Figure 4); distortion of a droplet stream by a transverse acoustic wave (Figure 5); and droplet induced triggering of a shock in axial acoustic wave propagation.

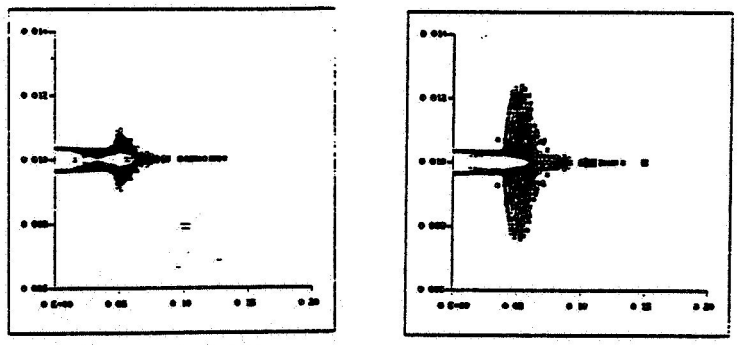

Figure 4. Spray Deformation in a Resonant Tube with Axial Acoustic Waves for: (a) unreacting flow and (b) flow with heat release

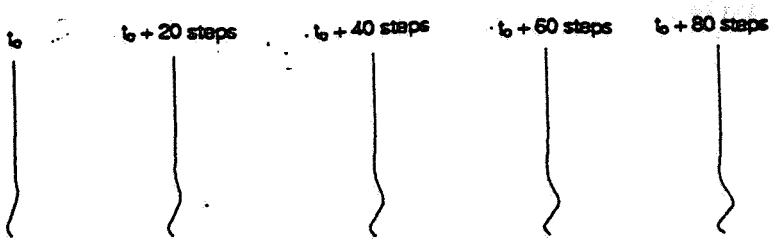

Figure 5. Droplet Stream in a Transverse Acoustic Field

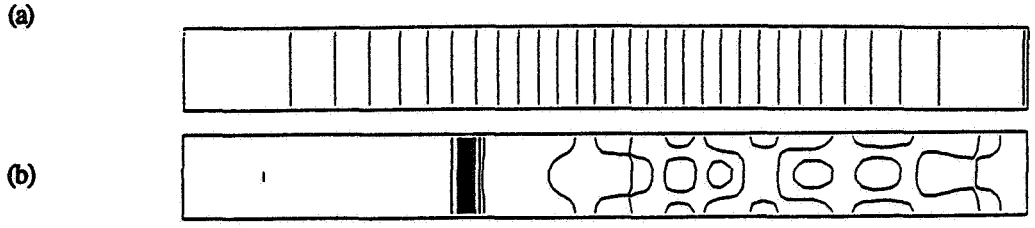

Figure 6. Pressure Contours in a Resonant Tube with Axial Acoustic Waves for (a) base flow with no spray and (b) flow with spray

3. CONCLUSIONS

The numerical model being developed during the course of this work, has shown strong coupling between acoustic waves and spray motion. The model is currently undergoing systematic parametric and verification studies for two and three-dimensional non-reacting and reacting flows. Liquid sheet (and jet) formulations, such as ones described by Equation s(4) are being developed for shear coaxial and impinging element injectors. Parametric studies will be conducted to quantify the dependence of combustion instabilities on: vaporization rate, droplet stripping rate model, droplet size spectrum, chemical kinetics, and liquid core formulations. Tests are also planned for comparisons with experimental data in single and multi-element injection configurations.

4. ACKNOWLEDGEMENTS

We thank Dr. R. Eskridge, NASA MSFC for performing and allowing us to use his experimental data. We also thank Dr. J. Hutt, NASA MSFC Contract Monitor, for his continued support.

5. REFERENCES

1. Levine, R.S., "Development Problems in Large Liquid Rocket Engines," Third AGARD, 1958.
2. Lambiris, S., et al, "Stable Combustion Processes in Liquid Propellant Rocket Engines," 5th AGARD, 1963.
3. Strang, G., SIAM J. Numerical Analysis, vol. 5, no. 3, September.
4. Spalding, D.B., The Aeronautical Quarterly, X, pp. 1-27, Feb. 1959.
5. Bittner, D.A., Brokaw, R.S., J. Amer. Rocket Soc., vol. 30, no. 2, 1960.
6. Green, A.E. and Naghdi, P.M., *J. of Elasticity*, vol. 9, pp. 1, 1979.
7. Naghdi, P.M., *Proc. 12th Symp. on Naval Hydrodynamics*, National Academy of Sciences, Washington DC, pp. 500, 1979.
8. Naghdi, P.M., *J. of Non-Newtonian Fluid Mechanics*, vol. 5, pp. 233, 1979.
9. Green, A.E., *Int. J. Engng. Sci.*, vo.. 14, pp. 49, 1976.
10. Green, A.E. and Naghdi, P.M., *Proc. R. Soc. London A.*, vol. 347, pp. 447, 1976.

427230
Pg 5

N95- 70906

VELOCITY-MODULATION ATOMIZATION OF LIQUID JETS

John L. Dressler
Fluid Jet Associates
1216 Waterwyck Trail
Spring Valley, OH, U.S.A.

SUMMARY A novel atomizer based on high-amplitude velocity atomization has been developed. Presently, the most common methods of atomization can use only the Rayleigh instability of a liquid cylinder and the Kelvin-Helmholtz instability of a liquid sheet. Our atomizer is capable of atomizing liquid jets by the excitation and destabilization of many other higher-order modes of surface deformation. The potential benefits of this sprayer are more uniform fuel air mixtures, faster fuel-air mixing, extended flow ranges for commercial nozzles, and the reduction of nozzle plugging by producing small drops from large nozzles. The piezoelectric driver can be included into schemes for feedback control of combustion instabilities. To create this atomization by high-order modes, we excite the jet both spatially and temporally. We exploit the mathematical similarity between a compressible gas and a liquid jet to create steepening of the waves on the liquid jet. If the applied velocity perturbation is sufficiently large, the pulse steepens into a form of shock and atomization occurs. The temporal excitation of the fluid jet is created by a piezoelectric driver. The spatial excitation of the fluid jet is created by placing perturbations in the perimeter of the electroformed nozzle that forms the jet. No electrostatic force or air supply is used. The atomization of many liquid jets in the forms of cylinders, sheets, cones, and rectangles has been observed. Quantitative measurements of the sprays from several of these electroformed nozzles and the spray from a commercial conical nozzle have been made. The spray from a commercial nozzle can be drastically altered, with respect to the wavelength of the drop clusters and the spatial distribution of the fluid mass. Sprays from circular nozzles have a Sauter mean diameter less than half the jet (equivalent) diameter. A rectangular orifice requires lower electrical power to generate a spray than a circular orifice. The sprayer has been used with flow rates from .06 ml/min. to 30 gallons/hr. Sprays with a Sauter mean diameter of
This atomizer is suitable for both fundamental studies and practical applications.

DISCUSSION Many types of drop generators and sprayers have been developed for diverse applications such as ink-jet printing, calibration standards, agricultural spraying, spray drying, and combustion. These drop generators use many methods for creating

the spray such as air-blast, electrostatic forces, electromechanical vibrations, mechanical shutters, and impact of the fluid with a wall or another fluid jet. Most commonly sprays are formed using pressure nozzles that create a cone or sheet of fluid which atomizes due to contact with the surrounding air. Two naturally occurring instabilities that are frequently seen in spray formation are the Rayleigh capillary instability and the Kelvin-Helmholtz instability [1,2,3]. The Rayleigh instability is the sausage or varicose instability, driven by surface tension, that appears on a cylinder of fluid. The Kelvin-Helmholtz instability is the flag-flapping instability and it is driven by the difference in velocities of a fluid sheet and the surrounding air. The Kelvin-Helmholtz instability usually breaks the sheet into ligaments which then break into drops by the Rayleigh instability.

The problem with the Rayleigh instability is that the drops that form are usually twice the diameter of the initial fluid cylinder. To obtain small drops, a smaller cylinder must be formed.

The Kelvin-Helmholtz instability is commonly used by pressure-swirl atomizers [4] to produce fuel sprays for combustion. The instability causes the sheet to flap; consequently, the droplets tend to be concentrated in packets (or clusters), thereby making the spray spatially and temporally nonuniform [5]. The combustion of these clusters can lead to periodic variations in the heat-release rate and pressure in the combustor and, in turn, may result in various combustion problems such as combustion roar, combustion-driven oscillations, various pollutants formation, and even lower combustion efficiency.

POTENTIAL ATOMIZATION TECHNOLOGIES Rose [6] published photographs that show unstable, star-shaped,higher-order magnetohydrodynamic modes on a cylindrical plasma. Chandrasekhar [3] shows the similarity between these unstable modes on cylindrical plasmas and stable modes on liquid cylinders. Electrohydrodynamic and magnetohydrodynamic instabilities of liquid jets [7] and liquid sheets have been studied because of their similarity to magnetohydrodynamic instabilities in plasma containment devices for thermonuclear power generation. The idea was to sense the instability, in both space and time, and create a drive signal, in both space and time, that eliminates the liquid instability.

Another potential concept for atomization is shock formation. Shapiro [8], in his video lecture series, explains how waves propagating along a cylindrical jet of liquid are mathematically similar to waves propagating in a compressible gas. One can therefore look at a cylindrical liquid column as analogous to a compressible gas, with the pressure-density relationship for the gas replaced by a pressure-radius relationship for the jet.

Several papers describe the application of large perturbations to liquid jets and the atomization resulting from the steepening of the pulse front. By dropping a weight, Dunne and Cassen [9] probably were first in creating what may be described as a shock on a cylindrical jet and creating a spray. Others have used magnetic drivers to improve the shock forming process [10,11].

For our approach to atomization, we reverse the control process used in the earlier research and apply a drive signal in space and time to make the fluid jet unstable. Our temporal drive signal is sufficiently large that the pulse steepens into a discontinuity that atomizes the jet. We can drive the fluid cylinder unstable in the higher modes which Rose showed to be unstable on a cylindrical plasma.

DROP GENERATOR CONSTRUCTION The key development of this project has been the design of the piezoelectric driver which produces large velocity perturbations on the liquid jet [12].

The high-amplitude velocity-modulation atomizer assembly, shown in Figure 1, and described in detail [13], consists of a piezoelectric crystal driver in a circular fluid manifold with an orifice plate across the end of the manifold. The model of the current atomizer contains four functional elements:

(1) the piezoelectric transducers which receive the electrical signal and convert it to mechanical motion,

(2) a mechanical structure that amplifies the motion produced by the transducers,

(3) a pump that converts the amplified mechanical motion to a pressure perturbation in the working fluid, and

(4) a nozzle that creates a fluid stream whose velocity is modulated by the pressure perturbation.

The mechanical structure is a resonant device which can exhibit large mechanical deflections at specific resonant frequencies. At these resonant frequencies, the current and voltage to the piezoelectric transducer are in phase; thus, energy loss is minimized. Unlike other ultrasonic atomizers that have fluid manifolds designed to be resonant at the operating frequency, the pump in this device does not have a resonance at the operating frequency.

NOZZLE CONSTRUCTION We use a photofabrication process to form nozzles of practically any shape or size. We have made circular nozzles as small as 12 microns in diameter. We have also made rectangular nozzles which contain width perturbations. Better atomization is obtained if the nozzle perimeter has perturbations placed on it.

These perturbations provide initial conditions for the high-order modes which can then be driven to create the jet instabilities.

QUANTITATIVE TESTS Takahashi has made quantitative measurements of the sprays produced by photofabricated nozzles [14] and also from a commercial cone nozzle [15]. He found that with a round nozzle, the spray had a Sauter mean diameter less than half the jet diameter. Less electrical power was required to create sprays from a rectangular nozzle than from a circular nozzle. The range of flow rates which gave acceptable atomization from a commercial nozzle was extended and the spatial distribution of the spray was expanded.

ACKNOWLEDGMENTS This work was supported by the U.S. Air Force, Wright Laboratory, Aero Propulsion and Power Directorate, Wright-Patterson AFB, under Contracts F33615-92-C-2207 and F33615-89-C-2973. (Technical Monitors: C. W. Frayne, W. M. Rocquemore).

REFERENCES

1. J. W. S. Rayleigh. On the instability of jets. *Proc. London Math. Society*, 10:4, 14-Nov 1878.

2. G. D. Crapper, Norman Dombrowski, and G. A. D. Pyott. Large amplitude Kelvin-Helmholtz waves on thin liquid sheets. *Proceedings of the Royal Society, London*, A(342):209–224, 1975.

3. S. Chandrasekhar. *Hydrodynamic and Hydromagnetic Stability.* Oxford University Press at the Clarendon Press, Ely House, London W.I., 1961.

4. C. J. Clark and N. Dombrowski. On the formation of drops from the rims of fan spray sheets. *Aerosol Science*, 3(3):173–183, 1972.

5. Adel Mansour and Norman Chigier. Disintegration of liquid sheets. *Physics of Fluids A*, 2(5):706–719, May 1990.

6. David J. Rose and Jr. Melville Clark. *Plasmas and Controlled Fusion.* The M.I.T. Press, Massachusetts Institute of Technology, Cambridge, Massachusetts, Feb 1961. Chap. 14, Chap. 15.

7. Joseph M. Crowley. Stabilization of a spatially growing wave by feedback. *The Physics of Fluids*, 10(6):1170–117, Jun 1967.

8. A.H. Shapiro. MIT Video Course, Fluid Dynamics, Part 1

9. Brian Dunne and Benedict Cassen. Velocity discontinuity instability of a liquid jet. *Journal of Applied Physics*, 27(6):577–582, Jun 1956.

10. L. Crane, S. Birch, and P. D. McCormack. The effect of mechanical vibration on the break-up of a cylindrical water jet in air. *Britt. J. Appl. Phys.*, 15(6):743–751, Jun 1964.

11. Milton Van Dyke. *An Album of Fluid Motion*, volume 0-91576-03-7. The Parabolic Press, P.O. Box 3032, Stanford CA, 1982. Photograph 149.

12. J. L. Dressler. *U.S. Patent 5,248,087*. 28-Sep-1993.

13. J. L. Dressler. WL-TR-93-2049, Mar 1993.

14. F. Takahashi, W. J. Schmoll, J. L. Dressler. Characterization of a velocity-modulation atomizer. *Review of Scientific Instruments*, in press.

15. F. Takahashi, W. J. Schmoll, J. L. Dressler. Characteristics of a velocity-modulated pressure swirl spray measured by the phase doppler method. *Journal of Propulsion and Power*, in press.

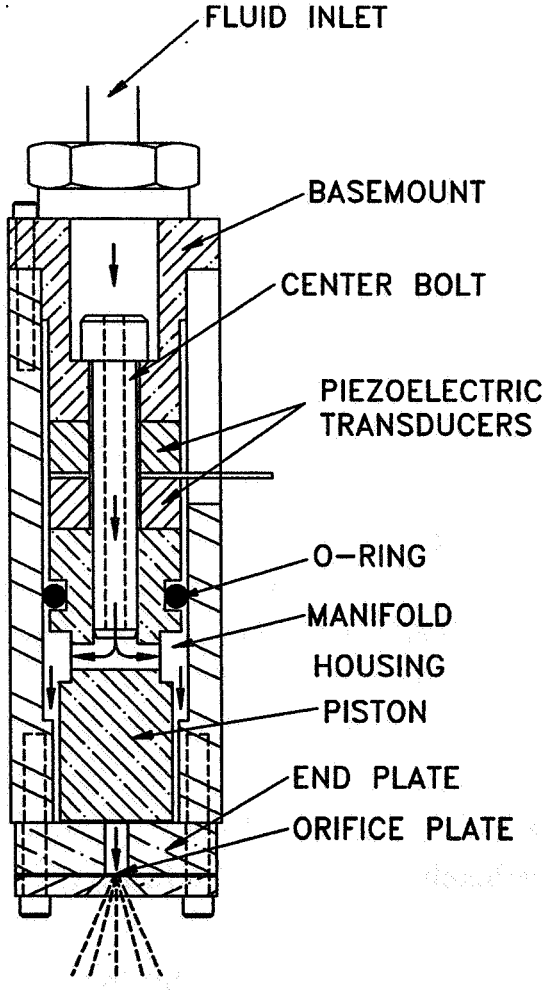

Figure 1: Schematic of the high-amplitude velocity-modulation atomizer.

Pg 5 6
427232

N95- 70907

Picosecond Imaging of Sprays

L. Wang*, X. Liang*, P. Galland*
Kevin Breisacher and Larry Liou, NASA Lewis , Cleveland, Ohio
P. P. Ho* and R.R. Alfano*, CCNY IUSL (NASA/IRA), New York, N.Y.*

Summary

Preliminary results from applying a Kerr-Fourier imaging system to a water/air spray produced by a shear coaxial element are presented. The physics behind ultrafast time-gated optical techniques is discussed briefly. A typical setup of a Kerr-Fourier time gating system is presented.

Discussion

In attempts to characterize the spray of a simulated coaxial rocket engine injector[1] it became clear that it was not possible to make drop size measurements any closer than 2 in. downstream of the injector face. The applicability of dropsize correlations developed from cold flow measurments 2 in. downstream of the injector face is debatable. The details of the evolution from jet to spray (critical to modeling) are lost. Ultrafast optical imaging provides the possibility of making diagnostic measurements in dense sprays.

Various ultrafast time-gated optical imaging techniques[2-6] such as Kerr-gate, holography, streak camera, etc., have been used in attempts to identify hidden obects in turbid media for use in medical diagnosis. Recently, a collaborative effort was established between researchers at Lewis Research Center and the Institute for Ultrafast Spectroscopy and Lasers (NASA/IRA) at the City College of New York to see if these techniques might be applicable to making diagnostic measurements in the dense sprays encountered in liquid rocket engines.

When ultrashort laser pulses are incident upon a slab of scattering medium the transmitted pulses consist of a ballistic component, a diffuse component, and a snake component. The intensity of the ballistic component (consisting of photons traveling along a straight line path) is attenuated exponetially with the thickness of the material they are traversing.This attenuation puts a severe limitation on the use of ballistic photons in imaging applications. The diffuse component consists of photons that have been scattered randomly in all directions and have different path histories through the material. The snake component consists of early-

arriving photons that have undergone only a few scatterings along an almost straight path through the material. The snake photons form the early component of the diffuse photons and carry information about the optical characteristics of the material they have traversed. Time resolved detection techniques separate these snake photons from the rest of the diffuse component and use them to construct images of objects in the material with different optical characteristics.

As part of the collaborative effort between Lewis and CCNY, a spray rig (Figure 1.) has been installed at the Mediphotonics Laboratory at CCNY. The spray rig consists of a single, water/air coaxial element spraying into a plexiglass test section. The inner diameter of the water tube is .078" and the inner and outer diameters of the air annulus .125" are .219" and respectively. The dimensions are similar to those used in the test program of refernce 1. The test section is approximately high and 3.75 by 8 inches. Provisions have been made for optical access through two windows at the top of the test section near the injector face.

In the first phase of this effort a Kerr-Fourier picosecond imaging system developed by CCNY will be used to image the water jet through the dense spray of the coaxial element. The Kerr-Fourier imaging system is shown in Figure 2. The imaging system consists of three main parts: a laser source, an optical Kerr gate (which acts as an ultrafast shutter) , and a detector. A picosecond mode locked Nd^+ glass laser laser system which emits a 1054 nm 10 ps laser pulse is used as an illumination source. Its second harmonic (527 nm)is used as the gating source. The Kerr gate consists of a pair of calcite crossed polarizers and a 1cm CS_2 Kerr cell. A cooled CCD camera system was used to detect the gated image.

Figures 3 and 4 show the preliminary results obtained with the ultrafast imaging system. All flowrates quoted are approximate due to unsteadiness in the supply system. Figure 3 shows an image of a water jet at approximately 1.5 cm downstream of the injector face. The water and air flowrates were 10 g/s and .8 g/s respectively. The image system configuration used to produce Figure 3 did not include a Kerr gate. The circular border corresponds to the 1 cm diameter region illumunated. At this relatively low air flowrate, the jet remains largely intact and its sinuous, helical structure is evident. The contrast obtained is at least as good as that obtained with laser sheet imaging. A result obtained with the Kerr-Fourier imaging system is displayed in Figure 4. The water and air flowrates were 5 g/s and 1.1 g/s respectively. In Figure 4, the imaging region is at the injector face. The tip of the water tube is visible as it

protruded several millimeters from the injector face. The tube was extended from the injector face so that the imaging system would not encounter liquid hanging from from the injector face due to recirculated drops. At this higher air flowrate, the stripping of liquid ligaments and drops is evident. However, a contiguous liquid jet remains. Image contrast remains relatively sharp but it is apparent that better resolution is required in imaging individual drops or ligaments. CCNY is currently at work on a lens arrangment for increased resolution. Further work will include attempts to image regions of the spray donstream of the jet at this higher resolution.

References

1) Zaller, M. Z. and Klem, M. D., "Shear Coaxial Injector Spray Characterization"
2) Wang, L., Ho, P.P., Liang, H. D., and Alfano, R. R., "Kerr Fourier imaging of hidden objects in thick turbid medium", Optics Letters, 1993.
3) M. A. Duguay and Mattick, Applied Optics, 10, 1971.
4) Alfano, R. R., Liang, X., Wang, L. and Ho, P.,"Time Resolved Imaging of Translucent Droplets in Highly Turbid Media",Science, pp. 1913-1915, June 1994.
5) Rebane, A. and Feinberg, J., Nature, 351, 1991.
6) Yoo, K. M. and Alfano, R. R., Opt. Letters, 15, 1990.

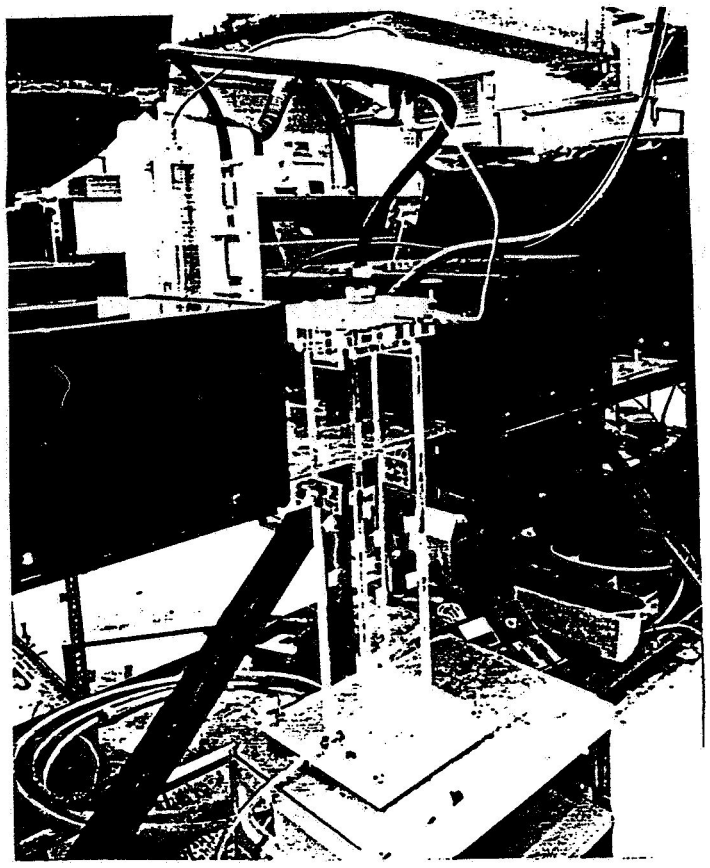

Figure 1. - Water / Air Spray Rig

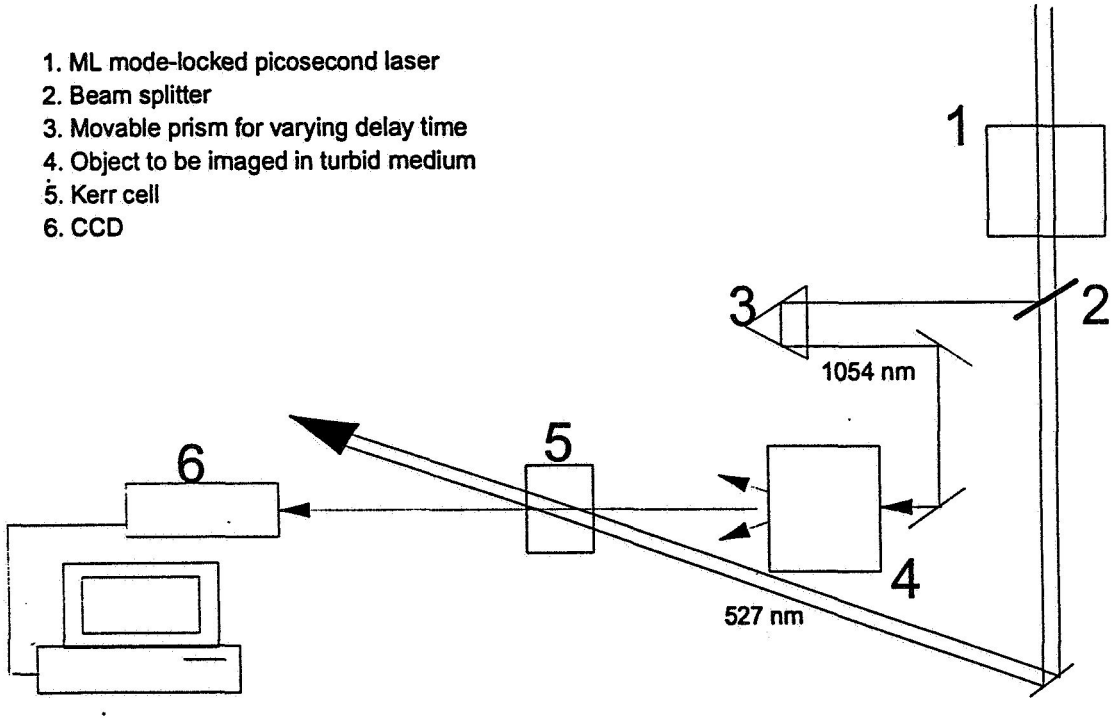

Figure 2. - Kerr - Fourier Imaging Setup (CCNY)

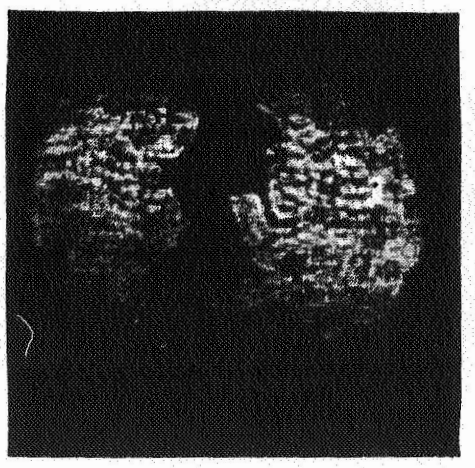

Figure 3. - Non - Kerr gated image

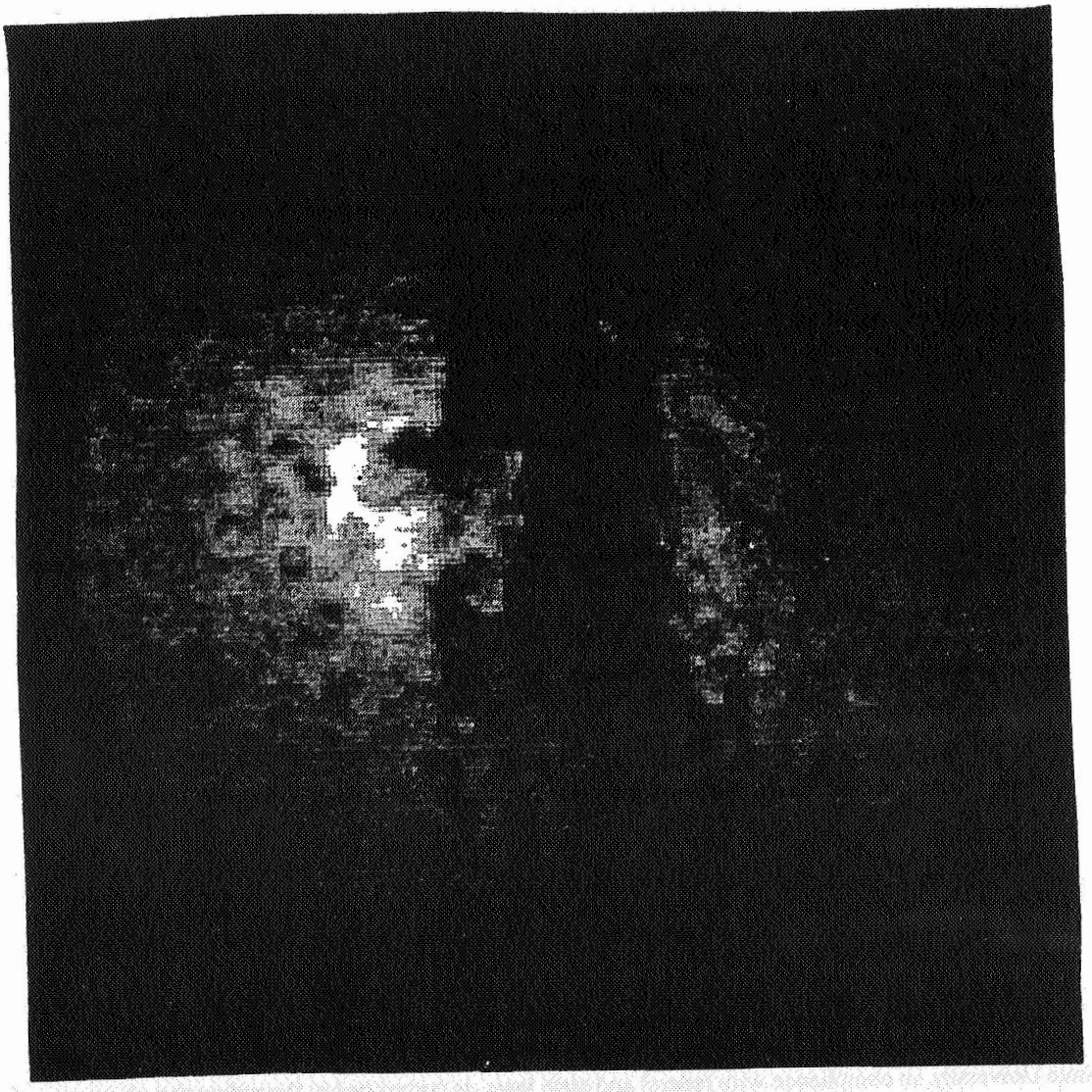

Figure 4. - Kerr gated jet image

The Pennsylvania State University, in compliance with federal and state laws, is committed to the policy that all persons shall have equal access to programs, admission, and employment without regard to race, religion, sex, national origin, handicap, age or status as a disabled or Vietnam-era veteran. Direct all affirmative action inquiries to the Affirmative Action Office, 201 Willard Building, University Park, PA 16802; (814) 863-0471.
U. Ed. ENG 91-79